

Encoding a Qubit into an Oscillator with Near-Term Experimental Devices

Weigand, D.J.

DOI

[10.4233/uuid:72abf99f-dd2d-42a1-8c59-7a83870c9d3c](https://doi.org/10.4233/uuid:72abf99f-dd2d-42a1-8c59-7a83870c9d3c)

Publication date

2020

Document Version

Final published version

Citation (APA)

Weigand, D. J. (2020). *Encoding a Qubit into an Oscillator with Near-Term Experimental Devices*. [Dissertation (TU Delft), Delft University of Technology]. <https://doi.org/10.4233/uuid:72abf99f-dd2d-42a1-8c59-7a83870c9d3c>

Important note

To cite this publication, please use the final published version (if applicable).
Please check the document version above.

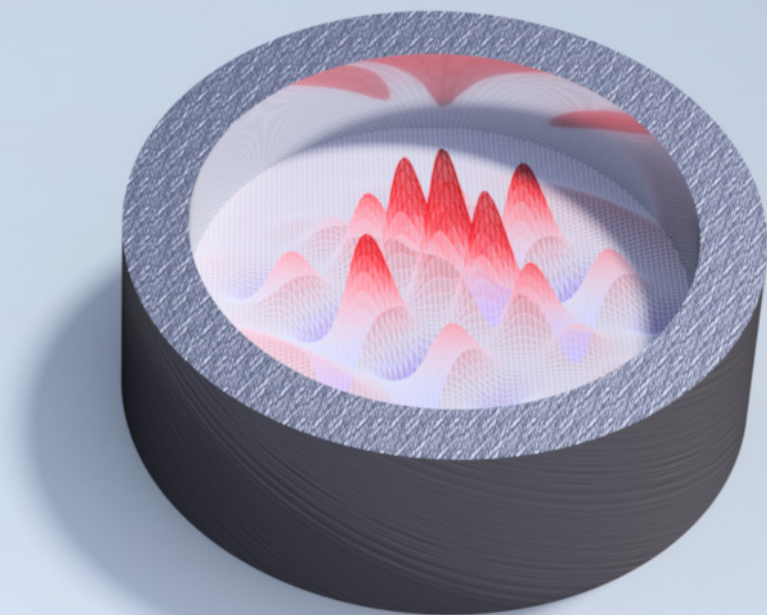
Copyright

Other than for strictly personal use, it is not permitted to download, forward or distribute the text or part of it, without the consent of the author(s) and/or copyright holder(s), unless the work is under an open content license such as Creative Commons.

Takedown policy

Please contact us and provide details if you believe this document breaches copyrights.
We will remove access to the work immediately and investigate your claim.

Encoding a Qubit into an Oscillator with Near-Term Experimental Devices



Daniel J. Weigand

ENCODING A QUBIT INTO AN OSCILLATOR WITH NEAR-TERM EXPERIMENTAL DEVICES

Dissertation

for the purpose of obtaining the degree of doctor
at Delft University of Technology
by the authority of the Rector Magnificus, Prof. dr. ir. T.H.J.J. van der Hagen,
chair of the Board for Doctorates
to be defended publicly on
Wednesday 2 December 2020 at 10:00 o'clock

by

Daniel Jonathan WEIGAND

Master of Science RWTH Aachen University, RWTH Aachen University, Germany,
born in Neustadt an der Weinstraße, Germany.

This dissertation has been approved by the promotor.

Composition of the doctoral committee:

Rector magnificus,	chairman
Prof. dr. B. M. Terhal,	Delft University of Technology, promotor

Independent Members:

Dr. P. Campagne-Ibarcq	INRIA Paris
Prof. dr. A. L. Grimsmo	University of Sydney
Prof. dr. R. Hanson	Delft University of Technology
Prof. dr. M. Müller	RWTH Aachen University
Prof. dr. G. A. Steele	Delft University of Technology



Keywords: Quantum Error Correction, Bosonic Codes, Circuit QED

Front & Back: The Wigner function of an approximate GKP state arising from squeezed vacuum states.

Copyright © 2020 by D. J. Weigand

ISBN 978-94-6421-139-9

An electronic version of this dissertation is available at
<http://repository.tudelft.nl/>.

CONTENTS

Summary	ix
Samenvatting	xi
Preface	xiii
1 Introduction	1
1.1 Error Correction	4
1.1.1 Classical Error Correction	4
1.1.2 Quantum Error Correction	5
1.1.3 Quantum Error Correction with Superconducting Qubits	7
1.2 Bosonic Encodings of Qubits	9
1.3 Applications Related to the Gottesman - Kitaev - Preskill (GKP) Code	13
1.3.1 Maximal Violation of Bell Inequalities	14
1.3.2 The von Neumann Lattice	14
1.3.3 Displacement Sensing Below the Heisenberg Limit	15
1.3.4 Protecting Gaussian Information	15
1.4 Outline of the Thesis	16
2 Theoretical Background	23
2.1 Fundamental Definitions and Derivations	24
2.1.1 Quantum Optics	24
2.1.2 The Gottesman-Kitaev-Preskill (GKP) Code	25
2.1.3 Stabilizers, Logical Operations, and Code States of the GKP Code	27
2.1.4 Logical and Physical Qubits	27
2.2 Representations of GKP Code States	28
2.2.1 Position or Momentum Wave Function	28
2.2.2 Shifted Code States.	30
2.2.3 GKP Code States in the Fock Basis	32
2.3 Quality Measures for the GKP Code	33
2.3.1 Ideal Decoder	33
2.3.2 Why the Overlap is Not a Good quality Measure	34
2.3.3 Holevo Phase Variance	35
2.3.4 Characterizing Wave Functions in a Quadrature Basis	37
3 Encoding a GKP Qubit using Phase Estimation	43
3.1 Phase Estimation	44
3.1.1 Standard Phase Estimation.	44
3.1.2 Phase Estimation by Repetition	46
3.1.3 Adaptive Phase Estimation.	46
3.1.4 Maximal Information Gain Strategy	49

3.2	Implementations of a Controlled Displacement	50
3.2.1	Direct Controlled Displacement	50
3.2.2	Controlled Displacement by Rotation	51
3.2.3	Controlled Displacements in Trapped Ions.	55
3.3	Numerical Analysis of Noise During Preparation and Measurement	55
3.3.1	Choice of Phase Estimation	56
3.3.2	Hamiltonian and Noise Model	56
3.3.3	Simulation Results	58
4	Generating Grid States from Schrödinger Cat States without Post-Selection	63
4.1	Background	65
4.1.1	Grid States	65
4.1.2	Effective Squeezing Parameters	67
4.1.3	Adaptive Phase Estimation.	68
4.2	Breeding	69
4.2.1	Slow Breeding	70
4.2.2	Efficient Breeding	71
4.3	Analytic Discussion of Breeding.	74
4.3.1	Scale-Dependent Shifted Grid States.	75
4.3.2	Breeding Shifted Grid States	76
4.3.3	Choice of Wave Function $\Theta(u, v)$	77
4.3.4	Choice for Wave Function $V(u)$	79
4.4	Asymptotic Behavior	80
4.5	Simulation	83
4.6	Discussion	85
5	Realizing Modular Quadrature Measurements via a Tunable Photon-Pressure Coupling in Circuit-QED	89
5.1	Preliminaries	91
5.2	Overview of Measurement Protocol	92
5.2.1	GKP Qubit Readout	94
5.2.2	Why Probing the Ancilla Oscillator's Frequency Reveals the Wrong Information	94
5.3	Circuit-QED Setup	96
5.3.1	Previous Circuit-QED Work on Photon-Pressure and Longitudinal Coupling.	96
5.3.2	Mechanical Analogue	97
5.3.3	Circuit Analysis and Approximations.	98
5.3.4	Release of Ancilla Oscillator State	104
5.4	Parametric Flux Drive	104
5.4.1	Parametric Flux Drive	105
5.4.2	Use of a Microwave Drive	107
5.5	Modeling The Modular Quadrature Measurement	107
5.5.1	Effective Squeezing	108
5.5.2	Measurement Squeezing Strength	109

5.6	Heterodyne Measurement via Release of Coherent Oscillator State into a Transmission Line	112
5.7	Effective Squeezing with Vacuum Input State	116
5.8	Noise and Imperfections	117
5.8.1	Photon Loss in Ancilla Oscillator during Photon-Pressure Interaction	118
5.8.2	Comparison with Sequential-Qubit Phase Estimation Measurement and Photon Loss on Target Oscillator	119
5.8.3	Readout Loss.	121
5.8.4	Expansion of the Circuit Hamiltonian	122
5.8.5	Third-Order Nonlinearity	123
5.8.6	Flux Noise	125
5.8.7	Flux Noise with Reduced Drive Amplitude	126
5.9	Discussion	126
6	Conclusion and Outlook	133
6.1	Conclusion	134
6.2	Outlook	136
A	Appendix	139
A.1	Details of Numerical Simulations	140
A.1.1	Stabilizer Measurements using Phase Estimation	140
A.1.2	Simulation of Breeding.	140
A.1.3	Simulations of Modular Quadrature Measurements	142
A.2	Relating a Photon-Pressure Coupling to Phase Estimation	143
A.2.1	Initial State.	143
A.2.2	Photon-Pressure Hamiltonian	144
A.2.3	Heterodyne Measurement	145
	Curriculum Vitæ	149
	List of Publications	151

SUMMARY

A universal, large-scale quantum computer would be a powerful tool with applications of high value to mankind. For example, such a computer could significantly speed up the search for new medications or materials. However, the error rates of current qubit designs are simply too large to enable interesting computations. Therefore, both error correction and improved designs of qubits are needed.

In 2001, Gottesman, Kitaev and Preskill proposed an encoding (GKP code) where a qubit is stored in a harmonic oscillator — a system that can be controlled and manufactured with high precision, and therefore have comparatively high coherence times. Moreover, the code offers good protection against losses, a simple gate set, and error correction circuits that are comparatively easy to implement. The drawback is that encoding a qubit into a GKP code state is a challenging task. In this thesis, we develop efficient schemes to encode a GKP qubit.

Bosonic codes, where a qubit is stored in an oscillator, and in particular the GKP code are still relatively unknown. Therefore, we will start the thesis with an overview of the field, and provide the reader with the tools to analyze a GKP code, as these are quite different from standard error correcting codes. A tool which is important to understand, and that describes a protocol that encodes a GKP qubit is the so-called phase estimation algorithm. This algorithm allows to measure the eigenvalue of any unitary operation, and is one of the cornerstones of quantum information. We will show how phase estimation can be applied to encode a GKP qubit, and what the requirements for an experiment attempting to do so are.

A major advantage of the GKP code over other encodings is that it can tolerate significant photon loss before the encoded information is lost. In addition, states that are closely related to the GKP qubit can be used to violate Bell's inequalities (i. e. prove the presence of entanglement), even in the presence of large noise. Both these applications make the code particularly interesting in the optical regime, where error correction usually cannot be done while the signal is travelling. In this thesis, we will analyze an encoding protocol originally proposed by H. M. Vasconcelos, L. Sanz, and S. Glancy, [Optics Letters 35, 3261 \(2010\)](#) that relied on post-selection, and show that any output state can be used as a GKP code state with a simple change of frame, providing an exponential speedup.

In 2019, two separate experiments generated a GKP code state for the first time: C. Flühmann et al., [Nature 566, 513 \(2019\)](#) realized a GKP qubit in the motional mode of a trapped ion, while P. Campagne-Ibarcq et al., [Nature 584, 368 \(2020\)](#) realized it with a transmon qubit coupled to a microwave cavity. However, both these experiments employ phase estimation, which is slow because it requires many measurements in sequence. We propose a circuit that allows a single-shot measurement of the GKP stabilizers, and analyze the performance of such a measurement as well as the impact of noise.

SAMENVATTING

Een universele, grootschalige kwantumcomputer zou een krachtig hulpmiddel kunnen zijn met toepassingen die van grote waarde zijn voor de mensheid. Zo'n computer zou bijvoorbeeld het zoeken naar nieuwe medicijnen of materialen aanzienlijk kunnen versnellen. De foutenpercentages van de huidige qubit-ontwerpen zijn echter gewoonweg te groot om interessante berekeningen mogelijk te maken. Daarom zijn zowel foutcorrectie als verbeterde ontwerpen van qubits nodig.

In 2001 hebben Gottesman, Kitaev en Preskill een codering (GKP-code) voorgesteld waarbij een qubit wordt opgeslagen in een harmonische oscillator — een systeem dat met hoge precisie kan worden gecontroleerd en gefabriceerd, en daardoor relatief hoge coherentietijden heeft. Bovendien biedt de code een goede bescherming tegen energie verlies, een eenvoudige poortset en foutcorrectie circuits die relatief eenvoudig te implementeren zijn. Het nadeel is dat het coderen van een qubit in een GKP-codetoestand een uitdagende taak is. In dit proefschrift ontwikkelen we efficiënte schema's om een GKP qubit te genereren.

Bosonische codes, waarbij een qubit in een oscillator wordt opgeslagen, en met name de GKP-code zijn nog relatief onbekend. Daarom beginnen we de scriptie met een overzicht van het veld, en geven we de lezer de tools om een GKP code te analyseren, omdat deze heel anders zijn dan de standaard foutcorrectie codes. Een tool die belangrijk is om te begrijpen, en die een protocol beschrijft dat een GKP qubit codeert, is het zogenaamde “phase estimation” algoritme. Dit algoritme maakt het mogelijk om de eigenwaarde van elke unitaire bewerking te meten, en is een van de hoekstenen van de kwantuminformatie. We zullen laten zien hoe “phase estimation” kan worden toegepast om een GKP-qubit te coderen, en wat de vereisten zijn voor een experiment die dat probeert te doen.

Een groot voordeel van de GKP-code ten opzichte van andere coderingen is dat deze een significant foton verlies kan tolereren voordat de gecodeerde informatie verloren gaat. Bovendien kunnen staten die nauw verwant zijn aan de GKP qubit gebruikt worden om de ongelijkheden van Bell te schenden (d.w.z. de aanwezigheid van verstrengeling te bewijzen), zelfs in de aanwezigheid van grote ruis. Beide toepassingen maken de code bijzonder interessant in het optische regime, waar foutcorrectie meestal niet mogelijk is terwijl het signaal onderweg is. In dit proefschrift analyseren we een coderingsprotocol dat oorspronkelijk is voorgesteld door H. M. Vasconcelos, L. Sanz en S. Glancy, [Optics Letters 35, 3261 \(2010\)](#) en dat gebaseerd is op post-selectie, we laten zien dat elke uitgangstoestand kan worden gebruikt als een GKP code toestand met een eenvoudige verandering van het referentiekader, waardoor een exponentiële snelheidsverhoging wordt verkregen.

In 2019 hebben twee afzonderlijke experimenten voor het eerst een GKP-codetoestand gegenereerd: C. Flühmann e.a., [Nature 566, 513 \(2019\)](#) realiseerde een GKP qubit in de bewegingsmodus van een gevangen ion, terwijl P. Campagne-Ibarcq e.a., [Nature 584,](#)

368 (2020) het realiseerde met een transmon qubit gekoppeld aan een microgolffholte. In beide experimenten wordt echter gebruik gemaakt van “phase estimation”, die langzaam verloopt omdat er veel metingen achter elkaar nodig zijn. We stellen een circuit voor dat een single-shot meting van de GKP stabilisatoren mogelijk maakt, en analyseren de prestaties van zo’n meting en de impact van de ruis.

PREFACE

First of all, I would like to say a very big thank you to my supervisor, Barbara Terhal. She has always supported me over the years and also made a great choice for the topic of my thesis: It has been both interesting and challenging, and it was very exciting to see my field grow over the years. Back in late 2014 when I started with my Master's thesis, I would never have thought that bosonic codes would actually be used, and that I would have any impact — however small — on one of the first quantum error correction schemes with a proven benefit.

Over the years, I frequently witnessed Barbara's excellent sense for promising areas of research. In fact, she pointed out to me that having another look at the breeding protocol by Vasconcelos with our knowledge of phase estimation could be interesting. She also organized a lunch with Gary Steele, which was the first step towards chapter five. Barbara is excellent to work with. She was always patient with me, but gave me a kick or two when I needed it. She was always supportive and always fair.

Finally, I would like to thank her for recommending to apply for my current position with Pavel Bushev at Forschungszentrum Jülich. The transition from theoretician to experimentalist came with its own set of challenges, and has been nothing short of enjoyable so far.

I would also like to thank the other members of my committee, Phillipe Campagne-Ibarcq, Arne Grimsmo, Ronald Hanson, Markus Müller and Gary Steele, for reading this thesis and for all helpful comments.

A special mention goes to Phillipe and also to Christa Flühmann for making GKP states a reality in their labs. This thesis had the objective of finding experimentally “feasible” ways how the GKP code could become a reality, but it is still a very long way from a theory paper to an experiment, with many improvements needed along the way. It was absolutely amazing to hear that someone actually did it.

Another thanks goes to Gary along with Ines Corveira Rodrigues and Daniel Bothner for our discussions about their experiments and how a strong optomechanical coupling is realized — I think this reality check significantly improved chapter five.

Finally, I would like to thank Arne for organizing the Byron Bay Quantum Workshop 2019 together with Ben Baragiola and Josh Combes. It was a crowning event of my time as a PhD student, getting to know many more people from our growing community of error correction with bosonic codes.

Back in 2017, I was not exactly thrilled to leave Aachen and move to Delft. However, the warm welcome I received at Qutech helped me to settle in quickly, and the environment there has been ripe with great opportunities to interact with other people from the quantum information community. A special mention goes to my colleagues both from

Aachen and Delft: Francesco Battistel, Alessandro Ciani, Ben Criger, Joel Klassen, Xiaotong Ni, Daniel Otten, Manuel Rispler, Marco Roth, Christophe Vuillot and Yang Wang. You all have been great office mates, friends and teachers, and always had time when I had a question or needed someone to discuss. I would have loved to meet you all again at the defence ceremony.

In hindsight, I would not have wanted to miss my time in Delft. It is a great city to live in, and thanks to Nederlandse Spoorwegen I enjoyed frequent, punctual and cheap transportation between Aachen and Delft — along with the excellent cycling infrastructure, this is a superb novelty for someone coming from Germany.

Finally, I would like to thank my friends and family for their continuous support. A particular thanks goes to my girlfriend Miriam for proofreading this thesis and her almost endless patience. We have had many great years, with many more to come.

*Daniel Jonathan Weigand
Aachen, December 2020*

1

INTRODUCTION

This chapter provides the context for this thesis. We briefly discuss the importance of quantum error correction and introduce the concept of bosonic error correcting codes. Afterwards, we give an overview of various such codes, in particular the Gottesman-Kitaev-Preskill (GKP) code, and show some interesting applications of the GKP code. The chapter ends with an outline of the thesis.

COMPUTATIONAL devices have been in use for many centuries and assist humankind in various tasks, ranging from simple addition of small numbers to weather prediction and video streaming. Although they offer ever increasing power, some important questions will always be difficult to solve with standard computers. Especially calculating properties of quantum mechanical systems has proven to be nearly intractable for a sufficiently “large” system, for example a complex molecule. But it is precisely this type of system that is often of interest in solid state physics, material science, or medicine. For example, evaluating the dynamics of a drug candidate would allow to test how it interacts with a certain target protein [1]. As a reference for typical system sizes, the penicillin class of antibiotics consists of 27 or more atoms.

The underlying problem when simulating a quantum mechanical system is that the state space of a quantum system scales exponentially with its size. Given a system of n spins, we would need 2^n complex numbers in order to store an arbitrary state. If we wanted to simulate the dynamics of this system, i.e. apply a Hamiltonian, we would need to represent this Hamiltonian as a complex $2^n \times 2^n$ matrix. Around 1980, scientists suggested to use *quantum computers* for the simulation of quantum systems to solve this issue (see e.g. [2]): A computer that acts as a quantum mechanical system obeys the same rules as the simulated quantum system and has therefore the same scaling of complexity with the system size.

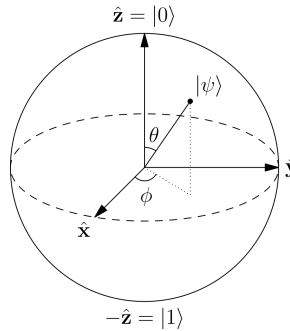



Figure 1.1: The state space of a qubit, depicted as a Bloch sphere. Reprinted from [3], licensed under CC-BY-SA 3.0 [4] .

The smallest computational unit in a quantum computer (the *qubit*) is a two-dimensional quantum system. While the smallest computational unit in a classical computer (the bit) is a binary value that can be either 0 or 1, the state of a qubit can be any linear combination of the form (see Fig. 1.1):

$$|\psi\rangle = \cos(\theta) |0\rangle + e^{i\phi} \sin(\theta) |1\rangle.$$

Moreover, if we have multiple qubits, they can be in an *entangled* state, i.e. a state that cannot be written as a product of single qubit states. One example is the so-called *Bell state*: $2^{-1/2}(|0\rangle|0\rangle + |1\rangle|1\rangle)$. Entanglement is also the reason why it takes so much memory to store a quantum state. This is in stark contrast to a classical computer, where the

state of multiple bits is always simply a string describing every bit on its own. Although the state space of a quantum computer is exponentially large in the number of bits, this does not necessarily mean that the computational power also scales exponentially because the measurement of a qubit probabilistically projects the state: A measurement of state $|\psi\rangle$ in the basis $\{|0\rangle, |1\rangle\}$ yields $|0\rangle$ with probability $\cos(\theta)^2$ and $|1\rangle$ with probability $\sin(\theta)^2$.

Quantum computers are not only useful for simulating quantum systems. They also perform better than classical computers for some computational tasks. Below, two important quantum algorithms are described: *Grover's algorithm* is provably faster than the best possible classical algorithm. *Shor's algorithm*, on the other hand, provides an exponential speedup for factoring large numbers, and is (in)famous for breaking the widely used RSA (Rivest-Shamir-Adleman) cryptosystem.

Grover's algorithm [5]: Consider a function f that is defined on N possible inputs, and returns 1 for a single entry and 0 for all others. Two examples are a search in an unstructured database of size N or a password check with N possible combinations. With a standard computer, the best possible algorithm simply checks all elements until it finds the correct one. Therefore, the runtime on a classical computer is $\mathcal{O}(N)$. Grover's algorithm, on the other hand, solves the same problem using only $\mathcal{O}(\sqrt{N})$ queries. This might not seem like a big speedup — considering that input sizes for quantum computers are currently tens of qubits, while classical computers routinely handle trillions of bits. However, if a sufficiently large quantum computer is ever built, this algorithm will be very useful because it provides a speedup for any problem where no efficient solution is known.

Shor's algorithm [6]: This algorithm can be used to retrieve the prime factors of a big integer stored in n bits that was obtained by multiplying two or more prime numbers. The best known classical algorithm for this problem has a runtime which scales $\mathcal{O}(e^{\sqrt[3]{n}})$. The assumed complexity of factoring such a large number is what secures the RSA cryptosystem, one of the most used cryptography procedures. Shor's algorithm could factor a number of n bits using only $\mathcal{O}(n)$ qubits and a computing time of $\mathcal{O}(n^2 \log(n) \log(\log(n)))$, thus breaking RSA encryption. Fortunately, n is typically 2048 or more for encryption, meaning that the algorithm will probably not be useful for attacking cryptography for several more decades.

Over the last years, significant progress has been made towards building a quantum computer that solves real world problems. At the end of 2019, Google (Arute *et al.* [7]) published the results of a so-called “quantum supremacy experiment”. Quantum supremacy refers to a computation — any computation, no matter if it is useful or not — that can be done on a quantum computer, but not on a classical computer [8]. In this experiment, the authors used a chip with 53 superconducting qubits¹ and run 20 cycles of gates on this chip, where each cycle consists of one round of random single-qubit gates followed by one round of random two-qubit gates. For simulating a large quantum de-

¹The chip houses 54 qubits, but one of them was not usable.

vice such as the one by google, two approaches have been presented so far: Using the whole secondary storage of the Summit supercomputer², up to 54 qubits can be simulated with full state simulation in about two and a half days [10]. A tensor network based approach has recently been presented by Huang *et al.* (2020) [11], they estimate that the Summit supercomputer would need 20 days for the task. Although slower, the second approach does not rely on storing the full state. The memory requirements are vastly reduced and the second approach can therefore still be used for more than 54 qubits. Furthermore, the authors claim that their runtime estimate is likely more accurate than the full state approach by Pednault *et al.* Taking the peak power consumption of 13 MW into account, the total power cost would be around 780 MWh or 6200 MWh for the two simulation approaches, respectively.

The superconducting processors by Google [7] are so-called “Noisy Intermediate-Scale Quantum” devices (NISQ [12]). Such devices are still far away from the full-scale quantum computer required for simulating complex quantum systems. As the name suggests, they are simply too noisy to allow for complex quantum algorithms. In the quantum supremacy experiment, the circuit had a depth of up to 20 cycles (with 2 gates each), with an error rate of about 0.93% per cycle. The total runtime of this circuit was about 200 μ s [7].

In contrast, a typical algorithm factoring an $n = 2048$ -bit RSA key with Shor’s algorithm takes more than $n = 2048$ qubits with a depth of at least $n^2 \log(n) \log(\log(n)) \approx 5 \times 10^7$ gates. Besides the fact that the output of the algorithm would be almost completely uncorrelated to the desired result if we assumed similar gate error rates, the runtime would also be several orders of magnitude larger than even the best superconducting qubit designs permit. To bridge the enormous gap between realistically achievable error rates and what would be needed for complex algorithms on a universal quantum computer, we need *quantum error correction* (QEC).

1.1. ERROR CORRECTION

ERROR correction describes the idea that a *logical* qubit is embedded into a larger, but faulty Hilbert space — usually realized with many *physical* qubits. In the following, some of the key aspects of (quantum) error detection and correction will be discussed.

1.1.1. CLASSICAL ERROR CORRECTION

The idea to protect logical information by embedding it into a larger space is not new to quantum computation. It is widely spread in classical computation and especially in (wireless) communication.

In classical computation, the error rate is usually very low (in the order of 1 error per machine and year [13]) so that they can usually be either caught by the operating system or solved by simply repeating the task.³ In classical communication, errors are much more common than in computation, but still seldom enough that they can be mitigated using checksums, like in the specification of the IPv6 protocol [15]. If the checksum computed from the received data does not match the checksum of the sent data, the

²The Summit supercomputer is currently the most powerful supercomputer available to the public [9].

³In critical applications, Error-Correcting Code memory (ECC) is used to further reduce this rate [14].

receiver simply asks the sender to transmit the data again. A similar approach is used for human interaction, for example with the International Bank Account Number (IBAN). It is designed in such a way that omitting, duplicating, mistyping, or switching of numbers does not yield a valid account number, thus reducing the risk of erroneous transactions.

ERROR DETECTION

As a simple example to illustrate classical error detection, we consider the following toy model: We want to send a classical bit $x \in \{0, 1\}$, which will be flipped along the way with a probability p . Using the simplest possible code, we encode one logical bit in two physical bits:

$$\bar{0} = 00, \quad \bar{1} = 11,$$

i. e. we simply send the bit twice. If the receiver measures e. g. $\tilde{x} = 01$, they know that this matches neither $\bar{0}$ nor $\bar{1}$ and that an error must have occurred. The protocol succeeds with a probability of $(1 - p)^2$ on the first try. If an error is detected at the receiver, the sender will need to send the bit again. The protocol fails on the first attempt (both bits are flipped) with a probability p^2 . Assuming that at most one bit flip occurs, the number of bits that need to be sent in order to obtain one logical bit (bandwidth) is on average: $2 \times (1 - p)^2 + (2 + 1 + 2) \times 2p(1 - p)$ bits.⁴

ERROR CORRECTION (BIT-FLIP CODE)

In the setting of wireless communication, error rates reach an appreciable level so that error correction needs to be used to go beyond a certain range (as done in Bluetooth v5 [16]). Error correction means that we enable the receiver to correct for a small number of errors himself, at the cost of some additional bandwidth. In the above toy model, we now encode one logical bit in three physical bits:

$$\bar{0} = 000, \quad \bar{1} = 111,$$

i. e. we simply send the bit in triplicate. Now, if the receiver measures e. g. $\tilde{x} = 001$, they know again that this matches neither $\bar{0}$ nor $\bar{1}$ and that an error must have occurred. However, assuming that only a single error occurred, they can simply take a majority vote and see that the originally sent bit was $\bar{0}$, without further communication with the sender. The error correction protocol succeeds with a probability of $(1 - 3p^2)$, where failure (two bits are flipped) occurs with a probability of $3p^2$, and no further communication is necessary. Assuming that at most one bit flip occurred, we always need a bandwidth of 3 bits. When comparing the error detection and correction schemes, we see that error correction will need a lower bandwidth if the probability of a bit flip is about 25%.

1.1.2. QUANTUM ERROR CORRECTION

When protecting a quantum state against errors, there are several fundamental differences to the classical case:⁵

⁴If the protocol succeeds (with probability $(1 - p)^2$), only 2 bits will be sent. If an error is detected (with probability $2p(1 - p)$), the receiver will need to inform the sender (+ 1 bit) and the sender will repeat the message (+ 2 bits).

⁵This subsection follows Nielsen and Chuang [17, Sec. 10.1.1].

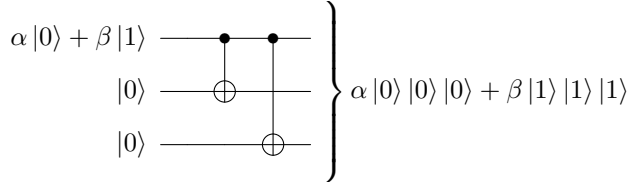


Figure 1.2: Encoding circuit for the quantum bit-flip code. By using the CNOT gate, an arbitrary state can be encoded without knowledge or measurement of the input. If the *control* qubit (black dot) is in state $|1\rangle$, the NOT gate is applied to the *target* qubit (circle with cross), i.e. the qubit is flipped (from $|0\rangle$ to $|1\rangle$, and vice versa). Reproduced from Fig. 10.2 in [17].

- *Measurement collapses superpositions:* Measuring a qubit is usually only allowed at the end of a quantum computation, otherwise we would simply have a classical bit. Therefore, we cannot simply measure an encoded state and take a majority vote, as done in the classical bit-flip code discussed above.
- *No-Cloning Theorem:* The theorem states that it is not possible to create copies of an unknown state. This means that we cannot simply store multiple copies of the same state to encode it without measurement.
- *Errors are continuous:* In contrast to classical computation, where a bit can only take two discrete states, there exists an infinite set of valid qubit states. This means that any unitary operation takes a qubit state to another valid qubit state, and we have to devise ways to distinguish errors from logical operations.

QUANTUM BIT-FLIP CODE

In order to illustrate quantum error correction with a simple toy model, we modify the classical bit-flip code such that it can correct for any bit-flip error. The logical codewords of this quantum bit-flip code are:

$$|\bar{0}\rangle = |0\rangle |0\rangle |0\rangle, \quad |\bar{1}\rangle = |1\rangle |1\rangle |1\rangle.$$

The set of errors to be corrected are the identity, a single-qubit bit flip acting on any of the three qubits, or any linear combination thereof. In general, the state we want to encode is unknown, and due to the no-cloning theorem, we cannot simply produce three copies of it. In order to encode some unknown state $|\Psi\rangle = \alpha|0\rangle + \beta|1\rangle$ into an encoded state $|\bar{\Psi}\rangle = \alpha|\bar{0}\rangle + \beta|\bar{1}\rangle$, we can use the circuit shown in Fig. 1.2.

In order to correct errors, we need a measurement that identifies an error without obtaining information about the encoded state. To this end, we make use of the fact that the parities between the first and second, and the second and third qubit are both even on the code space. However, if a bit-flip error occurs, one or both parities will be odd, uniquely identifying the faulty qubit. A circuit achieving such a parity measurement is shown in Fig. 1.3. Assuming that only a single qubit error happened, we can identify the faulty qubit in the following way: If the measurement of the first (second) ancilla qubit yields the $|1\rangle$ state, the first (third) data qubit will be identified as faulty. If both ancilla qubits are in the $|1\rangle$ state, we can infer that the second data qubit must have flipped.

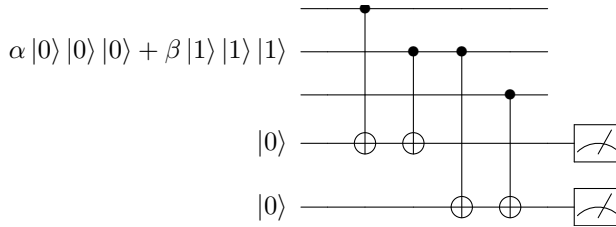


Figure 1.3: Decoding circuit for the quantum bit-flip code. If the input state is, as depicted, a state encoded in the bit-flip code (without errors), it is straight forward to see that both *ancilla* qubits (bottom two lines) will remain in the $|0\rangle$ state, independent of the encoded state. If one of the *data* qubits (top three lines) is flipped, one or both ancilla qubits will be in the $|1\rangle$ state, uniquely identifying the erroneous data qubit.

We also see that the code is not particularly useful for a realistic setting, as it offers no protection whatsoever against *phase flips*: $\alpha|0\rangle + \beta|1\rangle \rightarrow \alpha|0\rangle - \beta|1\rangle$. In fact, we can see that a phase flip applied to any of the physical qubits acts also as a phase flip on the logical qubit. This is an important difference to classical error correction: Usually, there are several types of errors, and a good quantum error correction should provide protection against all of them.

1.1.3. QUANTUM ERROR CORRECTION WITH SUPERCONDUCTING QUBITS

The basic principle of error correction is that information is protected by encoding it redundantly. In a standard quantum computing setup, this means that we protect one logical qubit by using many physical qubits. To give some context, to be able to correct any single qubit error, one needs to encode the logical information into at least five physical qubits [18]⁶, but realistic implementations of an error correcting code usually require much more qubits.

A popular code in the setting of superconducting qubits is the so-called *surface code*. This particular code lends itself well to this type of setup, as it features local connectivity (physical qubits only interact with neighbors) on a plane (well suited for chip designs) as well as a high threshold (slightly below 1%) [19]. The threshold is a formal statement about the asymptotic scaling of a code class: If the error rate of the physical qubits is below the threshold, the performance of the logical qubits will improve with the number of physical qubits used.

The smallest surface code that can correct any single qubit error is surface-17,⁷ using 17 qubits (see Fig. 1.4 for a proposal of a layout that could be used in experiments). In a simulation by O’Brien *et al.* (2017) [22], the quality of state-of-the-art transmon qubits was shown to be sufficient so that a logical qubit encoded in surface-17 would have a longer lifetime than its components. However, the authors showed that the break-even point in terms of the number of gates used for any computation requires the even larger surface-49 code, which is capable of correcting up to two errors. Implementing

⁶In order to identify errors without measuring the data qubits, we usually need at least one more ancilla qubit, depending on implementation details. Also, note that the article was only published in 2000, while the original proof is from 1995 and published on the arXiv in 1996.

⁷Note that in contrast to other codes where only data qubits are counted, the size of a surface code is usually specified by the *total* number of physical qubits, i. e. both data and ancilla qubits.

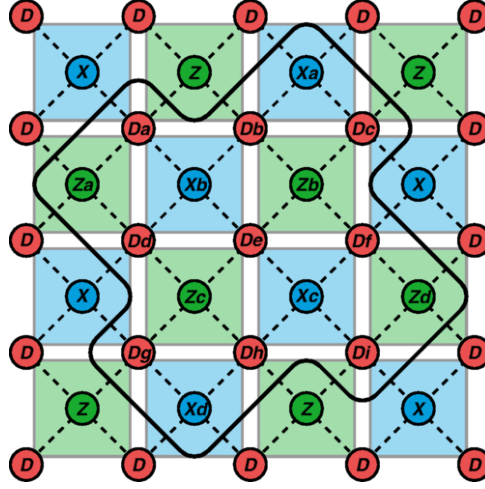


Figure 1.4: Proposed layout for the surface code with 17 qubits (black line), shown as part of a larger lattice. Circles denote qubits, while the solid white and dashed black lines show the connections. For surface-17, there are nine data qubits (D_a-D_i) and eight ancilla qubits (X_a-X_d), (Z_a-Z_d). Reprinted figure with permission from [20]. © (2020) by the American Physical Society.

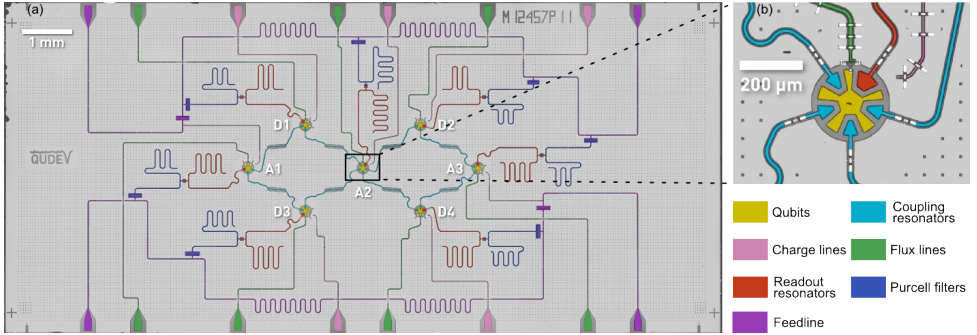


Figure 1.5: Chip used in the surface-7 experiment by Andersen *et al.* (2019) [21] demonstrating repeated error correction measurements. Note the dimensions of the chip, and that every qubit has a dedicated readout resonator, which is coupled via a second resonator (Purcell filter) to the readout line. Reprinted by permission from Springer Nature Customer Service Centre GmbH: Nature Physics, Andersen *et al.* (2020) [21], © (2020) by Springer Nature.

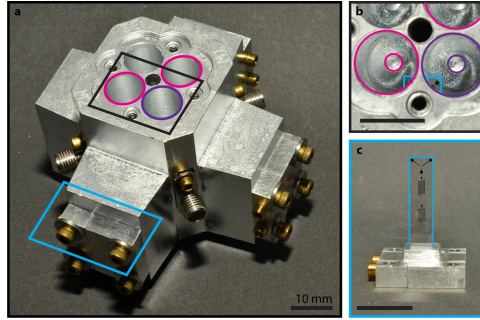


Figure 1.6: Superconducting cavities used for a logical gate between two qubits encoded in the binomial code defined in Eq. (1.1) [28]. The system accommodates four cylindrical cavities, three of which are used in the experiment. The two logical qubits are stored in the cavities marked in magenta, the cavity in purple is used together with a transmon qubit (cyan) to enable the coupling. Reprinted by permission from Springer Nature Customer Service Centre GmbH: Nature, Chou *et al.* (2018) [28], © (2020) by Springer Nature.

the surface code experimentally remains a major challenge. Quantum error detection has already been shown to be useful on the IBM Q Experience 5 qubit chip by C. Vuillot (2018) [23] and Harper and Flammia (2019) [24]. Multiple rounds of error detection with the smallest member of the surface code family (7 qubits) have only recently been demonstrated by Andersen *et al.* (2019) [21]. The chip used by Andersen *et al.* is shown in Fig. 1.5.

1.2. BOSONIC ENCODINGS OF QUBITS

THE large Hilbert space required to encode logical information does not need to be comprised of many physical qubits. This is precisely the idea used in bosonic error correcting codes. The Hilbert space of the harmonic oscillator is infinite, which allows for encoding of a logical qubit within a single harmonic oscillator and also to perform error correction.

Of course, things are not quite as simple as simply mapping a code defined on many qubits into the Hilbert space of a harmonic oscillator. The reason is that the dominant sources of noise of a harmonic oscillator, for example photon loss or anharmonicity, grow stronger with the number of photons in the oscillator, i. e. with the size of the Hilbert space that is used for the code. Therefore, bosonic codes usually do not feature a threshold in the same sense as traditional quantum error correcting codes, where we can simply increase the size of the code in order to reduce noise. In fact, for any particular bosonic code and parameters of the oscillator, there will be a “sweet spot” for the size of the code, after which the performance decreases again. This is not a major problem, however, as the aim is to use this class of codes in order to encode a (very) good qubit, which can then be used as “physical qubit” in standard error correcting codes (see, e. g. [25]). A recent experiment has demonstrated about $200\mu\text{s}$ lifetime in a resonator with $245\mu\text{s}$ single-photon lifetime [26]. To give a brief overview of the current state of experimental implementations of bosonic codes, we will follow DiVincenzo’s criteria for a physical implementation of a quantum computer [27]:

- *Scalability.* The harmonic resonators typically used for bosonic codes are not particularly small, as the dimensions are typically in the order of a centimeter for the microwave regime (see Fig. 1.6). This is in the same order of magnitude as the vacuum tubes used in early computers and therefore not a fundamental problem, provided that the encoded qubits have sufficiently low error rates. However, current experimental devices need to be cooled to $\mathcal{O}(10)$ mK. To solve this issue, either the microwave resonators need to be miniaturized, the volume of dilution refrigerators needs to be increased, and/or schemes to couple separate refrigerators need to be developed.
- *Initialization.* Although preparing a vacuum state in a harmonic oscillator is standard practice in many quantum experiments, initializing a qubit in a harmonic oscillator is challenging, depending on the code. If an ancillary qubit is used, *any* state in the oscillator could be prepared, although the accuracy is limited by the performance of the qubits [29]. (In this thesis, the main focus will be to find efficient protocols to initialize the GKP code, see below.)
- *Long coherence times.* Long coherence times are one of the main selling points of the harmonic oscillator as a system to realize a qubit. Depending on the specific oscillator, single photon life times in the order of $200\mu\text{s}$ to 1ms are routinely available, in both 2D and 3D architectures [26, 30].
- *Universal gate set.* The availability of a universal gate set depends very much on the chosen encoding of a qubit in the oscillator: For the cat code (see below), a universal gate set is available and has been experimentally implemented [31]. For the GKP code, many gates (Clifford gates) can easily be implemented, and a scheme to obtain universality is known [32]. For the binomial codes (see below), more complicated schemes using an ancilla qubit and optimal control pulses or gate teleportation are needed [33–35].
- *Qubit-specific measurements.* Targeting a specific oscillator with a measurement is not a problem — this capability is a prerequisite for the operation of superconducting qubit designs like the *transmon*, which is measured via an ancilla oscillator. Moreover, a wide range of measurement types is available (see Chapter 2): In addition to the standard homodyne and heterodyne⁸ measurements, also photon number resolving measurements [29] and direct measurements of the Wigner function (quasi-probability distribution) at any point in phase space [36] have been experimentally demonstrated. A non-destructive measurement of code states remains however challenging, depending on the code in question.

Besides the Gottesman-Kitaev-Preskill (GKP) code, which is the main focus of this thesis, there are several other interesting bosonic codes. To put the different codes and experimental progress into context, we use the complexity stages outlined by Devoret and Schoelkopf [37] as a guideline, see Fig. 1.7. For comparison: The fourth stage, a logical memory with longer lifetime than the physical qubits, has only recently been partially

⁸Homodyne measurements measure position *or* momentum. Heterodyne measurements measure position and momentum simultaneously.

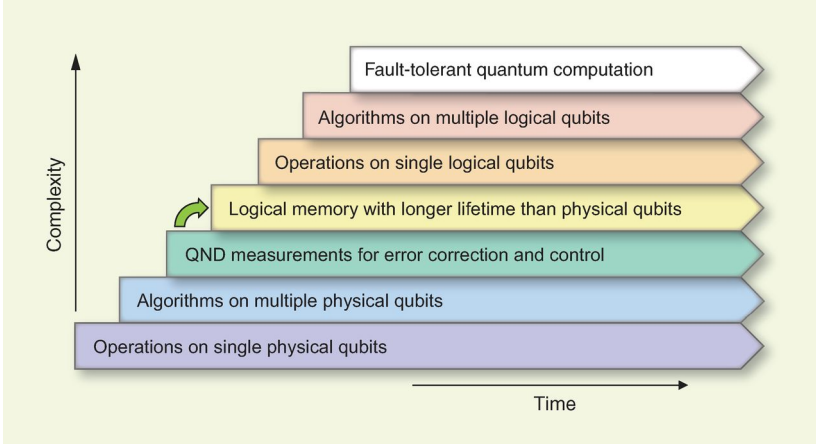


Figure 1.7: Complexity stages on the way towards fault-tolerant quantum computation. Bosonic codes are very competitive in this respect: Error correction, enhanced logical lifetimes, and even logical two-qubit gates have now been demonstrated for multiple codes. The cost is that the 3D microwave cavities used in these experiments are harder to scale than e.g. superconducting qubits. On the other hand, a logical qubit with enhanced lifetime still has to be demonstrated in superconducting qubits (green arrow), seven years after this figure has been originally made (QND = quantum non-demolition). From Devoret and Schoelkopf (2013) [37]. Reprinted with permission from AAAS.

reached for superconducting qubits [21].⁹ A more detailed overview of different bosonic codes and their performance can be found in [38]. In the following, we give an overview of bosonic codes and their applications, without going into details. (A more detailed introduction follows in Chapter 2.)

BINOMIAL CODES

A very simple bosonic code family are the so-called *binomial codes* [34]. Using the photon number basis, the logical $|\bar{+}\rangle$ and $|\bar{-}\rangle$ states are defined as:

$$|\bar{\pm}\rangle = 2^{-\frac{N+1}{2}} \sum_{m=0}^{N+1} (-1)^{\pm m} \sqrt{\binom{N+1}{m}} |(S+1)m\rangle.$$

If we choose $S = L + G$ and $N = \max(L, G, 2D)$, this code can correct L photon-loss events (\hat{a}), G photon-gain events (\hat{a}^\dagger) and D dephasing events ($\hat{a}^\dagger \hat{a}$). A simple example designed to protect against photon loss, which usually is the dominant source of errors in a harmonic oscillator, is given by:

$$|\bar{0}\rangle = \frac{|0\rangle + |4\rangle}{\sqrt{2}}, \quad |\bar{1}\rangle = |2\rangle. \quad (1.1)$$

Neither the state $\hat{a}|\bar{0}\rangle = |3\rangle$ nor $\hat{a}|\bar{1}\rangle = |1\rangle$ has support on the code space. Note that two photon losses cannot be corrected by this code, as $\hat{a}\hat{a}|\bar{0}\rangle = |2\rangle = |\bar{1}\rangle$ and $\hat{a}\hat{a}|\bar{1}\rangle =$

⁹The stage has only partially been reached because Andersen *et al.* used an error detecting code and therefore had to post-select on no error being detected.

$|0\rangle \not\propto |\bar{0}\rangle$. We note that the photon number parity of both codewords is even (they are a superposition of states with even photon number). This means that photon loss can be detected by a measurement of the photon number parity with an ancilla qubit, using the qubit-cavity coupling ($e^{i2\pi\sigma_z\hat{a}^\dagger\hat{a}}$) [29] and the ancilla qubit initialized in the $|+\rangle$ state. Hu *et al.* recently demonstrated active error correction and logical gates with this code in an experiment [39]. In this experiment, the lifetime of the encoded qubit was $> 92\%$ of the single-photon lifetime of the employed oscillator, which is close to break even for error correction.

CAT CODE

The family of so-called *cat codes* encodes a qubit into Schrödinger cat states [40]. A cat code designed to protect against loss of k photons is formed by a superposition of $2(k+1)$ coherent states on a circle in phase space. The simplest ($k=0$) cat code is defined as:

$$|\bar{0}\rangle = \frac{1}{\mathcal{N}_0} (|-\alpha\rangle + |\alpha\rangle), \quad |\bar{1}\rangle = \frac{1}{\mathcal{N}_1} (|-\alpha\rangle - |\alpha\rangle). \quad (1.2)$$

This code does not protect against photon loss, the annihilation operator \hat{a} actually acts as a bit flip. The phase flip is realized by the rotation $e^{i\pi\hat{a}^\dagger\hat{a}}$. As the resonance frequency of an oscillator is usually very stable, this means that phase flip errors happen on a much longer time scale than photon loss. In a recent (2019) experiment with this code, Grimm *et al.* reported a lifetime around $2.5\mu\text{s}$ for bit flip errors and about $105\mu\text{s}$ for phase flip errors, with a single-photon lifetime of about $3.4\mu\text{s}$ [31].¹⁰ A major advantage of the cat code is that the code space can be stabilized by engineered photon loss [41] or with a two-photon drive [31]. Another feature is that only measurements of the photon-number parity, but no active error correction are needed.

For cat codes, a certain number of losses will act as the identity (depending on the distance), meaning that tracking photon losses is sufficient and the errors can be corrected by simply changing the reference frame. The cat code protecting against a single photon loss was the first code where a logical lifetime longer than all constituent systems could be demonstrated [42].

THE GOTTESMAN-KITAEV-PRESKILL (GKP) CODE

In 2001, Gottesman, Kitaev and Preskill proposed a stabilizer code to encode a qubit into an oscillator [32], named *GKP code* after the authors. The code is designed to protect against small translations in phase space: It is defined as the common $+1$ eigenspace of the two commuting displacement operators (*stabilizers*):

$$S_p = e^{-i2\sqrt{\pi}\hat{p}}, \quad S_q = e^{i2\sqrt{\pi}\hat{q}}.$$

The logical Pauli operations (see Section 2.1 for definition) are also displacements that commute with both stabilizers, but not with each other:

$$X = e^{-i\sqrt{\pi}\hat{p}}, \quad Z = e^{i\sqrt{\pi}\hat{q}}.$$

¹⁰The choice of the computational basis varies between papers. Some authors choose the basis as in Eq. (1.2), in other papers, those states would be the $|\mp\rangle, |\bar{\mp}\rangle$ states.

The logical qubit states $|\bar{0}\rangle, |\bar{1}\rangle$ are infinite combs in the position basis:

$$|\bar{0}\rangle \propto \sum_n |q = 2\sqrt{\pi}n\rangle, \quad |\bar{1}\rangle \propto \sum_n |q = (2n+1)\sqrt{\pi}\rangle.$$

The code and code states will be derived in more detail in Sections 2.1.2 and 2.1.3. The code states as defined above are not normalizable — these are infinite energy states. For this reason, the code states will always be approximated in a physical system, see Section 2.2 for details.

Although counter-intuitive — the dominant sources of noise in a harmonic oscillator are typically photon loss, followed by dephasing and nonlinearity, while displacements are unlikely — this code performs very well against photon loss [38]. In fact, the code is “optimal” for both pure loss and a Gaussian thermal loss channel, in the sense that GKP encoded states are only a constant away from the quantum capacity of such a channel [43].

Besides good error correction capability, an important group of gates (Clifford gates) can be implemented in a fault-tolerant way using phase shifting, displacements, beam splitters, and moderate squeezing [32, 44]. Fault-tolerance means that small errors are not amplified or spread by the gate. The code has been first implemented in the trapped-ion setting [45, 46], although this approach required post-selection. In a second experiment, the code was implemented in a circuit-QED (quantum electrodynamics) setting, achieving a lifetime of about 205 μs , in an oscillator with a single-photon lifetime of 245 μs [26].

OTHER BOSONIC CODES

For arbitrary bosonic codes in the setting where a transmon qubit is coupled to a superconducting resonator, both a release of encoded states to a transmission line [47] and a universal entangling gate between two cavities [48] have now been experimentally demonstrated. The cat and binomial codes have been generalized in the common framework of rotationally symmetric codes by Grimsmo *et al.* (2019) [35]. This thesis focuses mostly on the encoding of a GKP qubit. A recent review on decoding, embedding with other qubit types, and concatenation with the surface code can be found in Ref. [49].

1.3. APPLICATIONS RELATED TO THE GOTTESMAN - KITAEV - PRESKILL (GKP) CODE

BESIDES enabling a very competitive qubit design, the stabilizers of the GKP code are of interest in multiple other applications.

1.3.1. MAXIMAL VIOLATION OF BELL INEQUALITIES

Wenger *et al.* (2003) [50] proposed a scheme for maximal violation of Bell inequalities¹¹, using only homodyne detection. To this end, they define two resource states:

$$\begin{aligned} |f\rangle &\propto \sum_{n=-\infty}^{\infty} (-1)^n \left(\left| q = 2n\sqrt{\pi} + \frac{\sqrt{\pi}}{2} \right\rangle + \left| q = 2n\sqrt{\pi} - \frac{\sqrt{\pi}}{2} \right\rangle \right), \\ |g\rangle &\propto \sum_{n=-\infty}^{\infty} (-1)^n \left(\left| q = 2n\sqrt{\pi} + \frac{\sqrt{\pi}}{2} \right\rangle - \left| q = 2n\sqrt{\pi} - \frac{\sqrt{\pi}}{2} \right\rangle \right). \end{aligned}$$

The Bell test is then done using entangled states of the form

$$|\Psi\rangle = \frac{1}{\sqrt{2}} \left(|ff\rangle + e^{i\theta} |gg\rangle \right).$$

As the authors note, these states are very similar to the GKP code states. We can write these states as a function of the ideal GKP code states:

$$|f\rangle \propto (\mathbb{1} + X) \sqrt{Z} \sqrt{X} |\bar{0}\rangle \quad |g\rangle \propto (\mathbb{1} - X) \sqrt{Z} \sqrt{X} |\bar{0}\rangle,$$

where Z, X are the logical Pauli operators and $|\bar{0}\rangle$ is the ideal code state of the GKP code (see Section 2.1.2).

An important advantage of this protocol compared to the more common schemes relying on single photon detection is that it can tolerate photon losses of up to 26% [51]. Apart from the inherent robustness of the states against photon loss, this also stems from the fact that the detection efficiency of homodyne detection (>98%) is much greater than single photon detection efficiency.

1.3.2. THE VON NEUMANN LATTICE

The idea to define commuting observables acting on a harmonic oscillator originates from John von Neumann. In his book “Mathematische Grundlagen der Quantenmechanik”, first published in 1932, he investigated how classical, commuting observables arise from the non-commuting position and momentum quadratures [52, pp. 214–217]. To this end, von Neumann proposed to use a particular set of coherent states

$$|\alpha_{mn}\rangle = \left\{ \left| \sqrt{\pi}(m + in) \right\rangle \right\}, \quad m, n \in \mathbb{Z},$$

which are arranged on a rectangular lattice. Note that this is precisely the set of states generated by the stabilizers of the one-dimensional GKP code acting on the vacuum. A Gaussian superposition of these states forms a displacement sensor state, see also the next section and [53]. Von Neumann claimed that these states are linearly independent and complete, which “can be proven without greater difficulties”¹² — the statement was proven by Perelomov and by Bargman *et al.* independently in 1971 [54, 55]. Having shown that the set of coherent states $|\alpha_{mn}\rangle$ is both linearly independent and complete,

¹¹The Bell inequalities can only be violated if entanglement has been achieved in the experiment.

¹²Translated from German. The original wording is: “Wenn wir sie [The set of coherent states] nach dem E. Schmidtschen Verfahren ‘orthogonalisieren’, [...] so kann man für das entstehende normierte Orthogonalsystem $\psi'_{\mu,\nu}$ ohne besondere Schwierigkeiten die Vollständigkeit beweisen, ...”

one can then orthogonalize them with the Gram-Schmidt procedure, yielding finally a complete, orthogonal set of states which are also localized in phase space. In the limit $\hbar \rightarrow 0$, the measurement basis defined by these states is continuous, i. e. we recover a commuting and continuous (i. e. classical) measurement of position and momentum.

Using a lattice of coherent states as measurement basis requires a significantly increased effort compared to standard heterodyne measurements. Therefore, it has little advantages for experiments because the accuracy in phase space of both measurements is similar. However, the von Neumann lattice is still useful for numerical simulations. The fact that the lattice points are localized in phase space, together with the completeness of the lattice, allows to approximate states in an oscillator, see e. g. [56, 57].¹³

1.3.3. DISPLACEMENT SENSING BELOW THE HEISENBERG LIMIT

One of the fundamental results of quantum mechanics is Heisenberg's uncertainty principle. The combined standard deviation of a simultaneous measurement of two non-commuting observables A, B is lower bound by the expectation value of their commutator:

$$\sigma_A \sigma_B \geq \frac{1}{2} |\langle [A, B] \rangle|.$$

A common example are the position \hat{q} and momentum \hat{p} quadratures of a harmonic oscillator, for which the uncertainty relation reads:

$$\sigma_{\hat{q}} \sigma_{\hat{p}} \geq \frac{1}{2}.$$

Using a similar construction as the GKP code, there is a way around the uncertainty principle [53]: Let the operators A, B be the displacements $S_q = e^{i\sqrt{2\pi}\hat{q}}, S_p = e^{i\sqrt{2\pi}\hat{p}}$. These two displacements commute, and therefore:

$$\sigma_{S_q} \sigma_{S_p} \geq 0,$$

where σ_{S_q} and σ_{S_p} are the standard deviation of the eigenvalues of S_q and S_p , respectively. The relation between the eigenvalues of \hat{q} and those of S_q is simply: $\arg(S_q) = \sqrt{2\pi}\hat{q} \bmod 2\pi$, the relation for S_p is analogous. Thus, such a displacement sensor allows to measure $\hat{q} \bmod \sqrt{2\pi}$ and $\hat{p} \bmod \sqrt{2\pi}$ simultaneously with unlimited accuracy. This procedure has been demonstrated experimentally in an experiment with trapped ions by Flühmann *et al.* (2018) [46].

1.3.4. PROTECTING GAUSSIAN INFORMATION

A well established no-go theorem is that it is impossible to correct against Gaussian errors with only Gaussian operations [25, 58], i. e. it is not possible to protect an arbitrary state in a harmonic oscillator against photon loss. Noh *et al.* (2019) showed that it is nevertheless possible to protect arbitrary states against Gaussian noise, by encoding the single harmonic oscillator into many harmonic oscillators. They achieve this by using the

¹³Halverson *et al.* [57] use a “doubly dense” von Neumann lattice, which is actually the space spanned by the GKP code stabilizers. They do so in order to ensure locality of the orthogonalized lattice states.

displacement sensing method from the previous section (which is not a Gaussian operation) as a resource [59]. As bosonic modes are used as couplers in virtually all quantum computing and communication settings, this oscillator-into-oscillator code has a wide range of possible applications.

1.4. OUTLINE OF THE THESIS

As we have seen, the GKP code is a promising encoding for a qubit in an oscillator. With this code, one can achieve good protection against photon loss and a set of gates and error correction schemes that can be implemented with standard techniques. However, the challenges using this code are “front-loaded”, i. e. especially the initialization of a GKP qubit is difficult in comparison to other codes. Furthermore, there exists a wealth of applications which all rely on resource states similar to a GKP code state. Two examples are sensing beyond the limits set by Heisenberg’s uncertainty principle and correction of Gaussian noise, both feats long thought to be impossible. If a reliable procedure to generate GKP qubit states was available, it could be easily amended for these other applications.

The aim of this thesis is twofold: First, we want to develop efficient schemes to encode a GKP qubit. Second, we collect and present the concepts and techniques needed for this goal, which will also allow us to connect some seemingly unconnected ideas.

CHAPTER 2

First, we discuss the technical background related to the Gottesman-Kitaev-Preskill code. This chapter serves not only as background for this thesis, but also as a reference for readers unfamiliar with the code and some of the technical intricacies. The chapter is also intended as a reference for experts familiar with bosonic codes, as the concepts collected here may be known, but they are spread across multiple papers and only briefly discussed there. For example, the question how the quality of a GKP code state should be assessed was still subject of debate at the recent Byron Bay Quantum Workshop (November 2019) which was dedicated entirely to bosonic codes.

CHAPTER 3

In this chapter, we will introduce phase estimation and discuss how this class of algorithms can be used to encode a GKP qubit. Similar in spirit as the second chapter, the aim is to collect and explain important concepts for the GKP code, even for readers not interested in the rest of the thesis. As it will turn out, phase estimation is a central theme of this thesis, even though it is not used directly in the following chapters. (In Chapter 4, we will improve a known algorithm by mapping it to phase estimation. In Chapter 5, the developed protocol can be seen as a limiting case of one particular phase estimation algorithm.) The chapter concludes with a numerical simulation where a GKP code state is generated taking noise into account.

CHAPTER 4

Here, we discuss a protocol to encode a GKP state using Schrödinger cat states, beam splitters, and homodyne detection. The experimental setup was originally proposed by Vasconcelos *et al.* (2010) [60], but relied on post-selection. By mapping the protocol

onto phase estimation, we can show that post-selection is not necessary, resulting in an exponential increase of the probability of success of the scheme. The chapter is divided into three parts: First, we show the mapping to phase estimation and how the final state of the protocol can be recovered using classical processing of the results. In the second part, we prove analytically that the scheme converges to an ideal GKP code state, given a sufficient number of measurements. Finally, we demonstrate the efficacy of the protocol numerically.

CHAPTER 5

Although schemes to encode a GKP qubit using phase estimation are so far the only proposals that have been verified experimentally [26, 45], they suffer from a major drawback: Because the encoding procedure relies on a series of ancilla qubit measurements, the speed of this procedure is rather limited. In this chapter, we make a proposal to encode the qubit with a single-shot measurement, following an idea originally by Gottesman *et al.* (2001) [32], where a Hamiltonian of the type $\hat{a}_A^\dagger \hat{a}_A \hat{q}_T$ is used to map the eigenvalue from the stabilizer S_q in the target oscillator T to an ancillary oscillator A . By using heterodyne measurement of the ancilla oscillator, this eigenvalue can then be retrieved in a single measurement. In the chapter, we present a circuit that is tailored to the task and therefore particularly well suited, although any circuit that implements the correct Hamiltonian can be used. We also discuss noise and imperfections at various stages of the protocol, and show the requirements needed for an experiment implementing our scheme.

REFERENCES

- [1] The Royal Swedish Academy of Sciences, *Nobel prize in chemistry 2013*, <https://www.nobelprize.org/prizes/chemistry/2013/press-release>.
- [2] R. P. Feynman, “Simulating physics with computers”, *International Journal of Theoretical Physics* **21**, 467 (1982).
- [3] Glosser.ca, *Bloch sphere*, Wikimedia Commons, (2012) https://commons.wikimedia.org/wiki/File:Bloch_Sphere.svg.
- [4] *Creative Commons Attribution 4.0 International License*, Creative Commons Corporation, <https://creativecommons.org/licenses/by/4.0/>.
- [5] L. K. Grover, “A fast quantum mechanical algorithm for database search”, in *Proceedings of the twenty-eighth annual ACM symposium on theory of computing - STOC '96* (1996).
- [6] P. Shor, “Algorithms for quantum computation: discrete logarithms and factoring”, in *Proceedings 35th annual symposium on foundations of computer science* (1994).

- [7] F. Arute, K. Arya, R. Babbush, D. Bacon, J. C. Bardin, R. Barends, R. Biswas, S. Boixo, F. G. S. L. Brandao, D. A. Buell, B. Burkett, Y. Chen, Z. Chen, B. Chiaro, R. Collins, W. Courtney, A. Dunsworth, E. Farhi, B. Foxen, A. Fowler, C. Gidney, M. Giustina, R. Graff, K. Guerin, S. Habegger, M. P. Harrigan, M. J. Hartmann, A. Ho, M. Hoffmann, T. Huang, T. S. Humble, S. V. Isakov, E. Jeffrey, Z. Jiang, D. Kafri, K. Kechedzhi, J. Kelly, P. V. Klimov, S. Knysh, A. Korotkov, F. Kostritsa, D. Landhuis, M. Lindmark, E. Lucero, D. Lyakh, S. Mandrà, J. R. McClean, M. McEwen, A. Megrant, X. Mi, K. Michielsen, M. Mohseni, J. Mutus, O. Naaman, M. Neeley, C. Neill, M. Y. Niu, E. Ostby, A. Petukhov, J. C. Platt, C. Quintana, E. G. Rieffel, P. Roushan, N. C. Rubin, D. Sank, K. J. Satzinger, V. Smelyanskiy, K. J. Sung, M. D. Trevithick, A. Vainsencher, B. Villalonga, T. White, Z. J. Yao, P. Yeh, A. Zalcman, H. Neven, and J. M. Martinis, “Quantum supremacy using a programmable superconducting processor”, *Nature* **574**, 505 (2019).
- [8] J. Preskill, “Quantum computing and the entanglement frontier”, Mar. 26, 2012.
- [9] IBM, *The most powerful computers on the planet*, IBM, <https://www.ibm.com/thought-leadership/summit-supercomputer/>.
- [10] E. Pednault, J. A. Gunnels, G. Nannicini, L. Horesh, and R. Wisnieff, “Leveraging secondary storage to simulate deep 54-qubit Sycamore circuits”, Oct. 21, 2019.
- [11] C. Huang, F. Zhang, M. Newman, J. Cai, X. Gao, Z. Tian, J. Wu, H. Xu, H. Yu, B. Yuan, M. Szegedy, Y. Shi, and J. Chen, “Classical simulation of quantum supremacy circuits”, May 14, 2020.
- [12] J. Preskill, “Quantum computing in the NISQ era and beyond”, *Quantum* **2**, 79 (2018).
- [13] B. Schroeder, E. Pinheiro, and W.-D. Weber, “DRAM errors in the wild”, *Communications of the ACM* **54**, 100 (2011).
- [14] S. Mittal and M. S. Inukonda, “A survey of techniques for improving error-resilience of DRAM”, *Journal of Systems Architecture* **91**, 11 (2018).
- [15] D. S. E. Deering and B. Hinden, *Internet protocol, version 6 (IPv6) specification*, tech. rep. 8200 (2017), 42 pp.
- [16] M. Collotta, G. Pau, T. Talty, and O. K. Tonguz, “Bluetooth 5: a concrete step forward toward the IoT”, *IEEE Communications Magazine* **56**, 125 (2018).
- [17] M. Nielsen and I. Chuang, *Quantum computation and quantum information*, Cambridge Series on Information and the Natural Sciences (Cambridge University Press, 2000).
- [18] E. Knill, R. Laflamme, and L. Viola, “Theory of quantum error correction for general noise”, *Physical Review Letters* **84**, 2525 (2000).
- [19] E. T. Campbell, B. M. Terhal, and C. Vuillot, “Roads towards fault-tolerant universal quantum computation”, *Nature* **549**, 172 (2017).
- [20] R. Versluis, S. Poletto, N. Khammassi, N. Haider, D. J. Michalak, A. Bruno, K. Bertels, and L. DiCarlo, “Scalable quantum circuit and control for a superconducting surface code”, *Physical Review Applied* **8**, 034021 (2017).

- [21] C. K. Andersen, A. Remm, S. Lazar, S. Krinner, N. Lacroix, G. J. Norris, M. Gabureac, C. Eichler, and A. Wallraff, “Repeated quantum error detection in a surface code”, *Nature Physics* (2020) **16**, 875 (2019).
- [22] T. E. O’Brien, B. Tarasinski, and L. DiCarlo, “Density-matrix simulation of small surface codes under current and projected experimental noise”, *npj Quantum Information* **3**, 39 (2017).
- [23] C. Vuillot, “Is error detection helpful on ibm 5q chips?”, *Quantum Information & Computation* **18**, 0949 (2017).
- [24] R. Harper and S. T. Flammia, “Fault-tolerant logical gates in the ibm quantum experience”, *Physical Review Letters* **122**, 080504 (2018).
- [25] C. Vuillot, H. Asasi, Y. Wang, L. P. Pryadko, and B. M. Terhal, “Quantum error correction with the toric Gottesman-Kitaev-Preskill code”, *Physical Review A* **99**, 032344 (2019).
- [26] P. Campagne-Ibarcq, A. Eickbusch, S. Touzard, E. Zalys-Geller, N. E. Frattini, V. V. Sivak, P. Reinhold, S. Puri, S. Shankar, R. J. Schoelkopf, L. Frunzio, M. Mirrahimi, and M. H. Devoret, “Quantum error correction of a qubit encoded in grid states of an oscillator”, *Nature* **584**, 368 (2020).
- [27] D. P. DiVincenzo, “The physical implementation of quantum computation”, *Fortschritte der Physik* **48**, 771 (2000).
- [28] K. S. Chou, J. Z. Blumoff, C. S. Wang, P. C. Reinhold, C. J. Axline, Y. Y. Gao, L. Frunzio, M. H. Devoret, L. Jiang, and R. J. Schoelkopf, “Deterministic teleportation of a quantum gate between two logical qubits”, *Nature* **561**, 368 (2018).
- [29] R. W. Heeres, B. Vlastakis, E. Holland, S. Krastanov, V. V. Albert, L. Frunzio, L. Jiang, and R. J. Schoelkopf, “Cavity state manipulation using photon-number selective phase gates”, *Physical Review Letters* **115**, 137002 (2015).
- [30] A. Bruno, G. de Lange, S. Asaad, K. L. van der Enden, N. K. Langford, and L. DiCarlo, “Reducing intrinsic loss in superconducting resonators by surface treatment and deep etching of silicon substrates”, *Applied Physics Letters* **106**, 182601 (2015).
- [31] A. Grimm, N. E. Frattini, S. Puri, S. O. Mundhada, S. Touzard, M. Mirrahimi, S. M. Girvin, S. Shankar, and M. H. Devoret, “Stabilization and operation of a kerr-cat qubit”, *Nature* **584**, 205 (2020).
- [32] D. Gottesman, A. Kitaev, and J. Preskill, “Encoding a qubit in an oscillator”, *Physical Review A* **64**, 012310 (2001).
- [33] N. Khaneja, T. Reiss, C. Kehlet, T. Schulte-Herbrüggen, and S. J. Glaser, “Optimal control of coupled spin dynamics: design of NMR pulse sequences by gradient ascent algorithms”, *Journal of Magnetic Resonance* **172**, 296 (2005).
- [34] M. H. Michael, M. Silveri, R. T. Brierley, V. V. Albert, J. Salmilehto, L. Jiang, and S. M. Girvin, “New class of quantum error-correcting codes for a Bosonic mode”, *Physical Review X* **6**, 031006 (2016).
- [35] A. L. Grimsmo, J. Combes, and B. Q. Baragiola, “Quantum computing with rotation-symmetric Bosonic codes”, *Physical Review X* **10**, 011058 (2020).

- [36] B. Vlastakis, G. Kirchmair, Z. Leghtas, S. E. Nigg, L. Frunzio, S. M. Girvin, M. Mirrahimi, M. H. Devoret, and R. J. Schoelkopf, “Deterministically encoding quantum information using 100-photon Schrödinger cat states”, *Science* **342**, 607 (2013).
- [37] M. H. Devoret and R. J. Schoelkopf, “Superconducting circuits for quantum information: an outlook”, *Science* **339**, 1169 (2013).
- [38] V. V. Albert, K. Noh, K. Duivenvoorden, D. J. Young, R. T. Brierley, P. Reinhold, C. Vuillot, L. Li, C. Shen, S. M. Girvin, B. M. Terhal, and L. Jiang, “Performance and structure of single-mode Bosonic codes”, *Physical Review A* **97**, 032346 (2018).
- [39] L. Hu, Y. Ma, W. Cai, X. Mu, Y. Xu, W. Wang, Y. Wu, H. Wang, Y. P. Song, C. -L. Zou, S. M. Girvin, L.-M. Duan, and L. Sun, “Quantum error correction and universal gate set operation on a binomial Bosonic logical qubit”, *Nature Physics* **15**, 503 (2019).
- [40] Z. Leghtas, G. Kirchmair, B. Vlastakis, R. J. Schoelkopf, M. H. Devoret, and M. Mirrahimi, “Hardware-efficient autonomous quantum memory protection”, *Physical Review Letters* **111**, 120501 (2013).
- [41] M. Mirrahimi, Z. Leghtas, V. V. Albert, S. Touzard, R. J. Schoelkopf, L. Jiang, and M. H. Devoret, “Dynamically protected cat-qubits: a new paradigm for universal quantum computation”, *New Journal of Physics* **16**, 045014 (2014).
- [42] N. Ofek, A. Petrenko, R. Heeres, P. Reinhold, Z. Leghtas, B. Vlastakis, Y. Liu, L. Frunzio, S. M. Girvin, L. Jiang, M. Mirrahimi, M. H. Devoret, and R. J. Schoelkopf, “Extending the lifetime of a quantum bit with error correction in superconducting circuits”, *Nature* **536**, 441 (2016).
- [43] K. Noh, V. V. Albert, and L. Jiang, “Quantum capacity bounds of Gaussian thermal loss channels and achievable rates with Gottesman-Kitaev-Preskill codes”, *IEEE Transactions on Information Theory* **65**, 2563 (2019).
- [44] B. M. Terhal and D. J. Weigand, “Encoding a qubit into a cavity mode in circuit QED using phase estimation”, *Physical Review A* **93**, 012315 (2016).
- [45] C. Flühmann, T. L. Nguyen, M. Marinelli, V. Negnevitsky, K. Mehta, and J. P. Home, “Encoding a qubit in a trapped-ion mechanical oscillator”, *Nature* **566**, 513 (2019).
- [46] C. Flühmann, V. Negnevitsky, M. Marinelli, and J. P. Home, “Sequential modular position and momentum measurements of a trapped ion mechanical oscillator”, *Physical Review X* **8**, 021001 (2018).
- [47] W. Pfaff, C. J. Axline, L. D. Burkhardt, U. Vool, P. Reinhold, L. Frunzio, L. Jiang, M. H. Devoret, and R. J. Schoelkopf, “Controlled release of multiphoton quantum states from a microwave cavity memory”, *Nature Physics* **13**, 882 (2016).
- [48] Y. Y. Gao, B. J. Lester, K. Chou, L. Frunzio, M. H. Devoret, L. Jiang, S. M. Girvin, and R. J. Schoelkopf, “Entanglement of Bosonic modes through an engineered exchange interaction”, *Nature* **566**, 509 (2018).
- [49] B. M. Terhal, J. Conrad, and C. Vuillot, “Towards scalable bosonic quantum error correction”, *Quantum Science and Technology* **5**, 043001 (2020).

- [50] J. Wenger, M. Hafezi, F. Grosshans, R. Tualle-Brouri, and P. Grangier, “Maximal violation of Bell inequalities using continuous-variable measurements”, [Physical Review A](#) **67**, 012105, 012105 (2003).
- [51] J. Etesse, R. Blandino, B. Kanseri, and R. Tualle-Brouri, “Proposal for a loophole-free violation of Bell’s inequalities with a set of single photons and homodyne measurements”, [New Journal of Physics](#) **16**, 053001, 053001 (2014).
- [52] J. von Neumann, *Mathematische Grundlagen der Quantenmechanik* (Dover Publications, New York, 1943).
- [53] K. Duivenvoorden, B. M. Terhal, and D. J. Weigand, “Single-mode displacement sensor”, [Physical Review A](#) **95**, 012305 (2017).
- [54] A. M. Perelomov, “On the completeness of a system of coherent states”, [Theoretical and Mathematical Physics](#) **6**, 156 (1971).
- [55] V. Bargmann, P. Butera, L. Girardello, and J. R. Klauder, “On the completeness of the coherent states”, [Reports on Mathematical Physics](#) **2**, 221 (1971).
- [56] L. K. Stergioulas, V. S. Vassiliadis, and A. Vourdas, “Construction of quantum states from an optimally truncated Von Neumann lattice of coherent states”, [Journal of Physics A: Mathematical and General](#) **32**, 3169 (1999).
- [57] T. Halverson and B. Poirier, “Accurate quantum dynamics calculations using symmetrized Gaussians on a doubly dense Von Neumann lattice”, [The Journal of Chemical Physics](#) **137**, 224101 (2012).
- [58] J. Niset, J. Fiurášek, and N. J. Cerf, “No-go theorem for Gaussian quantum error correction”, [Physical Review Letters](#) **102**, 120501 (2009).
- [59] K. Noh, S. M. Girvin, and L. Jiang, “Encoding an oscillator into many oscillators”, [Physical Review Letters](#) **125**, 080503 (2020).
- [60] H. M. Vasconcelos, L. Sanz, and S. Glancy, “All-optical generation of states for “Encoding a qubit in an oscillator””, [Optics Letters](#) **35**, 3261 (2010).

2

THEORETICAL BACKGROUND

This chapter lays the theoretical foundations for this thesis. We start with some basic definitions and conventions, and define the Gottesman-Kitaev-Preskill (GKP) code. As the ideal GKP code states are not normalizable, it is necessary to approximate them. We discuss various representations and bases that are useful when working with GKP code states, in particular the shifted code states. Finally, we present different quality measures for the GKP code and introduce the effective squeezing parameters, which will be used throughout the thesis.

The proof of orthonormality and completeness of the shifted code states in Section 2.2.2 has been published with minor differences in D. J. Weigand and B. M. Terhal, “Generating grid states from Schrödinger-cat states without postselection”, *Physical Review A* **97**, 022341 (2018).

2.1. FUNDAMENTAL DEFINITIONS AND DERIVATIONS

In this section, we will discuss some basic definitions and conventions. We start with some fundamentals of quantum optics. Then, we present a compact derivation of the GKP code based on group theory. Of special interest to the reader are Sections 2.1.3 and 2.1.4, where we define shorthands and establish conventions used in the rest of this thesis.

2.1.1. QUANTUM OPTICS

Consider a harmonic oscillator, with creation and annihilation operators \hat{a}^\dagger, \hat{a} . The dimensionless *position* and *momentum quadrature* operators are defined as:

$$\hat{q} = \frac{1}{\sqrt{2}}(\hat{a}^\dagger + \hat{a}), \quad \hat{p} = \frac{i}{\sqrt{2}}(\hat{a}^\dagger - \hat{a}), \quad (2.1)$$

with the commutation relation

$$[\hat{q}, \hat{p}] = i. \quad (2.2)$$

A standard operation on the harmonic oscillator are so-called *displacements*. In this thesis, we will use the standard definition:

$$D(\alpha) = \exp(\alpha \hat{a}^\dagger - \alpha^* \hat{a}) = \exp(i\sqrt{2}(\Im(\alpha)\hat{q} - \Re(\alpha)\hat{p})),$$

where $\Re(\alpha)$ and $\Im(\alpha)$ denote the real and imaginary parts of a complex number α . Note that there is a factor $\sqrt{2}$ when we apply displacements to the \hat{q} and \hat{p} quadrature eigenstates¹:

$$\begin{aligned} D(u) |\hat{q} = q\rangle &= \exp(-i\sqrt{2}u\hat{p}) |\hat{q} = q\rangle &= |\hat{q} = q + \sqrt{2}u\rangle, & u \in \mathbb{R} \\ D(iv) |\hat{p} = p\rangle &= \exp(i\sqrt{2}v\hat{q}) |\hat{p} = p\rangle &= |\hat{p} = p + \sqrt{2}v\rangle. & v \in \mathbb{R} \end{aligned}$$

This factor $\sqrt{2}$ is important to keep in mind when working with the GKP code. Generically, displacement operators do not commute. For two displacements $D(\alpha), D(\beta)$ holds:

$$D(\alpha)D(\beta) = e^{i\Im(\alpha\beta^*)} D(\alpha + \beta). \quad (2.3)$$

The coherent states $|\alpha\rangle$ are eigenstates of the annihilation operator \hat{a} . They can be generated by applying a displacement operator to the vacuum state, and are complete, i. e. any state can be written as a superposition of coherent states:

$$D(\alpha) |\text{vac}\rangle = |\alpha\rangle, \quad \mathbb{1} = \frac{1}{\pi} \iint d^2\alpha |\alpha\rangle\langle\alpha|.$$

PERELOMOV'S GENERALIZED COHERENT STATES

Perelomov developed a compact derivation of coherent states starting from the Lie algebra of the harmonic oscillator. Here, we will summarize this approach following a review

¹Reference [2] uses a convention where $D(x) |q\rangle = |x + q\rangle$ and $D(\sqrt{2}\alpha) |\text{vac}\rangle = |\alpha\rangle$.

by Perelomov (1977) [3]. In the next section, we will present a compact derivation of the GKP code building upon the same construction.

The Lie algebra of the harmonic oscillator is the *Heisenberg-Weyl algebra*, with the generators $\hat{a}, \hat{a}^\dagger, \mathbb{1}$ and the commutation relations:

$$[\hat{a}, \hat{a}^\dagger] = \mathbb{1}, \quad [\hat{a}, \mathbb{1}] = [\hat{a}^\dagger, \mathbb{1}] = 0.$$

Any element of the algebra is of the form:

$$t\mathbb{1} + i(\alpha^* \hat{a} - \alpha \hat{a}^\dagger) \quad t \in \mathbb{R}, \alpha \in \mathbb{C}.$$

In order to obtain the Lie group of the Heisenberg-Weyl algebra, we use the exponential map and a unitary representation of the Heisenberg-Weyl group with elements

$$T(t, \alpha) = e^{it} D(\alpha), \quad D(\alpha) = e^{\alpha^* \hat{a} - \alpha \hat{a}^\dagger},$$

where we see that $D(\alpha)$ are the displacements defined before. By acting with $T(t, \alpha)$ on *any* fixed state $|\psi_0\rangle$ of the harmonic oscillator, we obtain the generalized coherent states.² Acting with $T(s, \beta)$ on such a (generalized) coherent state maps it to another coherent state. This representation with elements $T(t, \alpha)$ of the Heisenberg-Weyl group is irreducible. Due to the Stone-von Neumann theorem, this is also the only such representation [4]. From this follows that the coherent states are complete, and that any operation on the harmonic oscillator can be written in terms of the translations $T(t, \alpha)$.

2.1.2. THE GOTTESMAN-KITAEV-PRESKILL (GKP) CODE

The GKP code is a stabilizer code acting on a harmonic oscillator. This means that the code space is defined as the common $+1$ eigenspace of a group of operators called *stabilizers*. In the 2001 paper, Gottesman *et al.* derive their code by first defining shift-resistant codes in a qudit³ and then taking the limit $d \rightarrow \infty$. Here, we will present a very compact definition based on group theory.⁴

As discussed in the previous section, any operation acting on a harmonic oscillator can be written as a linear combination of displacements $D(\alpha)$, as they are an irreducible representation of the Heisenberg-Weyl group. If we define a code on the harmonic oscillator, the stabilizer group should be Abelian and finitely generated. From Eq. (2.3), we see that the condition for two displacements $D(\alpha), D(\beta)$ to commute is $2\Im(\alpha\beta^*) = 2n\pi, n \in \mathbb{Z}$. Without loss of generality, we can assume $\alpha \in \mathbb{R}$. If we choose $|\alpha| = |\beta|$ and $\Re(\beta) = 0$, we see that any group \mathcal{S}_k with the generators

$$\langle D(\sqrt{\pi k}), D(-\sqrt{\pi k}), D(i\sqrt{\pi k}), D(-i\sqrt{\pi k}) \rangle, \quad (2.4)$$

where k is an arbitrary positive integer, fulfills our requirements. Note that we included not only two displacements but also their inverse, as we also need to include the inverse

²Although arbitrary, $|\psi_0\rangle$ is assumed to be fixed from now on. If we choose the vacuum state $|\psi_0\rangle = |\text{vac}\rangle$ as reference state, we will recover the standard coherent states, which are a special case of the generalized coherent states. Because any translation $T(t, 0)$ does not change the state $|\psi_0\rangle$, we may as well choose $t = 0$.

³The term qubit refers to a two-dimensional system, qudits are d -dimensional systems.

⁴A generalization of this approach has recently been published by Albert *et al.* (2019) [5].

of our generators of choice in order to form a group. Because the elements of \mathcal{S}_k are commuting unitary operators, they have a common set of eigenstates, and the eigenvalues can be measured simultaneously.

For $k = 1$, we see that there are no displacements outside of the group \mathcal{S}_1 that commute with the whole group.⁵ In the case $k = 2$, the group \mathcal{P}_2 generated by

$$\left\langle D(\sqrt{\pi/2}), D(-\sqrt{\pi/2}), D(i\sqrt{\pi/2}), D(-i\sqrt{\pi/2}) \right\rangle, \quad (2.5)$$

commutes with \mathcal{S}_2 . We can also easily verify that the generators of \mathcal{P}_2 have the same commutation relations as the Pauli group of a qubit, but the group is of course infinite as the generators do not square to the identity. However, the generators of \mathcal{P}_2 all square to a member of the group \mathcal{S}_2 , so they will *act* as the identity on any subspace of the harmonic oscillator that is in a common eigenspace of the elements of \mathcal{S}_k . The group \mathcal{S}_2 is the stabilizer group of the GKP code, and the group \mathcal{P}_2 includes the logical operators.

GKP HEX AND SQUARE CODE

In the derivation above, we made some choices for the displacements $D(\alpha), D(\beta)$ to obtain the GKP code. One might ask how these choices change the obtained code and if other choices are also valid. First, note that the choice $\alpha \in \mathbb{R}$ was without loss of generality, as it corresponds simply to a choice of reference frame.

The stabilizer group can be seen as a lattice in the (two-dimensional) phase space. This means that the crystallographic restriction theorem applies: There are only five different types of discrete lattices in the plane, all other choices of unit cell (and therefore of generators for the stabilizer group) cover the whole plane. Therefore, there are five equivalence classes of choices for the generators of the stabilizer group such that the stabilizer group defines a non-trivial subspace of the harmonic oscillator. Furthermore, we wish the rotational symmetry of the stabilizer group to be as large as possible: On the one hand, the dominant error channel of typical harmonic oscillators — photon loss — acts in a radially symmetric way in phase space. On the other hand, the quadratures \hat{q}, \hat{p} are always defined with respect to some external drive. In the absence of such an external drive, there is typically no preferred direction of displacements in the phase space of the oscillator. All together, there remain only two “good” choices for the stabilizers:

The square lattice described above, and the hexagonal lattice. In the latter case, the stabilizer group is generated by:

$$\left\langle D\left(\sqrt{2\pi k/\sqrt{3}}\right), D\left(-\sqrt{2\pi k/\sqrt{3}}\right), D\left(e^{i\pi/3}\sqrt{2\pi k/\sqrt{3}}\right), D\left(-e^{i\pi/3}\sqrt{2\pi k/\sqrt{3}}\right) \right\rangle.$$

The performance of this code with respect to photon loss is slightly better than for the standard GKP code [2, 7, 8]. However, the analysis of the code is slightly more complicated, and all results and techniques derived for the standard GKP code with a square lattice also hold for the hexagonal GKP code. For this reason, the rest of this thesis will focus on the square GKP code.

⁵This is the basis for displacement sensing, see Section 1.3.3 and [6].

2.1.3. STABILIZERS, LOGICAL OPERATIONS, AND CODE STATES OF THE GKP CODE

For convenience, we define the following shorthands for the stabilizers and logical Pauli gates of the GKP code:

$$S_q = e^{i2\sqrt{\pi}\hat{q}}, \quad S_p = e^{-i2\sqrt{\pi}\hat{p}}, \quad (2.6)$$

$$Z = e^{i\sqrt{\pi}\hat{q}}, \quad X = e^{-i\sqrt{\pi}\hat{p}}. \quad (2.7)$$

We choose the common +1 eigenspace of the stabilizers as the code space. The logical state $|\bar{0}\rangle$ is therefore the common +1 eigenstate of S_p, S_q and Z .

The projector $\Pi(\theta)$ onto the $e^{i\theta}$ eigenspace of a unitary operator U can be formally written as:

$$\Pi(\theta) = \frac{1}{2\pi} \sum_{n=-\infty}^{\infty} e^{-i\theta n} U^n. \quad (2.8)$$

To show this, consider the action of $\Pi(\theta)$ on an arbitrary eigenstate $|\vartheta\rangle$ of U :

$$\frac{1}{2\pi} \sum_{n=-\infty}^{\infty} e^{-i\theta n} U^n |\vartheta\rangle = \frac{1}{2\pi} \sum_{n=-\infty}^{\infty} e^{i(\vartheta-\theta)n} |\vartheta\rangle = \delta(\vartheta-\theta) |\vartheta\rangle,$$

where we used the representation of the Dirac delta distribution as an infinite sum.

Using Eq. (2.8), logical state $|\bar{0}\rangle$ is given by

$$|\bar{0}\rangle \propto \sum_{k,m,n=-\infty}^{\infty} S_p^n S_q^k Z^m |\psi\rangle = \sum_{m,n} S_p^n Z^m |q=0\rangle = \sum_m |q=2\sqrt{\pi}m\rangle,$$

where we made use of the fact that the arbitrary state $|\psi\rangle$ can be chosen to be the position eigenstate $|q=0\rangle$. These states are not normalizable, meaning that we need to approximate them for a physical implementation. This question will be discussed in more detail in Section 2.2.

2.1.4. LOGICAL AND PHYSICAL QUBITS

Throughout this thesis, we usually deal with multiple coupled physical systems. In particular, it is important to distinguish between operators acting on a *physical* ancillary qubit and *logical* operators that act on a logical qubit encoded in an oscillator space. Unless the system an operator acts on is obvious from the context, operations on physical qubits will be expressed in terms of spin- $\frac{1}{2}$ operators:

$$\sigma_x = \frac{1}{2} \begin{pmatrix} 0 & 1 \\ 1 & 0 \end{pmatrix}, \quad \sigma_y = \frac{i}{2} \begin{pmatrix} 0 & -1 \\ 1 & 0 \end{pmatrix}, \quad \sigma_z = \frac{1}{2} \begin{pmatrix} 1 & 0 \\ 0 & -1 \end{pmatrix}, \quad \sigma_+ = \begin{pmatrix} 0 & 1 \\ 0 & 0 \end{pmatrix}, \quad \sigma_- = \begin{pmatrix} 0 & 0 \\ 1 & 0 \end{pmatrix}.$$

One notable exception are Pauli gates in a circuit (where the system the gate acts on is well defined). In this case, we write the Pauli gates in the computational basis of the qubits:

$$X = e^{i\pi\sigma_x - i\pi/2} = \begin{pmatrix} 0 & 1 \\ 1 & 0 \end{pmatrix}, \quad Y = e^{i\pi\sigma_y - i\pi/2} = \begin{pmatrix} 0 & -i \\ i & 0 \end{pmatrix}, \quad Z = e^{i\pi\sigma_z - i\pi/2} = \begin{pmatrix} 1 & 0 \\ 0 & -1 \end{pmatrix},$$

so that for example $X|0\rangle = |1\rangle$.

For logical qubits encoded in an oscillator, we will use the symbols X, Y, Z to indicate the logical Pauli gates. For the Gottesman-Kitaev-Preskill code, the logical gates are defined as

$$X = D\left(\frac{\sqrt{\pi}}{\sqrt{2}}\right) = e^{-i\sqrt{\pi}\hat{p}}, \quad Y = D\left(\frac{(1+i)\sqrt{\pi}}{\sqrt{2}}\right) = e^{i\sqrt{\pi}(\hat{q}-\hat{p})}, \quad Z = D\left(\frac{i\sqrt{\pi}}{\sqrt{2}}\right) = e^{i\sqrt{\pi}\hat{q}},$$

with the displacement operator $D(\alpha)$ defined in the previous section.

2.2. REPRESENTATIONS OF GKP CODE STATES

As the GKP code is defined with respect to unitary stabilizer operators acting on a harmonic oscillator, there are multiple different representations. In this section, we present some of these representations, and discuss the advantages and disadvantages of each representation.

2.2.1. POSITION OR MOMENTUM WAVE FUNCTION

In this section, we follow the derivation by Gottesman *et al.* [7]. In phase space, we can construct the ideal GKP code states as follows: Given the definition of the logical operator $Z = e^{i\sqrt{\pi}\hat{q}}$, it is straight forward to see that its ± 1 eigenstates are:

$$\begin{aligned} Z|\hat{q} = 2n\sqrt{\pi}\rangle &= e^{2n\pi i}|\hat{q} = 2n\sqrt{\pi}\rangle = |\hat{q} = 2n\sqrt{\pi}\rangle, & n \in \mathbb{Z}, \\ Z|\hat{q} = (2n+1)\sqrt{\pi}\rangle &= -|\hat{q} = (2n+1)\sqrt{\pi}\rangle. \end{aligned}$$

As $S_q = Z^2$, these states are already $+1$ eigenstates of the stabilizer S_q as well. The stabilizer S_p on the other hand has the action $S_p|\hat{q} = q'\rangle = |\hat{q} = q' + 2\sqrt{\pi}\rangle$. Therefore, a simultaneous ± 1 eigenstate of Z, S_q and S_p is some superposition of position eigenstates $|\hat{q} = 2n\sqrt{\pi}\rangle$ that is invariant under translation by $2\sqrt{\pi}$:

$$|\bar{0}\rangle \propto \sum_{n=-\infty}^{\infty} |\hat{q} = 2n\sqrt{\pi}\rangle, \quad |\bar{1}\rangle \propto \sum_{n=-\infty}^{\infty} |\hat{q} = (2n+1)\sqrt{\pi}\rangle. \quad (2.9)$$

Using the same approach, we can see that the eigenstates of the logical Pauli X operator in the momentum basis have the same form:

$$|\bar{+}\rangle \propto \sum_{n=-\infty}^{\infty} |\hat{p} = 2n\sqrt{\pi}\rangle, \quad |\bar{-}\rangle \propto \sum_{n=-\infty}^{\infty} |\hat{p} = (2n+1)\sqrt{\pi}\rangle. \quad (2.10)$$

As also discussed in Section 2.1.3, these states are clearly not normalizable. In order to obtain physical, finite energy code states, it is necessary to approximate the ideal GKP code states. To this end, Gottesman *et al.* first replace the (infinitely squeezed) position eigenstates by displaced squeezed vacuum states [7]:

$$|\hat{q} = 2\sqrt{\pi}n\rangle \approx D(\sqrt{2\pi}n)S(\Delta_q)|q\rangle = \frac{1}{(\pi\Delta_q^2)^{1/4}} \int_{-\infty}^{\infty} e^{-\frac{(q-2\sqrt{\pi}n)^2}{2\Delta_q^2}} dq |q\rangle,$$

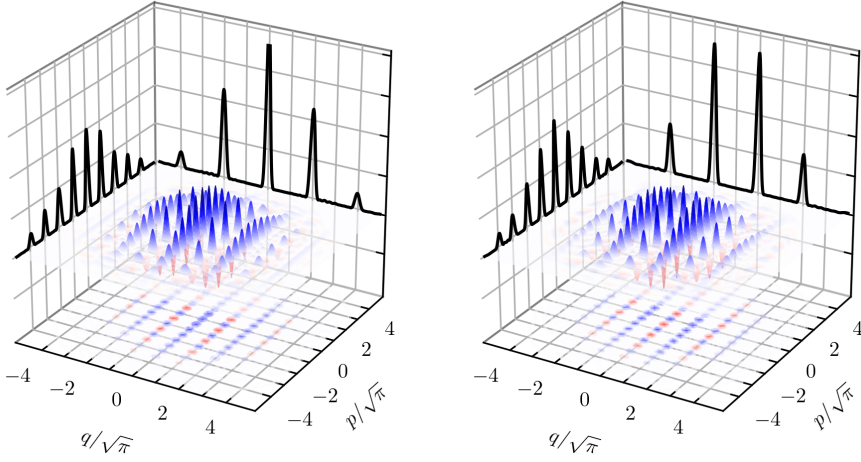


Figure 2.1: Wigner function and probability distributions in q and p of approximate GKP code states. Left: Approximate code state $|\tilde{0}\rangle$, Right: Approximate code state $|\tilde{1}\rangle$.

where $S(\Delta) = \exp((- \ln(\Delta) \hat{a}^2 + \ln(\Delta) (\hat{a}^\dagger)^2)/4)$ is the squeezing operator. Its action on the quadrature operators is $S(\Delta) \hat{q} S(\Delta)^\dagger = \hat{q}/\Delta$, and $S(\Delta) \hat{p} S(\Delta)^\dagger = \hat{p}\Delta$. In the limit $\Delta \rightarrow 0$, the squeezed vacuum states go to a Dirac delta distribution and we recover again the position eigenstates. In the second step, we add a Gaussian envelope to the infinite sum:

$$|\tilde{0}\rangle = \frac{1}{\mathcal{N}_0} \sum_{n=-\infty}^{\infty} e^{-2\pi\Delta_p^2 n^2} \int_{-\infty}^{\infty} dq e^{-\frac{(q-2\sqrt{\pi}n)^2}{2\Delta_q^2}} |q\rangle, \quad (2.11)$$

$$|\tilde{1}\rangle = \frac{1}{\mathcal{N}_+} \sum_{n=-\infty}^{\infty} e^{-2\pi\Delta_q^2 n^2} \int_{-\infty}^{\infty} dp e^{-\frac{(p-2\sqrt{\pi}n)^2}{2\Delta_p^2}} |p\rangle. \quad (2.12)$$

In order to compute the normalization, we proceed in the following way: First, we assume that the overlap between two different squeezed vacuum states is negligible so that we can normalize them individually. In order to also normalize the envelope, we assume $\Delta_p \ll 1$ so that the infinite sum can be approximated as an integral. With these considerations, the norm \mathcal{N}_0 can be approximated as:

$$\begin{aligned} \mathcal{N}_{\text{sq.vac}}^2 &= \int_{-\infty}^{\infty} dq e^{-\frac{(q-2\sqrt{\pi}n)^2}{2\Delta_q^2}} = \Delta_q \sqrt{\pi}, \\ \mathcal{N}_{\text{envelope},0}^2 &\approx \int_{-\infty}^{\infty} dn \exp(-4\pi\Delta_p^2 n^2) = \frac{1}{2\Delta_p}, \\ \mathcal{N}_0 &\approx \mathcal{N}_{\text{sq.vac}} \mathcal{N}_{\text{envelope},0} \approx \sqrt{\frac{\Delta_q \sqrt{\pi}}{2\Delta_p}}. \end{aligned}$$

In Fig. 2.1, the Wigner functions and the probability distribution in p and q of the approximate code states $|\tilde{0}\rangle, |\tilde{1}\rangle$ defined in Eq. (2.11) are shown.

2.2.2. SHIFTED CODE STATES

The shifted code states, also called Zak basis, were originally introduced by Zak in 1967 as a basis associated with the eigenvalues of finite displacements [9]. In the context of the GKP code, they were first used by Glancy and Knill in order to obtain a “threshold”⁶ [10]. For the GKP (qubit) code, they are defined as:

$$\begin{aligned} |u, v\rangle &= \frac{1}{\pi^{1/4}} e^{-iv\hat{p}} e^{iu\hat{q}} |\bar{0}\rangle = \frac{1}{\pi^{1/4}} \sum_{s=-\infty}^{\infty} \exp(iu2s\sqrt{\pi}) |q = 2s\sqrt{\pi} + v\rangle \\ &= \frac{1}{\pi^{1/4}} \sum_{s=-\infty}^{\infty} \exp(iv(s\sqrt{\pi} + u)) |p = s\sqrt{\pi} + u\rangle, \end{aligned} \quad (2.13)$$

with $v \in [-\sqrt{\pi}/2, \sqrt{\pi}/2)$ and $u \in [-\sqrt{\pi}/2, 3\sqrt{\pi}/2)$.⁷ These states form an orthonormal basis for the Hilbert space of the Harmonic oscillator, which we will prove below.

ORTHONORMALITY AND COMPLETENESS OF SHIFTED GRID STATES

In this section, we show that the shifted code states form an orthonormal basis. The proof will be split in two parts, showing orthonormality first and completeness afterwards, see the lemmas below. The proof will be done for a generalized class of shifted code states, which will be used in Chapter 4 to analyze an optical “breeding protocol” for GKP states.

In the breeding protocol, phase space will be rescaled between each round m . Furthermore, we would like the proof to be applicable to any qudit (including $d = 1$, i. e. the sensor state). To take this into account, we introduce a scaling factor $s_m \xi$, where $\xi = \sqrt{2\pi d}$ for a qudit with d dimensions and $s_m \in (0, 1]$ is the rescaling between rounds. With these new scaling factors, the distance $2\sqrt{\pi}$ does not have a special meaning anymore. Therefore, we also rescale the variables u, v of the shifted code states to $u, v \in [-\pi, \pi)$. With these changes, we define the generalized shifted grid states as

$$|u, v, m\rangle = \frac{\sqrt{s_m \xi}}{2\pi} \sum_{s=-\infty}^{\infty} \exp\left(iv\left(s + \frac{u}{2\pi}\right)\right) \left|p = s_m \xi \left(s + \frac{u}{2\pi}\right)\right\rangle, \quad (2.14)$$

with $u, v \in [-\pi, \pi)$, and $m \in \mathbb{N}_0$. As the relation between Eq. (2.14) and Eq. (2.13) are simple rescalings, the proofs of orthonormality and completeness are still valid for the original definitions by Glancy and Knill.

Lemma 2.2.1. *The class of shifted grid states as defined in Eq. (2.14) is orthonormal, i. e. it holds that $\langle u', v', m | u, v, m \rangle = \delta(u - u') \delta(v - v')$.*

⁶Usually, the threshold of a code is defined as follows: If the error rate of the constituent (physical) qubits is below the threshold, the logical error rate will decrease if the number of physical qubits is increased (using concatenation, increasing the lattice size of the code etc.). The threshold defined by Glancy and Knill is a statement about error correction of a GKP code state using noisy, GKP encoded ancilla qubits: If the only noise process are mixtures of small displacements, and the total amplitude per qubit and error correction cycle is below $\sqrt{\pi}/6$, the errors are correctable indefinitely.

⁷In the GKP (qubit) code, the eigenvalues of the stabilizers are twofold degenerate. In order to obtain a set of linearly independent eigenstates, the shifted code states are the common eigenstates of one logical operator and one stabilizer. Here, the choices for the two operators are X, S_q , implying the domain as chosen above. This choice is arbitrary, one could easily also use Z, S_p .

Proof. From the definition of shifted grid states (Eq. (2.14)) and the orthonormality of the momentum eigenstates it follows

$$\langle u', v', m | u, v, m \rangle = \frac{s_m \xi}{(2\pi)^2} \sum_{s, t=-\infty}^{\infty} \exp \left(i v \left(s + \frac{u}{2\pi} \right) - i v' \left(t + \frac{u'}{2\pi} \right) \right) \delta \left(s_m \xi \left(s - t + \frac{u - u'}{2\pi} \right) \right).$$

The difference $u - u'$ needs to be an integer multiple of 2π for the Dirac delta-function to be non-zero. Since $u, u' \in [-\pi, \pi)$, i. e. $u - u' \in (-2\pi, 2\pi)$, the only solution is $u = u'$ and $s = t$. With $\delta(x) = |a| \delta(ax)$ and $\delta(x) = \frac{1}{2\pi} \sum_{s=-\infty}^{\infty} \exp(isx)$ the claim follows:

$$\begin{aligned} \langle u', v', m | u, v, m \rangle &= \frac{1}{2\pi} \sum_s \exp \left(i(v - v') \left(s + \frac{u}{2\pi} \right) \right) \delta(u - u'), \\ &= \delta(v - v') \delta(u - u'). \end{aligned}$$

□

To complete the proof that the shifted grid states form an orthonormal basis, we also show their completeness. We do this by showing $\int du \int dv |u, v, m\rangle \langle u, v, m| p\rangle = |p\rangle$ for any momentum eigenstate $|p\rangle$.

Lemma 2.2.2. *The class of shifted grid states as defined in Eq. (2.14) is complete, i. e. it holds that $\int du \int dv |u, v, m\rangle \langle u, v, m| = \mathbb{1}$.*

Proof. The wave function of a momentum state in the shifted grid state basis is

$$\langle u, v, m | \hat{p} = p \rangle = \sqrt{\frac{s_m \xi}{(2\pi)^2}} \sum_{s=-\infty}^{\infty} \exp \left(-i v \left(s + \frac{u}{2\pi} \right) \right) \delta \left(\xi s_m \left(s + \frac{u}{2\pi} \right) - p \right).$$

Since $u \in [-\pi, \pi)$, the Dirac delta distribution is only non-zero for a specific value $s = \tilde{s}$ with $\tilde{p} := p - \xi s_m \tilde{s}$, $\tilde{p} \in [-\pi, \pi)$. Using $\delta(x) = |a| \delta(ax)$, we can simplify the wave function of a momentum state in the basis of shifted grid states to

$$\langle u, v, m | \hat{p} = p \rangle = \sqrt{\frac{1}{\xi s_m}} \exp \left(-i v \left(\tilde{s} + \frac{u}{2\pi} \right) \right) \delta \left(u - \frac{2\pi}{\xi s_m} \tilde{p} \right).$$

Using the definition of a shifted grid state (see Eq. (2.14)) and the wave function of a momentum state in the basis of shifted grid states, we obtain

$$\begin{aligned} \iint du dv |u, v, m\rangle \langle u, v, m | \hat{p} = p \rangle &= \sqrt{\frac{1}{\xi s_m}} \iint du dv e^{-i v \left(\tilde{s} + \frac{u}{2\pi} \right)} \delta \left(u - \frac{2\pi}{\xi s_m} \tilde{p} \right) |u, v, m\rangle \\ &= \frac{1}{2\pi} \int dv \sum_s e^{i v (s - \tilde{s})} |\hat{p} = s_m \xi s + \tilde{p}\rangle \\ &= |\hat{p} = s_m \xi \tilde{s} + \tilde{p}\rangle = |\hat{p} = p\rangle. \end{aligned}$$

In the second step, we used the integral representation of the Kronecker delta:

$$\frac{1}{2\pi} \int_0^{2\pi} dx \exp(ix(n - m)) = \delta_{mn}.$$

□

ANALYTICAL WAVEFUNCTION FOR GKP STATES

Using the basis of the shifted code states, we can define an approximate code state with a “simple” wave function⁸:

$$|\tilde{0}\rangle = \iint du dv \frac{\exp(\Delta^{-2}(\cos(\sqrt{\pi}u) + \cos(2\sqrt{\pi}v)))}{\sqrt{2\pi}I_0(2\Delta^{-2})} |u, v\rangle. \quad (2.15)$$

Here, the wave function is a von Mises probability distribution and I_0 is the modified Bessel function of the first kind of order 0. In the limit $\Delta \rightarrow 0$, the von Mises probability distribution goes to a normal distribution, using Eq. (2.13) we then recover the original approximate code state Eq. (2.11). In contrast to other definitions of approximate code states, the norm of the state can be evaluated analytically without approximations. A hybrid between Eqs. (2.11) and (2.15) will be used in Chapter 4 in order to obtain a class of states that is closed under multiplication in one quadrature and closed under convolution in the other.

2.2.3. GKP CODE STATES IN THE FOCK BASIS

In numerical simulations, the standard way to represent a state is in the *Fock basis*. Although not well suited for analytical considerations, the major advantage of this basis is that it is discrete and therefore better suited for numerics than, for example, the quadrature bases or the shifted code states. However, only a finite number of Fock states can be stored, meaning that there will always be rounding errors (see Appendix A.1). Therefore, it is important to analyze the average photon number and variance of approximate GKP code states.

First, we can show an (approximate) GKP code state has only support on even photon number Fock states. Consider the approximate code state in Eq. (2.11). It is clearly symmetric with respect to reflection along the y -axis, i. e. the operation $\hat{q} \rightarrow -\hat{q}$.⁹ This operation is implemented by the unitary operator $e^{i\pi\hat{a}^\dagger\hat{a}}$. Therefore, we have

$$e^{i\pi\hat{a}^\dagger\hat{a}}|\tilde{0}\rangle = |\tilde{0}\rangle, \quad \Rightarrow \quad |\tilde{0}\rangle = \sum_{n=0}^{\infty} c_n |2n\rangle, c_n \in \mathbb{C}.$$

We can also compute the average photon number and its variance. First, we rewrite

$$\hat{a}^\dagger\hat{a} = \frac{1}{2}(\hat{q} - i\hat{p})(\hat{q} + i\hat{p}) = \frac{1}{2}(\hat{q}^2 + \hat{p}^2 + i(\hat{q}\hat{p} - \hat{p}\hat{q})) = \frac{1}{2}(\hat{q}^2 + \hat{p}^2 - 1). \quad (2.16)$$

Because the approximate code states are eigenstates of $e^{i\pi\hat{a}^\dagger\hat{a}}$, the expectation value of the \hat{p} and \hat{q} operators is zero:

$$\langle\tilde{0}|\hat{q}|\tilde{0}\rangle = \langle\tilde{0}|e^{-i\pi\hat{a}^\dagger\hat{a}}\hat{q}e^{i\pi\hat{a}^\dagger\hat{a}}|\tilde{0}\rangle = -\langle\tilde{0}|e^{-i\pi\hat{a}^\dagger\hat{a}/2}\hat{p}e^{i\pi\hat{a}^\dagger\hat{a}/2}|\tilde{0}\rangle = -\langle\tilde{+}|\hat{p}|\tilde{+}\rangle = -\langle\tilde{0}|\hat{q}|\tilde{0}\rangle = 0.$$

Using Eqs. (2.11) and (2.12) and $|0\rangle = \frac{1}{\sqrt{2}}(|+\rangle + |-\rangle)$, we can simply evaluate the expectation values $\langle\hat{q}^2\rangle, \langle\hat{p}^2\rangle$ and obtain (assuming $\Delta_p = \Delta_q = \Delta$) [7, 11]

$$\bar{n} = \langle\hat{a}^\dagger\hat{a}\rangle \approx \frac{1}{2\Delta^2} + \frac{\Delta^2}{2} - \frac{1}{2},$$

⁸For a derivation, see later in Section 4.3.4.

⁹The same argument can also be used to show that a Schrödinger cat state $|\alpha\rangle + |-\alpha\rangle$ has an even photon number.

where the approximation is due to the normalization of the approximate code state, and we assume $\Delta \ll 1$. In order to compute the standard deviation of the photon number, we use that $\langle \hat{p}^4 \rangle = \langle \hat{q}^4 \rangle$ and $\hat{p} = -i \frac{d}{d\hat{q}}$. We arrive at [11]

$$\sigma_n = \sqrt{\langle \hat{a}^\dagger \hat{a}^2 \rangle - \langle \hat{a}^\dagger \hat{a} \rangle^2} \approx \frac{1}{2\Delta^2} + \mathcal{O}(\Delta^2),$$

which is equal to the average photon number \bar{n} in the leading order of Δ . This means that, when using approximate GKP states with effective squeezing parameters $\Delta_q = \Delta_p = \Delta$ in numerical simulations, the size of the Hilbert space should be around $\frac{2}{\Delta^2}$ for a confidence of 3σ , or about 50 for an effective squeezing of $\Delta = 0.2$.¹⁰

In [12], an expression for the normalization constant and the coefficients of a Fock basis representation of the GKP code states is derived. The authors show that asymptotically in n , the coefficients have the same scaling as a thermal distribution

$$p_n = \frac{1}{\bar{n} + 1} \left(\frac{\bar{n}}{\bar{n} + 1} \right)^n, \quad \text{with} \quad \bar{n} = \frac{e^{-2\Delta^2}}{1 - e^{-2\Delta^2}}.$$

2.3. QUALITY MEASURES FOR THE GKP CODE

IN contrast to standard qubit codes, quantifying the quality of any particular approximate code state of the GKP code is not straight forward. The issue stems from the fact that the Hilbert space of the harmonic oscillator is infinite, therefore the space of correctable states is also infinite. In this section, we will discuss how the quality of any approximate GKP code state can be quantified.

2.3.1. IDEAL DECODER

The simplest solution to interpret an arbitrary state as an approximate GKP code word is to evaluate the state with an ideal decoder, and compare the resulting state to a target state. In the position and shifted code state representations, this decoder is given by

$$\mathcal{D}_q \propto \sum_{n=-\infty}^{\infty} \int_{-\sqrt{\pi}/2 + n\sqrt{\pi}}^{\sqrt{\pi}/2 + n\sqrt{\pi}} dq \left(|\bar{0}\rangle \langle q| + |\bar{1}\rangle \langle q + \sqrt{\pi}| \right), \quad (2.17)$$

$$\mathcal{D}_{u,v} \propto \int_{-\sqrt{\pi}/2}^{\sqrt{\pi}/2} du \int_{-\sqrt{\pi}/2}^{\sqrt{\pi}/2} dv \left(|\bar{0}\rangle \langle u, v| + |\bar{1}\rangle \langle u + \sqrt{\pi}, v| \right). \quad (2.18)$$

Note that output of this decoder is not normalized. For an illustration of the ideal decoder $\mathcal{D}_{u,v}$, see the sketches in Fig. 2.2. The ideal decoder maps everything in the regions shaded in yellow to the code state $|\bar{0}\rangle$, and all of the region shaded in green to the code state $|\bar{1}\rangle$. As the decoder always gives a binary result, the information one can obtain using it is very coarse-grained. Below, we will discuss methods that are better suited for analyzing a GKP code state.

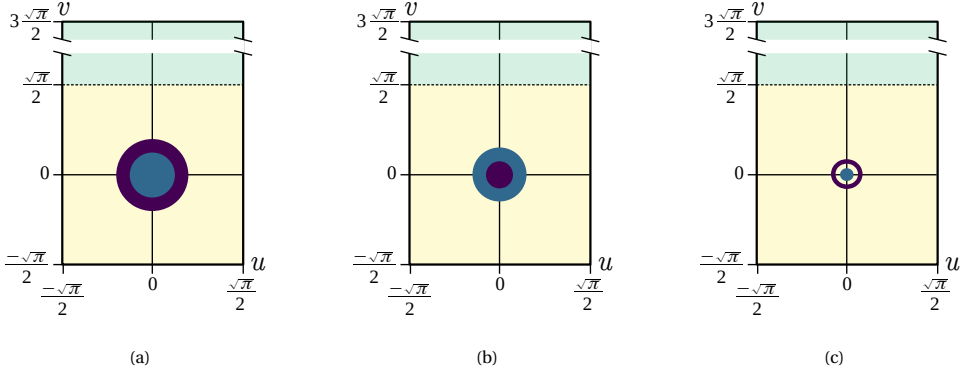


Figure 2.2: Overlap of an approximate GKP code state of interest with a target state. The ideal decoder (Eq. (2.18)) assigns the region shaded in yellow (green) to the logical $|\bar{0}\rangle$ ($|\bar{1}\rangle$) state, respectively. The state of interest is shaded purple, the target state is shown in blue. (a): The state of interest has support on a larger region than the target state. The overlap increases the closer the state of interest is to an ideal GKP code state. (b): If the situation is reversed, i. e. the target state has support on a larger region of phase space the state of interest. Now, the overlap decreases the closer the state of interest is to an ideal GKP code state, which can lead to misleading results. (c): In an extreme situation, both the target state and the state of interest have support on small regions of phase space. Here, these regions are disjoint. This means that the overlap is zero, even if we take an approximation where both code states go towards an ideal code state.

2.3.2. WHY THE OVERLAP IS NOT A GOOD QUALITY MEASURE

In quantum optics, a standard way to quantify the quality of some state is to compute the overlap between the state of interest and the target state. For the GKP code, this is however not a good choice. It is not possible to choose a target state where the overlap with some state of interest is a monotonic function of the logical error rate of the state of interest.

As an example, suppose that the target state is an approximate GKP code state of the form of Eq. (2.15), with some fixed, small squeezing parameter Δ . Now suppose that the state of interest $|\Psi\rangle$ has the same form, but with squeezing parameter

$$\kappa = 10^x \Delta, \quad x \approx 0.$$

We are interested in the overlap as a function of x (i. e. the relation of Δ and κ). Ideally, the overlap increases, the closer the state of interest gets to an ideal code state. For $x > 0$ (see Fig. 2.2a for a sketch in the basis of shifted code states) this is the case. However, the overlap decreases again for $x < 0$, (see Fig. 2.2b for a sketch in the basis of shifted code states), and it goes to zero for $x \rightarrow -\infty$, i. e. the ideal GKP code state has negligible overlap with the target state. For small Δ and $\kappa \approx \Delta$ (and therefore $x \approx 0$), the overlap is approximately

$$|\langle \Psi | \bar{0} \rangle| \approx 1 - \frac{\ln(10^x)^2}{2} + \mathcal{O}(x^3).$$

¹⁰This estimation is a minimum. Depending on details of the simulation, a significantly higher number might be needed.

Thus, as mentioned before, the overlap decreases if the squeezing parameter of the state of interest is smaller than the target state, even though that means that the state of interest is a better approximation of the ideal GKP code state.

With these considerations, it seems best to choose the target state with a very small Δ , such that the squeezing parameter of the target state most likely is smaller than that of a state of interest. However, there is a further complication in this case: For small Δ , the target state only has support on a small fraction of phase space. This means that the target state may have very small overlap with a state of interest, even if the state of interest is a good approximate code state.

Suppose that the target state is again of the form of Eq. (2.15), with small Δ . Now suppose that the state of interest is of similar form with squeezing parameter $\kappa \gtrsim \Delta$ which is similar to, but slightly larger than Δ . To construct a (pathological) example, we can orthogonalize this state with respect to the target state. For an exaggerated sketch, see Fig. 2.2c. It is easy to verify that both states will become very close to the ideal GKP code state if both Δ and κ go to zero. However, by construction, the two states will always be orthogonal.

This means that the overlap with some target state underestimates the quality of an approximate code state, in some cases by a large margin. Furthermore, measuring the overlap requires knowledge of the state of interest. For numerical simulations, this is feasible, but it can be very challenging in an experiment.

2.3.3. HOLEVO PHASE VARIANCE

One way to interpret a state as an approximate GKP state is using that the ideal GKP code states are eigenstates of unitary operators (the stabilizers). Any state can be expressed as some superposition or mixture of eigenstates of the stabilizers. To quantify how close any state ρ is to an eigenstate of some unitary operator U , one can use the *Holevo phase variance*. It is defined as

$$\sigma_H = \sqrt{|\text{Tr}(\rho U)|^{-2} - 1}.$$

The GKP code space is defined by the common eigenspace of the unitary stabilizers S_p, S_q with eigenvalues $+1$. Displacements by some $D(\alpha)$ will leave any state within the GKP code space unchanged, they simply change the pair of eigenvalues for S_p, S_q that defines the eigenspace. The simultaneous eigenstates of the stabilizers S_q and S_p are the shifted code states $|u, v\rangle$, see Eq. (2.13). These states form a basis for the Harmonic oscillator, see Section 2.2.2.

We will now evaluate the Holevo phase variance for a typical approximate GKP state. For simplicity, we discuss only the eigenvalues of the stabilizer S_q , the eigenvalues of the stabilizer S_p are completely analogous. Consider an approximate GKP code state $|\tilde{0}\rangle$ as defined in Eq. (2.11), with an additional displacement $D(\mu/\sqrt{2})$:

$$|\Psi\rangle = D\left(\frac{\mu}{\sqrt{2}}\right)|\tilde{0}\rangle = \frac{1}{\mathcal{N}_0} \sum_{n=-\infty}^{\infty} e^{-2\pi\Delta_p^2 n^2} \int_{-\infty}^{\infty} dq e^{-\frac{(q-2\sqrt{\pi}n-\mu)^2}{2\Delta_q^2}} |q\rangle. \quad (2.19)$$

The probability distribution in q is

$$\begin{aligned} \mathbb{P}_\Psi(q) &= \frac{1}{\mathcal{N}_0^2} \sum_{n,k} e^{-2\pi\Delta_p^2(n^2+k^2)} \exp\left(-\frac{(q-2\sqrt{\pi}n)^2 - (q-2\sqrt{\pi}k-\mu)^2}{2\Delta_q^2}\right) \\ &\approx \frac{1}{\mathcal{N}_0^2} \sum_n e^{-4\pi\Delta_p^2 n^2} \exp\left(-\frac{(q-2\sqrt{\pi}n-\mu)^2}{\Delta_q^2}\right), \end{aligned} \quad (2.20)$$

where the approximation is $n = k$ for $\Delta_q \ll 1$. This approximation is very accurate, the error is $\mathcal{O}(10^{-11})$ for $\Delta_q = 0.5$. Because the state is pure, we can easily evaluate the Holevo phase variance with a simple integral:

$$\begin{aligned} \text{Tr}(|\Psi\rangle\langle\Psi|S_q) &= \int_{-\infty}^{\infty} dq e^{i2\sqrt{\pi}q} \mathbb{P}_\Psi(q) \\ &\approx \frac{1}{\mathcal{N}_0^2} \sum_n \int_{-\infty}^{\infty} dq e^{i2\sqrt{\pi}q} e^{-4\pi\Delta_p^2 n^2} \exp\left(-\frac{(q-2\sqrt{\pi}n-\mu)^2}{\Delta_q^2}\right) \\ &= e^{i2\sqrt{\pi}\mu} e^{-\Delta_q^2 \pi} \end{aligned} \quad (2.21)$$

Which gives the Holevo phase variance

$$\begin{aligned} \sigma_H &= \sqrt{e^{2\Delta_q^2 \pi} - 1} \\ &\approx \sqrt{2\pi}\Delta_q + \frac{\sqrt{2\pi}^3}{2}\Delta_q^2 + \mathcal{O}(\Delta_q^4), \end{aligned} \quad (2.22)$$

where the approximation is for small Δ_q .

EFFECTIVE SQUEEZING PARAMETERS

Because we have some knowledge about typical approximate code states, we can improve upon the Holevo phase variance. Namely, typical approximate code states are close to a superposition of squeezed vacuum states with a Gaussian envelope (i.e. of the form of Eq. (2.19)). This knowledge allows us to define a different quality measure that recovers the parameters of these two Gaussian distributions directly.

Thus, we can simply solve Eq. (2.21) for Δ_q and μ , defining the *mean shifts* and the *effective squeezing parameters*:

$$\mu_q(\rho) \equiv \frac{\arg\left(|\text{Tr}(S_q \rho)|^2\right)}{2\sqrt{\pi}}, \quad \Delta_q(\rho) \equiv \sqrt{\frac{1}{2\pi} \ln\left(\frac{1}{|\text{Tr}(S_q \rho)|^2}\right)}, \quad (2.23)$$

where μ_p, Δ_p are defined analogously and where the subscript q (p) indicates that the stabilizer S_q (S_p) was used. When $|\text{Tr}(S_q \rho)|$ is close to 1, i.e. ρ is close to an ideal GKP code state, one can use $\ln(1+x) = x + \mathcal{O}(x^2)$ to show that $\Delta_q(\rho) = \frac{1}{\sqrt{2\pi}} \sqrt{|\text{Tr}(S_p \rho)|^{-2} - 1}$, thus relating the effective squeezing parameter to the Holevo phase variance. For a squeezed vacuum state $|\text{sq. vac.}\rangle$ in q with squeezing parameter $\Delta_q < 1$ such that $\text{Var}(q) = \frac{1}{2}\Delta_q^2$, one has $\langle \text{sq. vac.} | S_q | \text{sq. vac.} \rangle = \exp(-\Delta_q^2 \pi)$ from which it follows that $\Delta_q(\text{sq. vac.}) = \Delta_q$ and $\Delta_p(\text{sq. vac.}) = 1/\Delta_q$. Each state ρ can thus be characterized by two effective squeezing parameters $\Delta_p(\rho)$ and $\Delta_q(\rho)$. For the grid state in Eq. (2.11), one has $\Delta_p \approx \Delta_q = \Delta$.

2.3.4. CHARACTERIZING WAVE FUNCTIONS IN A QUADRATURE BASIS

The question of characterizing an approximate GKP code state can also be interpreted as a statistical question: The square absolute wave function of an approximate GKP code state can be seen as a probability distribution. This probability distribution has multiple modes¹¹, each mode corresponding to a different displaced squeezed vacuum state (see Eq. (2.11)). The standard deviation of the modes (the initial squeezing Δ) is similar, and the modes themselves are periodic with known distance (displacement by one stabilizer), but the amplitude of each mode changes (due to the envelope). Therefore, we can employ methods from directional statistics in order to obtain the properties of the underlying distribution.

An equivalent alternate point of view is that every approximate GKP code state is characterized as a probability distribution over the eigenvalues of the stabilizers S_p and S_q .¹² Because the stabilizers are unitary operators, their eigenvalues are complex phases, and it is therefore appropriate to employ methods from the field of directional statistics. The derivation of the circular mean and variance in this section follows [13, 14], adjusting the derivations there to continuous variables.

Consider an approximate GKP code state $|\tilde{0}\rangle$ as defined in Eq. (2.11). The probability distribution of the position quadrature for this state is given by:

$$\begin{aligned} \mathbb{P}_0(q) &= \frac{1}{\mathcal{N}_0^2} \sum_{n,k} e^{-2\pi\Delta_p^2(n^2+k^2)} \exp\left(-\frac{(q-2\sqrt{\pi}n)^2 - (q-2\sqrt{\pi}k)^2}{2\Delta_q^2}\right) \\ &\approx \frac{1}{\mathcal{N}_0^2} \sum_n e^{-4\pi\Delta_p^2 n^2} \exp\left(-\frac{(q-2\sqrt{\pi}n)^2}{\Delta_q^2}\right), \end{aligned} \quad (2.24)$$

where the approximation is $n = k$ for $\Delta_q \ll 1$, see Eq. (2.20). While the mean value of this probability distribution is $\langle \hat{q} \rangle = 0$ as expected, it is obvious that the variance $\text{Var}(q) = \langle \hat{q}^2 \rangle - \langle \hat{q} \rangle^2$ is misleading and has no relation to Δ_q , and only an indirect dependence on Δ_p . A simple solution is to capture the periodicity of the distribution by “wrapping it up”. This means that we cut the domain into pieces of the same length as the desired period — here $\sqrt{\pi}$ — and then shift all those pieces such that they have the same domain, in our case $[-\sqrt{\pi}/2, \sqrt{\pi}/2]$. With this procedure, we obtain a new probability distribution

$$\begin{aligned} \mathbb{P}_{0,W}(q) &= \sum_{s=-\infty}^{\infty} \mathbb{P}_0(q + \sqrt{\pi}s), \\ &= \frac{1}{\mathcal{N}_0^2} \sum_{s,n=-\infty}^{\infty} e^{-4\pi\Delta_p^2 n^2} \exp\left(-\frac{(q - \sqrt{\pi}(2n+s))^2}{\Delta_q^2}\right), \quad q \in [-\sqrt{\pi}/2, \sqrt{\pi}/2] \\ &= \frac{1}{\sqrt{\Delta_q\pi}} \sum_{s=-\infty}^{\infty} \exp\left(-\frac{(q - \sqrt{\pi}s)^2}{\Delta_q^2}\right), \end{aligned} \quad (2.25)$$

where the approximation is again $n = k$ for $\Delta_q \ll 1$. In the last step, we shifted the sum over s such that only a single Gaussian remains. The domain of q is now restricted to $q \in$

¹¹Note that the “mode” is to be understood as a mode of a probability distribution, and not as a resonance mode of a physical system.

¹²This is simply rephrasing of the statement that the shifted code states are a basis for the Hilbert space of the harmonic oscillator, see Section 2.2.2.

$[-\sqrt{\pi}/2, \sqrt{\pi}/2]$. This wrapped up probability distribution is simply a wrapped Gaussian distribution, the mean value $\langle \hat{q} \rangle = 0$ is still correct. Furthermore, the variance now is given by $\text{Var}(q) = \frac{\Delta_q^2}{2}$, as expected for a squeezed vacuum state.

However, the method above relies on the fact that the initial state is close to the GKP code space. Suppose that an approximate code state $|\bar{0}\rangle$ is displaced by $D(\sqrt{\pi}/8)$ (half the displacement implementing a logical Pauli X). In this case, the corresponding (wrapped) probability distribution is given by

$$\mathbb{P}_{\sqrt{\pi}/2, W}(q) = \frac{1}{\sqrt{\Delta_q \pi}} \sum_{s=-\infty}^{\infty} \exp\left(-\frac{(q - \sqrt{\pi}(s + 1/2))^2}{\Delta_q^2}\right), \quad q \in [-\sqrt{\pi}/2, \sqrt{\pi}/2]. \quad (2.26)$$

and the mean and variance are given by

$$\langle \hat{q} \rangle = 0 \neq \frac{\sqrt{\pi}}{2}, \quad \text{Var}(q) \approx \Delta_q^2/2 + \pi - 2\Delta_q,$$

where the variance was approximated for small Δ_q . Note that the mean is clearly wrong, and the variance — although related to the desired value — does not correspond to the variance of the underlying squeezed states. The reason why the cases behave differently is that although all points $q = n\sqrt{\pi}, n \in \mathbb{Z}$ are identified, this unit circle is cut open at these points when the statistical moments are computed directly. If the cut is in the middle of a peak located around $q \approx n\sqrt{\pi}, n \in \mathbb{Z}$, this will result in the peak being cut in half so that there are two “virtual” peaks in the distribution that are actually the same.

To see how this dependence on the initial state can be resolved, we first consider the more general problem of a probability distribution $\mathbb{P}(\theta)$, where $\theta = \theta + 2\pi$ is a periodic variable. We now follow the books [13, 14], extending their analysis to probability distributions over continuous variables.

Usually, the variance and mean are defined with the metric

$$d_L(x, y) = (x - y)^2$$

in mind. However, this metric is not well suited for variables defined on a circle: For $x = \pi, y = -\pi$, we have $d_L(-\pi, \pi) = (2\pi)^2 \neq 0$ even though the two points are identical. In order to take this periodicity into account, one defines a new metric:

$$d_C(\theta, \vartheta) = 1 - \cos(\theta - \vartheta). \quad (2.27)$$

This function is non-negative, symmetric and fulfills the triangle inequality. It also correctly captures the periodic nature of the variables and is therefore a suitable metric for the circle. Because the metric is periodic, using this metric is equivalent to wrapping up a probability distribution, as all distances are measured modulo 2π .

Note that there are also multiple other ways to define a metric on a circle, we will see how this particular choice is motivated in Lemma 2.3.1. To proceed, we first define a mean:

$$\bar{\theta} = \arctan 2(\langle \sin(\theta) \rangle, \langle \cos(\theta) \rangle) = \arg\left(\left\langle e^{i\theta} \right\rangle\right), \quad (2.28)$$

where

$$\langle f(\theta) \rangle = \int_{-\pi}^{\pi} d\theta \mathbb{P}(\theta) f(\theta),$$

and $\arctan 2$ is the inverse function of the tangent that takes the quadrant into account. For now, this is simply a definition, we will see how it is justified below. Analogous to the usual variance, one defines the circular variance V_C as the expectation value of the distance to some reference point $\bar{\theta}$, with the circular metric from Eq. (2.27):

$$V_C = \langle d_C(\theta, \bar{\theta}) \rangle = 1 - \langle \cos(\theta - \bar{\theta}) \rangle. \quad (2.29)$$

In the following lemma, we show that the circular variance is minimized if $\bar{\theta}$ is chosen according to Eq. (2.28), analogous to the usual variance and mean.

Lemma 2.3.1. *The circular variance $V_C = \langle d_C(\theta, \mu) \rangle$ (see Eq. (2.29)) is minimized if $\mu = \bar{\theta}$ is the circular mean defined in Eq. (2.28).*

Proof. For the proof, we differentiate $\langle d_C(\theta, \mu) \rangle$ and equate to zero:

$$\begin{aligned} 0 &= \frac{d\langle d_C(\theta, \mu) \rangle}{d\mu} = -\langle \sin(\theta - \mu) \rangle = -\int_0^{2\pi} d\theta \mathbb{P}(\theta) \sin(\theta - \mu) \\ &= -\Im \left(\int_0^{2\pi} d\theta \mathbb{P}(\theta) e^{i(\theta - \mu)} \right) = -\Im \left(r e^{i\bar{\theta}} e^{-i\mu} \right), \end{aligned} \quad r \in [0, 1], \quad (2.30)$$

where $\mathbb{P}(\theta)$ is some probability distribution over θ and we used Eq. (2.28) for the last equality. This equation has two solutions, $\mu = \bar{\theta}$ and $\mu = \bar{\theta} + \pi$. To check whether the solutions are a minimum or maximum, we differentiate again:

$$\frac{d^2 \langle d_C(\theta, \mu) \rangle}{d\mu^2} = \langle \cos(\theta - \mu) \rangle = \Re \left(r e^{i\bar{\theta}} e^{-i\mu} \right), \quad r \in [0, 1],$$

where we used the same steps as for the first derivative. Thus we have

$$\begin{aligned} \frac{d^2 \langle d_C(\theta, \mu) \rangle}{d\mu^2} &> 0 & \text{for} & \mu = \bar{\theta}, \\ \frac{d^2 \langle d_C(\theta, \mu) \rangle}{d\mu^2} &< 0 & \text{for} & \mu = \bar{\theta} + \pi, \end{aligned} \quad (2.31)$$

proving the claim that the variance is minimized if $\mu = \bar{\theta}$. \square

From Eqs. (2.30) and (2.31) follows $|\langle e^{i\theta} \rangle| = \langle \cos(\theta - \bar{\theta}) \rangle$, and therefore

$$V_C = 1 - \left| \langle e^{i\theta} \rangle \right| \quad (2.32)$$

where $\bar{\theta}$ is defined as in Eq. (2.28). The quantity

$$S = \left| \langle e^{i\theta} \rangle \right|, \quad (2.33)$$

is also called the *sharpness*, and commonly used as an alternative to the circular variance defined in Eq. (2.29). We can see that mean value, circular variance and sharpness are all defined as a simple function of the expectation value $\langle e^{i\theta} \rangle$, see Eqs. (2.28), (2.32) and (2.33).

We learned that the circular mean and variance defined in Eqs. (2.28) and (2.32) are well suited to classify probability distributions over periodic variables. In order to analyze a GKP state in a way that is easy to compare to experimental data, we have two further adjustments: The mean values should correspond to position and momentum in phase space, and we want to scale the circular variance V_C such that it directly yields the parameters Δ_p, Δ_q of an approximate GKP state of the form Eq. (2.11). By change of variables from $\theta \in [0, 2\pi)$ to $q \in [-\sqrt{\pi}/2, \sqrt{\pi}/2)$, we see that both the mean value and the circular variance are functions of the expectation value of the stabilizer S_q .

To choose the scaling for the mean value and the circular variance, we first compute the expectation value $\langle S_q \rangle$ of an approximate code state $|\tilde{0}\rangle$ from Eq. (2.11) with an additional displacement $D(\mu/\sqrt{2})$, i. e. the state given in Eq. (2.19). We already computed this expectation value in order to compute the Holevo phase variance, it is given by

$$\text{Tr}(|\Psi\rangle\langle\Psi|S_q) = e^{i2\sqrt{\pi}\mu} e^{-\Delta_q^2\pi}$$

see Eq. (2.21). To recover μ and Δ_q , we can now simply solve for these variables. As expected from Eqs. (2.28) and (2.32), they are a function of the argument and absolute value of $\langle S_q \rangle$, respectively. Not surprisingly, we obtain the *effective squeezing parameters* Δ_q, Δ_p and the corresponding *mean shifts* μ_q, μ_p we also obtained from the Holevo phase variance:

$$\mu_q(\rho) \equiv \frac{\arg\left(|\text{Tr}(S_q\rho)|^2\right)}{2\sqrt{\pi}}, \quad \Delta_q(\rho) \equiv \sqrt{\frac{1}{\pi} \ln\left(\frac{1}{|\text{Tr}(S_q\rho)|^2}\right)}, \quad (2.34)$$

A significant advantage of using either the effective squeezing parameters or the sharpness is that it is very efficient to evaluate them numerically, and they can also easily be evaluated experimentally. This is because a measurement of the sharpness is the same, or a very similar measurement to, the measurement one would do to encode a GKP state in the first place.

EXPECTATION VALUE OF PAULI OPERATORS

Perhaps the most direct way to measure the quality of a GKP state is to determine the expectation values $\langle X \rangle, \langle Y \rangle, \langle Z \rangle$ of the logical Pauli operators. The measurements required to obtain these are of the same type as the encoding itself, they are realized by the same circuit. As both the sharpness and the effective squeezing are a function of these expectation values, relating an expectation value to an effective squeezing is straight forward. If the encoded state is symmetric around the vacuum state, i. e. $\mu_q \approx \mu_p \approx 0$, the imaginary part of all these expectation values is close to 0, meaning that they are approximating the sharpness (up to the sign). In fact, both experimental implementations of the GKP code use

$$\Re\langle X \rangle, \Re\langle Y \rangle, \Re\langle Z \rangle$$

as a quality measure for the generated GKP states [2, 15].

REFERENCES

- [1] D. J. Weigand and B. M. Terhal, “Generating grid states from Schrödinger-cat states without postselection”, [Physical Review A](#) **97**, 022341 (2018).
- [2] P. Campagne-Ibarcq, A. Eickbusch, S. Touzard, E. Zalys-Geller, N. E. Frattini, V. V. Sivak, P. Reinhold, S. Puri, S. Shankar, R. J. Schoelkopf, L. Frunzio, M. Mirrahimi, and M. H. Devoret, “Quantum error correction of a qubit encoded in grid states of an oscillator”, [Nature](#) **584**, 368 (2020).
- [3] A. M. Perelomov, “Generalized coherent states and some of their applications”, [Soviet Physics Uspekhi](#) **20**, 703 (1977).
- [4] B. Hall, *Quantum Theory for Mathematicians* (Springer, 2013).
- [5] V. V. Albert, J. P. Covey, and J. Preskill, “Robust encoding of a qubit in a molecule”, [Phys. Rev. X](#) **10**, 031050 (2020) **10**, 031050 (2019).
- [6] K. Duivenvoorden, B. M. Terhal, and D. J. Weigand, “Single-mode displacement sensor”, [Physical Review A](#) **95**, 012305 (2017).
- [7] D. Gottesman, A. Kitaev, and J. Preskill, “Encoding a qubit in an oscillator”, [Physical Review A](#) **64**, 012310 (2001).
- [8] V. V. Albert, K. Noh, K. Duivenvoorden, D. J. Young, R. T. Brierley, P. Reinhold, C. Vuillot, L. Li, C. Shen, S. M. Girvin, B. M. Terhal, and L. Jiang, “Performance and structure of single-mode Bosonic codes”, [Physical Review A](#) **97**, 032346 (2018).
- [9] J. Zak, “Finite translations in solid-state physics”, [Physical Review Letters](#) **19**, 1385 (1967).
- [10] S. Glancy and E. Knill, “Error analysis for encoding a qubit in an oscillator”, [Physical Review A](#) **73**, 012325 (2006).
- [11] B. M. Terhal and D. J. Weigand, “Encoding a qubit into a cavity mode in circuit QED using phase estimation”, [Physical Review A](#) **93**, 012315 (2016).
- [12] B. M. Terhal, J. Conrad, and C. Vuillot, “Towards scalable bosonic quantum error correction”, [Quantum Science and Technology](#) **5**, 043001 (2020).
- [13] S. R. Jammalamadaka and A. Sengupta, *Topics in circular statistics* (World Scientific, 2001).
- [14] K. V. Mardia and P. E. Jupp, *Directional statistics* (Wiley, 1999).
- [15] C. Flühmann, T. L. Nguyen, M. Marinelli, V. Negnevitsky, K. Mehta, and J. P. Home, “Encoding a qubit in a trapped-ion mechanical oscillator”, [Nature](#) **566**, 513 (2019).

3

ENCODING A GKP QUBIT USING PHASE ESTIMATION

In this chapter, we discuss how phase estimation can be used to encode a GKP qubit. First, we will introduce the standard phase estimation algorithm, as well as several variations that are useful for encoding a GKP code state. The core piece of all encoding schemes using phase estimation is a controlled displacement of an oscillator, conditioned on the state of an ancilla qubit. Therefore, we will discuss how this operation can be implemented in various physical systems. Finally, we present a numerical simulation of a scheme to encode a GKP qubit, taking noise and imperfections into account.

Sections 3.1.4 and 3.3 have been published with minor differences in K. Duivenvoorden, B. M. Terhal, and D. J. Weigand, “Single-mode displacement sensor”, [Physical Review A](#) **95**, 012305 (2017). Section 3.1.1 follows Nielsen and Chuang [2]. The discussion of the adaptive phase estimation algorithm by Berry *et al.* [3] in Section 3.1.3 follows [4].

3.1. PHASE ESTIMATION

As the GKP code is a stabilizer code, encoding and error correction are simply a question of fixing the eigenvalues of the stabilizers. Because the stabilizers are unitary, the task is to fix the eigenvalue of a unitary operator. This problem has been widely studied, and the quantum algorithm that achieves this is *phase estimation*. To be more precise, phase estimation can refer to a whole class of algorithms based on the same computational unit, see Fig. 3.1. In this section, we will discuss various implementations of phase estimation, their scaling, and the criteria for efficiently encoding GKP code states.

3.1.1. STANDARD PHASE ESTIMATION

The most well known phase estimation algorithm is *standard phase estimation*, in the literature often referred to as “phase estimation”. The algorithm uses M ancilla qubits in order to measure the eigenvalue of some unitary operator U acting on some target system, see Fig. 3.2. The target system may be a single qubit, but can also be a system with multiple qubits or an entirely different physical system, like a harmonic oscillator. The algorithm starts with the target system in some eigenstate $|\theta\rangle_T$ with eigenvalue θ of U and the ancilla qubits all in the $|+\rangle$ state. Then, we apply a series of controlled unitaries $U^{2^{M-k}}$ to the target system, where k is the index of the controlling ancilla qubit. Because the state $|\theta\rangle_T$ is an eigenstate of the unitary operator U , the controlling ancilla qubits simply acquire a phase:

$$|\theta\rangle_T |+\rangle_1 \dots |+\rangle_M \rightarrow \frac{1}{\sqrt{2^M}} |\theta\rangle_T \prod_{k=1}^M \left(|0\rangle_k + e^{i2^{M-k}\theta} |1\rangle_k \right).$$

Now we represent the eigenvalue θ as a bit string, $\theta = 2\pi \times 0.\theta_1 \dots \theta_M$ (assuming that θ can be expanded exactly with M bits) where $\theta_l \in \{0, 1\}$ and $0.\theta_1 \dots \theta_M$ is shorthand for $\sum_{l=1}^M 2^{-l} \theta_l$. With this notation, the state can be simplified as

$$\frac{1}{\sqrt{2^M}} |\theta\rangle_T \prod_{k=1}^M \left(|0\rangle_k + e^{i2\pi 0.\theta_k \dots \theta_M} |1\rangle_k \right). \quad (3.1)$$

The quantum Fourier transform acts as

$$\mathcal{F} |\theta_1\rangle_1 \dots |\theta_M\rangle_M \rightarrow \prod_{k=1}^M \left(|0\rangle_k + e^{i2\pi 0.\theta_k \dots \theta_M} |1\rangle_k \right),$$

where $\theta_l \in \{0, 1\}$ is the representation of θ as a bit string. Therefore, a measurement of the ancilla qubits after the inverse quantum Fourier transform directly yields the desired eigenvalue, bit by bit, see Fig. 3.2.

SEMI-CLASSICAL PHASE ESTIMATION

If the quantum Fourier transform is followed by a measurement, it can be separated into a sequence of single qubit measurements, combined with classical control. Consider again Eq. (3.1). The state of ancilla qubit M is given by

$$\frac{1}{\sqrt{2}} (|0\rangle + e^{2\pi i 0.\theta_M} |1\rangle) = \frac{1}{\sqrt{2}} (|0\rangle + (-1)^{\theta_M} |1\rangle) = H |\theta_M\rangle,$$

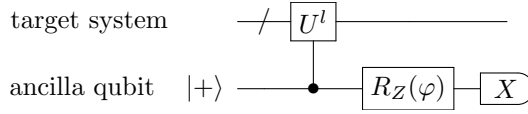


Figure 3.1: Phase estimation unit for a unitary operator U acting on some target system. The target system may be any physical system, for example a single qubit, a collection of qubits, or a harmonic oscillator (symbolized by the slash). This circuit is repeated for M rounds, with l, φ varying, possibly depending on the measurement results from previous rounds. If the input state of the target system is an eigenstate of U with eigenvalue $e^{i\theta}$, then the probability for outcome 0 for the qubit measurement will be given by $\mathbb{P}(0|\varphi) = \frac{1}{2}(1 + \cos(l\theta + \varphi))$.

3

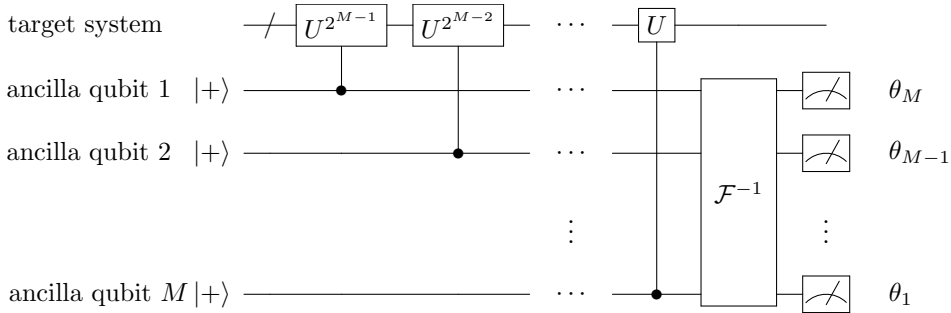


Figure 3.2: Standard phase estimation using the inverse quantum Fourier transform for a unitary operator U acting on some target system. The target system may be any physical system, for example a single qubit, a collection of qubits, or a harmonic oscillator (symbolized by the slash). If the initial state of the target system is an eigenstate of U where the eigenvalue is an M -bit string of the form $\theta = 2\pi \times 0.\theta_1 \dots \theta_M$, a circuit with M ancilla qubits will be sufficient to measure the eigenvalue.

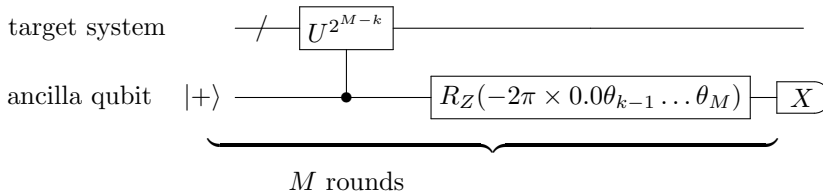


Figure 3.3: Standard phase estimation for a unitary operator U acting on some target system. The target system may be any physical system, for example a single qubit, a collection of qubits, or a harmonic oscillator (symbolized by the slash). This circuit is repeated for M rounds, the integer k indicates the current round. If the input state of the target system is an eigenstate of U with eigenvalue $e^{i2\pi \times 0.\theta_1 \dots \theta_M}$, then the probability for outcome 0 for the qubit measurement is θ_k .

where H is the Hadamard gate. Thus, the M^{th} bit of θ can be obtained by simply measuring the ancilla qubit in the X basis, i. e. applying a Hadamard gate. The state of ancilla qubit $(M-1)$ is given by $\frac{1}{\sqrt{2}}(|0\rangle + e^{2\pi i 0.\theta_{M-1}\theta_M}|1\rangle)$. We wish to measure the value of the $(M-1)^{\text{th}}$ bit θ_{M-1} . Because we already measured θ_M , we can map ancilla qubit $(M-1)$ to the state $|\theta_{M-1}\rangle$, by first applying a rotation around the Z axis by $-\theta_M/4$, followed by a Hadamard gate, see Fig. 3.3.

In terms of the number of rounds, standard phase estimation (and also the semi-classical variant) is clearly optimal: Each measurement yields one bit of the measured eigenvalue. If the computational cost is measured in the number of applications of the unitary U , where U^k counts as k applications, the cost of standard phase estimation will be $(2^{M+1} - 1)$ for a measurement of M bits. The latter metric is more important for many applications, in particular for the GKP code: If the measured unitary operator is a displacement, each application of the displacement adds a fixed number of photons, so M rounds of standard phase estimation add $\mathcal{O}(2^{M+1})$ photons to the oscillator [4].

3.1.2. PHASE ESTIMATION BY REPETITION

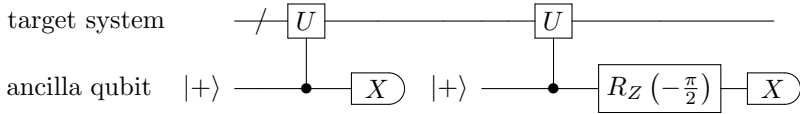


Figure 3.4: Phase estimation by repetition for a unitary operator U acting on some target system. The target system may be any physical system, for example a single qubit, a collection of qubits, or a harmonic oscillator (symbolized by the slash). This circuit is repeated for $M/2$ rounds. If the input state of the target system is an eigenstate of U with eigenvalue $e^{i\theta}$, then the probability for outcome 0 for the first qubit measurement is given by $\mathbb{P}(0) = \frac{1}{2}(1 + \cos(\theta))$, and for the second qubit measurement by $\mathbb{P}(0) = \frac{1}{2}(1 + \sin(\theta))$.

A simple variant of phase estimation that does not require adaptive feedback uses only the circuit shown in Fig. 3.1. The circuit is repeated $M/2$ times with $l = 1, \varphi = 0$ and $M/2$ times with $l = 1, \varphi = \pi/2$, see Fig. 3.4. The probabilities to obtain outcome 0 are

$$\begin{aligned}\mathbb{P}_{\cos} &\equiv \mathbb{P}(0|\varphi = 0) = \frac{1}{2}(1 + \cos(\theta)), \\ \mathbb{P}_{\sin} &\equiv \mathbb{P}(0|\varphi = \pi/2) = \frac{1}{2}(1 + \sin(\theta)),\end{aligned}$$

for $\varphi = 0$ and $\varphi = \pi/2$, respectively. Assuming that θ does not change over time and that the number of measurements M is sufficiently large, \mathbb{P}_{\cos} is the frequency of measurement result 0 for $\varphi = 0$, and \mathbb{P}_{\sin} is the frequency of measurement result 0 for $\varphi = \pi/2$. The eigenvalue θ can now be obtained as a function of \mathbb{P}_{\cos} and \mathbb{P}_{\sin} :

$$\theta = \arg(2(\mathbb{P}_{\cos} + i\mathbb{P}_{\sin}) - (1 + i)). \quad (3.2)$$

3.1.3. ADAPTIVE PHASE ESTIMATION

An important advantage of phase estimation by repetition compared to standard phase estimation in the context of encoding a GKP code state is the linear scaling of the cost in terms of the photon number with respect to the number of rounds. Keeping a form

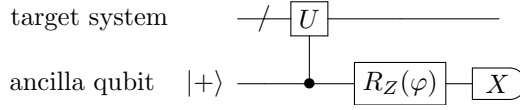


Figure 3.5: Phase estimation unit for a unitary operator U acting on some target system. The target system may be any physical system, for example a single qubit, a collection of qubits, or a harmonic oscillator (symbolized by the slash). This circuit is repeated for M rounds, φ varying, depending on the measurement results from previous rounds. If the input state of the target system is an eigenstate of U with eigenvalue $e^{i\theta}$, then the probability for outcome 0 for the qubit measurement will be given by $\mathbb{P}(0|\varphi) = \frac{1}{2}(1 + \cos(l\theta + \varphi))$.

3

of phase estimation where the only power of the unitary U is 1 ($l = 1$ in Fig. 3.1), one can ask about strategies that offer a faster scaling, see Fig. 3.5. Berry *et al.* developed a protocol that optimizes¹ the feedback phase for the next measurement [3]. This is also the algorithm that was used in the proposal to encode a GKP qubit using phase estimation [4]. Even though the asymptotic scaling of the effective squeezing is the same for this protocol and for phase estimation by repetition, it performs significantly better in the initial measurements. First, let us define what Berry *et al.* mean by optimal:

Their quality measure of choice is the sharpness $S(\rho)$, see Eq. (2.33). Both the effective squeezing parameters and the Holevo phase variance are monotonic functions of the sharpness, see Eqs. (2.22) and (2.23). Therefore, minimizing the sharpness also minimizes either quality measure. The objective is to choose the feedback such that the sharpness after the *next* measurement is maximized. Suppose that we already did $(M-1)$ measurements, with a measurement record \mathbf{x}_{M-1} and a history of feedback $\boldsymbol{\varphi}_{M-1}$. Because the measurement result of the next, M^{th} measurement is of course unknown, we maximize the sharpness over a weighted average of both possible outcomes:

$$\varphi = \operatorname{argmax}_{\phi[M]} \sum_{x[M]=0,1} \mathbb{P}(x[M]|\rho(\mathbf{x}_M, \boldsymbol{\varphi}_M)) S(\rho(\mathbf{x}_M, \boldsymbol{\varphi}_M)),$$

where $\rho(\mathbf{x}_M, \boldsymbol{\varphi}_M)$ is the posterior state after round M with result $x[M]$ and feedback phase $\varphi[M]$.² To proceed, we need a method to obtain the posterior state.

One way to achieve this is to simply use a brute force approach, simulating every possible measurement result numerically. In the noiseless case, there is a much more efficient way, as the post measurement state can be obtained analytically. Assume that the probability distribution $\mathbb{P}(\theta|\mathbf{x}_{M-1})$ of eigenvalues in round k with measurement history \mathbf{x}_{M-1} is known. We can then use a Bayesian update in order to obtain the posterior

¹Note that there are many different measures of optimality. Furthermore, Berry *et al.* only perform a local optimization for each measurement round and do not claim that their strategy is globally optimal. Although their strategy could easily be extended to a globally optimal one, the computational cost scales exponentially with the number of rounds and doing so is computationally unfeasible.

²Because we are taking the weighted average, it *does* change the result slightly if we optimize the sharpness, the Holevo phase variance, or an effective squeezing parameter. This is because the scaling of the different parameters with respect to $\phi[M]$ is different. Taking this change into account is possible for slightly increased computational cost, but the expected gains are minimal, because these quality measures are asymptotically equivalent.

probability distribution:

$$\begin{aligned}\mathbb{P}(\theta|\mathbf{x}_M, \boldsymbol{\varphi}_M) &= \frac{\mathbb{P}(\theta|\mathbf{x}_{M-1}, \boldsymbol{\varphi}_{M-1})\mathbb{P}(x[M]|\theta, \mathbf{x}_{M-1}, \boldsymbol{\varphi}_{M-1}, \varphi[M])}{\mathbb{P}(x[M]|\mathbf{x}_{M-1}, \boldsymbol{\varphi}_{M-1}, \varphi[M])} \\ &= \frac{\mathbb{P}(\theta|\mathbf{x}_{M-1}, \boldsymbol{\varphi}_{M-1})\mathbb{P}(\mathbf{x}_M|\theta, \boldsymbol{\varphi}_M)}{\mathbb{P}(y|\mathbf{x}_{M-1}, \boldsymbol{\varphi}_{M-1}, \phi)\mathbb{P}(\mathbf{x}_{M-1}|\theta, \boldsymbol{\varphi}_{M-1})},\end{aligned}\quad (3.3)$$

where $x[M]$ is the measurement result and $\varphi[M]$ is the feedback used in round M . Recall that the sharpness can be written as an integral over the probability distribution $\mathbb{P}(\theta|\mathbf{x}_M)$. Using the Bayesian update, we can simplify the expression for the optimal feedback phase:

$$\varphi[M] = \operatorname{argmax}_{\phi[M]} \sum_{y=0,1} \left| \int d\theta e^{i\theta} \frac{\mathbb{P}(\theta|\mathbf{x}_{M-1}, \boldsymbol{\varphi}_{M-1})\mathbb{P}(\mathbf{x}_M|\theta, \boldsymbol{\varphi}_M)}{\mathbb{P}(\mathbf{x}_{M-1}|\theta, \boldsymbol{\varphi}_{M-1})} \right|,$$

Because the measurement results of each round are independent, we can easily obtain the probability distribution $\mathbb{P}(\mathbf{x}_M|\theta, \boldsymbol{\varphi}_M)$:

$$\mathbb{P}(\mathbf{x}_M|\theta, \boldsymbol{\varphi}_M) = \prod_{i=1}^M \mathbb{P}(x[i]|\theta, \varphi[i]) = \prod_{i=1}^M \cos^2\left(\frac{\theta + \varphi[i] + x[i]}{2}\right).$$

To simplify the optimization further, we use the following proposition:

Proposition 3.1.1. *Assuming no prior knowledge about θ , it holds $\mathbb{P}(\theta|\mathbf{x}_{M-1}, \boldsymbol{\varphi}_{M-1}) \propto \mathbb{P}(\mathbf{x}_{M-1}|\theta, \boldsymbol{\varphi}_{M-1})$, where the proportionality constant is independent of both θ and $\varphi[M]$.*

Proof. Using Eq. (3.3) and assuming no prior knowledge, the claim holds for $M = 2$:

$$\mathbb{P}(\theta|\mathbf{x}_1, \boldsymbol{\varphi}_1) = \frac{\mathbb{P}(\theta)\mathbb{P}(x[1]|\theta, \varphi[1])}{\mathbb{P}(x[1]|\varphi[1])} = \frac{\mathbb{P}(x[1]|\theta, \varphi[1])}{4\pi},$$

which is independent of θ and $\varphi[2]$. Here we used that $\mathbb{P}(\theta)$ and $\mathbb{P}(x[1]|\varphi[1])$ are uniform distributions if we assume no prior knowledge. Assuming the claim holds for round $M = m$, we have for $M = m + 1$:

$$\frac{\mathbb{P}(\theta|\mathbf{x}_m, \boldsymbol{\varphi}_m)}{\mathbb{P}(\mathbf{x}_m|\theta, \boldsymbol{\varphi}_m)} = \frac{\mathbb{P}(\theta|\mathbf{x}_{m-1}, \boldsymbol{\varphi}_{m-1})}{\mathbb{P}(y|\mathbf{x}_{m-1}, \boldsymbol{\varphi}_{m-1}, \phi)\mathbb{P}(\mathbf{x}_{m-1}|\theta, \boldsymbol{\varphi}_{m-1})} \propto \frac{1}{\mathbb{P}(y|\mathbf{x}_{m-1}, \boldsymbol{\varphi}_{m-1}, \varphi[m])}.$$

The right hand side is independent of both θ and $\varphi[m + 1]$, proving the claim by induction. \square

Using the proposition, the feedback phase for round M is given as

$$\begin{aligned}\varphi[M] &= \operatorname{argmax}_{\phi[M]} \sum_{x[M]=0,1} \left| \int d\theta e^{i\theta} \mathbb{P}(\mathbf{x}_M|\theta, \boldsymbol{\varphi}_M) \right| \\ &= \operatorname{argmax}_{\phi[M]} \sum_{x[M]=0,1} \left| \int d\theta e^{i\theta} \prod_{i=1}^M \cos^2\left(\frac{\theta + \varphi[i] + x[i]}{2}\right) \right|.\end{aligned}$$

3.1.4. MAXIMAL INFORMATION GAIN STRATEGY

Although the number of rounds needed to obtain a good GKP code state using optimized feedback is small [4], the optimization requires a significant amount of (classical) computational resources. This is not relevant if the optimization of the feedback angle is done on a classical computer, but might introduce a significant delay between phase estimation measurements if the feedback is computed during an experiment. As the feedback angle is unique for every bit string of measurement results, storing feedback in a lookup table is only possible for a small number of measurements. A simpler strategy with similar performance is the following *maximal information gain strategy* [1].

Given a sequence of qubit measurement outcomes x_1, \dots, x_{M-1} , assume that one somehow determines an estimate $\tilde{\theta}_{M-1}$ for the phase θ . Given this estimate $\tilde{\theta}_{M-1}$, we will then choose the next circuit with a feedback phase φ such that the probability for qubit outcome 0 and qubit outcome 1 are equally likely. Hence, given the estimate, we choose our next feedback phase such that we gain maximal information of 1 bit. If the input to the phase estimation circuits is the eigenstate $|\psi_\theta\rangle$, then the probability for outcome x will equal $\mathbb{P}(x) = \frac{1}{2}(1 + (-1)^x \cos(\theta + \varphi))$ so that the maximal-information gain condition simply reads:³

$$\varphi_M = \tilde{\theta}_{M-1} + \frac{\pi}{2}.$$

The current estimate $\tilde{\theta}_{M-1}$ can be easily obtained using the mean shift, see Eq. (2.23). For analytical considerations, the state of the system is given by (see Section 3.1.3):

$$\mathbb{P}(\mathbf{x}_M | \theta, \boldsymbol{\varphi}_M) \propto \prod_{i=1}^M \cos^2 \left(\frac{\theta + \varphi[i] + x[i]}{2} \right).$$

For numerical simulations, the algorithm is even simpler: As the state of the system is already in memory anyway, calculating the expectation value $\langle e^{i\theta} \rangle$ is straight forward. The description of the state used to obtain the mean shift can also include the noise in the protocol, e.g. measurement errors, in order to best describe the state that the protocol produces.

For all algorithms presented in this section, the accuracy with which the eigenvalue θ is determined scales linearly with the number of photons added by the algorithm, albeit with different prefactors and different behavior for a small number of measurements. Standard phase estimation adds one bit of information per round and also adds an exponential number of photons. For all other strategies presented here, both the accuracy of the eigenvalue and the number of photons in the oscillator scale linearly with the number of rounds.

³Note that this strategy can be employed in any phase estimation, using any integer l , which proceeds by several rounds of circuits of the form in Fig. 3.1: Given the data, one can always get a current estimate of the phase and make sure that the next measurement with some number of outcomes gives equal probability to all these outcomes. Standard phase estimation based on the semi-classical quantum Fourier transform follows this strategy as well, see Fig. 3.3: The lowest significant bit of the phase is estimated with a binary measurement first, then the feedback phase is adapted such that the next measurement comes out 0 or 1 with probability 1/2, only depending on the next significant bit and so on.

3.2. IMPLEMENTATIONS OF A CONTROLLED DISPLACEMENT

IN order to be able to use phase estimation to encode a GKP state in an oscillator, it is necessary to be able to implement a controlled displacement of the oscillator, where the displacement amplitude is conditioned on an ancilla qubit, i. e. implementing the controlled- U operation from Fig. 3.1. Such a controlled displacement enables to implement controlled applications of either stabilizers or logical operations. In this section, we present various approaches to achieve this goal. There are three requirements for any such operation: The controlled displacement should be sufficiently accurate, sufficiently fast so that photon loss, for example, is not dominant and, preferably, experimentally viable.

3.2.1. DIRECT CONTROLLED DISPLACEMENT

In a circuit QED setting, the qubit-cavity interaction can be approximated by the Jaynes-Cummings Hamiltonian [4, 5]:

$$H_{JC} = -\omega_q \sigma_z + \omega_r \hat{a}^\dagger \hat{a} + g(\sigma_- \hat{a}^\dagger + \sigma_+ \hat{a}).$$

Here, and throughout the rest of this thesis, we will use the convention $\hbar = 1$. If the detuning $\Delta = \omega_q - \omega_r$ is chosen to be much larger than the coupling strength g , we can take the so-called dispersive limit $\frac{g}{\Delta} \ll 1$.⁴ In this limit, the effective Hamiltonian is given by:⁵

$$H_{\text{disp}} = \omega_r \hat{a}^\dagger \hat{a} - (\omega_q + \chi) \frac{\sigma_z}{2} - \chi \hat{a}^\dagger \hat{a} \sigma_z + \mathcal{O}\left(\frac{g^3}{\Delta^3}\right), \quad \chi \approx \frac{g^2}{\Delta}, \quad (3.4)$$

see [5] for a detailed derivation. Note that this approximation is only valid if the number of photons in the oscillator is below the critical photon number $n_{\text{crit}} = \frac{\Delta^2}{4g^2}$.

In principle, one could use this Hamiltonian to implement a displacement of the oscillator, conditioned on the qubit state directly. In the rotating frame of the qubit, the interaction Hamiltonian is simply

$$H_{\text{int}} = \omega_r \hat{a}^\dagger \hat{a} - \chi \hat{a}^\dagger \hat{a} \sigma_z + \mathcal{O}\left(\frac{g^3}{\Delta^3}\right) + \alpha e^{i\omega_d t} \hat{a}^\dagger - \alpha^* e^{-i\omega_d t} \hat{a},$$

where we also added a drive at frequency ω_d . We can interpret the Hamiltonian as a change of the resonance frequency of the cavity, depending on the state of the qubit. This allows to drive the cavity, conditioned on the state of the qubit. A drive at frequency $\omega_r \mp \frac{\chi}{2}$ will be on resonance if the qubit is in the $|0\rangle$ or $|1\rangle$ states, respectively. As an example, assume that $\omega_d = \omega_r + \chi/2$. In a rotating frame of the oscillator at frequency $\omega_r + \chi/2$, we have

$$H_{\text{rot}} = \alpha e^{i\chi(1/2 - \sigma_z)t} \hat{a}^\dagger + \alpha^* e^{-i\chi(1/2 - \sigma_z)t} \hat{a}. \quad (3.5)$$

⁴As g is typically small ($\mathcal{O}(\text{MHz})$), this is the case unless the system is specifically designed to be on resonance.

⁵Note that Ref. [5] uses a different convention for the sign of the qubit energy. Here, we use the convention that the ground state is the lower energy state.

If the qubit is in the ground state, the phases will cancel, so that the oscillator will be displaced by $D(\alpha t)$. If the qubit is in the excited state, on the other hand, the rotating wave approximation applies and the Hamiltonian is approximately zero.

However, we need to take into account that any drive with a finite duration also has a finite resolution in the frequency domain. If the time profile of the chosen pulse is a Gaussian with a standard deviation σ_t , the width of the pulse in the frequency domain will be $\sigma_\omega = 1/\sigma_t$, which should be small compared to the dispersive shift χ . If we assume that the total duration of the pulse is $t_{\text{pulse}} = 2\sigma_t$ and $\chi > 2\sigma_\omega$, we will see that the duration of the pulse should be at least $t_{\text{pulse}} > \frac{4}{\chi}$, which is several μs in most settings.

Although a controlled displacement implemented by a drive (like Eq. (3.5)) is challenging, there has been significant progress in the last years to implement a controlled displacement of an oscillator, depending on the state of the qubit. The coupling is of interest because it not only enables a measurement of the GKP stabilizers, but also has the potential to improve the standard dispersive readout of transmon qubits. In 2018, Touzard *et al.* could demonstrate such a coupling experimentally [6] (some of their techniques were also used in the simulated photon pressure coupling discussed in Chapter 5). Although a conditional displacement controlled by an ancilla qubit has not yet been used for the GKP code, it seems promising because the nonlinearity of the oscillator is $\mathcal{O}(10\text{MHz})^6$ while the photon number is, by construction, much lower than that in the experimental implementation of the GKP code in circuit QED [7].

3.2.2. CONTROLLED DISPLACEMENT BY ROTATION

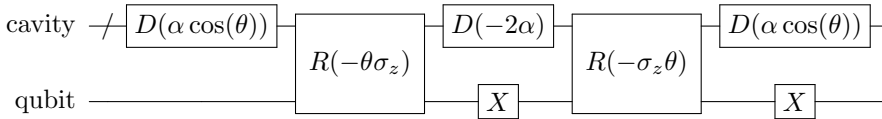


Figure 3.6: Equivalent circuit for the conditional displacement $D(i2\alpha \sin(-\theta\sigma_z))$ (see Eq. (3.6)), developed by van Look *et al.* [8]. The conditional rotation $R(-\theta\sigma_z)$ is implemented by the Hamiltonian $\sigma_z \hat{a}^\dagger \hat{a}$ applied for time θ .

Direct controlled displacements as discussed in the previous section are generally very challenging to implement. A much more reasonable alternative based on controlled rotations of the phase space has been proposed by van Look *et al.* in 2008 [8]. Similar to the direct controlled displacement discussed in Section 3.2.1, these controlled rotations are based on the dispersive shift in Eq. (3.4). It is straightforward to check that simply letting a qubit-oscillator system evolve under the dispersive shift for time t yields the time evolution operator

$$R(\chi t \sigma_z) = \exp(-it\chi\sigma_z\hat{a}^\dagger\hat{a}),$$

i. e. a controlled rotation. Applied to a coherent state $|\alpha\rangle$, such a controlled displacement yields the state(s) $|e^{-it\chi\sigma_z}\alpha\rangle$. Using controlled rotations and unconditional dis-

⁶This value is not given in the paper, it is estimated using the dispersive shift $\chi_{qc} \approx 100\text{kHz}$ and the nonlinearity $\chi_{qq} = 251\text{MHz}$ reported by the authors.

placements one can show that

$$\begin{aligned}
 D(i2\alpha \sin(-\theta\sigma_z)) &\equiv D(\alpha \cos(\theta))e^{-i\theta\sigma_z\hat{a}^\dagger\hat{a}}D(-2\alpha)e^{i\theta\sigma_z\hat{a}^\dagger\hat{a}}D(\alpha \cos(\theta)) \\
 &= D(\alpha \cos(\theta))D(-e^{-i\theta\sigma_z}2\alpha)D(\alpha \cos(\theta)) \\
 &= D(2\alpha \cos(\theta) - 2\cos(-\theta\sigma_z) - i2\alpha \sin(-\theta\sigma_z)) \\
 &= D(i2\alpha \sin(-\theta\sigma_z)),
 \end{aligned} \tag{3.6}$$

see also Fig. 3.6. When using this gate sequence, there are two main limiting factors for any experimental implementation: On the one hand, the number of photons that can be used in the oscillator is often limited, enforcing a limit on the amplitude of the displacement α . On the other hand, the strength of the dispersive shift is set by the design of an experiment, and it dominates the total time needed to implement a controlled displacement.

In the following, we will discuss two limits of these conditions, namely minimizing the photon number or minimizing the dispersive shift. While the former approach seemed more promising in 2015 [4], advances in the fabrication and control of 3D cavities made the latter more advantageous in the experimental implementation of the GKP code in circuit QED [7].

MINIMAL PHOTON NUMBER

Even in the early circuit QED experiments where transmon qubits are coupled to high quality 3D cavities, a dispersive shift in the order 1–20 MHz was readily available [9–11]. However, the photon number was severely limited: As a simple estimate, the critical photon number for a typical setup of the time with $\Delta = 1$ GHz, $\chi = 2.5$ MHz is given by $n_{\text{crit}} = \frac{\Delta}{4\chi} = 100$, see also Section 3.2.1. In an experiment specifically designed to use superpositions of many photons by Vlastakis *et al.* in 2013, they estimate the maximum allowed photon number to be around 300, and demonstrate Schrödinger cat states $|\alpha\rangle + |-\alpha\rangle$ up to about 55 photons [10].⁷ With these parameters in mind, the proposal to encode a GKP state using phase estimation referred to an implementation of the controlled displacement where the strength of the unconditional displacements is limited [4]. To this end, Eq. (3.6) is used with the choice $\theta = \chi t = \pi$. The gate sequence to implement a controlled displacement is then

$$D(i2\alpha\sigma_z) \equiv e^{-i\pi\sigma_z\hat{a}^\dagger\hat{a}}D(-\alpha)e^{i\pi\sigma_z\hat{a}^\dagger\hat{a}}.$$

Figure 3.7 shows a phase-space sketch of a controlled displacement $D(i\sqrt{2\pi}\sigma_z)$ applied to a coherent state $|\sqrt{2\pi}\rangle$, with the ancilla qubit in the $|+\rangle$ state.

Unconditional displacements are very fast, taking only about 10 ns to complete. This implies that the amplitude of a controlled displacement does not change the time needed significantly. Given a dispersive shift of 10–20 MHz, the time needed for the desired controlled rotations is about 200 ns each. If we also take into account that the readout time for an ancilla transmon qubit is typically 100–300 ns, one round of phase estimation will take around 600 ns, depending on details of the experiment.

⁷Note that Vlastakis *et al.* use an unconventional definition of the photon number: They define the size S of a Schrödinger cat state $|\beta_1\rangle + |\beta_2\rangle$ as $S = |\beta_1 - \beta_2|^2$ and use “photons” as unit for the size. With this convention, the state $|\sqrt{55}\rangle + |\sqrt{55}\rangle$ has a size of $S = 110$ “photons”, even though the average photon number of this state is $\bar{n} = 55$.

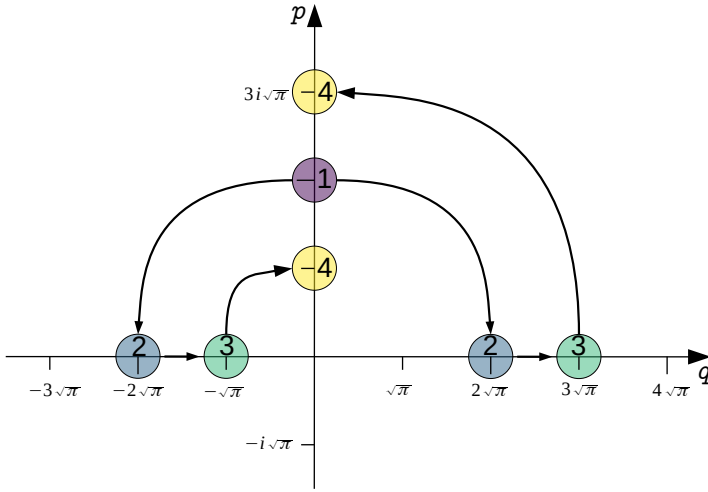


Figure 3.7: Controlled displacement using two controlled rotations. (1) We start with the coherent state $|i\sqrt{2\pi}\rangle$ (in purple), and want to apply a controlled displacement $D(i\sqrt{2\pi}\sigma_z)$. The ancilla qubit is assumed to be in the state $|+\rangle$. (2) In the first step, we apply a controlled rotation $R(\pi\sigma_z)$, creating two coherent states $|\pm\sqrt{2\pi}\rangle$ (in blue). (3) In the third step, we apply a Pauli X gate to the ancilla qubit, and displace the two coherent states by $D(\sqrt{\pi}/2)$ to $|\pm\sqrt{\pi}/2\rangle$ and $|3\sqrt{\pi}/2\rangle$, respectively (in green). (4) Finally, a second controlled rotation $R(\pi\sigma_z)$ (now with the state of the ancilla qubit flipped) rotates the states back to the p quadrature, leaving us with an equal superposition of the two coherent states $|i\sqrt{\pi}\rangle$ and $|i\sqrt{3\pi}\rangle$ (in yellow), corresponding to the desired state $D(i\sqrt{2\pi}\sigma_z)|i\sqrt{2\pi}\rangle$.

MINIMAL TIME

Although the GKP code is very efficient for protecting a qubit against Gaussian noise, and in particular photon loss, it performs poorly if the harmonic oscillator is slightly anharmonic (see Section 3.3 and [1, 12]). Therefore, making the oscillator used to encode a qubit as harmonic as possible is crucial to obtain a long-lived GKP state. However, this comes at a cost: Because the nonlinear interactions and the dispersive shift arise due to the same qubit-cavity coupling [7, 13], a very harmonic oscillator usually also implies that the dispersive shift is small, meaning that a controlled rotation with $\theta = \chi t = \pi$ would take an unreasonably long time.

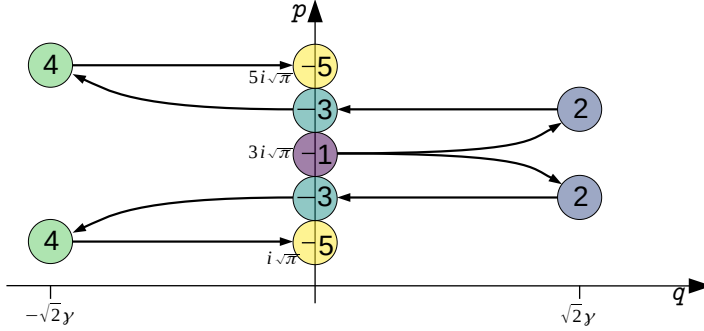


Figure 3.8: Controlled displacement using two controlled rotations. (1) We start with the coherent state $|i3\sqrt{\pi}/2\rangle$ (in purple) and want to apply a controlled displacement $D(i2\sqrt{2\pi}\sigma_z)$. The ancilla qubit is assumed to be in the state $|+\rangle$. (2) In the first step, we apply an unconditional displacement $D(\gamma)$, for some $\gamma \in \mathbb{R}$. Then, we apply the controlled rotation $R(\epsilon\sigma_z)$ for some small $\epsilon \in \mathbb{R}$ (chosen according to Eq. (3.6)), creating the two coherent states in blue. (3) In the second step, we apply a Pauli X gate to the ancilla qubit, and displace the two coherent states by $D(-\gamma)$ (in turquoise). (4) Then, we again displace by $D(-\gamma)$ and apply the controlled rotation $R(\epsilon\sigma_z)$ (with the qubit now flipped), creating the two coherent states $|i\sqrt{\pi}/2 - \gamma\rangle$ and $|i5\sqrt{\pi}/2 - \gamma\rangle$ (in light green). (5) Finally, an unconditional displacement $D(\gamma)$ creates the two coherent states $|i\sqrt{\pi}\rangle$ and $|i5\sqrt{\pi}\rangle$ (in yellow), corresponding to the desired state $D(2i\sqrt{2\pi}\sigma_z)|i\sqrt{3\pi}\rangle$ if γ and ϵ are chosen to fulfill Eq. (3.6).

In the experimental realization of the GKP code in circuit QED, Campagne-Ibarcq *et al.* solve this issue by improving the cavity such that very large photon numbers can be used [7]. They approximate Eq. (3.6) in the limit $\theta \ll 1$, displacing the GKP state to $|\alpha|^2 \approx 1000$ photons during the protocol. Neglecting the (very small) time needed for the unconditional displacements and the finite rise time of the microwave equipment, their approach can be approximated by the gate developed by van Loock *et al.* :

$$D(-i2\beta\sigma_z) \approx D(\alpha)e^{-i\theta\sigma_z\hat{a}^\dagger\hat{a}}D(-2\alpha)e^{i\theta\sigma_z\hat{a}^\dagger\hat{a}}D(\alpha), \quad \beta = \alpha\theta.$$

Figure 3.8 shows a phase-space sketch of a controlled displacement $D(i\sqrt{2\pi}\sigma_z)$ applied to a coherent state $|3\sqrt{\pi}/2\rangle$, with the ancilla qubit in the $|+\rangle$ state. The change of direction between the two controlled rotations is achieved by conjugating one of the two operations with Pauli X gates applied to the ancilla qubit. Similar to the unconditional displacement, these operations can be done in about 10 ns. In their implementation, the dispersive shift between the ancilla qubit and the storage oscillator is only 28 kHz, and the dispersive shift between the qubit and its readout resonator about 1 MHz [7].

For these reasons, the controlled displacement takes about $1.1\ \mu\text{s}$ and the readout of the qubit about $650\ \text{ns}$, so that each round takes about $1.8\ \mu\text{s}$ to complete. Although this is slower than the approach discussed in the previous section, these choices reduce the Kerr nonlinearity of the oscillator to only about $1\ \text{Hz}$, in contrast to the $\mathcal{O}(10)\ \text{kHz}$ typical for setups with a large dispersive shift, significantly improving the overall performance of the protocol.

3.2.3. CONTROLLED DISPLACEMENTS IN TRAPPED IONS

The first experimental realization of the GKP code has been in a trapped ion setup, realizing first the sensor state and then a GKP qubit [1, 14]. In this setup, the motional mode of a trapped ion is used to store a GKP state, and the spin of the same ion is used as ancilla qubit. A major drawback of this setup is that the encoding procedure requires post-selection: If the measurement of the spin projects the ion into the bright state, many photons will be scattered on the ion, randomizing the state of the motional mode. On the other hand, the big advantage of the trapped ion setup is that it natively brings the ability for controlled displacements, the so-called state- (or spin)-dependent force. That is, in a trapped ion setting, driving the red and blue sidebands simultaneously and symmetrically in the rotating frame gives the interaction Hamiltonian [15]

$$H_{int} = \omega(e^{-i\phi}\sigma_+ + e^{i\phi}\sigma_-)(\hat{a}^\dagger + \hat{a}).$$

Choosing appropriate phases, this Hamiltonian becomes $\sigma_z \hat{q}$ in the rotating frame, corresponding to the desired controlled displacement. A controlled displacement $\sigma_z \hat{p}$ can be also easily achieved by changing the phases of the employed lasers.

3.3. NUMERICAL ANALYSIS OF NOISE DURING PREPARATION AND MEASUREMENT

To better understand how encoding a GKP qubit using phase estimation works and to see the influence of various error processes, we can perform numerical simulations. Note that the encoding procedure in this section has been chosen in 2016 with the given experimental settings of that time in mind and is now outdated. The scheme to stabilize a qubit with the controlled displacement using large displacements (see Fig. 3.8) is superior to the approach used here. However, it is still educational for understanding the different noise processes.

A high-coherence superconducting transmon qubit dispersively coupled to a high-Q microwave cavity is a good candidate for an experimental realization of a grid state as was argued in [4]. A single round of phase estimation has (almost) identical experimental components as a photon parity measurement performed in [11, 16] (where such measurement rounds are performed repeatedly). Protocols with $M = 4\text{--}8$ of rounds of non-adaptive and adaptive phase estimation which save on photon use as compared to standard phase estimation are described in Section 3.1 (see also [4]). Note that the number of photons in the sensor state made in M rounds is half that of an M -round encoded state in [4] as the two displacement operators S_p and S_q for the sensor *state* are weaker in strength than the displacement checks which define a code *space*. An alternative platform could be the creation of a grid state in a microwave cavity by sequentially passing

Rydberg atoms through the cavity [17] implementing the 4–8 rounds of Ramsey phase estimation in Fig. 3.5. The advantage of this set-up is that the cavity-atom interaction is only ‘on’ while the atom is in transit through the cavity, but the feasibility of this scheme has not yet been analyzed. For superconducting transmon qubits coupled to microwave cavities, the preparation protocols that we consider may not even be needed as it is possible to create any state of the cavity by numerically optimizing microwave pulses on cavity and qubit [18].

In this section, we analyze a phase estimation preparation protocol which is based on a dispersive qubit-cavity interaction of the form $\sigma_z \hat{a}^\dagger \hat{a}$. We first introduce our performance measure which captures how well one prepares a grid state. We then discuss our choice of information-gain-optimized phase estimation and present the Hamiltonian and simulated noise models.

3.3.1. CHOICE OF PHASE ESTIMATION

For phase estimation, we will only use the circuit in Fig. 3.1 with $l = 1$. Many variants of phase estimation could be considered, e. g. going beyond Fig. 3.5 by entangling qubits between rounds or performing joint measurements on qubits, but simplicity is what we opt for here. Our only choice for optimization is thus the choice of feedback phase φ which can depend on outcomes of previous qubit measurements. A strategy which is then performing similar to the one that we originally chose in [4], is the following maximal-information gain strategy (see Section 3.1.4 for details). Given an estimate $\tilde{\theta}_{M-1}$ for the eigenvalue θ after $(M-1)$ measurements, we choose the feedback φ_M in the M^{th} measurement as

$$\varphi_M = \tilde{\theta}_{M-1} + \frac{\pi}{2}.$$

The estimate $\tilde{\theta}_{M-1}$ is obtained according to Eq. (2.23). In our simulations, we assume that the distribution $\mathbb{P}(\theta)$ of the initial state is uniform, which is warranted for our input state. The fact that $\mathbb{P}(\mathbf{x}_{M-1})$ is independent of θ then allows for the simple expression $\tilde{\theta}_{M-1} = \arg \int d\theta \mathbb{P}(\mathbf{x}_{M-1}|\theta) e^{i\theta}$, which is also what we have used previously [4]. In our simulations we have found that using the noisy $\rho(\mathbf{x}_{M-1})$ to estimate the current phase always gives slightly better or equal results (depending on the setting, the effective squeezing Δ of the final state can change up to 0.01).⁸ Because the improvements are minimal, we always use the state produced by the noiseless protocol to estimate the current phase in our plots.

3.3.2. HAMILTONIAN AND NOISE MODEL

A single round of phase estimation can be implemented using the circuit in Fig. 3.5 which uses controlled-displacements (and optionally cavity pre-displacement). We will assume that the qubit that is measured is again used in the next round. If we imagine using the qubit-cavity interaction $2\chi\sigma_z\hat{a}^\dagger\hat{a}$, we use the maximal information gain phase estimation strategy (Section 3.1.4) using the circuit depicted in Fig. 3.9, where the controlled displacement is implemented with a controlled rotation by $\pm\pi/2$, see Fig. 3.7.

⁸Doing so would not rely on information that is not available in an experiment. If a good noise model is known, we can obtain an estimate of the noisy state in numerical simulations in real time, following the results of an

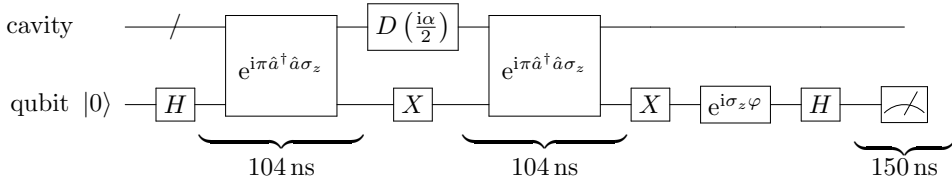


Figure 3.9: Gate sequence and durations used in the numerical simulations. The gates where the duration is given explicitly are simulated using a Lindblad master equation, see Eq. (3.7). The measurement is modeled as an instant projection of the qubit, followed by an idling time used for readout.

3

In order to include nonlinearities, photon loss, qubit decay and measurement errors in the simulation, we use a simplified model for when these unwanted processes act. Namely, we let them operate during the operations which take the longest to enact in practice. We will assume that all gates which act either on the qubit or on the cavity mode are very fast compared to all other timescales: We approximate them as taking place instantaneously. The conditional rotation gates $R(-\sigma_z\pi)$ take a time $\pi/(2\chi) \approx 104$ ns each when $\chi/2\pi = 2.4$ MHz. In the simulation, it is assumed that cavity and qubit can be decoupled, i. e. χ can be turned “off” when this interaction should not take place. The measurement process is modeled as an instantaneous (possibly faulty) projection followed by a finite readout idling time of 150 ns. The outcome of the projection is used to reset the qubit to $|0\rangle$ for the next round (assuming a noiseless instantaneous Pauli X gate). However, during the measurement idling time, the qubit can still decay from $|1\rangle$ to $|0\rangle$ which would imply that we start the next round with the qubit in a wrong state. When we show data for qubit amplitude damping, we thus include this error process. The time-scale of a single phase estimation round is thus determined by χ and the measurement time, both of which are taken to be reasonable values of superconducting transmon qubit experiments [16]. The simulated circuit and gate durations are summarized in Fig. 3.9.

NONLINEARITY

We have previously identified nonlinearities as a possible cause for bad errors for a GKP state [4]: We thus simulate the effect of two different nonlinearities. One is the cavity anharmonicity, also called Kerr interaction,

$$H_{Kc} = -\frac{K_c}{2} (\hat{a}^\dagger)^2 \hat{a}^2.$$

The other is the nonlinear dispersive shift

$$H_{Kcq} = -K_{cq} (\hat{a}^\dagger)^2 \hat{a}^2 \sigma_z.$$

For both these interactions, we assume that they are only present during the $R(-\sigma_z\pi)$ gates (which is roughly 2/3 of the total time duration, assuming the measurement takes 1/3 of the time).

experiment.

STOCHASTIC ERRORS

The unitary operation generated by $H = 2\chi\hat{a}^\dagger\hat{a}\sigma_z + H_{Kc} + H_{Kcq}$ is simulated using a Lindblad master equation for the qubit-cavity system for the duration of the qubit-cavity gates. In this Lindblad master equation, we can also include stochastic sources such as photon loss from the cavity and amplitude damping for the qubit. We do not consider qubit dephasing. We will thus simulate the dynamics of a Lindblad equation of the form

$$\dot{\rho} = -i[H, \rho] + \mathcal{D}(\sqrt{\kappa}\hat{a})\rho + \mathcal{D}(\sqrt{\gamma}\sigma_-)\rho \quad (3.7)$$

with the compactly-defined superoperator

$$\mathcal{D}(A)\rho = A\rho A^\dagger - \frac{1}{2}(A^\dagger A\rho + \rho A^\dagger A).$$

Due to limitations in the accuracy of the employed master equation solver (Python QuTip package [19]), the study of these types of stochastic errors is limited to $M = 8$ rounds (see Appendix A.1.1). Note that stochastic errors also play a role during qubit measurements.

MEASUREMENT ERRORS

We will model two types of measurement errors: imperfect projection and readout errors. A *readout error* refers to the scenario in which a qubit is projected onto a state $|x\rangle$ and we learn x with probability $1 - p$ but \bar{x} with probability p . Let $\Pi_x = |x\rangle\langle x|$, i. e. the projector onto qubit in state $|x\rangle$, $x \in \{0, 1\}$. Our lack of information about the qubit outcome can be modeled as the following map applied to the qubit-cavity density matrix ρ per round:

$$\rho \rightarrow (1 - p)\Pi_x\rho\Pi_x + p\Pi_{\bar{x}}\rho\Pi_{\bar{x}}.$$

Imperfect projection of the qubit refers to the scenario where a measurement of the ancilla qubit leads to us learning result x while the cavity-qubit system undergoes the map:

$$\rho \rightarrow A_x\rho A_x^\dagger, \quad A_x = \sqrt{1 - p}\Pi_x + \sqrt{p}\Pi_{\bar{x}}.$$

These models are not identical in the sense that there are coherent cross error terms of the form $\Pi_x\rho\Pi_{\bar{x}}$ in the latter model while these are absent in the first. Note that both these errors will not only affect the current round, but also change the qubit input state of the next measurement if the ancilla is reset by a X flip depending on the measurement outcome.

3.3.3. SIMULATION RESULTS

When simulating phase estimation for S_p for M rounds, all possible 2^M measurement results are simulated, each giving rise to a state $\rho(\mathbf{x}_M)$. We then calculate the average squeezing parameter $\langle\Delta_p\rangle = \sum_M \mathbb{P}(\mathbf{x}_M)\Delta_p(\rho(\mathbf{x}_M))$, this is labeled as Δ on the vertical axis in Figs. 3.10 to 3.13. Note that this average does not depend on the value of $\tilde{\theta}_M = \arg(\text{Tr}(S_p\rho(\mathbf{x}_M)))$. The numerical simulations are discussed in more detail in Appendix A.1.1.

We start each simulation with a squeezed vacuum state in q with $\Delta = 0.2$, hence $\Delta_q = \Delta$ and $\Delta_p = 1/\Delta$. By performing the M -round phase estimation circuits for S_p , Δ_p

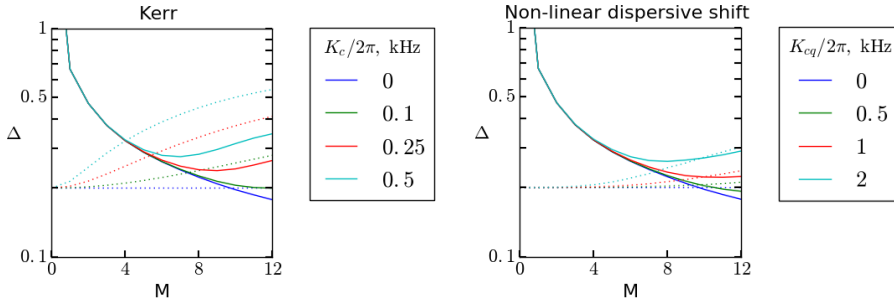


Figure 3.10: Effective squeezing after M rounds, starting with a squeezed state, $\Delta = 0.2$. Solid Lines: Δ_p . Dashed lines: Δ_q . Left: $H = \chi a^\dagger a 2\sigma_z + H_{Kc}$, Right: $H = \chi a^\dagger a 2\sigma_z + H_{Kcq}$. Reprinted figure with permission from K. Duivenvoorden, B. M. Terhal, and D. J. Weigand, “Single-mode displacement sensor”, *Physical Review A* **95**, 012305 (2017). © (2020) by the American Physical Society.

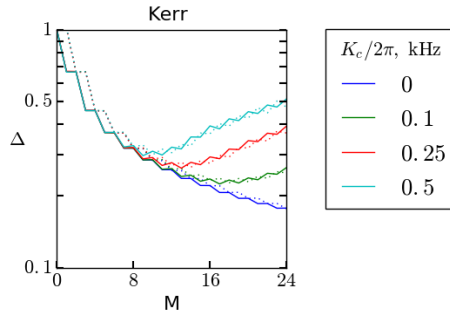


Figure 3.11: Effective squeezing after M rounds of interleaved phase estimation with Kerr interaction, starting with the vacuum state. Solid Lines: Δ_p . Dashed lines: Δ_q . Odd round numbers represent a measurement of S_p , even rounds a measurement of S_q . Reprinted figure with permission from K. Duivenvoorden, B. M. Terhal, and D. J. Weigand, “Single-mode displacement sensor”, *Physical Review A* **95**, 012305 (2017). © (2020) by the American Physical Society.

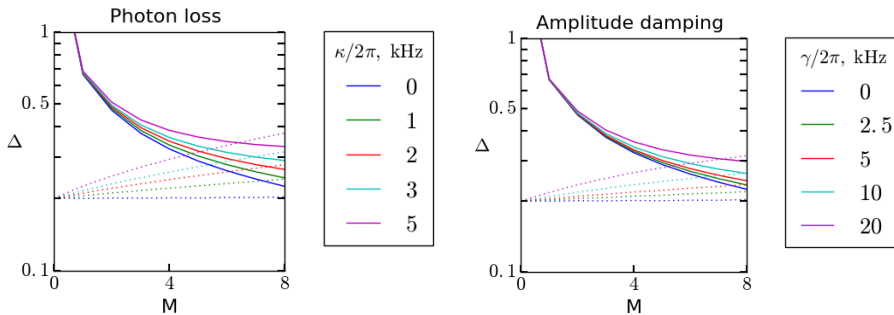


Figure 3.12: Effective squeezing after M rounds, starting with a squeezed state, $\Delta = 0.2$. Solid Lines: Δ_p . Dashed lines: Δ_q . Left: Photon loss, Right: Amplitude Damping. Reprinted figure with permission from K. Duivenvoorden, B. M. Terhal, and D. J. Weigand, “Single-mode displacement sensor”, *Physical Review A* **95**, 012305 (2017). © (2020) by the American Physical Society.

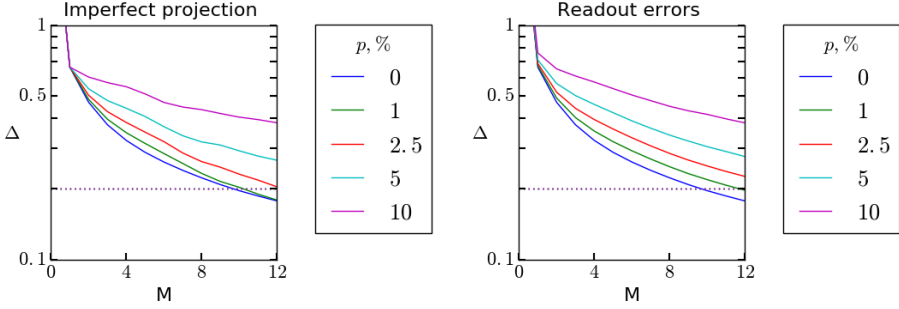


Figure 3.13: Effective squeezing after M rounds, starting with a squeezed state, $\Delta = 0.2$. Solid Lines: Δ_p . Dashed lines: Δ_q . Left: Imperfect projection, Right: Readout Errors. Reprinted figure with permission from K. Duivenvoorden, B. M. Terhal, and D. J. Weigand, “Single-mode displacement sensor”, [Physical Review A](#) **95**, 012305 (2017). © (2020) by the American Physical Society.

is gradually shrinking, but Δ_q will be gradually increasing due to photon loss and nonlinearities if no phase estimation measurements for S_q are performed. This decrease in S_p and increase in Δ_q is visible in all the data plots, see Figs. 3.10 to 3.12. One can thus roughly take the increase in Δ_q as a measure of how the grid state deteriorates passively under photon loss or nonlinearities in time.

What is noticeable is that in the presence of nonlinearities, say the Kerr nonlinearity, Δ_p starts *increasing* after a certain number of rounds, implying that applying more rounds of phase estimation in fact decreases the quality of the state. Already a Kerr interaction of the order $K_c/2\pi = 500\text{ Hz}$ is sufficient to limit the procedure to 4 rounds. For the nonlinear anharmonicity, the situation is slightly better, i. e. $K_{cq}/2\pi = 2\text{ kHz}$ can be tolerated. As the typical rates for both effects in an experimental setting are $\mathcal{O}(1) - \mathcal{O}(10)\text{ kHz}$, treating them as systematic errors and correcting for them [16] is very relevant.

This effect is clearly not present for photon loss and amplitude damping of the qubit (see Fig. 3.12), where the quality of the state gets better with the number of rounds. The highest amplitude damping rate of 20 kHz corresponds to a reasonable qubit decay time of $50\text{ }\mu\text{s}$. The effect of amplitude damping is small since qubit and cavity are only coupled for a short amount of time per round, about 200 ns. However, note that if the qubit jumps from $|1\rangle$ to $|0\rangle$, the state will suffer a large stochastic displacement.

The robustness against photon loss, amplitude damping, and measurement errors also suggests that a wider range of experimental settings could be explored for this type of encoding. For example, photon loss rates of the order 5 kHz are achievable in 2D microwave cavities [20].

Since S_p and S_q commute, one can alternate or interleave the single round circuits in Fig. 3.5 for S_p and S_q , so that both Δ_p and Δ_q decrease or remain low. Since we actually use the circuit in Fig. 3.9 which contains a qubit-independent pre-displacement, e. g. $S_p^{-1/2}$ which does not commute with S_q , one needs to correct for these additional displacements when estimating the phase θ . Since the number of possible results is squared for alternating measurements, it is no longer possible to simulate all possible outcomes. Instead, the measurement process of the ancilla qubit is simulated, i. e. we take a total of 2000 samples from the distribution of outcomes $\mathbb{P}(\mathbf{x}_M)$. Afterwards, the

results are weighed and averaged as before.

In Fig. 3.11, we show how interleaving the measurement of S_p and S_q , starting from the vacuum state, leads to a grid state. Without the Kerr effect, the quality of the state improves with the number of measurement rounds. Including the Kerr effect gives rise to an optimal number of rounds. Essentially, we expect that for a larger number of rounds (which means effectively a larger number of photons in the state), the Kerr effect introduces larger errors (see also the discussion in [4]). It is not visible from this numerical data whether or when the same saturation occurs in the presence of photon loss.

The preparation protocol by multiple consecutive rounds of phase estimation is inherently robust against measurement errors. This is because all measurements contain some information of the whole eigenvalue distribution of the target state. Thus, if a single measurement result is flipped, it will be overridden after some number of additional measurements. In fact, we expect that this form of phase estimation is much more robust to read-out noise than standard phase estimation and could thus more generally be a preferred phase estimation protocol on partially-coherent qubits.

The preparation protocol is robust against photon loss, amplitude damping, and readout errors. Even large rates do not prohibit the generation of grid states, while additional measurements always improve the state in the cavity for all presented numerical simulations. Some robustness against photon loss can be understood by expanding low-strength photon loss in terms of small displacements (see [4]).

REFERENCES

- [1] K. Duivenvoorden, B. M. Terhal, and D. J. Weigand, “Single-mode displacement sensor”, [Physical Review A 95, 012305 \(2017\)](#).
- [2] M. Nielsen and I. Chuang, *Quantum computation and quantum information*, Cambridge Series on Information and the Natural Sciences (Cambridge University Press, 2000).
- [3] D. W. Berry, H. M. Wiseman, and J. K. Breslin, “Optimal input states and feedback for interferometric phase estimation”, [Physical Review A 63, 053804 \(2001\)](#).
- [4] B. M. Terhal and D. J. Weigand, “Encoding a qubit into a cavity mode in circuit QED using phase estimation”, [Physical Review A 93, 012315 \(2016\)](#).
- [5] M. Boissonneault, J. M. Gambetta, and A. Blais, “Dispersive regime of circuit QED: photon-dependent qubit dephasing and relaxation rates”, [Physical Review A 79, 013819 \(2008\)](#).
- [6] S. Touzard, A. Kou, N. E. Frattini, V. V. Sivak, S. Puri, A. Grimm, L. Frunzio, S. Shankar, and M. H. Devoret, “Gated conditional displacement readout of superconducting qubits”, [Physical Review Letters 122, 080502 \(2019\)](#).
- [7] P. Campagne-Ibarcq, A. Eickbusch, S. Touzard, E. Zalys-Geller, N. E. Frattini, V. V. Sivak, P. Reinhold, S. Puri, S. Shankar, R. J. Schoelkopf, L. Frunzio, M. Mirrahimi, and M. H. Devoret, “Quantum error correction of a qubit encoded in grid states of an oscillator”, [Nature 584, 368 \(2020\)](#).

- [8] P. van Loock, W. J. Munro, K. Nemoto, T. P. Spiller, T. D. Ladd, S. L. Braunstein, and G. J. Milburn, “Hybrid quantum computation in quantum optics”, [Physical Review A](#) **78**, 022303 (2008).
- [9] G. Kirchmair, B. Vlastakis, Z. Leghtas, S. E. Nigg, H. Paik, E. Ginossar, M. Mirrahimi, L. Frunzio, S. Girvin, and R. Schoelkopf, “Observation of quantum state collapse and revival due to the single-photon Kerr effect”, [Nature](#) **495**, 205 (2013).
- [10] B. Vlastakis, G. Kirchmair, Z. Leghtas, S. E. Nigg, L. Frunzio, S. M. Girvin, M. Mirrahimi, M. H. Devoret, and R. J. Schoelkopf, “Deterministically encoding quantum information using 100-photon Schrödinger cat states”, [Science](#) **342**, 607 (2013).
- [11] L. Sun, A. Petrenko, Z. Leghtas, B. Vlastakis, G. Kirchmair, K. M. Sliwa, A. Narla, M. Hatridge, S. Shankar, J. Blumoff, L. Frunzio, M. Mirrahimi, M. H. Devoret, and R. J. Schoelkopf, “Tracking photon jumps with repeated quantum non-demolition parity measurements”, [Nature](#) **511**, 444 (2014).
- [12] V. V. Albert, K. Noh, K. Duivenvoorden, D. J. Young, R. T. Brierley, P. Reinhold, C. Vuillot, L. Li, C. Shen, S. M. Girvin, B. M. Terhal, and L. Jiang, “Performance and structure of single-mode Bosonic codes”, [Physical Review A](#) **97**, 032346 (2018).
- [13] S. E. Nigg, H. Paik, B. Vlastakis, G. Kirchmair, S. Shankar, L. Frunzio, M. H. Devoret, R. J. Schoelkopf, and S. M. Girvin, “Black-box superconducting circuit quantization”, [Physical Review Letters](#) **108**, 240502, 240502 (2012).
- [14] C. Flühmann, V. Negnevitsky, M. Marinelli, and J. P. Home, “Sequential modular position and momentum measurements of a trapped ion mechanical oscillator”, [Physical Review X](#) **8**, 021001 (2018).
- [15] E. Solano, R. L. de Matos Filho, and N. Zagury, “Mesoscopic superpositions of vibronic collective states of n trapped ions”, [Physical Review Letters](#) **87**, 060402 (2001).
- [16] N. Ofek, A. Petrenko, R. Heeres, P. Reinhold, Z. Leghtas, B. Vlastakis, Y. Liu, L. Frunzio, S. M. Girvin, L. Jiang, M. Mirrahimi, M. H. Devoret, and R. J. Schoelkopf, “Extending the lifetime of a quantum bit with error correction in superconducting circuits”, [Nature](#) **536**, 441 (2016).
- [17] S. Haroche and J.-M. Raimond, *Exploring the quantum: atoms, cavities, and photons* (Oxford University Press, USA, Oxford, 2006).
- [18] R. W. Heeres, P. Reinhold, N. Ofek, L. Frunzio, L. Jiang, M. H. Devoret, and R. J. Schoelkopf, “Implementing a universal gate set on a logical qubit encoded in an oscillator”, [Nature Communications](#) **8**, 94 (2016).
- [19] J. Johansson, P. Nation, and F. Nori, “QuTiP 2: a Python framework for the dynamics of open quantum systems”, [Computer Physics Communications](#) **184**, 1234 (2013).
- [20] A. Bruno, G. de Lange, S. Asaad, K. L. van der Enden, N. K. Langford, and L. DiCarlo, “Reducing intrinsic loss in superconducting resonators by surface treatment and deep etching of silicon substrates”, [Applied Physics Letters](#) **106**, 182601 (2015).

4

GENERATING GRID STATES FROM SCHRÖDINGER CAT STATES WITHOUT POST-SELECTION

Grid states (also called comb or GKP states) are an interesting class of bosonic states introduced by Gottesman, Kitaev and Preskill [1] to encode a qubit into an oscillator. A method to generate or “breed” a grid state from Schrödinger cat states using beam splitters and homodyne measurements is known [2], but this method requires post-selection. In this chapter, we show how post-processing of the measurement data can be used to entirely remove the need for post-selection, making the scheme much more viable. We bound the asymptotic behavior of the breeding procedure and demonstrate the efficacy of the method numerically. In the analytical discussion of breeding in Section 4.3, we derive a class of states that is closed under the breeding operation, so that we can make statements about the asymptotic behavior of the protocol. This section has a lot of lengthy calculations and may be skipped. The rest of the chapter only relies on the result of the section, but not on details of the derivation.

This chapter has been published with minor differences in D. J. Weigand and B. M. Terhal, “Generating grid states from Schrödinger-cat states without postselection”, *Physical Review A* **97**, 022341 (2018).

THE *grid states* — also called *comb* or *GKP states* — are a class of bosonic states with various interesting possible applications. Grid states were introduced in [1] as simultaneous eigenstates of two commuting displacement operators. In this scheme, grid states can be used to encode a qubit (or qudit) into an oscillator or bosonic mode so that small displacement errors can be corrected. As outlined in [1], universal quantum computation can be achieved using grid states: Clifford gates can be implemented via linear optics while one may invoke magic-state-distillation techniques to get to universality. Grid states also play a crucial role in fault-tolerant continuous-variable computation using cluster states [4].

First proposals to generate grid states use, e. g. , the coupling between a micro-mirror and an optical mode [1], the oscillatory motion of a trapped atom [5, 6], or a Kerr interaction between two bosonic modes [5]. Recent ideas on generated grid states in an atomic ensemble using squeezed light can be found in [7], while an optical breeding protocol for cat states was considered in [8]. In earlier work, we have shown how grid states can be generated without post-selection using phase estimation and a qubit-bosonic mode coupling of the form $Za^\dagger a$ [9], focusing on a circuit-QED setting. Very recent experiments [10, 11] show how a grid state can be constructed in the motional mode of an ion using post-selection.

In the linear optics setting, Vasconcelos *et al.* [2] and Etesse *et al.* [12] have independently developed a *breeding* protocol to generate grid states from Schrödinger cat states, using linear optics and homodyne post-selection [2]. A similar breeding protocol, used to generate Schrödinger cat states from Fock states, has been demonstrated in an experiment by Etesse *et al.* [13]. However, the protocol has an important drawback: The success probability of post-selection diminishes rapidly with the number of rounds.

In this chapter, we show that classical post-processing can be used to correct the grid state generated by a breeding protocol. This allows the use of any state generated by breeding, independent of the measurement results, showing that no post-selection is necessary. Our understanding of the protocol is formed by showing that a breeding protocol has identical action as a phase estimation protocol of multiple rounds, with specific (known) feedback phases and measurement results. Through this identification, the breeding protocol implements a particular phase estimation protocol which by definition gradually projects onto a grid state (since one is gradually learning bits of the phase). The feedback phases used and bits obtained in phase estimation inform us about the grid state that we have obtained, namely the information gives us an estimate of the eigenvalues of the commuting displacement operators thus fixing the eigenstate.

By describing a toy model, the so-called *slow breeding protocol*, we can show how breeding can be related to phase estimation. However, this slow breeding protocol is non-optimal in its requirement for very large cat states. We then examine an efficient breeding protocol, which is the protocol in [2], and show how the measurement record can be used to correct any final state to a good grid state. Proving convergence of this breeding protocol towards a good grid state by invoking phase estimation is not simple. Instead, by using a new class of approximate grid states which is closed under the efficient breeding step, we can bound the asymptotic behavior of the protocol. Finally, we confirm the performance of the protocol with numerics.

We will first review some background concepts concerning grid states, squeezing pa-

rameters, and phase estimation in Section 4.1. In Section 4.2, we show how a breeding protocol can be mapped onto a phase estimation scheme, giving some intuition how a protocol works without post-selection. Then we focus on analyzing the efficient breeding protocol by Vasconcelos *et al.* [2] without post-selection. In Section 4.4, we introduce a very useful class of approximate grid states and present some bounds on the probability of improving the state in a breeding round using these approximate states. We close the chapter with a numerical simulation of the breeding protocol in Section 4.5 and a Discussion (Section 4.6).

4.1. BACKGROUND

In this section, we give a short review of previous results and the formalism needed in the rest of this chapter. We start in Section 4.1.1 with a short introduction of grid states, following mostly the paper by Gottesman *et al.* [1]. In Section 4.1.2, we review the effective squeezing parameters, a versatile metric for the quality of a grid states which we introduced in [14]. In Section 4.1.3, we introduce a formalism which enables the construction of a map between breeding and phase estimation in an efficient manner.

4.1.1. GRID STATES

Consider a bosonic mode with dimensionless quadrature operators $\hat{q} = \frac{1}{\sqrt{2}}(a + a^\dagger)$ and $\hat{p} = \frac{i}{\sqrt{2}}(a^\dagger - a)$ obeying $[\hat{q}, \hat{p}] = i$. A grid state in this mode is a simultaneous, approximate, $+1$ eigenstate of two commuting displacement operators $S_p = e^{iu\hat{p}}$ and $S_q = e^{iv\hat{q}}$ where $u \cdot v \mod 2\pi = 0$ ensures commutativity of S_p and S_q . Note that it is not necessary that the displacements S_p, S_q form a square lattice in phase space. In fact, grid states can be defined on any two dimensional lattice where the area of the unit cell is a multiple of 2π [1].

In this chapter, we will investigate grid states with a symmetric choice $u = v = \xi$. For example, for the choice $\xi = \sqrt{2\pi}$, the space fixed by $S_p = +1, S_q = +1$ is one-dimensional. This state will be referred to as the *sensor state* [14].

Whenever a choice for ξ is necessary (e. g. for the numerical analysis or the Wigner function of a state), we investigate protocols generating this sensor state. In case of the choice $\xi = 2\sqrt{\pi}$ the $+1$ eigenspace of S_p and S_q is two-dimensional and thus encodes a qubit [1]. From here on, we will refer to ξ as the *spacing* of a grid state. For both the wave function in quadrature space and the Wigner function of a grid state, the spacing corresponds to the distance between the sharp peaks in these functions. We use the notation for displacement $D(\alpha) = \exp(\alpha a^\dagger - \alpha^* a)$ so that $S_p = D(\sqrt{\pi})$ for the sensor state. Spacing ξ thus corresponds to the action of a displacement with coherent amplitude $\xi/\sqrt{2}$.

Since a perfect eigenstate of these displacement operators (i. e. an ideal grid state) has infinite energy, it is only possible to generate approximate grid states. One possible approximation is a grid state of the form

$$|\Psi\rangle \propto \sum_{t=-\infty}^{\infty} e^{-\pi\kappa^2 t^2} S_p^t S(\Delta) |\text{vac}\rangle, \quad (4.1)$$

where S_p^t corresponds to the displacement $D(t\xi/2)$ and $S(\Delta)$ is the squeezing operator

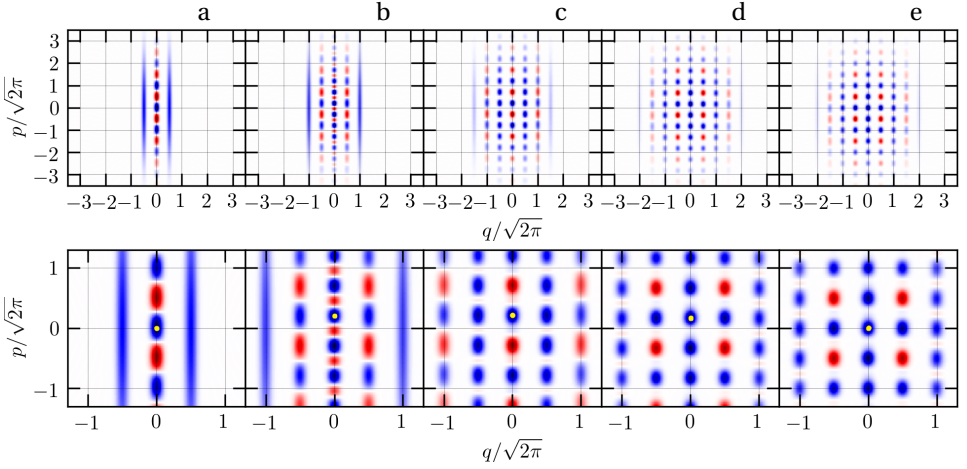


Figure 4.1: An example of breeding of the approximate $+1$ eigenstate of $S_p = e^{i\sqrt{2\pi}\hat{p}}$ and $S_q = e^{i\sqrt{2\pi}\hat{q}}$ (sensor state). Top row: Panels (a) to (d) show the Wigner functions of states generated by resp. $N = 1, 2, 3, 4$ measurement operators \mathcal{M} (as in Eq. (4.3) with some particular choice of phases φ_j which provide a good illustration of how the grid is shifted) where the horizontal axis is the q -coordinate and the vertical axis is the p -coordinate. Panel (a) is the Wigner function of a squeezed cat state with squeezing parameter $\Delta = 0.2$. The grid state is gradually built by displacements (translations) to the left and right with $S_p^{-1/2}$ and $S_p^{1/2}$. For the state with $N = 4$ in panel (d), we show the same state after applying the correction D_{correct} in panel (e). Bottom row: Shown are the same Wigner functions, zoomed in around the origin. The yellow dots mark the “center” of the state, for a $+1$ eigenstate of S_p it lies at the origin. Reprinted figure with permission from D. J. Weigand and B. M. Terhal, “Generating grid states from Schrödinger-cat states without postselection”, [Physical Review A 97, 022341 \(2018\)](#). © (2020) by the American Physical Society.

which has the action $\hat{q} \rightarrow \hat{q}\Delta, \hat{p} \rightarrow \hat{p}/\Delta$, so that

$$\langle \text{vac} | S^\dagger(\Delta) \text{Var}(q) S(\Delta) | \text{vac} \rangle = \Delta^2 \langle \text{vac} | \text{Var}(q) | \text{vac} \rangle = \frac{\Delta^2}{2}.$$

The squeezing parameter $\Delta < 1$ and the width of the Gaussian envelope can be chosen to be the same, i. e. $\kappa = \Delta$ [1].

In this form, the squeezed vacuum can be understood as an approximate +1 eigenstate of S_q , while the weighted sum over powers of S_p is an approximation of the projector onto the +1 eigenspace of S_p . Essentially, the ideal grid state is invariant under the two translations S_p and S_q (and their inverses) in phase space, hence a +1 eigenstate of these operators. Any finite-photon number version of this state occupies a bounded volume in phase space and cannot be fully translationally-invariant, but a Gaussian envelope allows the non-translational invariance of the tails to play a relatively small role.

4

4.1.2. EFFECTIVE SQUEEZING PARAMETERS

In order to characterize the quality of an approximate grid state we have introduced so-called *effective squeezing parameters* for both quadratures in [14], see Section 2.3.4 for a detailed derivation. A “squeezing” parameter can be generally used for capturing how well a state ρ is an approximate eigenstate of a unitary operator U . The idea is based on the fact that a state ρ is an eigenstate of the operator U iff $|\text{Tr}(\rho U)| = 1$. For such a state the mean phase $\theta \in [-\pi, \pi)$ equals $\theta(\rho) = \arg(\text{Tr}(\rho U))$. Because of the 2π -periodicity of the phase, the variance should not be taken to be the standard variance, but can be chosen as a phase variance equal to $\text{Var}(\rho) = \ln(|\text{Tr}(\rho U)|^{-2})$ [14]. This variance is identical to the more commonly used Holevo phase variance [15] for small $|\text{Tr}(\rho U)|$.

For a displacement $\mathcal{D} := D(ue^{i\phi})$ with $\phi, u \in \mathbb{R}$, the variance should be rescaled by u , i. e. we define the mean phase $\theta_{\mathcal{D}}$ and the effective squeezing parameter $\Delta_{\mathcal{D}}$ as:

$$\theta_{\mathcal{D}} := \arg(\text{Tr}(\rho \mathcal{D})), \quad \Delta_{\mathcal{D}} := \frac{1}{u} \sqrt{\ln(|\text{Tr}(\rho \mathcal{D})|^{-2})}. \quad (4.2)$$

As grid states are defined with respect to the displacement S_p (S_q) along the real (imaginary) axis in phase space, it is convenient to use the short-hand $\Delta_p := \Delta_{S_p}$ and $\Delta_q := \Delta_{S_q}$ for the two effective squeezing parameters. The squeezing parameters of an approximate grid state as defined in Eq. (4.1) are $\Delta_q = \Delta$, $\Delta_p \approx \kappa$. For a squeezed vacuum state $S(\Delta)|\text{vac}\rangle$, one has $\Delta_q = \Delta = 1/\Delta_p$. The effective squeezing parameter and mean phase have a very natural relation to grid states:

Protocols to generate an approximate eigenstate of S_p and S_q will produce a state ρ with certain values for $\theta_p := \theta_{S_p}$, $\theta_q := \theta_{S_q}$, Δ_p and Δ_q . The effective squeezing parameters then give a direct measure of the quality of the state ρ . In case of the sensor state, they directly relate to the measurement precision that can be achieved using ρ as a sensor [14]. In case of the GKP code, the probability of a logical X (or Z) error in the encoding can be bounded as $P_{\text{error}} < \frac{2\Delta}{\pi} e^{-\pi/(4\Delta^2)}$ with $\Delta = \Delta_q = \Delta_p$ [1].

The mean values θ_p and θ_q which are extracted from the protocol can be used to correct the resulting state by displacing this state by D_{correct} , i. e. $\rho \rightarrow \rho' = D_{\text{correct}} \rho D_{\text{correct}}^\dagger$ such that $\theta_p(\rho') \approx \theta_q(\rho') \approx 0$. For example, to shift the mean phase θ_p back to 0, we

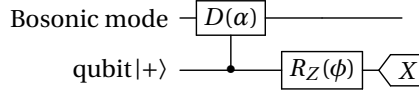


Figure 4.2: Single round of an adaptive phase estimation protocol which estimates the eigenvalue of $D(\alpha)$. The output state goes back into the next round of the protocol and the feedback phase ϕ can be chosen depending on earlier rounds. The collection of bits obtained, together with the chosen feedback phases, will gradually project the input state onto an approximate eigenstate of $D(\alpha)$ as the approximate eigenvalue is learned. Reprinted figure with permission from D. J. Weigand and B. M. Terhal, “Generating grid states from Schrödinger-cat states without postselection”, *Physical Review A* **97**, 022341 (2018). © (2020) by the American Physical Society.

4

choose α in $D_{\text{correct}} = \exp(i\alpha\hat{q})$ such that $S_p D_{\text{correct}} = \exp(-i\theta_p) D_{\text{correct}} S_p$. A simple visual representation of this procedure is that the positive parts of the Wigner function form a grid in phase space for grid states and this grid is aligned with the $p = 0, q = 0$ axes for a $+1$ eigenstate of S_p, S_q (see Figs. 4.1 and 4.4).

The final state is then an approximate $+1$ eigenstate of S_p and S_q . However, it will not be necessary to perform such a correcting displacement if one uses the concept of a phase or displacement frame [9] (in analogy with a Pauli frame for qubits).

Clearly, approximate grid states are not unique. For example, two grid states for which the grid envelope is displaced or translated by one unit cell can have the same values for θ_p, θ_q and Δ_p, Δ_q but contain a different mean number of photons. Similarly, one can note that the corrective displacement is not unique: In practice, one may opt for the smallest displacement shifting the grid envelope to the correct position, see Fig. 4.1(e).

4.1.3. ADAPTIVE PHASE ESTIMATION

Phase estimation refers to a whole class of algorithms that measure the eigenvalue of a unitary operator U . A recent overview of some of these schemes can be found e.g. in [16]. All phase estimation procedures, including textbook phase estimation [17], Kitaev’s phase estimation [18], and variants thereof can be executed in an iterative form with a single-qubit applying controlled- U^k gates. An in-depth analysis of some adaptive schemes can be found in works by Berry *et al.* [19]. We are interested in this case when the unitary operator to be measured is some displacement and we consider performing such a measurement by repeating a circuit of the form of Fig. 4.2.

A convenient formalism to describe such adaptive phase estimation uses the following “measurement” operator:

$$\mathcal{M}(\varphi, \alpha) := 1 + e^{i\varphi} D(\alpha),$$

with $\varphi \in [0, 2\pi)$ and α is a coherent amplitude. In all what follows, we focus on breeding an approximate eigenstate of $S_p = D(\xi/\sqrt{2})$ and assume that α is real, but the same method can be used for complex α . With this operator, a squeezed Schrödinger cat state, i.e. a single application of the measurement operator onto a squeezed vacuum state plus an additional displacement, has the form $D(-\alpha/2) \mathcal{M}(0, \alpha) S(\Delta) |\text{vac}\rangle$.

One can also see that the circuit shown in Fig. 4.2 acts on an input state $|\Phi_0\rangle$ as $\mathcal{M}(\phi + \pi x, \alpha) |\Phi_0\rangle$ where $x \in \{0, 1\}$ is the measurement result, i.e. it applies one additional measurement operator to the initial state. Thus, *any* state generated by a sequence of N

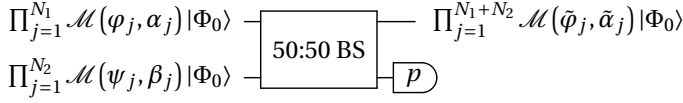


Figure 4.3: Single round of a breeding protocol. The round takes approximate grid states defined by N_1 and N_2 measurement operators \mathcal{M} as inputs. It returns an approximate grid state with $N_1 + N_2$ (possibly changed) measurement operators. The second output port is subject to a homodyne measurement of the \hat{p} quadrature. The initial state $|\Phi_0\rangle$ is chosen to be invariant under the action of a beam splitter, e.g. a squeezed vacuum state. Reprinted figure with permission from D. J. Weigand and B. M. Terhal, “Generating grid states from Schrödinger-cat states without postselection”, *Physical Review A* **97**, 022341 (2018). © (2020) by the American Physical Society.

of these circuits is of the form

$$|\Psi\rangle \propto \prod_{j=1}^N \mathcal{M}(\varphi_j, \alpha_j) |\Phi_0\rangle, \quad (4.3)$$

where $|\Phi_0\rangle$ is the initial state and $\varphi_j = \phi_j + x_j \alpha_j$ with measurement outcome x_j , feedback phase ϕ_j of round j and α_j possibly varying per round.

It can be observed that the class of states which is described by fixing the outcome to be $x = 0$ and letting the feedback phase vary captures all states in Eq. (4.3) since $\phi_j \in [0, 2\pi)$ can be freely chosen. We will show that the state obtained by a breeding protocol is identical to a state obtained by such a phase estimation protocol with all outcomes $x_j = 0$ and with varying $\phi_j = \varphi_j$. A (trivial) example is that a squeezed Schrödinger cat state is equivalent to a single round of phase estimation with $x = \phi = 0$ applied to a squeezed vacuum state. This map gives some intuition why breeding gives rise to a grid state. Using the form of the state allows one to estimate the mean phase and the effective squeezing parameters of the state using Eq. (4.2).

As mentioned before, even given θ_p and Δ_p , a grid state is not unique since it can be shifted by any S_p without affecting these parameters. Thus, to place the grid state symmetrically around the vacuum state and minimize photon number, it is better to perform a pre-displacement by $D(-\alpha/2)$ in each phase estimation round in Fig. 4.2 and similarly use the measurement operator $D(-\alpha/2) + e^{i\varphi} D(\alpha/2)$. Since our analysis does not depend on these shifts, we have opted to not include them.

4.2. BREEDING

Breeding protocols refer to a procedure where a grid state is gradually constructed from input (squeezed) Schrödinger cat states. These input states can be regarded as a very poor approximation (panel (a) in Fig. 4.1) to a grid state and the goal is to gradually improve these states. The circuit in Fig. 4.3 shows a single round of breeding. We will denote the number of breeding rounds by M , while N , which is a function of M , refers to the number of measurement operators acting on some initial state as in Eq. (4.3). In a single breeding round, partially bred grid states that will be of the same form as Eq. (4.3) are fed into a beam-splitter. After the beam-splitter, the p -quadrature of one of the states is measured (for breeding of a S_p eigenstate). For $N_2 = 1$ in Fig. 4.3, the input of the bottom port (port 2) plays the role of squeezed cat state modulo the additional

pre-displacement, i. e. $(D(-\beta/2) + D(\beta/2))|\Phi_0\rangle = D(-\beta/2)\mathcal{M}(0, \beta)|\Phi_0\rangle$. The aim of the Breed operation is to map the measurement operators in port 2 to port 1, i. e. the state at the output port is still of the form of Eq. (4.3), but with $N_1 + N_2$ measurement operators.

Since we would like to produce a state which is both an approximate eigenstate of S_p and S_q , we choose the input state $|\Phi_0\rangle$ as a squeezed vacuum state $|\Phi_0\rangle = S(\Delta)|\text{vac.}\rangle$ providing an approximate eigenstate of S_q . It is important that the effective squeezing parameter Δ_q is approximately preserved under the breeding operation so that the outgoing state is both an approximate eigenstate of S_p and S_q : We will verify this at the end of Section 4.2.2.

The rounds of this breeding procedure could be repeated in at least two ways. In the first manner, which we call *slow breeding*, we always use a squeezed cat state at input port 2 and input port 1 contains the state that came out of port 1 in the previous breeding round. This protocol can be seen as a toy model in the sense that it has several drawbacks, but we describe its functionality in order to understand how breeding works and how it maps onto phase estimation. In Section 4.2.2, we describe a parallelized distillation protocol in which 2^M squeezed cat states are fed into beam-splitters, leading to 2^{M-1} output states, which are subsequently used to produce 2^{M-2} states etc., eventually extracting one grid state after M breeding rounds, i. e. the setting proposed in [2, 12]. Then, we will show how a map to phase estimation can be constructed for this protocol, removing the need for post-selection.

4.2.1. SLOW BREEDING

Making use of the fact that the action \mathcal{B} of the beam splitter is given by

$$\begin{aligned}\hat{q}_1 &\rightarrow (\hat{q}_1 - \hat{q}_2)/\sqrt{2}, & \hat{p}_1 &\rightarrow (\hat{p}_1 - \hat{p}_2)/\sqrt{2}, \\ \hat{q}_2 &\rightarrow (\hat{q}_1 + \hat{q}_2)/\sqrt{2}, & \hat{p}_2 &\rightarrow (\hat{p}_1 + \hat{p}_2)/\sqrt{2},\end{aligned}\tag{4.4}$$

one can show that the output state of a breeding round in Fig. 4.3 equals

$$\prod_{j=1}^{N_1} \prod_{k=1}^{N_2} \tilde{\mathcal{M}}_1(\varphi_j, \alpha_j) \tilde{\mathcal{M}}_2(\psi_k, \beta_k) \mathcal{B}|\Phi_0, \Phi_0\rangle.\tag{4.5}$$

Here $\tilde{\mathcal{M}}_i(\varphi, \alpha) = \mathcal{B}\mathcal{M}_i(\varphi, \alpha)\mathcal{B}^\dagger$. For the input states $|\Phi_0, \Phi_0\rangle$, we use the invariance under beam-splitting, i. e. $\mathcal{B}S_1(\Delta)S_2(\Delta)|\text{vac}, \text{vac}\rangle_{1,2} = S_1(\Delta)S_2(\Delta)|\text{vac}, \text{vac}\rangle_{1,2}$. For real α , we have $\tilde{\mathcal{M}}_1(\varphi, \alpha) = I + e^{i\varphi}D_1(\alpha/\sqrt{2})D_2(-\alpha/\sqrt{2})$ and $\tilde{\mathcal{M}}_2(\psi, \beta) = I + e^{i\psi}D_1(\beta/\sqrt{2})D_2(\beta/\sqrt{2})$. When mode 2 is then measured via homodyne measurement of \hat{p} with outcome p , we can replace $D_2(\alpha)$ by $e^{-i\alpha\sqrt{2}p}$ (for real α). This implies that the output state of the protocol is as claimed in Fig. 4.3, i. e.

$$\begin{aligned}\prod_{j=1}^{N_1} \prod_{k=1}^{N_2} \mathcal{M}_1(\tilde{\varphi}_j, \tilde{\alpha}_j) \mathcal{M}_1(\tilde{\psi}_k, \tilde{\beta}_k) |\Phi_0\rangle, \\ \tilde{\varphi}_j = \varphi_j + \alpha_j p, \tilde{\alpha}_j = \frac{\alpha_j}{\sqrt{2}}, \tilde{\psi}_k = \psi_k - \beta_k p, \tilde{\beta}_k = \frac{\beta_k}{\sqrt{2}}.\end{aligned}\tag{4.6}$$

The probability to find outcome p for the homodyne measurement depends in detail on the state of the form Eq. (4.3) that goes into the beam-splitter, but the variance of this

probability distribution in p scales as $\sim 1/\Delta^2$. Hence, the more the input state $|\Phi_0\rangle$ is squeezed in q (by Δ), the larger the spread of measured values for p will be and hence the greater the need for not using post-selection on the outcome $p = 0$.

Consider now the *slow breeding* case where the state at input 2 is always a squeezed cat state i.e. $N_2 = 1$, and the output state is fed into port 1 of the next round. In order to breed a grid state, we take $\alpha_1 = \beta_1 = \alpha$ and $\varphi_1 = \psi_1 = 0$ for the first breeding round, meaning that the inputs in both ports are squeezed cat states.

In the second breeding round, one takes $\beta_2 = \alpha/\sqrt{2}, \psi_2 = 0$ and in the M^{th} round $\beta_M = \alpha/\sqrt{2^{M-1}}, \psi_M = 0$ so that the final state has spacing $\xi = \alpha/\sqrt{2^{M-1}}$. The evolution of mode 1 under the slow breeding protocol without post-selection and $M = 3$ rounds is shown in Fig. 4.1(a-d).

By post-selecting the measurement result onto $p = 0$, it is apparent from this choice for the β_i and Eq. (4.6) that M rounds of this procedure generate a binomial distribution of displacements, since all the phases are zero. Thus, clearly, when we post-select on outcome $p = 0$, one obtains a grid state with a binomial envelope (similar to the protocols shown in [2, 12]).

From Eq. (4.6), it follows immediately that M rounds of breeding in this setup with a final spacing $\xi = \alpha/\sqrt{2^{M-1}}$ can be mapped to $N = M + 1$ rounds of phase estimation with the choice $\varphi_m = \alpha(\sum_{k>m}^M 2^{-k/2} p_k - 2^{-m/2} p_m)$ for the feedback phase and measurement result $x_m = 0$, where p_m is the homodyne measurement result of \hat{p}_2 in round $m = 1, \dots, M$ and $p_0 = 0$ to fix the initial state ($m = 0$) to the squeezed cat state $\propto (I + D(\alpha))|\Phi_0\rangle$. It is noteworthy that the feedback phase depends on the outcomes of many “later” rounds: One can thus only construct the corresponding phase estimation protocol after the last homodyne measurement is done. This suggests that instead of post-selecting on $p = 0$, one can simply process the measurement information to infer the values of θ_p in Eq. (4.2) of the final state. This correction is demonstrated in Fig. 4.1(e), where a correcting displacement is applied to the final state of the protocol.

However, the slow breeding protocol suffers from a different problem. To get a grid state with final spacing $\xi = \sqrt{2\pi}$ after M rounds, the number of photons in the squeezed cat state used in the first round $\bar{n}_{\text{cat}} \geq 2^M \pi$. This is exponentially larger than the mean photon number of the final grid state which scales as $\bar{n}_{\text{grid}} \sim M$ [1, 9], i.e. the procedure is inefficient in its use of photons.

4.2.2. EFFICIENT BREEDING

A much better scheme is to use a partially-bred grid state in the ancilla mode as proposed in [2, 12], effectively performing a grid state distillation scheme. In this scheme, one starts with two cat states ($N_1 = N_2 = 1$), leading to a state with $N_{\text{out}} = 2$. Then, one takes two such states ($N_1 = N_2 = 2$) and feeds them into the beam-splitter to get a state with $N_{\text{out}} = 4$ etc. With Eq. (4.6), one can see that we have $N = 2^M$ for M repetitions of this scheme.

In this scheme, one will always have $\beta_j = \alpha_j$ for the two input ports, but the phases can vary depending on measurement results and do not need to be the same for both inputs. This parallelization leads to a much faster built-up of the grid state. For a final grid state with $N = 2^M$ applications of \mathcal{M} , one requires M rounds of beam-splitters in sequence. For the final grid state to have spacing ξ , one starts the protocol with cat

states with amplitude $\xi 2^{(M-3)/2} = \xi \frac{\sqrt{N}}{2\sqrt{2}}$, thus $\bar{n}_{\text{cat}} \sim \bar{n}_{\text{grid}} \sim N$. For example, generating a sensor state with $M = 2$ rounds would require $\bar{n}_{\text{cat}} = \frac{\pi}{2} + \bar{n}_{sq}$ photons, where \bar{n}_{sq} is the additional number of photons due to squeezing.

In order to estimate the effective squeezing after M rounds as well as the phase θ_p , one needs to describe the final state in terms of the measurement outcomes. A concise description of the output state of an M -round protocol is as follows. We label all 2^M ingoing modes of the protocol with a bit-string $\mathbf{x}[M]$ of length M . Two modes $x_1 \dots x_{M-1} x_M$ and $x_1 \dots x_{M-1} \bar{x}_M$ which differ only on the last bit x_M will enter into one beam-splitter and so the outgoing single mode can be labeled by the remaining $M-1$ bit string $x_1 \dots x_{M-1} = \mathbf{x}[M-1]$. The outcomes of these 2^{M-1} measurements of the first round forms a vector \mathbf{p}^1 with 2^{M-1} entries $p_{\mathbf{x}[M-1]}^1$ which are labeled by the bit strings $\mathbf{x}[M-1]$. The final measurement in round M is then \mathbf{p}^M with a single entry labeled by a bit string of length 0. An example of this labeling can be seen in Fig. 4.4. With this notation, the initial state is thus a product state proportional to

$$\prod_{\mathbf{x}[M]} \mathcal{M}_{\mathbf{x}[M]}(0, 2^{(M-1)/2} \xi) |\Phi_0\rangle_{\mathbf{x}[M]}.$$

Similarly, the state of the system after the first round of breeding is the product state

$$\prod_{\mathbf{x}[M]} \mathcal{M}_{\mathbf{x}[M-1]} \left(\xi (-1)^{x_M} 2^{\frac{M-2}{2}} p_{\mathbf{x}[M-1]}^1, 2^{\frac{M-2}{2}} \xi \right) |\Phi_0\rangle_{\mathbf{x}[M-1]},$$

where each state now gets two measurement operators applied to it since we are taking the product over all bit-strings of length M . After all $2^M - 1$ measurements, the final state is given by 2^M measurement operators acting on a single mode, i. e.

$$|\Psi_{\text{out}}(\mathbf{p}^1, \dots, \mathbf{p}^M)\rangle = \prod_{\mathbf{x}[M]} \mathcal{M}_{\mathbf{x}[0]} \left(\xi \sum_{j=1}^M (-1)^{x_j} 2^{\frac{j-2}{2}} p_{\mathbf{x}[j-1]}^{M-j+1}, \frac{\xi}{\sqrt{2}} \right) |\Phi_0\rangle_{\mathbf{x}[0]}. \quad (4.7)$$

with normalization $\mathbb{P}(\mathbf{p}^1, \dots, \mathbf{p}^M) = \langle \Psi_{\text{out}} | \Psi_{\text{out}} \rangle$.

In order to evaluate the expected eigenvalue of S_p , $\theta_p = \frac{\arg\langle \Psi_{\text{out}} | S_p | \Psi_{\text{out}} \rangle}{\langle \Psi_{\text{out}} | \Psi_{\text{out}} \rangle}$ for a given series of outcomes $\mathbf{p}_{\text{all}} := \mathbf{p}^1, \dots, \mathbf{p}^M$, it is convenient to write down the initial state as a wave function in p and use that $S_p |p\rangle = e^{i\xi p} |p\rangle$. The effect of this correction is shown in Fig. 4.4. Similarly, one can evaluate the average $\langle \Delta_p \rangle = \sum_{\mathbf{p}_{\text{all}}} \mathbb{P}(\mathbf{p}_{\text{all}}) \Delta_p(\mathbf{p}_{\text{all}})$. Note that, if minimizing the run-time of this procedure is crucial (e.g. for feedback in an experiment), the mean phases could be approximated using the mode of the probability distribution in p corresponding to the final state.

While the map between breeding and phase estimation derived in the previous section suggests that $\langle \Delta_p \rangle$ will decrease rapidly with breeding rounds, it is in fact not simple to use this mapping to analytically prove this. The difficulty is that since the phases can vary per round (depending on the homodyne measurement outcomes), arguments which use laws of large numbers, which apply when identical experiments are repeated, are not directly applicable.

In order to understand the outgoing state in terms of the initial squeezing, we note that the final state of the breeding protocol after M rounds consists of applying powers of

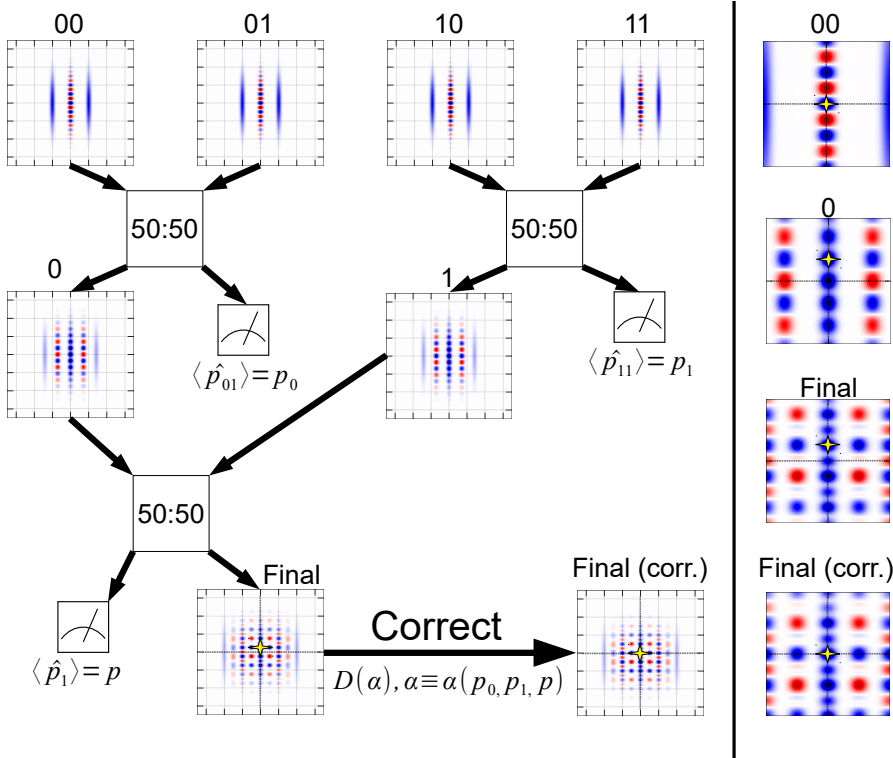


Figure 4.4: Left side: Efficient breeding protocol as proposed in [2, 12], with $M = 2$ rounds but without post-selection. The labeling of modes is according to the scheme introduced in Section 4.2.2: The initial $2^M = 4$ Schrödinger cat states are labeled by the 2-bit strings {00, 01, 10, 11}. Those are put pairwise into beam splitters, resulting in the states and measurement results labeled by the 1-bit strings {0, 1}. The phases and final state of the corresponding phase estimation setup are determined using Eq. (4.7), the correcting displacement is then obtained with Eq. (4.2). Right side: Shown are the Wigner functions of modes {00, 0, Final} and the final state after applying the correction, zoomed in around the origin. The yellow crosses mark the “center” of the state, for a +1 eigenstate of S_p they lie at the origin. Reprinted figure with permission from D. J. Weigand and B. M. Terhal, “Generating grid states from Schrödinger-cat states without postselection”, *Physical Review A* **97**, 022341 (2018). © (2020) by the American Physical Society.

$S_p = D(\xi/\sqrt{2})$ (with phases) to the initial state $|\Phi_0\rangle$ and S_q commutes with S_p . However, the input state is not an *exact* eigenstate of S_q . Furthermore, the full description of the unitary evolution involves the beam-splitter and the measured ancilla modes and the full action does not commute with S_q .

This means that a few steps are required to show that the expectation value of S_q of the output state is close to the expectation value of S_q of the input state. The output state of any breeding protocol will be $|\Psi_{\text{out}}\rangle = A|\Phi_0\rangle$ and $A = \sum_{j=-\infty}^{\infty} \alpha_j S_p^j$ (where the number of non-zero coefficients $\alpha_j \in \mathbb{C}$ is determined by the protocol). We can compute the normalization of $|\Psi_{\text{out}}\rangle$ by writing the initial squeezed state as a wave function in $|q\rangle$:

$$\begin{aligned} \langle \Psi_{\text{out}} | \Psi_{\text{out}} \rangle &= \sum_{j,k=-\infty}^{\infty} \frac{\alpha_j \alpha_k^*}{\sqrt{\pi \Delta^2}} \iint dq dq' e^{-\frac{q^2}{2\Delta^2}} e^{-\frac{(q'-(j-k)\xi)^2}{2\Delta^2}} \langle q | q' \rangle \\ &= \sum_{j,k} \frac{\alpha_j \alpha_k^*}{\sqrt{\pi \Delta^2}} \int dq e^{-\frac{(q-(j-k)\xi/2)^2}{\Delta^2}} e^{-\frac{\xi^2(j-k)^2}{4\Delta^2}} \\ &= \sum_{j,k} \alpha_j \alpha_k^* e^{-\frac{\xi^2(j-k)^2}{4\Delta^2}}. \end{aligned}$$

For small $\Delta \lesssim 0.5$, the last term vanishes for $j \neq k$ (ξ is at least $\sqrt{2\pi}$), i. e. $\sum_j |\alpha_j|^2 \approx \langle \Psi_{\text{out}} | \Psi_{\text{out}} \rangle = 1$. Using the same method one obtains:

$$\begin{aligned} \langle \Psi_{\text{out}} | S_q | \Psi_{\text{out}} \rangle &= \sum_{j,k} \frac{\alpha_j \alpha_k^*}{\sqrt{\pi \Delta^2}} \int dq e^{i\xi q} e^{-\frac{(q-(j-k)\xi/2)^2}{\Delta^2}} e^{-\frac{\xi^2(j-k)^2}{4\Delta^2}}, \\ &= \sum_{j,k} \frac{\alpha_j \alpha_k^*}{\sqrt{\pi \Delta^2}} e^{-\frac{\xi^2(j-k)^2}{4\Delta^2}} e^{-\frac{i(j-k)\xi^2}{2}} \int dq e^{i\xi q} e^{-\frac{q^2}{\Delta^2}}, \\ &= \sum_{j,k} \alpha_j \alpha_k^* e^{-\frac{\xi^2(j-k)^2}{4\Delta^2}} e^{-\frac{i(j-k)\xi^2}{2}} \langle \Phi_0 | S_q | \Phi_0 \rangle \approx \langle \Phi_0 | S_q | \Phi_0 \rangle, \end{aligned}$$

where we used the normalization condition obtained before. This implies that the squeezing in \hat{q} for the final state, $\Delta_q(\Psi_{\text{out}}) \approx \Delta_q(\Phi_0) = \Delta$ for initial squeezing $\Delta \lesssim 0.5$ (which corresponds to large squeezing in q). The effective squeezing parameter of a squeezed Schrödinger cat state $\propto (D(-\sqrt{\pi}/2) + D(\sqrt{\pi}/2))|\Phi_0\rangle$ is $\sqrt{\Delta^2 - \frac{2}{\pi} \ln(\tanh(\frac{\pi}{4\Delta^2}))}$, which differs from a squeezed vacuum state $|\Phi_0\rangle$ by $\mathcal{O}(10^{-17})$ for $\Delta = 0.2$. This is also expected, as $\Delta_q = \Delta$ for a squeezed vacuum state and $\Delta_q \approx \Delta$ for an approximate grid state as defined in [1].

4.3. ANALYTIC DISCUSSION OF BREEDING

In this section, we derive probability bounds for the breeding protocol showing how the effective squeezing parameter changes round-by-round. The known class of approximate grid states, which are described by a perfect grid state to which a Gaussian distribution of shift errors is applied [1], is not closed under a round of breeding, the same holds for squeezed Schrödinger cat states. Thus, analyzing the effect of the breeding

map for many rounds is a nontrivial problem when using either class of states. In this section, we discuss the breeding protocol analytically and derive a class of states that is closed under the breeding operation. This class of states will be used as initial states in Section 4.4 to investigate the asymptotic behavior of breeding.

To this end, we first analyze the action of breeding on a superposition of shifted grid states $|u, v, m\rangle$ (see Eq. (2.13) for details on these states) in Section 4.3.2, and simplify the state obtained after measurement. Then, we show in Section 4.3.3 that the action of breeding on the v shifts is that of a convolution of the ingoing wave functions, and that a Gaussian error model for these shifts is preserved under breeding. There, we also see that the action on the u shifts is that the ingoing wave functions of these shifts are multiplied. Finally in Section 4.3.4, we show that for the u shifts, an error model using the von Mises distribution is preserved under breeding, yielding the states used in Section 4.4.

4.3.1. SCALE-DEPENDENT SHIFTED GRID STATES

Since the breeding protocol changes the spacing of an approximate grid state round-by-round, the spacing of these states is round-dependent. To this end, we first define scale-dependent shifted grid states as

$$|u, v, m\rangle = \frac{\sqrt{s_m \xi}}{2\pi} e^{i \frac{v}{s_m \xi} \hat{p}} e^{i \frac{s_m \xi u}{2\pi} \hat{q}} |\Psi_m\rangle, \quad (4.8)$$

where $u, v \in [-\pi, \pi)$, see also earlier in Section 2.2.2. The parameter s_m is some scale parameter that we will choose below, ξ is the spacing of the final grid state, and $|\Psi_m\rangle \propto \sum_{s=-\infty}^{\infty} |p = s\xi s_m\rangle$. With the choice $s_m = 1, \xi = 2\sqrt{\pi}$, one obtains the shifted code states introduced by Glancy and Knill in the context of the GKP code [20]: The states above can be viewed as an extension of this concept. For any choice of m and $s_m \xi$, it can be verified that the class of states $|u, v, m\rangle$ forms an orthonormal basis of the whole Hilbert space of the oscillator, i. e.

$$\langle u, v, m | u', v', m \rangle = \delta(u - u') \delta(v - v') \quad \text{and} \quad \int_{-\pi}^{\pi} du \int_{-\pi}^{\pi} dv |u, v, m\rangle \langle u, v, m| = \mathbb{1},$$

see Section 2.2.2 for the proof.

If we extend the definition of these basis states so that $u \rightarrow x, v \rightarrow y$ with $x, y \in \mathbb{R}$, then we can observe that $|x + 2\pi, y, m\rangle = |x, y, m\rangle$ and $|x, y \pm 2\pi, m\rangle = e^{\pm i x} |x, y, m\rangle$. In this section, we will only consider states of the form

$$|\Psi\rangle = \int_{-\pi}^{\pi} du \int_{-\pi}^{\pi} dv \Theta(u, v) |u, v, m\rangle,$$

where the function $\Theta(x, y)$ is such that $\Theta(x + 2\pi, y) = \Theta(x, y)$ and $\Theta(x, y \pm 2\pi) = e^{\mp i x} \Theta(x, y)$. For such a choice, we observe that $\Theta(x, y) |x, y, m\rangle$ is 2π -periodic in both arguments, allowing us to write

$$\int_{-\pi}^{\pi} dx \int_{-\pi}^{\pi} dy \Theta(x, y) |x, y, m\rangle = \int_{-\pi+z_x}^{\pi+z_x} dx \int_{-\pi+z_y}^{\pi+z_y} dy \Theta(x, y) |x, y, m\rangle. \quad (4.9)$$

for any $z_x, z_y \in \mathbb{R}$.

For our application in the breeding protocol, we will choose $s_m = \sqrt{2^{m-M}}$ and one can confirm that this choice yields a shifted grid state with spacing ξ for $m = M$. Note that $|\Psi_m\rangle$ is a $+1$ eigenstate of the rescaled operators $S_q^{s_m}$ and $S_p^{2\pi/(\xi^2 s_m)}$, i.e. the spacing of the states is rescaled round by round since each beam-splitter will change the spacing by $\sqrt{2}$. We can see this by writing

$$|\Psi_m\rangle \propto \lim_{\Delta \rightarrow 0} \Pi_{S_q^{s_m}=1} S(1/\Delta) |\text{vac}\rangle, \quad \text{since} \quad \lim_{\Delta \rightarrow 0} S(1/\Delta) |\text{vac}\rangle = |p=0\rangle$$

and $\Pi_{S_q^{s_m}=1} \propto \sum_{t=-\infty}^{\infty} S_q^{t s_m}$ is the projector onto the $+1$ eigenspace of $S_q^{s_m}$.

4.3.2. BREEDING SHIFTED GRID STATES

Recall that the action \mathcal{B} of a beam splitter is given by

$$\begin{aligned} \hat{q}_1 &\rightarrow (\hat{q}_1 - \hat{q}_2)/\sqrt{2}, & \hat{p}_1 &\rightarrow (\hat{p}_1 - \hat{p}_2)/\sqrt{2}, \\ \hat{q}_2 &\rightarrow (\hat{q}_1 + \hat{q}_2)/\sqrt{2}, & \hat{p}_2 &\rightarrow (\hat{p}_1 + \hat{p}_2)/\sqrt{2}, \end{aligned}$$

where mode 1 is the target mode and mode 2 is the control mode (c.f. Eqs. 4.4).

Using conjugation one can see that two shifted grid states are transformed as

$$\begin{aligned} \mathcal{B} |x_1, y_1, m\rangle_1 |x_2, y_2, m\rangle_2 &= \\ &= \mathcal{B} \frac{s_m \xi}{(2\pi)^2} \sum_{s,t} e^{i(y_2(s + \frac{x_2}{2\pi}) + y_1(t + \frac{x_1}{2\pi}))} e^{i\hat{q}_2 \xi s_m (s + \frac{x_2}{2\pi})} e^{i\hat{q}_1 \xi s_m (t + \frac{x_1}{2\pi})} \mathcal{B}^\dagger \mathcal{B} |p=0\rangle_1 |p=0\rangle_2, \\ &= \frac{s_m \xi}{(2\pi)^2} \sum_{s,t} e^{i(y_2(s + \frac{x_2}{2\pi}) + y_1(t + \frac{x_1}{2\pi}))} e^{i\frac{\hat{q}_1 + \hat{q}_2}{\sqrt{2}} \xi s_m (s + \frac{x_2}{2\pi})} e^{i\frac{\hat{q}_1 - \hat{q}_2}{\sqrt{2}} \xi s_m (t + \frac{x_1}{2\pi})} |p=0\rangle_1 |p=0\rangle_2, \\ &= \frac{s_m \xi}{(2\pi)^2} \sum_{s,t} e^{i(y_2(s + \frac{x_2}{2\pi}) + y_1(t + \frac{x_1}{2\pi}))} \left| p = \frac{\xi s_m}{\sqrt{2}} \left(t + s + \frac{x_2 + x_1}{2\pi} \right) \right\rangle_1 \left| p = \frac{\xi s_m}{\sqrt{2}} \left(s - t + \frac{x_2 - x_1}{2\pi} \right) \right\rangle_2. \end{aligned}$$

The invariance of the formal state $|p=0\rangle_1 |p=0\rangle_2$ under beam-splitting can be understood from writing $\lim_{\Delta \rightarrow 0} S(1/\Delta) |\text{vac}\rangle = |p=0\rangle$ and conjugating the squeezing operators by beam-splitters.

Now, we can easily compute the action of a measurement of mode 2 with result p_{out} :

$$\begin{aligned} \langle \hat{p}_2 = p_{\text{out}} | \mathcal{B} |x_1, y_1, m\rangle_1 |x_2, y_2, m\rangle_2 &= \frac{s_m \xi}{(2\pi)^2} \sum_{s,t} e^{i(y_2(s + \frac{x_2}{2\pi}) + y_1(t + \frac{x_1}{2\pi}))} \\ &\times \delta \left(p_{\text{out}} - \frac{\xi s_m}{\sqrt{2}} \left(s - t + \frac{x_2 - x_1}{2\pi} \right) \right) \left| p = \frac{\xi s_m}{\sqrt{2}} \left(t + s + \frac{x_2 + x_1}{2\pi} \right) \right\rangle_1. \end{aligned} \quad (4.10)$$

As a warm-up, we consider the effect of the breeding step on two input modes both in a state of the form

$$|\Psi_{\text{in}}\rangle = \int_{-\pi}^{\pi} du V(u) |u, v, m\rangle,$$

where $V(u)$ is a wave function with normalization $\int_{-\pi}^{\pi} du |V(u)|^2 = 1$ that will be chosen in Section 4.3.4. In order to simplify the notation from now on, we define

$$\tilde{p} = \frac{2\pi p_{\text{out}}}{\xi s_{m+1}}, \quad (4.11)$$

using that $s_{m+1} = \sqrt{2}s_m$. In order to compute the output state $|\Psi_{\text{out}}\rangle$ obtained after breeding two modes with input states of the form $|\Psi_{\text{in}}\rangle$, we transform Eq. (4.10): First, we switch to variables x and y , and then substitute $\tilde{x}_2 = x_2 - 2\tilde{p}$. The output state is then given by

$$|\Psi_{\text{out}}\rangle = \frac{s_m \xi}{(2\pi)^2} \int_{-\pi+2\tilde{p}}^{\pi+2\tilde{p}} d\tilde{x}_2 \int_{-\pi}^{\pi} dx_1 V_1(x_1) V_2(\tilde{x}_2 + 2\tilde{p}) \sum_{s,t} e^{i(y_2(s + \frac{\tilde{x}_2}{2\pi} + \frac{\tilde{p}}{\pi}) + y_1(t + \frac{x_1}{2\pi}))} \\ \times \delta\left(\frac{\xi s_m}{\sqrt{2}}\left(s - t + \frac{\tilde{x}_2 - x_1}{2\pi}\right)\right) \left| p = \frac{\xi s_m}{\sqrt{2}}\left(t + s + \frac{\tilde{x}_2 + x_1 + 2\tilde{p}}{2\pi}\right) \right\rangle_1.$$

We can move the integration region for \tilde{x}_2 back to $[-\pi, \pi)$ as described in Eq. (4.9). Then, note that the Dirac delta distribution will only be non-zero if $s = t$ and $\tilde{x}_2 = x_1$:

First, note that the Dirac delta distribution can only be non-zero if $\frac{\tilde{x}_2 - x_1}{2\pi}$ is integer. In the case where this fraction is an integer k , the delta will be non-zero if and only if $t = s + k$. After moving the integration region for \tilde{x}_2 back, we have $x_i, \tilde{x}_2 \in [-\pi, \pi)$ and therefore $\tilde{x}_2 - x_1 \in (-2\pi, 2\pi)$. Thus, we only need to consider the cases $\tilde{x}_2 = x_1$ and $\tilde{x}_2 - x_1 = \pm 2\pi$. The solutions $\tilde{x}_2 - x_1 = \pm 2\pi$ are a null set: After applying the Dirac delta distribution, the second integral vanishes for these two solutions. Using $\delta(x) = |a|\delta(ax)$ we obtain:

$$|\Psi_{\text{out}}\rangle = \frac{\sqrt{2}}{2\pi} \int_{-\pi}^{\pi} d\tilde{x}_2 \int_{-\pi}^{\pi} dx_1 V_1(x_1) V_2(\tilde{x}_2 + 2\tilde{p}) \\ \times \sum_s e^{i(y_2(s + \frac{\tilde{x}_2}{2\pi} + \frac{\tilde{p}}{\pi}) + y_1(s + \frac{x_1}{2\pi}))} \delta(\tilde{x}_2 - x_1) e^{ip_{\text{out}}\hat{q}} \left| p = \frac{\xi s_m}{\sqrt{2}}\left(2s + \frac{\tilde{x}_2 + x_1}{2\pi}\right) \right\rangle_1 \\ = \frac{\sqrt{2}}{2\pi} \int_{-\pi}^{\pi} dx_1 V_1(x_1) V_2(x_1 + 2\tilde{p}) \sum_s \exp\left(i\left((y_2 + y_1)\left(s + \frac{x_1}{2\pi}\right) + y_2 \frac{\tilde{p}}{\pi}\right)\right) \\ \times e^{ip_{\text{out}}\hat{q}} \left| p = \frac{\xi s_m}{\sqrt{2}}\left(2s + \frac{2x_1}{2\pi}\right) \right\rangle_1. \quad (4.12)$$

4.3.3. CHOICE OF WAVE FUNCTION $\Theta(u, v)$

We now take the input states in both modes with a wave function $\Theta(x, y)$ (obeying the conditions set forth previously), namely we choose

$$\Theta(u, v) = \frac{1}{\mathcal{N}} V(u) \sum_{s=-\infty}^{\infty} e^{ius} G_{s_m \Delta}(v + 2\pi s), \quad (4.13)$$

where $V(u)$ is again the normalized wave function to be chosen in Section 4.3.4, and $G_{s_m \Delta}$ is a Gaussian distribution

$$G_{\Delta}(v) = \frac{1}{\sqrt{\Delta}\sqrt{\pi}} \exp\left(-\frac{v^2}{2\Delta^2}\right).$$

The wave function's dependence on v is thus that of wrapped Gaussian distribution and the e^{ius} factor in Eq. (4.13) is required for the 2π -periodicity of the states as explained

below Eq. (4.8). The normalization constant \mathcal{N} is given by

$$\begin{aligned}\mathcal{N}^2 &= \int_{-\pi}^{\pi} du \int_{-\pi}^{\pi} dv |V(u)|^2 \sum_{s,t=-\infty}^{\infty} e^{iu(s-t)} G_{s_m\Delta}(v+2\pi s) G_{s_m\Delta}(v+2\pi t) \\ &= \int_{-\pi}^{\pi} du |V(u)|^2 \sum_{s,t=-\infty}^{\infty} \frac{1}{2} e^{iu(s-t)} e^{-\frac{\pi^2(s-t)^2}{(s_m\Delta)^2}} \\ &\quad \times \left(\operatorname{erf}\left(\frac{\pi}{s_m\Delta}(s+t+1)\right) - \operatorname{erf}\left(\frac{\pi}{s_m\Delta}(s+t-1)\right) \right) \xrightarrow{s_m\Delta \ll 1} 1.\end{aligned}\quad (4.14)$$

In the limit $s_m\Delta \ll 1$, the exponential $e^{-\frac{\pi^2(s-t)^2}{(s_m\Delta)^2}}$ enforces $s-t=0$, while for the difference of error functions to be non-zero, we need $s+t=0$, hence together one has $s=t=0$. Note that $s_m \in (0, 1]$, i. e. if $\Delta \ll 1$, then also $s_m\Delta \ll 1$.

Using this wave function we can write the input state in one of the modes as

$$\begin{aligned}|\Psi_{\text{in}}\rangle &= \frac{1}{\mathcal{N}} \int_{-\pi}^{\pi} du \int_{-\pi}^{\pi} dv V(u) \sum_{s=-\infty}^{\infty} e^{ius} G_{s_m\Delta}(v+2\pi s) |u, v, m\rangle \\ &= \frac{1}{\mathcal{N}} \int_{-\pi}^{\pi} dx \int_{-\infty}^{\infty} dy V(x) G_{s_m\Delta}(y) |x, y, m\rangle.\end{aligned}$$

We will assume that the Gaussian wave function of both modes has the same variance, and mean equal to 0. This choice will be justified if the outgoing Gaussians only depend on the round m , which we will show below.

From the result for breeding states with arbitrary superpositions of shifts in \hat{p} , see Eq. (4.12), it follows that:

$$\begin{aligned}|\Psi_{\text{out}}\rangle &= \frac{\sqrt{2}}{2\pi\mathcal{N}^2} \int_{-\pi}^{\pi} dx_1 \int_{-\infty}^{\infty} dy_1 \int_{-\infty}^{\infty} dy_2 V_1(x_1) V_2(x_1+2\tilde{p}) G_{s_m\Delta}(y_1) G_{s_m\Delta}(y_2) \\ &\quad \times \sum_s e^{i\left((y_1+y_2)\left(s+\frac{x_1}{2\pi}\right)+y_2\frac{\tilde{p}}{\pi}\right)} e^{ip_{\text{out}}\hat{q}} \left| p = \xi s_{m+1} \left(s + \frac{x_1}{2\pi} \right) \right\rangle \\ &= \frac{\sqrt{2}}{2\pi\mathcal{N}^2} \int_{-\pi}^{\pi} dx_1 \int_{-\infty}^{\infty} dy_1 \int_{-\infty}^{\infty} dy_2 V_1(x_1) V_2(x_1+2\tilde{p}) G_{s_m\Delta}(\tilde{y}-y_2) G_{s_m\Delta}(y_2) \\ &\quad \times \sum_s e^{i\left(\tilde{y}\left(s+\frac{x_1}{2\pi}\right)+y_2\frac{\tilde{p}}{\pi}\right)} e^{ip_{\text{out}}\hat{q}} \left| p = \xi s_{m+1} \left(s + \frac{x_1}{2\pi} \right) \right\rangle \\ &= \frac{\sqrt{2s_{m+1}\Delta\sqrt{\pi}}}{2\pi\mathcal{N}^2} e^{-\frac{p_{\text{out}}^2\Delta^2}{2\xi^2}} \int_{-\pi}^{\pi} dx_1 \int_{-\infty}^{\infty} d\tilde{y} V_1(x_1) V_2(x_1+2\tilde{p}) G_{s_{m+1}\Delta}(\tilde{y}) \\ &\quad \times \sum_s e^{i\left(\tilde{y}\left(s+\frac{x_1}{2\pi}\right)+\tilde{y}\frac{\tilde{p}}{2\pi}\right)} e^{ip_{\text{out}}\hat{q}} \left| p = \xi s_{m+1} \left(s + \frac{x_1}{2\pi} \right) \right\rangle.\end{aligned}$$

Here, we used $s_{m+1} = \sqrt{2}s_m$ and the substitution $\tilde{y} = y_1 + y_2$ to write the integral over y_2 as a *convolution* of Gaussian wave functions. Comparing this state with the definition of shifted grid states, Eq. (4.8), we see that the outgoing state has a “simple” expression in terms of the shifted grid states with extended parameters:

$$|\Psi_{\text{out}}\rangle = \frac{\sqrt{2\Delta\sqrt{\pi}}}{\sqrt{\xi}N^2} e^{-\left(\frac{p_{\text{out}}\Delta}{\xi\sqrt{2}}\right)^2} \int_{-\pi}^{\pi} dx_1 \int_{-\infty}^{\infty} d\tilde{y} V_1(x_1) V_2(x_1+2\tilde{p}) G_{s_{m+1}\Delta}(\tilde{y}) |x_1 + \tilde{p}, \tilde{y}, m+1\rangle.$$

With $\tilde{x} = x_1 + \frac{2\pi p_{\text{out}}}{\xi s_{m+1}}$ and Eq. (4.9), we finally have

$$|\Psi_{\text{out}}\rangle = \frac{\sqrt{2\Delta\sqrt{\pi}}}{\sqrt{\xi}\mathcal{N}^2} e^{-\left(\frac{p_{\text{out}}\Delta}{\xi\sqrt{2}}\right)^2} \int_{-\pi}^{\pi} d\tilde{x} \int_{-\infty}^{\infty} d\tilde{y} V_1(\tilde{x} - \tilde{p}) V_2(\tilde{x} + \tilde{p}) \\ \times G_{s_{m+1}\Delta}(\tilde{y}) |\tilde{x}, \tilde{y}, m+1\rangle \quad (4.15)$$

$$= \frac{\sqrt{2\Delta\sqrt{\pi}}}{\sqrt{\xi}\mathcal{N}^2} e^{-\left(\frac{p_{\text{out}}\Delta}{\xi\sqrt{2}}\right)^2} \int_{-\pi}^{\pi} du \int_{-\pi}^{\pi} dv V_1(u - \tilde{p}) V_2(u + \tilde{p}) \\ \times \sum_{s=-\infty}^{\infty} e^{ius} G_{s_{m+1}\Delta}(v + 2\pi s) |u, v, m+1\rangle \quad (4.16)$$

Hence, we conclude that the outgoing state has the same wave function dependence in v as the ingoing states. The only change is $s_m \rightarrow s_{m+1}$. From this last equation, we can also immediately see the action of breeding on the wave function $V(u)$, i. e. $V(u) \rightarrow V(u + \tilde{p})V(u - \tilde{p})$.

4.3.4. CHOICE FOR WAVE FUNCTION $V(u)$

As can be seen in Eq. (4.16), the output state depends on a product of the form $V_1(u)V_2(u)$. For some choices for the ingoing wave functions, one can simplify $V_1(u)V_2(u) = V_{\text{out}}(u)$, where all V_i are in the same class of functions. One such class of functions is the set of von Mises distributions, which is closed under multiplication. Let

$$V(x - \mu)_{\kappa} = \frac{\exp\left(\frac{\kappa}{2} \cos(x - \mu)\right)}{\sqrt{2\pi I_0(\kappa)}}. \quad (4.17)$$

Assuming a von Mises wave function in u and a wrapped (signed) Gaussian wave function in v , the initial state of the system is thus chosen as

$$|\Psi_{\text{in}}\rangle = \frac{1}{\mathcal{N}} \int_{-\pi}^{\pi} du \int_{-\pi}^{\pi} dv V_{\kappa}(u - \mu) \sum_{s=-\infty}^{\infty} e^{ius} G_{s_m\Delta}(v + 2\pi s) |u, v, m\rangle \\ = \frac{1}{\mathcal{N}} \int_{-\pi}^{\pi} dx \int_{-\infty}^{\infty} dy V_{\kappa}(x - \mu) G_{s_m\Delta}(y) |x, y, m\rangle, \quad (4.18)$$

where $V_{\kappa}(u)$ is the distribution defined in Eq. (4.17). The normalization constant \mathcal{N} has the same form as Eq. (4.14), with the von Mises wave function defined above taking the role of $V(x)$. This is also the initial state used in Eq. (4.20). Using the result for a Gaussian error model in \hat{q} and an arbitrary wave function for \hat{p} , Eq. (4.15), the state after measurement is

$$|\Psi_{\text{out}}\rangle = \frac{\sqrt{2\Delta\sqrt{\pi}}}{\sqrt{\xi}\mathcal{N}_2\mathcal{N}_1} e^{-\left(\frac{p_{\text{out}}\Delta}{\xi\sqrt{2}}\right)^2} \int_{-\pi}^{\pi} d\tilde{x} \int_{-\infty}^{\infty} d\tilde{y} V_{\kappa_2}(\tilde{x} + \tilde{p} - \mu_2) V_{\kappa_1}(\tilde{x} - \tilde{p} - \mu_1) \\ \times G_{s_{m+1}\Delta}(\tilde{y}) |\tilde{x}, \tilde{y}, m+1\rangle, \quad (4.19)$$

where $\mathcal{N}_1, \mathcal{N}_2$ are the normalization constants of the initial state of modes 1 and 2, respectively. This expression can be simplified with the following lemma.

Lemma 4.3.1. *For a product of von Mises wave functions as defined in Eq. (4.17), it holds that*

$$V_{\kappa_1}(x - \mu_1) V_{\kappa_2}(x - \mu_2) = \sqrt{\frac{I_0(\kappa)}{2\pi I_0(\kappa_1) I_0(\kappa_2)}} V_{\kappa}(x - \mu),$$

with

$$\begin{aligned} \mu &= -\arctan 2(\kappa_1 \cos(\mu_1) + \kappa_2 \cos(\mu_2), \kappa_1 \sin(\mu_1) + \kappa_2 \sin(\mu_2)), \\ \kappa^2 &= \kappa_1^2 + \kappa_2^2 + 2\kappa_1 \kappa_2 \cos(\mu_1 - \mu_2). \end{aligned}$$

Proof. We can use the properties of linear combinations of trigonometric functions to show that the set of von Mises distributions is closed under multiplication. We have

$$V(x - \mu_1)_{\kappa_1} V(x - \mu_2)_{\kappa_2} = \frac{\exp\left(\frac{\kappa_1}{2} \cos(x - \mu_1) + \frac{\kappa_2}{2} \cos(x - \mu_2)\right)}{2\pi \sqrt{I_0(\kappa_1) I_0(\kappa_2)}}.$$

For the exponent on the right-hand side, it holds that

$$\begin{aligned} \kappa_1 \cos(x - \mu_1) + \kappa_2 \cos(x - \mu_2) &= \\ &= (\kappa_1 \cos(\mu_1) + \kappa_2 \cos(\mu_2)) \cos(x) + (\kappa_1 \sin(\mu_1) + \kappa_2 \sin(\mu_2)) \sin(x) \\ &= \sqrt{\kappa_1^2 + \kappa_2^2 + 2\kappa_1 \kappa_2 \cos(\mu_1 - \mu_2)} \cos(x - \mu) := \kappa \cos(x - \mu), \end{aligned}$$

with μ, κ as in the claim. In the first step, we used $\cos(x - y) = \cos(x) \cos(y) + \sin(x) \sin(y)$. In the second step, we used $a \cos(x) + b \sin(x) = \sqrt{a^2 + b^2} \cos(x + \arctan 2(a, b))$. \square

Using this lemma, the outgoing state is given by

$$\begin{aligned} |\Psi_{\text{out}}\rangle &= \sqrt{\frac{I_0(\kappa) \Delta}{\sqrt{\pi} I_0(\kappa_1) I_0(\kappa_2) \xi \mathcal{N}_2^2 \mathcal{N}_1^2}} e^{-\frac{p_{\text{out}}^2 \Delta^2}{2\xi^2}} \int_{-\pi}^{\pi} du \int_{-\pi}^{\pi} dv V_{\kappa}(u - \mu) \\ &\quad \times \sum_{s=-\infty}^{\infty} e^{ius} G_{s_{m+1}\Delta}(v + 2\pi s), |u, v, m + 1\rangle, \end{aligned}$$

with

$$\begin{aligned} \mu &= -\arctan 2(\kappa_2 \cos(\mu_2 - \tilde{p}) + \kappa_1 \cos(\mu_1 + \tilde{p}), \kappa_2 \sin(\mu_2 - \tilde{p}) + \kappa_1 \sin(\mu_1 + \tilde{p})), \\ \kappa^2 &= \kappa_2^2 + \kappa_1^2 + 2\kappa_2 \kappa_1 \cos(\mu_2 - \mu_1 - 2\tilde{p}). \end{aligned}$$

This state is not yet normalized. However, we can use Eq. (4.14) to obtain \mathcal{N}_{out} and both normalize this state and obtain the probability distribution of measurement results p_{out} .

4.4. ASYMPTOTIC BEHAVIOR

In general, a basis of shifted grid states can be used to write down an approximate code state as a Gaussian superposition of states with different shifts [1, 9]. Here, we will similarly use these states but the filter for the quadrature on which we apply the breeding will

not be Gaussian but determined by a von Mises probability distribution. We thus define the class of approximate shifted grid states (for general ξ) as:

$$|V_{\kappa,\mu,m}\rangle := \frac{1}{\mathcal{N}} \int_{-\pi}^{\pi} du \int_{-\pi}^{\pi} dv V(u-\mu)_{\kappa} \sum_{s=-\infty}^{\infty} e^{i u s} G(v+2\pi s)_{s_m \Delta} |u, v, m\rangle, \quad (4.20)$$

$$V(u-\mu)_{\kappa} := \frac{1}{\sqrt{2\pi} I_0(\kappa)} \exp\left(\frac{\kappa}{2} \cos(u-\mu)\right),$$

$$G(v)_{\sigma} := \frac{1}{\sqrt{\sigma\sqrt{\pi}}} \exp\left(-\frac{v^2}{2\sigma^2}\right). \quad (4.21)$$

In the limit of large initial squeezing $\Delta \ll 1$, the normalization constant \mathcal{N} goes to 1. Note that $\mathbb{P}_{\sigma}(v) = G(v)_{\sigma}^2$ is a Gaussian distribution with mean 0 and standard deviation $\sigma/\sqrt{2}$ so that when $m = M$, the standard deviation of $\mathbb{P}_{\Delta s_m}(v)$ is $\Delta/\sqrt{2}$. The choice of probability distribution on u and v is different because the breeding protocol acts differently on the \hat{p} and \hat{q} quadratures of the initial states. This choice ensures that the class of states $|V_{\kappa,\mu,m}\rangle$ is closed under breeding, see Eq. (4.23). The probability distribution $\mathbb{P}_{\kappa}(u-\mu) = V(u-\mu)_{\kappa}^2$ is the von Mises distribution and $I_{\nu}(\kappa)$ is the modified Bessel function of the first kind of order ν . The von Mises distribution $\mathbb{P}_{\kappa}(u-\mu)$ which models a Gaussian distribution for a circular phase variable u has mean μ . In the limit $\kappa \gg 1$, the probability distribution becomes Gaussian by approximating $\exp(\kappa \cos(u-\mu)) \approx \exp(-\kappa(u-\mu)^2/2) \exp(\kappa)$ with standard deviation $1/\sqrt{\kappa}$.

The index $m = 0, \dots, M$ will refer to the number of breeding rounds applied to being the initial state, with $m = 0$ the initial state and $m = M, s_M = 1$ the final state. Note that the shift error distribution in v gets rescaled each round: The standard deviation of $G(v)_{\Delta, m=0}^2$ is increasing in each round, but given a v , the shift induced in each round in Eq. (4.8) gets smaller, so that effectively the spread in p stays the same. Thus, $\Delta_q \approx \Delta$ where Δ is the initial squeezing.

For the approximate state with $m = M$, i. e. $|V_{\kappa,\mu,M}\rangle$, the mean phase θ_p is simply the mean μ of the distribution while the effective squeezing parameter Δ_p equals

$$\Delta_p = \sqrt{\ln(I_0^2(\kappa)/I_1^2(\kappa))/\pi}, \quad (4.22)$$

which for large κ becomes $1/\sqrt{\pi\kappa}$, hence directly connecting to the standard deviation of the Gaussian distribution.

Using the formula for linear combinations of trigonometric functions with a phase shift, one can show that the distribution over u of the outgoing state after a round of breeding is again a von Mises distribution (see e. g. [21, 22] in the context of the convolution of von Mises distributions). Using the convolution property of Gaussian distributions, one can show the same for the v shifts. Combining these two properties, one can show that a round of breeding with measurement outcome p_{out} maps two input states

of this form with label m onto an output state of the same form with label $m + 1$:

$$\begin{aligned} |V_{\kappa_1, \mu_1, m}\rangle |V_{\kappa_2, \mu_2, m}\rangle &\xrightarrow{\text{breeding}} |V_{\kappa_{\text{out}}, \mu_{\text{out}}, m+1}\rangle, \\ \kappa_{\text{out}}^2 &= \kappa_1^2 + \kappa_2^2 + 2\kappa_1\kappa_2 \cos(\mu_1 - \mu_2 - 2\tilde{p}), \\ \mu_{\text{out}} &= -\arctan 2[\kappa_1 \cos(\mu_1 - \tilde{p}) + \kappa_2 \cos(\mu_2 + \tilde{p}) \\ &\quad, \kappa_1 \sin(\mu_1 - \tilde{p}) + \kappa_2 \sin(\mu_2 + \tilde{p})], \end{aligned} \quad (4.23)$$

with $\tilde{p} = \frac{2\pi}{\xi s_{m+1}} p_{\text{out}}$. The details of this derivation can be found in Section 4.3.

Thus, if the two states fed into round m have the error model of Eq. (4.20), the outgoing state will be of the same type, with new parameters $\kappa_{\text{out}}, \mu_{\text{out}}$ which depend on measurement outcome p_{out} and the round m . Since the ingoing states are normalized, the probability of finding outcome p_{out} can be obtained by evaluating the norm of the outgoing state, see Section 4.3, and we obtain the oscillatory function

$$\mathbb{P}(p_{\text{out}}) = \frac{\Delta I_0(\kappa_{\text{out}}) \mathcal{N}_{\text{out}}^2}{\sqrt{\pi} \xi I_0(\kappa_1) I_0(\kappa_2) \mathcal{N}_1^2 \mathcal{N}_2^2} e^{-\frac{p_{\text{out}}^2 \Delta^2}{\xi^2}}. \quad (4.24)$$

Defining the variable $x = \mu_1 - \mu_2 - 2\tilde{p} \bmod 2\pi$ gives a concise description of the effect of one breeding round. The probability $\mathbb{P}(x)$ can be simplified in the limit of large initial squeezing, $s_m \Delta \ll 1$ from Eq. (4.24). Since x is 2π -periodic, we can use that the limit of a wrapped normal distribution with large variance is simply a circular uniform density of $1/(2\pi)$. Together with the fact that the normalization constants \mathcal{N} all go to 1 for large initial squeezing, one obtains

$$\kappa_{\text{out}}(x) = \sqrt{\kappa_1^2 + \kappa_2^2 + 2\kappa_1\kappa_2 \cos(x)} = (\kappa_1 + \kappa_2) \lambda, \quad (4.25)$$

$$\mathbb{P}(x) = \frac{I_0(\kappa_{\text{out}}(x))}{2\pi I_0(\kappa_1) I_0(\kappa_2)}, \quad (4.26)$$

where we defined $\lambda := \lambda(x, \kappa_1, \kappa_2)$ with $0 \leq \lambda \leq 1$.

Not surprisingly the growth of κ (or shrinking of Δ_p) with the number of rounds is upper bounded as $\kappa_M \leq 2^M \kappa_0$ for any protocol with M rounds and initial states all with equal κ_0 .

To get insight into the probabilistic behavior, we would like to bound the probability so that $\lambda \leq 1 - \epsilon$ for some ϵ , assuming $\kappa_1 \geq 1/(1 - \epsilon)$ and $\kappa_2 \geq 1/(1 - \epsilon)$ in a given round m .

Let $\mathbb{A} = \{x | \lambda \leq 1 - \epsilon\}$, i. e. the set of all events for which $\lambda \leq 1 - \epsilon$. Then:

$$\begin{aligned} \mathbb{P}(\lambda \leq 1 - \epsilon) &= \int_{\mathbb{A}} dx \frac{I_0((\kappa_1 + \kappa_2) \lambda)}{2\pi I_0(\kappa_1) I_0(\kappa_2)}, \\ &\leq \frac{I_0((\kappa_1 + \kappa_2)(1 - \epsilon))}{I_0(\kappa_1) I_0(\kappa_2)}, \end{aligned}$$

where we used that $I_0(x) < I_0(y)$ for $x < y$.

It has been shown by Pal'tsev that $\frac{1}{\sqrt{2\pi\kappa}} e^{\kappa - \frac{1}{2\kappa}} \leq I_0(\kappa) \leq \frac{1}{\sqrt{2\pi\kappa}} e^{\kappa + \frac{1}{2\kappa}}$, where the lower bound holds for $\kappa > 0$ and the upper bound was only proved for $\kappa > (\sqrt{7} + 2)/3$ [23]. The range for the upper bound is limited because Pal'tsev derived the bounds for $I_\nu(\kappa)$

with $\nu, \kappa \in \mathbb{R}_0^+$. In the special case of $I_0(\kappa)$, it is simple to show that the bound holds for all $\kappa > 0$: $\frac{1}{\sqrt{2\pi\kappa}}e^{\kappa + \frac{1}{2\kappa}}$ is minimal for $\kappa = 1$ and $I_0(\kappa), 0 \leq \kappa \leq (\sqrt{7} + 2)/3$ is maximal for $\kappa = (\sqrt{7} + 2)/3$. The bound holds because $\frac{1}{\sqrt{2\pi}}e^{\frac{3}{2}} > I_0((\sqrt{7} + 2)/3)$. Using these bounds, we get

$$\mathbb{P}(\kappa_{\text{out}} \geq (\kappa_1 + \kappa_2)(1 - \epsilon)) \geq \delta. \quad (4.27)$$

with

$$\delta \equiv 1 - \sqrt{\frac{2\pi\kappa_1\kappa_2}{(\kappa_1 + \kappa_2)(1 - \epsilon)}} \exp\left(-\epsilon(\kappa_1 + \kappa_2 + 1) + \frac{5}{4}\right). \quad (4.28)$$

For any choice of $\epsilon > 0$, this probability is exponentially close to 1 for large κ_1 or κ_2 . As a simple example of this bound one can take $\kappa_1 = \kappa_2 = \kappa_{\text{in}}$ and $\epsilon = 1/2$. Then we have

$$\mathbb{P}(\kappa_{\text{out}} \geq \kappa_{\text{in}}) \geq 1 - \sqrt{2\pi\kappa_{\text{in}}} \exp\left(-\kappa_{\text{in}} + \frac{3}{4}\right).$$

What we see in these bounds is that for sufficiently large κ_{in} , the protocol produces states with larger κ_{out} with high probability. For example, the probability that $\kappa_{\text{out}} \geq \kappa_{\text{in}}$ is at least 0.92 for $\kappa_{\text{in}} = 5$ (squeezing parameter roughly $\Delta \approx 0.25$). For $\kappa_{\text{in}} = 10$, the probability that $\kappa_{\text{out}} \geq \frac{3}{2}\kappa_{\text{in}}$ is at least 0.88.

Alternatively, one can phrase Eq. (4.27) for large κ , hence Gaussian-distributed states, in terms of the variance of the Gaussian distribution of shift errors: In this case, the variance of the outgoing state obeys with a probability larger than δ in Eq. (4.28):

$$\text{Var}_{\text{out}} \leq \frac{\text{Var}_{1,\text{in}} \text{Var}_{2,\text{in}}}{(1 - \epsilon)(\text{Var}_{1,\text{in}} + \text{Var}_{2,\text{in}})}. \quad (4.29)$$

For a grid state with Gaussian-distributed shift errors and spacing ξ , one has $\Delta_p \approx \text{Var}/\xi$ so we can see how Eq. (4.29) expresses the stochastic improvement of the effective squeezing parameter per round.

These bounds are not tight, the probability δ scales more favorably in practice than these bounds would suggest. In the next section, we examine how the mapping of the von Mises distributed states works out numerically as compared to an actual simulation of the protocol with squeezed cat states.

4.5. SIMULATION

To demonstrate the use of classical post-processing, we simulate the breeding of a grid state numerically. All the simulated breeding protocols aim to generate an eigenstate of $S_p = D(\sqrt{\pi})$, using M rounds with the efficient breeding protocol. The breeding is simulated by sampling each measurement result randomly from the state generated by the previous rounds. This is done for protocols with $M = 0, \dots, 6$ rounds, each protocol leading to an approximate grid state with the required spacing $\sqrt{2\pi}$ ($M = 0$ means just having a squeezed cat state). More details on the numerical simulations can be found in Appendix A.1.2.

In Fig. 4.5, we show the mean and standard deviation of the effective squeezing parameter Δ_p over 1000 simulated breeding experiments with M rounds. In this figure, the

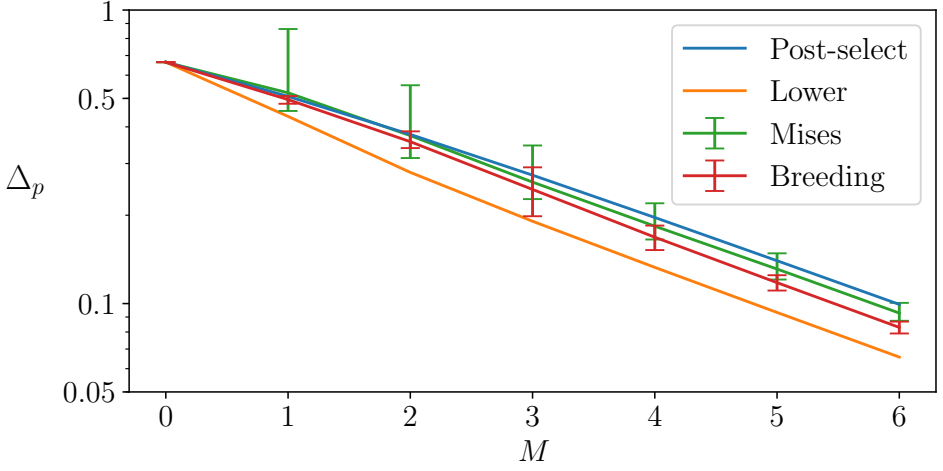


Figure 4.5: Simulated breeding of a sensor state ($S_p = D(\sqrt{\pi})$) with initial squeezing $\Delta = 0.2$. Shown is the (dimensionless) effective squeezing parameter Δ_p (averaged over the homodyne measurement outcomes) versus the number of rounds M of the protocol. “Post-select” refers to the protocol by Vasconcelos *et al.* [2], with squeezed Schrödinger cat states as input and post-selected onto the result $p_i = 0$ for all measurements. “Breeding” refers to the efficient breeding protocol without post-selection. “Mises” is the same efficient breeding protocol, but with von Mises distributed initial states, see Eq. (4.20). The error bounds in both Mises and Breeding are asymmetric, i. e. both the variance of all the data above the mean as well as the variance on all the data below the mean are plotted separately. “Lower” is the lower bound for the effective squeezing parameter, namely at round M $\Delta(\kappa_M) = \Delta(2^M \kappa_0)$ where $\Delta(\kappa)$ is given in Eq. (4.22). Reprinted figure with permission from D. J. Weigand and B. M. Terhal, “Generating grid states from Schrödinger-cat states without postselection”, *Physical Review A* **97**, 022341 (2018). © (2020) by the American Physical Society.

line “Breeding” shows the efficient breeding protocol using finitely-squeezed Schrödinger cat states, with $\Delta_q \approx \Delta = 0.2$. This corresponds to states with $\bar{n} \approx 2^M \pi/2 + 25$ photons in all rounds (where 25 is the contribution from initial squeezing by $S(\Delta)$).

In addition, we simulate the same protocol using the von Mises states (with infinite squeezing, corresponding to $\lim_{\Delta \rightarrow 0}$ in Eq. (4.20)) as initial states, starting at a κ and $\mu = 0$ which gives the same Δ_p as the squeezed cat states in the real protocol. For comparison, we also show the effective squeezing achieved by post-selecting onto $p = 0$ (“Post-select”) and the lower bound (“Lower”) on the decrease in the squeezing parameter for the von Mises states as follows from $\kappa_{\text{out}} \leq \kappa_1 + \kappa_2$. Since the lower bound has been derived only for von Mises distributed states and not for squeezed cat states as initial states, it does not necessarily hold for the latter. However, it gives a good estimate for the asymptotic behavior because grid states and the von Mises distributed states get arbitrarily close for small Δ_p .

As can be seen, the effective squeezing that is achieved on average is lower both for Breeding and Mises than for the post-selected protocol. Furthermore, the two lines are almost parallel after some rounds, showing that the von Mises error model is a good approximation after a small number of rounds. All lines show similar scaling with M which we asymptotically expect to be $\sim 2^{-M}$ (this scaling is hard to verify for $M \leq 6$).

4.6. DISCUSSION

In this chapter, we have shown that classical post-processing, combined with the breeding protocol by Vasconcelos *et al.* [2] yields an efficient method to generate grid states. By providing a map between breeding and phase estimation, we have argued that any state generated by breeding results in an approximate eigenstate of the commuting displacement operators, i. e. a grid state with an additional known displacement. We have introduced a new class of approximate grid states which are mapped onto themselves by the application of breeding and allow one to bound the success of the stochastic process implemented by breeding. In numerical simulations, we could confirm that the protocol discussed in this chapter generates grid states reliably, showing scaling close to the asymptotic behavior, even for a small number of rounds.

As we have observed, the action of each round of beam-splitting reduces the spacing of the grid, requiring one to use cat states with large spacing at the beginning of the protocol. An alternative solution is to squeeze the outgoing mode after each beam-splitter so one does not lose a $\sqrt{2}$ factor in each round, see e. g. the use of beam-splitting and $\sqrt{2}$ -squeezing in [20]. However, this precisely counteracts the initial squeezing in the q -quadrature, hence requires more initial squeezing by Δ . We thus expect that the average number of photons in the initial squeezed cat states scales the same in this alternative protocol, making it a slightly different but not necessarily better alternative.

In any real set-up, the measurement of the p -quadrature will have some variance, determined for example by the duration of the measurement. Using the mapping onto phase estimation, one can understand this as a spread or uncertainty in the circuit which has been applied to the state, leading to uncertainty of an estimate for the eigenvalue phase. In the efficient breeding protocol, the spread in p also leads to the preparation of a noisy state which contains additional shift or displacement errors.

While generating optical squeezed Schrödinger cat states on demand is a hard task, squeezed cat states with sufficient amplitude to generate the sensor state have been experimentally demonstrated in [13, 24]. The amplitudes of cat states demonstrated there are sufficiently large for 1–2 rounds of breeding with beam splitters only. Multiple rounds could be possibly achieved using additional squeezing in between rounds as suggested in the previous paragraph above. It might also be of interest to analyze the concrete implementation of this scheme for microwave cavities coupled to superconducting qubits where all components, i. e. the preparation of cat states [25, 26], beam-splitters, and homodyne measurement read-out are readily available. The scheme would lend itself well to a set-up in which cat states are prepared in microwave cavities and are then released [27, 28] onto transmission lines which couple via beam-splitters and allow for homodyne read-out.

ACKNOWLEDGEMENTS

We would like to thank Kasper Duivenvoorden and Christophe Vuillot for useful discussions and acknowledge support through the EU via the ERC GRANT EQEC. This research was supported in part by Perimeter Institute for Theoretical Physics. Research at Perimeter Institute is supported by the Government of Canada through Industry Canada and by the Province of Ontario through the Ministry of Economic Development & Innovation.

REFERENCES

- [1] D. Gottesman, A. Kitaev, and J. Preskill, “Encoding a qubit in an oscillator”, *Physical Review A* **64**, 012310 (2001).
- [2] H. M. Vasconcelos, L. Sanz, and S. Glancy, “All-optical generation of states for “Encoding a qubit in an oscillator””, *Optics Letters* **35**, 3261 (2010).
- [3] D. J. Weigand and B. M. Terhal, “Generating grid states from Schrödinger-cat states without postselection”, *Physical Review A* **97**, 022341 (2018).
- [4] N. C. Menicucci, “Fault-tolerant measurement-based quantum computing with continuous-variable cluster states”, *Physical Review Letters* **112**, 120504, 120504 (2014).
- [5] S. Pirandola, S. Mancini, D. Vitali, and P. Tombesi, “Constructing finite-dimensional codes with optical continuous variables”, *Europhysics Letters* **68**, 323 (2004).
- [6] B. C. Travaglione and G. J. Milburn, “Preparing encoded states in an oscillator”, *Physical Review A* **66**, 052322 (2002).
- [7] K. R. Motes, B. Q. Baragiola, A. Gilchrist, and N. C. Menicucci, “Encoding qubits into oscillators with atomic ensembles and squeezed light”, *Physical Review A* **95**, 053819 (2017).
- [8] D. V. Sychev, A. E. Ulanov, A. A. Pushkina, M. W. Richards, I. A. Fedorov, and A. I. Lvovsky, “Enlargement of optical Schrödinger’s cat states”, *Nature Photonics* **11**, 379 (2016).
- [9] B. M. Terhal and D. J. Weigand, “Encoding a qubit into a cavity mode in circuit QED using phase estimation”, *Physical Review A* **93**, 012315 (2016).
- [10] C. Flühmann, T. L. Nguyen, M. Marinelli, V. Negnevitsky, K. Mehta, and J. P. Home, “Encoding a qubit in a trapped-ion mechanical oscillator”, *Nature* **566**, 513 (2019).
- [11] D. Kienzler, H.-Y. Lo, V. Negnevitsky, C. Flühmann, M. Marinelli, and J. P. Home, “Quantum harmonic oscillator state control in a squeezed Fock basis”, *Physical Review Letters* **119**, 033602 (2017).
- [12] J. Etesse, R. Blandino, B. Kanseri, and R. Tualle-Brouri, “Proposal for a loophole-free violation of Bell’s inequalities with a set of single photons and homodyne measurements”, *New Journal of Physics* **16**, 053001, 053001 (2014).
- [13] J. Etesse, M. Bouillard, B. Kanseri, and R. Tualle-Brouri, “Experimental generation of squeezed cat states with an operation allowing iterative growth”, *Physical Review Letters* **114**, 193602 (2015).
- [14] K. Duivenvoorden, B. M. Terhal, and D. J. Weigand, “Single-mode displacement sensor”, *Physical Review A* **95**, 012305 (2017).
- [15] H. Wiseman and G. Milburn, *Quantum measurement and control* (Cambridge University Press, Cambridge, 2010).
- [16] K. M. Svore, M. B. Hastings, and M. Freedman, “Faster phase estimation”, *Quantum Information and Computation* **14**, 306 (2014).

- [17] M. Nielsen and I. Chuang, *Quantum computation and quantum information*, Cambridge Series on Information and the Natural Sciences (Cambridge University Press, 2000).
- [18] A. Y. Kitaev, “Quantum measurements and the Abelian stabilizer problem”, Nov. 1995.
- [19] D. W. Berry, H. M. Wiseman, and J. K. Breslin, “Optimal input states and feedback for interferometric phase estimation”, [Physical Review A](#) **63**, 053804 (2001).
- [20] S. Glancy and E. Knill, “Error analysis for encoding a qubit in an oscillator”, [Physical Review A](#) **73**, 012325 (2006).
- [21] K. Mardia, Z. Birnbaum, and E. Lukacs, *Statistics of directional data* (Elsevier Science, 2014).
- [22] S. R. Jammalamadaka and A. Sengupta, *Topics in circular statistics* (World Scientific, 2001).
- [23] B. V. Pal’tsev, “Two-sided bounds uniform in the real argument and the index for modified Bessel functions”, [Mathematical Notes](#) **65**, 571 (1999).
- [24] K. Huang, H. L. Jeannic, J. Ruadel, V. Verma, M. Shaw, F. Marsili, S. Nam, E. Wu, H. Zeng, Y.-C. Jeong, R. Filip, O. Morin, and J. Laurat, “Optical synthesis of large-amplitude squeezed coherent-state superpositions with minimal resources”, [Physical Review Letters](#) **115**, 023602, 023602 (2015).
- [25] B. Vlastakis, G. Kirchmair, Z. Leghtas, S. E. Nigg, L. Frunzio, S. M. Girvin, M. Mirrahimi, M. H. Devoret, and R. J. Schoelkopf, “Deterministically encoding quantum information using 100-photon Schrödinger cat states”, [Science](#) **342**, 607 (2013).
- [26] N. Ofek, A. Petrenko, R. Heeres, P. Reinhold, Z. Leghtas, B. Vlastakis, Y. Liu, L. Frunzio, S. M. Girvin, L. Jiang, M. Mirrahimi, M. H. Devoret, and R. J. Schoelkopf, “Extending the lifetime of a quantum bit with error correction in superconducting circuits”, [Nature](#) **536**, 441 (2016).
- [27] W. Pfaff, C. J. Axline, L. D. Burkhardt, U. Vool, P. Reinhold, L. Frunzio, L. Jiang, M. H. Devoret, and R. J. Schoelkopf, “Controlled release of multiphoton quantum states from a microwave cavity memory”, [Nature Physics](#) **13**, 882 (2016).
- [28] Y. Yin, Y. Chen, D. Sank, P. J. J. O’Malley, T. C. White, R. Barends, J. Kelly, E. Lucero, M. Mariantoni, A. Megrant, C. Neill, A. Vainsencher, J. Wenner, A. N. Korotkov, A. N. Cleland, and J. M. Martinis, “Catch and release of microwave photon states”, [Physical Review Letters](#) **110**, 107001 (2013).

5

REALIZING MODULAR QUADRATURE MEASUREMENTS VIA A TUNABLE PHOTON-PRESSURE COUPLING IN CIRCUIT-QED

One of the most direct preparations of a Gottesman-Kitaev-Preskill qubit in an oscillator uses a tunable photon-pressure (also called optomechanical) coupling of the form $\hat{q}\hat{b}^\dagger\hat{b}$, enabling to imprint the modular value of the position \hat{q} of one oscillator onto the state of an ancilla oscillator. We analyze the practical feasibility of executing such modular quadrature measurements in a parametric circuit-QED realization of this coupling. We provide estimates for the expected GKP squeezing induced by the protocol and discuss the effect of photon loss and other errors on the resulting squeezing.

This chapter has been published with minor differences in D. J. Weigand and B. M. Terhal, “Realizing modular quadrature measurements via a tunable photon-pressure coupling in circuit QED”, [Physical Review A](#) **101**, 053840 (2020).

BOSONIC quantum error correction encoding quantum information into oscillator space(s) has gained much experimental interest in the last few years (e. g. [2–7]). A good reason to use a single oscillator instead of multiple qubits to encode quantum information redundantly is that control, manipulation, and fabrication of a single oscillator can be easier than that of multiple oscillators or qubits. In other words, bosonic error correction can be a hardware-efficient way [8] of producing novel qubits which hopefully have longer coherence versus gate times than current popular members of the qubit family, such as the transmon qubit in superconducting devices. The GKP code [9] is a promising code for encoding a qubit into a single oscillator. It has the ability to correct small shifts in phase space, but has also been shown to be very competitive, as compared to other code contenders, with respect to photon loss errors [10, 11]. For an encoded qubit such as the GKP qubit, important aspects of its performance will be determined by the ability to reliably prepare or measure the qubit in the Z and X -basis, perform single- and two-qubit gates on it (CNOT, Hadamard and T gates), as well as execute quantum error correction in a fault-tolerant manner. Theoretical methods and circuits to obtain these components have been discussed, for example, in [9, 12, 13] and [14].

In particular, as the GKP qubit states are highly non-classical “grid” states, one can ask about the best method to prepare such states from the vacuum, given a coupling with an ancilla system which is subsequently measured. The original GKP paper [9] briefly suggested that a photon-pressure coupling between the target oscillator — in which the state is to be prepared — and an ancilla oscillator would be useful in this respect. Through such an interaction, the ancilla oscillator acquires a frequency shift which depends on the quadrature $\hat{q}_T = \frac{1}{\sqrt{2}}(\hat{b}_T + \hat{b}_T^\dagger)$ of the target oscillator T . Instead of measuring this frequency shift, the aim is then to measure just the effective rotation that it induces on an initial state in the ancilla oscillator after a specific interaction time. Eigenvalues for \hat{q} which differ in the ancilla oscillator state being rotated by a full period are thus not distinguished. This means that the interaction can be used to realize modular measurements of \hat{q} and \hat{p} . Such modular quadrature measurements commute when the product of the moduli is a multiple of 2π . It is precisely these modular quadrature measurements which are required to prepare a GKP qubit: They can also be used to stabilize a GKP qubit [5] or perform quantum error correction.

Modular quadrature measurements [15] are of fundamental interest since commuting quadrature measurements allow one to measure both quadratures without the fundamental Heisenberg uncertainty, with possible applications in displacement sensing in the microwave domain [16]. The use of such modular variables directly gives rise to a mixed position-momentum representation of a state in phase space: Zak first formulated this idea, giving a mixed momentum-position state of electrons in solids, see the review [17] and references therein.

In this chapter, we present a circuit-QED setup for coupling two (close to harmonic) oscillators via a tunable photon-pressure coupling with the aim of realizing a modular quadrature measurement in one of the oscillators, see Section 5.3. This measurement requires a full measurement of the ancilla oscillator state, which in circuit-QED can be obtained by releasing this state, via a lossy oscillator, to a transmission line where the signal gets amplified and finally read-out at room temperature. In Section 5.3.4, we briefly discuss previous work on such release or “switch” mechanism which can be turned on

and off to high approximation. Prior to this, we provide an overview of our modular quadrature measurement scheme in Section 5.2. Other and related means to obtain a photon-pressure coupling in circuit-QED are reviewed in Section 5.3.1.

In Section 5.5, we estimate the expected performance of the modular quadrature measurement: This is expressed in terms of how much squeezing in a GKP qubit can be obtained through this measurement. The squeezing effectively captures how close a state is to an eigenstate of the operator which is measured. The aim here is to do a strong modular quadrature measurement, unlike some of the previous work [4, 5, 13] in which the measurement is built up from a sequence of weak measurements via coupling to ancilla qubits. In the latter approach, the strong measurement — which is effectively a phase estimation or eigenvalue measurement of a unitary displacement operator — is obtained through a sequence of weak ancilla qubit measurements, each contributing at most 1 bit of phase information. The strength of the modular quadrature measurement proposed in this chapter will be governed by the number of photons in the ancilla oscillator used to perform the measurement: the more photons, the stronger the measurement.

We will compare our new proposal with a scheme of sequential measurements [13] using a transmon qubit [5] or Kerr-cat qubit [6, 18] in Section 5.8.2, also with respect to error feedback to the target oscillator. As the preparation protocol will inevitably suffer from imperfections, we discuss several noise mechanisms and their effect in Section 5.8. We end the chapter with a final discussion in Section 5.9, summarizing our findings.

5.1. PRELIMINARIES

This section collects a few conventions and the definition of the GKP code. We use $\hat{q} = \frac{1}{\sqrt{2}}(\hat{a} + \hat{a}^\dagger)$ and $\hat{p} = \frac{i}{\sqrt{2}}(\hat{a}^\dagger - \hat{a})$ so that $[\hat{q}, \hat{p}] = i\mathbb{1}$.¹ Phase space displacements (translations) are denoted, in standard form, as $D(\alpha) = \exp(\alpha\hat{a}^\dagger - \alpha^*\hat{a})$.

The (square) GKP code is defined by two commuting code stabilizers equal to $S_q = \exp(i2\sqrt{\pi}\hat{q})$ and $S_p = \exp(-i2\sqrt{\pi}\hat{p})$. These operators act as shift or displacement operators in phase-space, that is $S_q|p\rangle = |p + 2\sqrt{\pi}\rangle$ and $S_p|q\rangle = |q + 2\sqrt{\pi}\rangle$. States which have eigenvalue 1 with respect to these operators are thus invariant under these translations in phase space. There are two operators $X = \exp(-i\sqrt{\pi}\hat{p})$ and $Z = \exp(i\sqrt{\pi}\hat{q})$ which both commute with S_p and S_q , while $XZ = -ZX$ and hence they are the logical Pauli operators — equal to half-stabilizer shifts — of the encoded qubit. Note that the operators S_p, S_q, Z and X only square to the identity in the code space. Measuring the eigenvalue of a unitary operator such as S_q is equivalent to measuring the value for q modulo $\sqrt{\pi}$, as all values $q = q_{\text{meas}} + k\sqrt{\pi}$ for $k \in \mathbb{Z}$ give the same eigenvalue $\exp(i2\sqrt{\pi}q_{\text{meas}})$ for S_q . In different words, a modular quadrature measurement is the measurement of the eigenvalue of a unitary displacement operator.

Since the eigenvalue of a unitary operator is a phase, the phase variance of the post-measurement state captures how precisely the eigenvalue is measured. This phase variance or uncertainty is expressed by effective squeezing parameters, one for the mea-

¹In some texts, the quadrature operators are defined as $\hat{X} = \frac{1}{2}(\hat{a} + \hat{a}^\dagger)$ and $\hat{P} = \frac{i}{2}(\hat{a}^\dagger - \hat{a})$ instead, see e.g. [19]. The latter convention has the advantage of connecting directly to the real and imaginary part of a coherent state $|\alpha\rangle$, while our choice is used by [9] so we adhere to this convention.

surement of S_p , and one for the measurement of S_q . These squeezing parameters can be chosen (see details and relation with Holevo phase and regular quadrature variance in [16] and Section 2.3.4) as

$$\begin{aligned}\Delta_p &= \Delta_p(\rho) = \sqrt{\frac{1}{2\pi} \ln \left(\frac{1}{|\text{Tr}(S_p \rho)|^2} \right)}, \\ \Delta_q &= \Delta_q(\rho) = \sqrt{\frac{1}{2\pi} \ln \left(\frac{1}{|\text{Tr}(S_q \rho)|^2} \right)}.\end{aligned}\tag{5.1}$$

To get some intuition, note that $0 \leq |\text{Tr}(S_q \rho)| \leq 1$ in general. If ρ is an eigenstate with a particular eigenvalue for S_q , we have $|\text{Tr}(S_q \rho)| = 1$. If ρ is a superposition of many eigenvalues of S_q , e.g. a momentum eigenstate $|p\rangle$, we have $|\text{Tr}(S_q \rho)| = 0$. Thus, $|\text{Tr}(S_q \rho)|$ expresses the *sharpness* or concentration of ρ around an S_q eigenstate.

Classically, the topic of circular statistics is well-established, see e.g. [20]: For a probability distribution $\mathbb{P}(\theta)$ over an angle $\theta \in [0, 2\pi)$, the circular standard deviation is defined as $\sqrt{-2 \ln(|\int d\theta \mathbb{P}(\theta) \exp(i\theta)|)}$. The squeezing parameters in Eqs. 5.1 are thus a direct application of the circular standard deviation. With the convention in Eqs. 5.1, the vacuum state has $\Delta_p = \Delta_q = 1$ showing that it is not squeezed. A Δ -squeezed vacuum state (in q) has variance $\langle \text{sq.vac.} | (q - \langle q \rangle)^2 | \text{sq.vac.} \rangle = \Delta^2 \Delta_{\text{vac}}^2$ with $\Delta = \Delta_q$ and $\Delta_{\text{vac}} = \frac{1}{2}$.² For a Gaussian model wave function of an approximate GKP state holds that $\bar{n} \approx \frac{1}{2\Delta^2} - \frac{1}{2}$ [9, 13]. In this model, an approximate GKP state equals

$$\begin{aligned}|\tilde{\psi}\rangle &= \mathfrak{E}|\bar{\psi}\rangle, \\ \mathfrak{E} &= \frac{1}{\sqrt{\pi\Delta^2}} \iint_{\mathbb{R}^2} du dv \exp\left(-\frac{(u^2 + v^2)}{2\Delta^2} - iu\hat{p} + iv\hat{q}\right),\end{aligned}$$

where $|\bar{\psi}\rangle$ is a perfect GKP code state, i. e. a $+1$ eigenstate of S_p and S_q .

5.2. OVERVIEW OF MEASUREMENT PROTOCOL

We will refer to the oscillators as *target* and *ancilla* oscillators, with resonance frequencies ω_T resp. ω_A and $\omega_A \gg \omega_T$. The reason for this choice of frequencies is that the *instantaneous* potential of the ancilla oscillator depends on the current state of the target oscillator while the potential of the target oscillator is unchanged, which enables the photon-pressure interaction.

We will use \hat{a}, \hat{a}^\dagger (resp. \hat{b}, \hat{b}^\dagger) as annihilation and creation operators of the ancilla (resp. target oscillator). Targeted values of coupling strengths and oscillator decay rates are summarized in Table 5.1. The aim is to describe a set-up allowing for the measurement of both stabilizers S_p, S_q and/or the logical shifts X, Z . For example, one can prepare a GKP grid state in the target oscillator from the vacuum by performing a modular measurement of both \hat{p} and \hat{q} , i. e. measure S_p and Z in sequence.

²We remark that Ref. [5] uses a standard deviation σ as the absolute standard deviation of a squeezed peak while the Δ parameter is the relative enhancement of the standard deviation as compared to the vacuum state. This implies that we have the correspondence $\sigma^2 = \Delta^2/2$ since the vacuum has variance $1/2$ by definition.

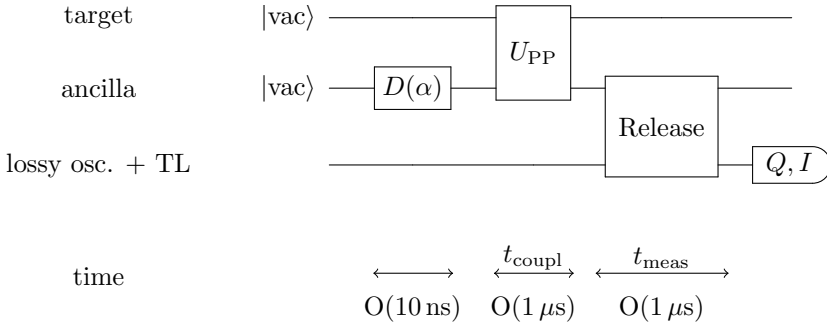


Figure 5.1: Timeline of the measurement protocol. First, the ancilla oscillator is initialized to a coherent state $|\alpha\rangle$. Then, the parametric drive is turned on for time t_{coup} , coupling the target and ancilla oscillators with the unitary U_{pp} . Finally, the parametric drive is turned off and the ancilla oscillator is coupled to a lossy oscillator. From this lossy oscillator, the state is released into a transmission line, where it is amplified and measured. Previously published in D. J. Weigand and B. M. Terhal, “Realizing modular quadrature measurements via a tunable photon-pressure coupling in circuit QED”, *Physical Review A* **101**, 053840 (2020), licensed under CC-BY 4.0 [21] ©.

5

The sequence of events to enact a single modular quadrature measurement of, say S_q , is shown in Fig. 5.1. We start both oscillators in the vacuum state. First we create a coherent state $|\alpha\rangle$ in the ancilla oscillator by driving this oscillator with a short ($O(10)$ ns) pulse. Now we turn on a strong photon-pressure coupling between target and ancilla oscillator for time t_{coup} : We discuss this in detail in Section 5.3.3. In the rotating frame of both oscillators (ancilla oscillator at ω_A and target oscillator at ω_T), we thus turn on the Hamiltonian

$$H_{\text{pp}} = g\hat{a}^\dagger\hat{a}(\hat{b}^\dagger + \hat{b}) = \sqrt{2}g\hat{a}^\dagger\hat{a}\hat{q}_T, \quad (5.2)$$

for some time t_{coup} . Here and throughout the rest of this chapter, we use the convention $\hbar = 1$. From now on, we will drop the subscript T in the stabilizers $S_{q,T}, S_{p,T}$, the logicals Z_T, X_T , and the quadrature operators \hat{q}, \hat{p} as all these operators always act on the target oscillator. We note that the fact that this Hamiltonian is time-independent in the rotating frame of target oscillator is non-trivial: A parametric drive by a classical field, i. e. a pump or a flux-drive is required to accomplish this. By changing the phase of this classical field we can change the coupling to be proportional to $\hat{a}^\dagger\hat{a}\hat{p}$ enabling to perform a modular measurement of \hat{p} (or any other rotated quadrature).

If the interaction in Eq. (5.2) is turned on for the time $t_{\text{coup}} = \sqrt{2\pi}/g$, it will implement the following unitary between target and ancilla oscillator:

$$U_{\text{pp}} = \exp(i2\sqrt{\pi}\hat{q}\hat{a}^\dagger\hat{a}) = S_q^{\hat{a}^\dagger\hat{a}}, \quad (5.3)$$

where S_q is a stabilizer of the GKP code acting on the target oscillator.

It follows that the coherent state $|\alpha\rangle$ in the ancilla oscillator rotates by an amount that depends on the eigenvalue phase of S_q . Thus, measuring the angle over which the state $|\alpha\rangle$ rotates corresponds to measuring the eigenvalues of S_q . A coherent state $|\alpha\rangle$ naturally has an angle uncertainty which gets larger with smaller amplitude $|\alpha|$, putting

an α -dependent bound on the accuracy with which one can project onto an eigenstate of S_q . Clearly, the larger the coherent amplitude is, the better one can resolve its phase and thus the more bits of information one gets about the eigenvalue phase of the measured operator S_q .

After the photon-pressure interaction is turned off and the oscillators no longer interact, the state of the ancilla oscillator has to be converted to a traveling signal so that the quadratures of the rotated coherent state can be read out via the standard “heterodyne” measurement chain [22], allowing one to determine the phase of the coherent state. We do not claim any original contribution for such a release mechanism, but discuss known previous work in Section 5.3.4.

In Section 5.5.1, we formally model the effect of the whole measurement protocol: In Fig. 5.2, we show the effect of the protocol using a coherent state with mean photon number $\bar{n} = 3$. When integrating the Wigner function of the outgoing state over the p -coordinate, we obtain the probability distribution over q which is clearly peaked, with periodicity $2\sqrt{\pi}$.

Note that the support of these peaks lies within the uncertainty of the original vacuum state: The measurement of S_q does not enlarge the q -support of the input wavefunction, it only applies a modular structure to it. The measurement of S_q *does* enlarge the p -support of the input wavefunction as is visible from the Wigner function of the outgoing state. Thus, if we were to follow the measurement of S_q by a measurement of S_p , we would obtain the signature grid-like Wigner function of an approximate GKP state. Alternatively, we start with a squeezed state (squeezing in p) and only measure S_q , see the bottom row in Fig. 5.2, to obtain a grid-like GKP Wigner function.

5

5.2.1. GKP QUBIT READOUT

The preparation of a GKP grid state should also be accompanied by a mechanism for measuring the GKP qubit in the Z or X -basis. A useful fault-tolerant Z -measurement is a measurement in which the quadrature q is measured so that finding the quadrature q closer to an even (resp. odd) multiple of $\sqrt{\pi}$ leads to inferring the state $|\bar{0}\rangle$ (resp. $|\bar{1}\rangle$). A simple method is to use the photon-pressure coupling and replace S_q by the logical operator Z to nondestructively measure Z . If t_{coupl} is turned on for half the time, such that the ancilla oscillator is either not rotated ($Z \approx 1$) or rotated by π ($Z \approx -1$), then subsequent release and measurement of the state of the ancilla oscillator will reveal the eigenvalue of Z . Readout of the Pauli X operator could proceed analogously.

5.2.2. WHY PROBING THE ANCILLA OSCILLATOR’S FREQUENCY REVEALS THE WRONG INFORMATION

Our scheme is demanding in requiring a high-Q ancilla oscillator (low κ_c) whose state should be measured through a tunable release or switch mechanism (switching to higher κ_{open}) followed by a circuit-QED heterodyne measurement. The photon-pressure coupling induces a frequency shift in the ancilla oscillator which depends on the quadrature of the target oscillator. We could imagine measuring such a frequency shift by probing the ancilla oscillator with a microwave tone as it is done in the standard dispersive measurement in circuit-QED [23], without switching the effective decay rate of the ancilla oscillator from low to high for state release. Here, we briefly comment on the fact that

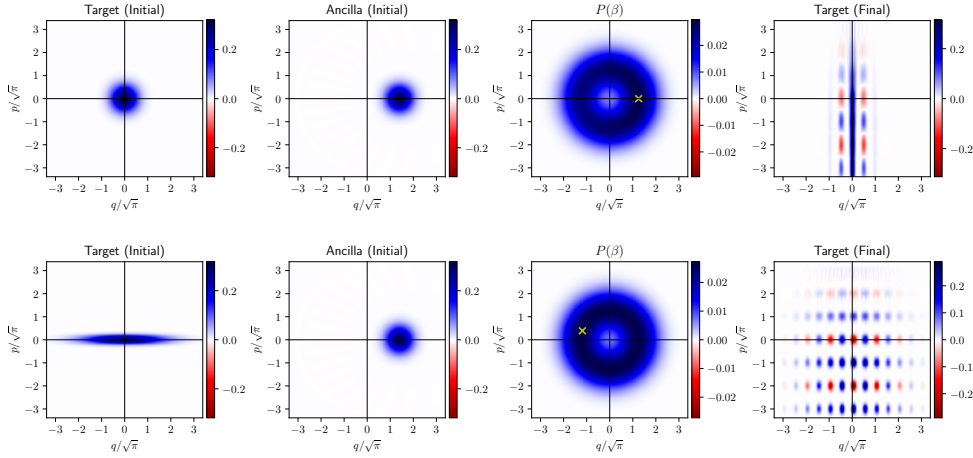


Figure 5.2: Wigner functions of states in the target and ancilla oscillators and probability distribution $\mathbb{P}(\beta)$ over measurement results of the heterodyne measurement of the ancilla oscillator mode. The initial state of the ancilla oscillator is the coherent state $|\alpha = \sqrt{3}\rangle$. The measurement result is the one with maximum likelihood with respect to $\mathbb{P}(\beta)$ (marked by a yellow cross). Top row: Starting with a vacuum state ($\Delta_q = \Delta_p = 1$) in the target mode, a measurement of S_q results in an effective squeezing of the final state of $\Delta_q = 0.18$, while $\Delta_p = 1$ is unchanged. The final state is most like the GKP $|-\rangle$ state for the following reason: We start with a vacuum state — which is closest to the $+1$ eigenstate of X . Besides, the measurement result gives an eigenvalue of S_q close to $+1$ so we are in the GKP code space. In order to center the outgoing state, we apply an additional unconditional displacement equal to Z^{-3} which changes the initial eigenvalue $+1$ of X to -1 . Bottom row: The initial state in the target mode is a squeezed vacuum state with $\Delta_q = 3$ and $\Delta_p = 1/3$. The effective squeezing of the final state $\Delta_p = 1/3$ is again unchanged, while $\Delta_q = 0.18$ for the outgoing state. The resulting state is squeezed with respect to both quadratures. Now the final state is close to a GKP $|-\rangle$ displaced by half a logical, i.e. $X^{-1/2}$, for the following reason. Again, we started with a squeezed vacuum state, which is closest to the $+1$ eigenstate of X and the unconditional displacement is Z^{-3} , which changes the eigenvalue to -1 . However, the measurement result now gives an eigenvalue of S_q close to -1 , indicating that the state is shifted out of the code space, by half a logical X . Previously published in D. J. Weigand and B. M. Terhal, “Realizing modular quadrature measurements via a tunable photon-pressure coupling in circuit QED”, *Physical Review A* **101**, 053840 (2020), licensed under CC-BY 4.0 [21] © ⓘ.

5

this method will not work as we will obtain direct rather than modular information about the target oscillator quadrature \hat{q}_T .

Imagine we would weakly apply a microwave drive to the ancilla oscillator (decay rate κ) at some frequency ω , starting at some initial time $t = 0$. Also at time $t = 0$, we have turned on the photon-pressure coupling so that the resulting Hamiltonian of ancilla and target oscillator is $H_{PP} = (\omega_A + g\hat{q})\hat{a}^\dagger\hat{a}$ in the rotating frame of the target oscillator at angular frequency ω_T . We can thus view the photon-pressure coupling as an effective change in the resonance frequency of the ancilla oscillator, which leads to a phase change of the outgoing field as compared to the incoming field. For simplicity, we take the weak drive to be modeled by a plane-wave input field $b_{\text{in}}[\omega]$ at frequency ω . The

input-output formalism (see e. g. [24, 25]) gives the phase of the reflected output field as

$$\hat{b}_{\text{out}}[\omega] = e^{i\varphi(\hat{q}, \omega)} \hat{b}_{\text{in}}[\omega],$$

$$\exp(i\varphi(\hat{q}, \omega)) = \frac{\kappa/2 + i(\omega_A + g\hat{q} - \omega)}{\kappa/2 - i(\omega_A + g\hat{q} - \omega)}.$$

If we choose $\omega = \omega_A$, i. e. drive the ancilla oscillator at its resonant frequency, then we will see that the phase shift $\varphi(\hat{q}, \omega_A)$ goes from $-\pi$ at large negative eigenvalues q of \hat{q} to π at large positive eigenvalues q and displays no periodicity in q since $\varphi = 2 \arctan(2g\hat{q}/\kappa)$. These considerations imply that the modular measurement of \hat{q} should take place in a very non-steady state regime where the ancilla resonator is first excited to create the state $|\alpha\rangle$ and decay of this state should be strongly suppressed during the photon-pressure interaction, as this decay will leak information about \hat{q} . We discuss the effect of photon loss in the ancilla oscillator during the interaction in Section 5.8.1.

5.3. CIRCUIT-QED SETUP

In this section, we discuss how a modular quadrature measurement can be realized. We start with a short review of previous work that realizes a photon-pressure or longitudinal coupling. We then introduce and analyze an electric circuit that achieves strong coupling. Finally, we discuss how the state in the ancilla oscillator can be released into a transmission line for readout.

5.3.1. PREVIOUS CIRCUIT-QED WORK ON PHOTON-PRESSURE AND LONGITUDINAL COUPLING

When the \hat{a} -mode of a photon-pressure coupling of the form $\hat{q}\hat{a}^\dagger\hat{a}$ is very anharmonic and is used to represent a qubit, the photon-pressure coupling can be recognized as a longitudinal coupling $\hat{q}(I - Z)/2$ with Pauli Z of the qubit. In this incarnation, the qubit induces a state-dependent displacement on the target oscillator which can be used for (improved) qubit read-out [26–28]. Note that in such settings the roles of ancilla and target are reversed as compared to the setting of the GKP code, i. e. the target oscillator is used for information gathering about the qubit instead of the target oscillator being used to store a GKP state.

In optomechanical systems, the coupling $\hat{q}\hat{a}^\dagger\hat{a}$, with \hat{q} the position of the mechanical oscillator and \hat{a} the annihilation operator of an optical cavity field, is arrived at naturally. In the rotating frame of these oscillators, this coupling averages out without further time-dependent driving. In a linearized regime where one expands around a driven optical field $\langle\hat{a}\rangle = \alpha(t)$, the coupling can be used to generate an effective beam splitter interaction with a strength depending on $|\alpha|^2$ [29, 30]. Although there has been a wide range of experimental setups and studies, the so-called single-photon coupling regime, $g \gg \kappa_A, \kappa_T$, i. e. the bare coupling strength exceeds the photon loss rate of both oscillators, has so far not been achieved [29]. One difficulty is that in a traditional optomechanical setting, the loss rate of the optical oscillator is relatively large, while the mechanical oscillator, being low in frequency, is susceptible to thermal excitations. Working with two oscillators both at some middling frequency (GHz range) can resolve this conundrum.

A good candidate to achieve a single-photon coupling at microwave frequencies is the so-called simulated optomechanical coupling, where a SQUID loop is used to couple two oscillators. The coupling of two co-planar waveguide resonators via a SQUID loop has been analyzed by Johansson *et al.* [31], two lumped element circuit variants have been implemented experimentally [30, 32]. We note that the experimental coupling achieved is not in the so-called single photon regime, i.e. the photon loss rate of the ancilla oscillator is larger than the coupling strength, $\kappa \geq g$. It will be necessary to be in this regime for our use of this coupling.

5.3.2. MECHANICAL ANALOGUE

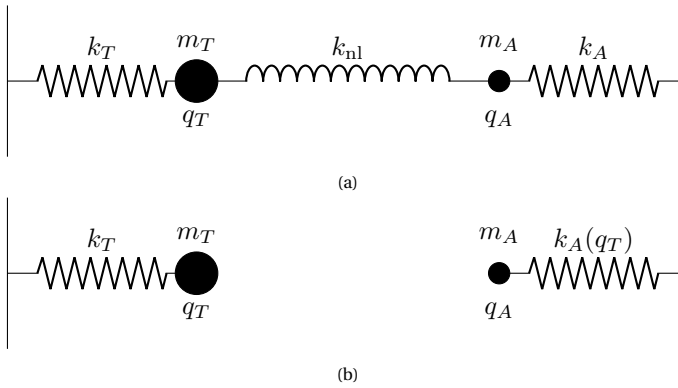


Figure 5.3: Mechanical approximation of a photon-pressure Hamiltonian. The system consists of two (mostly) independent harmonic oscillators, implemented by the masses m_T (m_A) at positions q_T (q_A), connected to immovable walls by springs with constant k_T (k_A). (a): The two harmonic oscillators are coupled by a third, weak and nonlinear spring with a force proportional to k_{nl} . (b): In the limit where $m_T \gg m_A$ with $k_T \approx k_A$, the resonance frequency of harmonic oscillator T is much lower than that of oscillator A . This allows us to solve the instantaneous potential of oscillator A dependent on the state of oscillator T . If we also assume that $k_{nl} \ll k_A, k_T$, oscillator T is mostly independent, but the effective spring constant $k_A(q_T)$ is now a function of the position of oscillator T .

The first step to obtain a Hamiltonian of the form of Eq. (5.2) is to achieve a strong photon-pressure coupling. To illustrate the strategy we use to this end, consider the sketches in Fig. 5.3. We start with two independent harmonic oscillators, implemented by the masses m_T (m_A) at positions q_T (q_A), connected to immovable walls by springs with constant k_T (k_A).

To obtain a photon-pressure coupling, we need to include a coupling in this setup. To this end, we add a third, nonlinear spring with a force proportional to $k_{nl} \ll k_A, k_T$ coupling the two masses (see Fig. 5.3). Because the mass m_T of the target oscillator is much larger than the mass of the ancilla oscillator $m_A \ll m_T$, this does not change the Hamiltonian of the target oscillator much. Instead, we can view this coupling as an effective potential of the ancilla oscillator, where the spring constant of the instantaneous Hamiltonian $k_A(q_T)$ is now a function of the state of the target oscillator, see Fig. 5.3b.

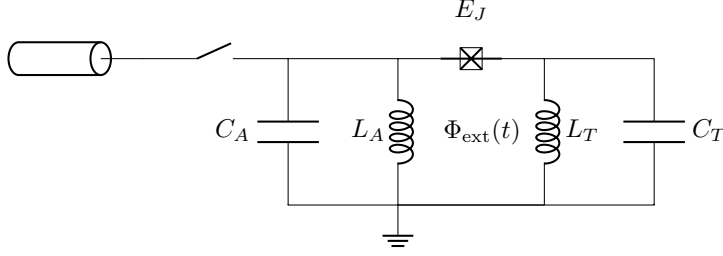


Figure 5.4: Electric circuit realizing the photon-pressure coupling. The target oscillator (label T , right) is coupled to the ancilla oscillator (label A , left) via a Josephson junction. The coupling between the ancilla oscillator and the readout line is tunable, and only turned on during readout. The loop formed by the Josephson junction and the inductances L_A, L_T is threaded by an external flux $\Phi_{\text{ext}}(t)$, which is a classical, time-dependent variable. Possible implementations of the readout switch are discussed in Section 5.3.4. Previously published in D. J. Weigand and B. M. Terhal, “Realizing modular quadrature measurements via a tunable photon-pressure coupling in circuit QED”, *Physical Review A* **101**, 053840 (2020), licensed under CC-BY 4.0 [21] © ⓘ.

5

5.3.3. CIRCUIT ANALYSIS AND APPROXIMATIONS

To achieve the desired photon-pressure coupling in circuit QED, we start with the electric circuit shown in Fig. 5.4, neglecting the switchable coupling to the external world. The GKP state will be encoded in the (low-frequency) target oscillator, shown on the right in the figure. It is coupled via a Josephson junction to an ancilla oscillator shown in the left. The two oscillators are almost harmonic, with the parameters chosen such that the *instantaneous* potential of the ancilla oscillator depends on the current state of the target oscillator while the potential of the target oscillator is unchanged. The ancilla oscillator dynamics is thus tracking the lower-frequency, slow and “heavy”, target oscillator dynamics. The change of potential changes the resonance frequency of the ancilla oscillator depending on the state of the target oscillator, enabling the photon-pressure coupling. The concept is similar to the approach used by Johansson *et al.*, where the effective length of the ancilla slit line resonator depends on the state of the target oscillator [31].

After the interaction between ancilla and target oscillators is turned off, we envision that a coupling between transmission line and ancilla oscillator is turned on, enabling fast readout. We note that this electric circuit has also been analyzed (operated in a different regime with very different parameters as compared to those in Table 5.1) in [33], with the aim to control individual Fock states as a qubit.

We envision that this circuit is realized as a superconducting lumped element circuit, using, for example, plate capacitances for getting a large C_A and C_T , and wire structures made of superconducting material as inductance (similar to the circuits in [30, 32]).

	Ancilla Oscillator	Target Oscillator
Resonance frequency f (GHz)	10	0.5
Frequency range $f_{\max} - f_{\min}$ (MHz)	500	5–10
Capacitance C_m (pF)	0.1–1	50–1000
Charging Energy $\frac{E_{Cm}}{2\pi}$ (MHz)	20–200	0.02–0.4
Inductance L_m (nH)	0.2–3	0.2–3
Inductive Energy $\frac{E_{Lm}}{2\pi}$ (GHz)	50–400	50–400
Third-order nonlinearity ($\sim \hat{q}^3/g$)	negl.	10^{-3} – 10^{-2}
Self-Kerr ($\sim (\hat{a}^\dagger \hat{a})^2, (\hat{b}^\dagger \hat{b})^2/g$)	50%–100%	10^{-3} – 10^{-2}
Targeted oscillator life time $1/\kappa$	100 μ s (closed), 1 μ s (open)	100 μ s
$\frac{E_J}{2\pi}$ (GHz)	5–40	
Capacitance C_J	$C_J \ll C_A$	
Photon-pressure coupling $\frac{g}{2\pi}$ (MHz)	3–15	
Cross-Kerr ($\sim \hat{a}^\dagger \hat{a} \hat{b}^\dagger \hat{b}/g$)	2%–5%	
Interaction time t_{coupl} (μ s)	0.2–1	

Table 5.1: Targeted parameters of the two oscillators, strength of the photon-pressure coupling g , and various error terms. The resonance frequency of the oscillators is dependent on the external flux, it is maximal for $x_{\text{ext}} = \pi$, and minimal for $x_{\text{ext}} = 0$. All frequencies except the frequency range f_{\max} – f_{\min} are given as mean values, i. e. for $x_{\text{ext}} = \pi/2$. The capacitance C_J of the Josephson junction is not particularly important, as long as it is small compared to the capacitance of the ancilla oscillator C_A , which is the case e. g. for the junction designs of the transmon and charge qubits. The photon-pressure coupling strength g is obtained by fixing the resonance frequency, inductance and Josephson energy for the two oscillators, choosing the capacitance accordingly and using Eq. (5.12). The capacitance of the Josephson junction was neglected because it is several orders of magnitude smaller than the capacitance of both oscillators. The nonlinear terms (third-order, self- and cross-Kerr) are given as a fraction of the coupling strength g because they are only relevant while the drive is on. Note that the listed values of the self- and cross-Kerr terms are the maximal values in time (not the echoed-out values). In our modeling, it is assumed that all losses on the ancilla oscillator are due to coupling to the transmission line. We denote the closed decay rate of the ancilla oscillator as κ_c and the open decay rate as κ_{open} , while the decay rate of the target oscillator is denoted as κ_T . This choice of parameters meets the condition $\kappa_c t_{\text{coupl}} |\alpha|^2 \ll 1$, ensuring low photon loss during the modular quadrature measurements easily for $\bar{n} \approx 2$ –4. Previously published in D. J. Weigand and B. M. Terhal, “Realizing modular quadrature measurements via a tunable photon-pressure coupling in circuit QED”, *Physical Review A* **101**, 053840 (2020), licensed under CC-BY 4.0 [21] ©.

CIRCUIT ANALYSIS

Consider the circuit in Fig. 5.4. The Lagrangian of the circuit in terms of node flux variables and their time-derivatives is

$$\begin{aligned} \mathcal{L} = & \frac{C_A \dot{\Phi}_A^2}{2} + \frac{C_T \dot{\Phi}_T^2}{2} + \frac{C_J}{2} \left(\dot{\Phi}_A + \dot{\Phi}_{\text{ext}}(t) - \dot{\Phi}_T \right)^2 \\ & - \frac{\hat{\Phi}_A^2}{2L_A} - \frac{\hat{\Phi}_T^2}{2L_T} + E_J \cos \left(\frac{2\pi}{\Phi_0} [\hat{\Phi}_T - \hat{\Phi}_A - \Phi_{\text{ext}}(t)] \right). \end{aligned}$$

Here, Φ_0 is the magnetic flux quantum and $\Phi_{\text{ext}}(t)$ is a classical, time-dependent flux due to an external field. Deriving the Hamiltonian from the Lagrangian in the standard way,

one arrives at

$$H = \frac{1}{2} \frac{C_T \hat{Q}_A^2 + C_A \hat{Q}_T^2 + C_J (\hat{Q}_A + \hat{Q}_T)^2 - C_J \dot{\Phi}_{\text{ext}}(t) (2C_T \hat{Q}_A - 2C_A \hat{Q}_T + C_A C_T \dot{\Phi}_{\text{ext}}(t))}{C_J C_T + C_J C_A + C_A C_T} + \frac{\hat{\Phi}_A^2}{2L_A} + \frac{\hat{\Phi}_T^2}{2L_T} - E_J \cos \left(\frac{2\pi}{\Phi_0} [\hat{\Phi}_T - \hat{\Phi}_A - \Phi_{\text{ext}}(t)] \right). \quad (5.4)$$

When we quantize this Hamiltonian, we have conjugate-variable commutation relations $[\hat{\Phi}_i, \hat{Q}_j] = i\delta_{ij}$ (with $i, j = T, A$) between the flux and charge variables of the target and ancilla systems. Both flux and charge operators have eigenvalues in \mathbb{R} .

In the following, we use that the capacitances of both oscillators are much larger than the capacitance of the Josephson junction, i. e. $C_T, C_A \gg C_J$. Up to first order in C_J , the Hamiltonian is then given by:

$$H = \frac{\hat{Q}_A^2}{2C_A} + \frac{\hat{Q}_T^2}{2C_T} - \frac{C_J}{2} \left(\frac{\hat{Q}_A}{C_A} - \frac{\hat{Q}_T}{C_T} \right)^2 - C_J \dot{\Phi}_{\text{ext}}(t) \left(\frac{\hat{Q}_A}{C_A} - \frac{\hat{Q}_T}{C_T} + \frac{\dot{\Phi}_{\text{ext}}(t)}{2} \right) + \frac{\hat{\Phi}_A^2}{2L_A} + \frac{\hat{\Phi}_T^2}{2L_T} - E_J \cos \left(\frac{2\pi}{\Phi_0} [\hat{\Phi}_T - \hat{\Phi}_A - \Phi_{\text{ext}}(t)] \right).$$

We will neglect the terms $\propto \dot{\Phi}_{\text{ext}}(t)$ from now on, as they will be dropped with the rotating wave approximation: With the drive of interest, see Section 5.4.1, $\dot{\Phi}_{\text{ext}}(t) \sim (-1) \lfloor \frac{\omega_T t}{2\pi} \rfloor$, such that both \hat{Q}_A, \hat{Q}_T will oscillate quickly and can be neglected, even with a time-dependent drive. The time derivative of the external flux is simply an energy shift, and will also be neglected as it does not change the system dynamics. To simplify notation, we define dimensionless conjugate variables $\hat{x}_i = \frac{2\pi\hat{\Phi}_i}{\Phi_0}$, $\hat{y}_i = \frac{\Phi_0\hat{Q}_i}{2\pi}$, with $[\hat{x}_i, \hat{y}_i] = i\delta_{ij}$ and a dimensionless variable

$$x_{\text{ext}}(t) = \frac{2\pi\Phi_{\text{ext}}(t)}{\Phi_0},$$

for the flux drive. We also define the charging energies $E_{C_m} = \frac{e^2}{2C_m}$ and inductive energies $E_{L_m} = \frac{1}{4e^2L_m}$ for $m = T, A$, where e is the elementary charge, so that

$$H = 4E_{C_A} \left(1 - \frac{E_{C_A}}{E_{C_J}} \right) \hat{y}_A^2 + 4E_{C_T} \left(1 - \frac{E_{C_T}}{E_{C_J}} \right) \hat{y}_T^2 + U(\hat{x}_A, \hat{x}_T), \quad (5.5)$$

with

$$U(\hat{x}_A, \hat{x}_T) = \frac{E_{L_A} \hat{x}_A^2}{2} + \frac{E_{L_T} \hat{x}_T^2}{2} - E_J \cos(\hat{x}_T - \hat{x}_A - x_{\text{ext}}(t)). \quad (5.6)$$

We note that the effect of the time-dependent flux-drive $x_{\text{ext}}(t)$ can also be realized with a microwave drive, see details in Section 5.4.2. Again, note that this Hamiltonian acts in the same way on the target and ancilla oscillators (as can also be seen from the circuit itself). This can be solved with a suitable choice of system parameters, see Table 5.1.

PHOTON PRESSURE HAMILTONIAN

Next, we expand the potential Hamiltonian, using that both \hat{x}_A and \hat{x}_T will be close to the minimum of their respective potentials, because $E_{C_A} \ll E_{L_A}$ and $E_{C_T} \ll E_{L_T}$ (see Table 5.1). Furthermore, these minima will be close to zero, $(\hat{x}_A, \hat{x}_T) = (0, 0)$, because the inductive energies $E_{L_A}, E_{L_T} \gg E_J$. Note that the minimum of the $\cos()$ potential is not exactly at $\hat{x}_A = 0, \hat{x}_T = 0$, as the exact location of the minimum depends on $x_{\text{ext}}(t)$. We discuss this approximation in more detail in Section 5.8.4. This expansion up to fourth order yields

$$U(\hat{x}_A, \hat{x}_T) \approx \frac{E_{L_A} \hat{x}_A^2}{2} + \frac{E_{L_T} \hat{x}_T^2}{2} + E_J \sin(x_{\text{ext}}(t)) \left(\hat{x}_T - \hat{x}_A + \frac{\hat{x}_T^2 \hat{x}_A - \hat{x}_A^2 \hat{x}_T}{2} + \frac{\hat{x}_A^3 - \hat{x}_T^3}{6} \right) \\ + E_J \cos(x_{\text{ext}}(t)) \left(\hat{x}_A \hat{x}_T - \frac{\hat{x}_T^2 + \hat{x}_A^2}{2} + \frac{\hat{x}_A^2 \hat{x}_T^2}{4} - \frac{\hat{x}_A^3 \hat{x}_T + \hat{x}_A \hat{x}_T^3}{6} + \frac{\hat{x}_T^4 + \hat{x}_A^4}{24} \right).$$

We can already see the desired coupling term, $E_J \sin(x_{\text{ext}}(t)) \hat{x}_A^2 \hat{x}_T / 2$. However, there are multiple undesired additional interactions. In addition, it is obvious (from the electric circuit itself) that the Hamiltonian acts the same way on target and ancilla oscillator. As will be seen in the following, a suitable choice of parameters addresses both these questions. We first define effective (flux-dependent) inductive and capacitive energies for both systems:

$$\tilde{E}_{L_m}(x_{\text{ext}}(t)) = E_{L_m} - E_J \cos(x_{\text{ext}}(t)), \quad \tilde{E}_{C_m} = E_{C_m} \left(1 - \frac{E_{C_m}}{E_{C_J}} \right) \approx E_{C_m}, \quad (5.7)$$

where the approximation comes about as $C_J \ll C_m$ for $m = A, T$. In addition, we define the flux-dependent frequency, and creation and annihilation operators for the two coupled oscillators:

$$\omega_m(x_{\text{ext}}(t)) = \sqrt{8\tilde{E}_{C_J} \tilde{E}_{L_m}(x_{\text{ext}}(t))}, \quad \xi_m = \left(\frac{2\tilde{E}_{C_m}}{\tilde{E}_{L_J}} \right)^{1/4}, \quad (5.8) \\ \hat{x}_A = \xi_A(\hat{a}^\dagger + \hat{a}), \quad \hat{x}_T = \xi_T(\hat{b}^\dagger + \hat{b}), \\ \hat{y}_A = i \frac{1}{2\xi_A}(\hat{a}^\dagger - \hat{a}), \quad \hat{y}_T = i \frac{1}{2\xi_T}(\hat{b}^\dagger - \hat{b}).$$

All uncoupled quadratic terms in H in Eq. (5.5) can be put together to give a term proportional to $\omega_A \hat{a}^\dagger \hat{a} + \omega_T \hat{b}^\dagger \hat{b}$, setting the oscillator frequencies.

In order to achieve the desired asymmetric coupling, we assume that $\xi_A \gg \xi_T$. Because the inductance of both systems is assumed to be comparable, this implies that $\omega_A \gg \omega_T$, see Table 5.1. In the final step, we also go to the rotating frame of both oscillators (at their frequencies ω_m) and use the rotating wave approximation, i. e. we only keep terms which are inherently time-independent or which are flux-dependent and oscillate

with frequency ω_T :

$$\begin{aligned}
 H_{\text{RWA}} = E_J \cos(x_{\text{ext}}(t)) & \left[\frac{\xi_A^2 \xi_T^2}{2} \left(\hat{a}^\dagger \hat{a} + \hat{b}^\dagger \hat{b} + 2\hat{a}^\dagger \hat{a} \hat{b}^\dagger \hat{b} \right) \right. \\
 & \left. + \frac{\xi_A^4}{4} \left(\hat{a}^\dagger \hat{a} + (\hat{a}^\dagger \hat{a})^2 \right) + \frac{\xi_T^4}{4} \left(\hat{b}^\dagger \hat{b} + (\hat{b}^\dagger \hat{b})^2 \right) \right] \\
 & + E_J \sin(x_{\text{ext}}(t)) \left[\xi_T \left(1 - \frac{\xi_A^2}{2} - \xi_A^2 \hat{a}^\dagger \hat{a} \right) \left(\hat{b}^\dagger e^{i\omega_T t} + \hat{b} e^{-i\omega_T t} \right) \right. \\
 & \left. - \frac{\xi_T^3}{6} \left(\hat{b}^\dagger e^{i\omega_T t} + \hat{b}^\dagger \hat{b} \left(\hat{b}^\dagger e^{i\omega_T t} + 2\hat{b} e^{-i\omega_T t} \right) + \text{h.c.} \right) \right]. \quad (5.9)
 \end{aligned}$$

The ξ_T^3 term comes about by writing \hat{x}_T^3 in terms of annihilation and creation operators, and neglecting the parts rotating at frequency $3\omega_T$. We then approximate this Hamiltonian using $\xi_A, \xi_T \ll 1$, dropping all fourth-order terms in ξ_i . We also assume that the system parameters are chosen such that $\xi_A \gg \xi_T$, allowing to also omit the ξ_T^3 term. Because the inductance of both systems is assumed to be comparable, this implies that $\omega_A \gg \omega_T$, see Table 5.1. With these approximations, the Hamiltonian coupling on the target and ancilla oscillators with the drive turned on is given by

$$H_{\text{RWA}} \approx E_J \sin(x_{\text{ext}}(t)) \left[\xi_T \left(1 - \frac{\xi_A^2}{2} \right) \left(\hat{b}^\dagger e^{i\omega_T t} + \hat{b} e^{-i\omega_T t} \right) - \xi_T \xi_A^2 \hat{a}^\dagger \hat{a} \left(\hat{b}^\dagger e^{i\omega_T t} + \hat{b} e^{-i\omega_T t} \right) \right]. \quad (5.10)$$

Although the prefactor ξ_T^3 is small, this term is still relevant because it will be made resonant by any drive that enables a photon-pressure coupling in the rotating frame. In Section 5.8.5, we will explicitly discuss the effect of the ξ_T^3 term. Modulo its time-dependence, the first term of this final Hamiltonian is a known displacement that commutes with the photon-pressure coupling, the second is the traditional photon-pressure coupling Hamiltonian $\sim \hat{a}^\dagger \hat{a} (\hat{b}^\dagger e^{i\omega t} + \hat{b} e^{-i\omega t})$ similar to the coupling in [30, 31].

If the external flux is set to some constant $x_{\text{ext},0}$, only the time-independent terms remain in Eq. (5.9) and the resulting Hamiltonian is given by

$$\begin{aligned}
 H_{\text{off}} \approx E_J \cos(x_{\text{ext},0}) & \left[\frac{\xi_A^2 \xi_T^2}{2} \left(\hat{a}^\dagger \hat{a} + \hat{b}^\dagger \hat{b} + 2\hat{a}^\dagger \hat{a} \hat{b}^\dagger \hat{b} \right) \right. \\
 & \left. + \frac{\xi_A^4}{4} \left(\hat{a}^\dagger \hat{a} + (\hat{a}^\dagger \hat{a})^2 \right) + \frac{\xi_T^4}{4} \left(\hat{b}^\dagger \hat{b} + (\hat{b}^\dagger \hat{b})^2 \right) \right]. \quad (5.11)
 \end{aligned}$$

We note that there is no photon-pressure coupling between the two modes if the external flux is constant, the only remaining non-linear terms are self-Kerr ($\sim (\hat{a}^\dagger \hat{a})^2, (\hat{b}^\dagger \hat{b})^2$) and cross-Kerr ($\sim \hat{a}^\dagger \hat{a} \hat{b}^\dagger \hat{b}$). The dependence of the Hamiltonian on $x_{\text{ext},0}$ means that these unwanted interactions can be turned off by setting $x_{\text{ext},0} = \pi/2$ i.e. $\Phi_{\text{ext}} = \Phi_0/4$. When the photon-pressure coupling should be on and x_{ext} is changing over time, we do not wish to have these self-Kerr and cross-Kerr terms. We will take a flux drive so that $x_{\text{ext}}(t)$

oscillates periodically around $\pi/2$ and this then directly leads to the terms proportional to $\cos(x_{\text{ext}}(t))$ averaging out, see Section 5.4.1 and Fig. 5.5.

To turn the photon-pressure coupling on, we assume a drive such that $\sin(x_{\text{ext}}(t)) = \cos(\omega_T t)$ ³. At first glance, such a drive seems to be difficult to achieve, as it would require a steadily increasing flux. However, one can use the symmetry of the sine around $\pi/2$ to obtain an oscillating function. The drive is in fact a triangle wave with frequency $\omega_T/2 \sim 250\text{MHz}$, an excellent approximation can easily be generated with standard equipment, see details in Section 5.4.1. We insert this drive choice in Eq. (5.10) and drop all terms which remain time-dependent to obtain the desired Hamiltonian

$$H_{\text{on}} \approx \frac{E_J}{2} \xi_T \left(1 - \frac{\xi_A^2}{2} \right) (\hat{b}^\dagger + \hat{b}) - g \hat{a}^\dagger \hat{a} (\hat{b}^\dagger + \hat{b}). \quad (5.12)$$

where we defined the photon-pressure coupling strength $g = \frac{1}{2} E_J \xi_T \xi_A^2$. We note that, besides the photon-pressure coupling, the Hamiltonian contains an additional displacement on the target oscillator. Since the displacement commutes with the coupling, it does not alter the effect of the coupling and can be seen a systematic error on the target oscillator which can be undone by a counter-displacement.

The Hamiltonian in Eq. (5.12) can be easily adjusted to a photon-pressure coupling with any rotated quadrature by choosing an appropriate offset between external flux and the target oscillator. For example, the choice $x_{\text{ext},\sin}(t) = x_{\text{ext}}(t + \frac{\pi}{2\omega_T})$ generates a Hamiltonian of the form $H \sim i\hat{a}^\dagger \hat{a}(\hat{b}^\dagger - \hat{b})$.

The Hamiltonian H_{on} realizes $U_{\text{PP}} = S_q^{\hat{a}^\dagger \hat{a}}$ (modulo the unconditional displacement), where the photon number operator only has non-negative eigenvalues. Therefore, if we view this interaction as an ancilla-oscillator dependent displacement on the target oscillator, all displacements $S_q^{\hat{a}^\dagger \hat{a}}$ point in the same direction, and the post-measurement state in the target oscillator will be off-center in phase space and contain an unnecessarily high number of photons.

In order to reduce the photon number, one can apply a displacement drive such that the unconditional displacement during the interaction is $S_q^{-\langle \hat{a}^\dagger \hat{a} \rangle/2} = Z^{-\langle \hat{a}^\dagger \hat{a} \rangle}$. The idea is the same as for phase estimation when using qubits as ancillas, see [13]. We use such a counter-displacement in all numerical simulations in this chapter. One thing to observe is that the frequency of the ancilla (and to a lesser amount the target) oscillator depends on the flux drive through Eq. (5.8). Hence, we are working in a flux-dependent rotating frame which has to be carefully tracked (in order to read out the phase of the ancilla oscillator and do additional counter-displacements on the ancilla oscillator). In some settings, it might be desirable to use a drive

$$\sin(x_{\text{ext}})(t) = 1 - \delta + \delta \cos(\omega_T t), 0 < \delta \leq 1.$$

It is possible to do so, and a drive with $\delta < 1$ is easier to generate, but this costs some coupling strength, see Section 5.4.1 for details. We will use the maximal possible coupling strength i. e. $\delta = 1$ unless mentioned otherwise.

³In principle, ω_T also depends on the external drive. This dependence is quite small, but it is also possible to include this effect in the external drive $x_{\text{ext}}(t)$.

The values for resonance frequency, coupling strength and the leading order error terms for a typical setup are given in Table 5.1. In order to maximize the coupling strength, it is beneficial to reduce the Josephson energy while simultaneously increasing the inductances of both circuits in order to keep $E_J \ll E_{L_m}$. Furthermore, it is beneficial to make the inductance of the target oscillator smaller than that of the ancilla oscillator: The ratio between the third-order nonlinearity and the photon-pressure coupling strength is proportional to the ratio of the inductances. For a Josephson energy around 10 GHz and an inductance of the ancilla oscillator around 2 nH, a coupling strength $g/(2\pi)$ well above 10 MHz can be achieved. Note that the Kerr and cross-Kerr effects on both oscillators might be large during the interaction due to the $\cos()$ term in Eq. (5.9), however the term oscillates in sign due to the drive and will therefore be echoed out (see Section 5.4.1).

5.3.4. RELEASE OF ANCILLA OSCILLATOR STATE

In order to meet both the demands of fast read-out and low photon loss, it is desirable to be able to effectively turn the ancilla oscillator decay rate from low to high. There are a few ways to achieve this, for example with a tunable inductive coupling [34], a frequency tunable oscillator [35] a pump-tunable beam splitter to a lossy oscillator [36] or a parametric coupler [37]. Note that most of these references work towards catch and release schemes, hence if the tunable coupling is simply used for readout the achieved fidelities can be expected to be larger. In particular, the Q-switch scheme in [36] in which a pump mode is used to temporally frequency-match the ancilla oscillator with a lossy oscillator seems attractive. In this work, the ratio between the closed and open decay rates is about 1000: The authors decrease the effective life-time of an oscillator from about 0.5ms to $0.5\mu\text{s}$, with efficiency exceeding 98%. The paper reports that the coherence and phase of oscillator states with up to 5 photons can be well resolved.

In the protocol presented here, it is also possible to use the fact that the ancilla oscillator has a tunable frequency. If a lossy fixed-frequency oscillator is placed between transmission line and ancilla mode, the ancilla mode can be brought into resonance with it, increasing its decay rate. Note that this idea is as in Ref. [35], but reversing the roles of the frequency-tunable and fixed-frequency oscillator. The lossy oscillator thus needs to be off-resonant with ancilla mode, effectively acting as a Purcell filter, except during readout. An advantage of this approach is that it does not require any further circuit elements. As an example, consider an ancilla oscillator with properties as in Table 5.1. In this case, the resonance frequency is between $f(x_{\text{ext}} = 0) = 9.75$ GHz and $f(x_{\text{ext}} = \pi) = 10.25$ GHz. If the lossy resonator has resonance frequency 9.75 GHz and we want lossy oscillator and ancilla oscillator to be separated by at least 250 MHz, we require that $\pi/2 \leq x_{\text{ext}} \leq \pi$. This can be achieved by modifying the drive during the interaction, see Section 5.4.1. After the interaction time, we set the external flux to $x_{\text{ext}} = 0$ in order to bring the ancilla oscillator into resonance with the lossy oscillator.

5.4. PARAMETRIC FLUX DRIVE

A key component to achieve a photon-pressure coupling in the rotating frame is a suitable flux drive that cancels the time-dependence of a Hamiltonian in the rotating frame.

In the following, we discuss how this drive can be achieved, and show how a microwave drive could be used instead of a flux drive.

5.4.1. PARAMETRIC FLUX DRIVE

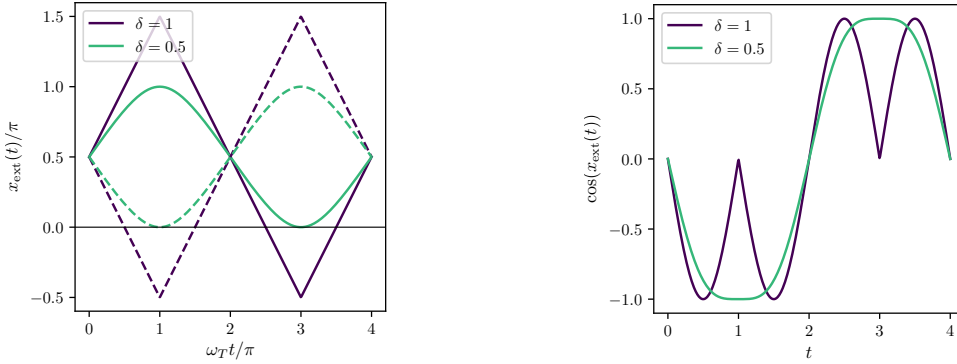


Figure 5.5: Left: The external drive $x_{\text{ext}}(t)$ required to obtain a photon-pressure coupling in the rotating frame, see Eq. (5.13). As can be seen, the lowest frequency component of $x_{\text{ext}}(t)$ is $\omega_T/2$. The starting point of $x_{\text{ext}}(t=0) = \pi/2$ corresponds to the “off” setting where the target and ancilla oscillators are completely decoupled. The solid and dashed lines correspond to choosing the drive with a positive or negative sign, $x_{\text{ext},\pm}(t)$, respectively. Right: The prefactor $\cos(x_{\text{ext}}(t))$ of the self- and cross Kerr terms in Eq. (5.9). The function is periodic and changes sign with frequency ω_T . Purple: Drive required to obtain the maximum coupling strength i.e. $\delta = 1$. The drive corresponds to a triangular wave. Green: The coupling strength is reduced to $\delta = 0.5$. In this case, the drive is close to a simple cosine. Previously published in D. J. Weigand and B. M. Terhal, “Realizing modular quadrature measurements via a tunable photon-pressure coupling in circuit QED”, *Physical Review A* **101**, 053840 (2020), licensed under CC-BY 4.0 [21] © ⓘ.

To achieve the desired photon-pressure coupling from Eq. (5.2), it is necessary to design an appropriate time-dependence of $x_{\text{ext}}(t)$ in Eq. (5.10) such that the phases $e^{\pm i\omega_T t}$ in that equation cancel. The idea is similar to the case of qubit readout, [26–28], but here we can use that the frequency of the target oscillator is relatively small in order to maximize the coupling strength, which is not the case for qubit readout. Furthermore, we can use a flux drive with an amplitude of 2π , cancelling the anharmonicity of both oscillators (something which is undesired in the case of qubit readout).

To this end, we consider a flux drive such that $\sin(x_{\text{ext}}(t)) = (1-\delta) + \delta \cos(\omega_T t)$, where $0 < \delta < 1$ is a freely chosen constant which serves to reduce the amplitude of the flux drive. Scenarios where this is desirable are, for example, if a lossy resonator is used to implement the tunable coupling, or if the range of resonance frequencies should be limited. One can easily verify that either drive

$$x_{\text{ext},\pm}(t) = \frac{\pi}{2} \pm (-1)^{\lfloor \frac{\omega_T t}{2\pi} \rfloor} \arcsin(1 - \delta + \delta \cos(\omega_T t)) \quad (5.13)$$

satisfies that condition. For $\delta = 1$, we can also see that

$$\cos(x_{\text{ext},\pm}(t)) = \pm (-1)^{\lfloor \frac{\omega_T t}{2\pi} \rfloor} |\sin(\omega_T t)|,$$

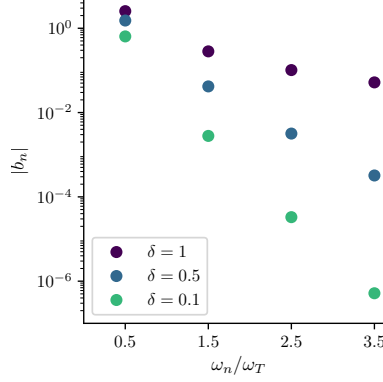


Figure 5.6: Amplitude $|b_n|$ of the first four harmonics with frequency ω_n of the Fourier series of either drive $x_{\text{ext},\pm}(t)$, see Eq. (5.13). Purple: Maximal coupling strength ($\delta = 1$), Blue: $\delta = 0.5$, Green $\delta = 0.1$. For $\delta = 0.5$, it is sufficient to use only two harmonics in order to achieve a relative error below 1%. Previously published in D. J. Weigand and B. M. Terhal, “Realizing modular quadrature measurements via a tunable photon-pressure coupling in circuit QED”, *Physical Review A* **101**, 053840 (2020), licensed under CC-BY 4.0 [21] © ⓘ.

5

corroborating the claim that the even order terms in Eq. (5.10) cancel. Although this drive seems to be very complex, this function can be easily synthesized with a small number of harmonics. In fact, the most complex possible drive (using the full flux range for maximal coupling strength, $\delta = 1$) yields a triangular wave which rolls off with the inverse harmonic number squared:

$$x_{\text{ext},+}(t) = \frac{\pi}{2} - \frac{8}{\pi} \sum_{n=0}^{\infty} \frac{(-1)^n}{(2n+1)^2} \sin\left(\frac{2n+1}{2} \omega_T t\right).$$

Although the Fourier series of the drive does not have such a simple solution for $\delta < 1$, it can be well approximated numerically, using $x_{\text{ext},\pm}(t) = \pi/2 \pm \sum_{n=0}^{\infty} b_n \sin((2n+1)\omega_T t/2)$. The amplitude $|b_n|$ of the Fourier series of the drive is shown in Fig. 5.6. As can be seen there, the roll off is fast, such that two harmonics are in many cases a sufficient approximation. In addition, the period $\frac{4\pi}{\omega_T}$ of this drive is rather long, as the resonance frequency ω_T is typically in the regime ~ 500 MHz, see Table 5.1. Due to the requirement that the resonance frequency of the ancilla oscillator should not exceed ~ 10 GHz, while there needs to be a separation of scales $\omega_A \gg \omega_T$ and ω_T should not be too small to avoid thermal excitations, this frequency range is not expected to change much for different setups. As an estimate for the most complex case with $\delta = 1$, the total error for a standard arbitrary waveform generator with 2.4 Giga-samples per second without any corrections to the signal is expected to be around 0.5%. Using either drive from Eq. (5.13), neglecting all terms rotating with frequency ω_T or above, the effective Hamiltonian from Eq. (5.10) yields the desired interaction:

$$H_{\text{on}} \approx \frac{\delta E_J \xi_T}{2} (\hat{b}^\dagger + \hat{b}) - g (\hat{b}^\dagger + \hat{b}) (2\hat{a}^\dagger \hat{a} + 1), \quad (5.14)$$

with the coupling strength $g = \frac{\delta}{2} E_J \xi_T \xi_A^2$.

5.4.2. USE OF A MICROWAVE DRIVE

In most experimental settings, it is preferable to use a microwave drive instead of a time-dependent flux. Here, we show how such a microwave drive can be used, employing a similar method as Touzard *et al.* in [26].

Consider again the Hamiltonian from Eq. (5.5), with the potential from Eq. (5.6) and a classical field $y_{\text{ext}}(t)e^{i\omega_d t}$ capacitively coupled to the ancilla oscillator. Here, the phase $e^{i\omega_d t}$ indicates the lowest frequency term of the external drive, see Section 5.4.1 for details. The system Hamiltonian is then given by

$$H_{CC} = 4E_{C_A} \left(1 - \frac{E_{C_A}}{E_{C_J}}\right) \hat{y}_A^2 + 4E_{C_T} \left(1 - \frac{E_{C_T}}{E_{C_J}}\right) \hat{y}_T^2 + \frac{i}{2} \hat{y}_A \Im(y_{\text{ext}}(t)e^{i\omega_d t}) \\ + \frac{E_{L_A} \hat{x}_A^2}{2} + \frac{E_{L_T} \hat{x}_T^2}{2} - E_J \cos(\hat{x}_T - \hat{x}_A - \pi/2),$$

where the flux x_{ext} has been set to a constant value of $\pi/2$. If we express this in terms of annihilation and creation operators, and collect all uncoupled quadratic terms into the harmonic part of the Hamiltonian, we have

$$H_{CC} = \omega_A \hat{a}^\dagger \hat{a} + \omega_T \hat{b}^\dagger \hat{b} - E_J \text{c}\ddot{\text{o}}\text{s} \left(\xi_T (\hat{b}^\dagger + \hat{b}) - \xi_A (\hat{a}^\dagger + \hat{a}) - \pi/2 \right) \\ - \frac{1}{4\xi_A} (\hat{a}^\dagger - \hat{a}) (y_{\text{ext}}^*(t)e^{-i\omega_d t} - y_{\text{ext}}(t)e^{i\omega_d t}).$$

Here, we use a notation analogous to Touzard *et al.* [26] and $\text{c}\ddot{\text{o}}\text{s}$ indicates that the second order terms $\xi_A^2 (\hat{b}^\dagger + \hat{b})^2/2$ and $\xi_T^2 (\hat{b}^\dagger + \hat{b})^2/2$ of the cosine have already been absorbed in the harmonic part of the Hamiltonian. Using the substitution $\hat{a}' = \hat{a} + \frac{1}{4\omega_A \xi_A} y_{\text{ext}}(t)e^{i\omega_d t}$, we get

$$H_{CC} = \omega_A \hat{a}'^\dagger \hat{a}' + \omega_T \hat{b}^\dagger \hat{b} - \frac{1}{4\xi_A} \left(\hat{a}'^\dagger y_{\text{ext}}^*(t)e^{-i\omega_d t} + \hat{a}' y_{\text{ext}}(t)e^{i\omega_d t} \right) \\ - E_J \text{c}\ddot{\text{o}}\text{s} \left(\xi_T (\hat{b}^\dagger + \hat{b}) - \xi_A (\hat{a}'^\dagger + \hat{a}') - \pi/2 - \frac{1}{2\omega_A} \Re(y_{\text{ext}}(t)e^{i\omega_d t}) \right).$$

The potential is again of the same form as Eq. (5.6) (if we were to write H_{CC} in terms of \hat{x}_m, \hat{y}_m again), where the microwave drive $\Re(y_{\text{ext}}(t)e^{i\omega_d t})/(2\omega_A)$ takes the role of the flux drive $x_{\text{ext}}(t)$. Note that there is an additional displacement acting on the ancilla oscillator ($\hat{a}'^\dagger, \hat{a}'$). If we go to a rotating frame and use the rotating wave approximation, this drive will vanish because it is very far off resonant (see Section 5.4.1). Note that this step means that a microwave drive can only be used to obtain an oscillating drive, in order to obtain a constant offset, it is still necessary to use a (constant) flux drive, hence why we set $x_{\text{ext}} = \pi/2$ in the beginning.

5.5. MODELING THE MODULAR QUADRATURE MEASUREMENT

In this section, we derive the effective squeezing due to the measurement protocol, averaged over all possible measurement outcomes, as a function of the number of photons in the ancilla oscillator. Our measurement model could be made more precise by including a description of the release mechanism discussed in Section 5.3.4, but this does

not change the main idea as long as the coherent state is heterodyne-measured at the end. In Section 5.6, we look at another aspect of the actual measurement as it is performed in the circuit-QED lab, namely the measurement outcome is only obtained as a time-integrated process on outgoing radiation which is leaking out of the lossy oscillator (which is in turn coupled to oscillator A via the switch discussed in Section 5.3.4). We verify that using the correct time-integration filter leads to no additional noise resulting in the same effective squeezing.

5.5.1. EFFECTIVE SQUEEZING

We will analyze a measurement of the S_q stabilizer using the photon-pressure interaction U_{PP} in Eq. (5.3). A similar measurement of S_p will commute with the measurement of S_q and will have identical features.

After the photon-pressure interaction with the target oscillator the goal is to measure the Husimi Q-function $Q(\beta) = \frac{1}{\pi} \langle \beta | \rho | \beta \rangle$ of the ancilla oscillator in single-shot fashion [22]. Such a “heterodyne” measurement of an oscillator can be modeled as a projective measurement in the overcomplete basis of coherent states [24]. The resulting coherent amplitude β has a real $\Re(\beta)$ (\propto “I”) and imaginary part $\Im(\beta)$ (\propto “Q”) and will leave some target oscillator state ρ_β . Using this measurement outcome $\beta = |\beta| \exp(i\varphi)$, one infers that the eigenvalue of S_q is $\exp(i\varphi)$. The uncertainty in this phase is captured by the phase variance which relates directly to the effective squeezing of S_q .

We assume that the initial state of the ancilla oscillator is a coherent state $|\alpha\rangle$ with $\alpha \in \mathbb{R}$. If we would apply a heterodyne measurement directly to a coherent state $|\alpha\rangle$, we expect that its outcome $\beta \in \mathbb{C}$ will be concentrated around α . In our scenario, when we apply such a measurement after the interaction U_{PP} , we obtain a measurement operator $M_\beta \equiv M_\beta(\alpha)$ corresponding to measurement result β as

$$M_\beta(\alpha) = \frac{1}{\sqrt{\pi}} \langle \beta |_A U_{PP} | \alpha \rangle_A.$$

We can evaluate the measurement operator explicitly, using that $\langle \beta | \alpha \rangle = \exp(-\frac{1}{2}|\alpha - \beta|^2) \exp(\frac{1}{2}(\beta^* \alpha - \beta \alpha^*))$, giving

$$\begin{aligned} M_\beta &= \frac{1}{\sqrt{\pi}} \langle \beta | \alpha e^{i2\sqrt{\pi}\hat{q}\hat{T}} \rangle \\ &= \frac{1}{\sqrt{\pi}} \exp\left(\frac{\alpha}{2} \left(\beta^* e^{i2\sqrt{\pi}\hat{q}} - \beta e^{-i2\sqrt{\pi}\hat{q}} \right) - \frac{1}{2} \left| \alpha e^{i2\sqrt{\pi}\hat{q}} - \beta \right|^2 \right). \end{aligned}$$

When we apply this to an initial input state ρ_{in} in the target oscillator, the output state will be $\rho_\beta = M_\beta \rho_{\text{in}} M_\beta^\dagger / \mathbb{P}(\beta)$. The probability for outcome β with the state

$$\rho_{\text{in}} = \iint_{\mathbb{R}^2} dq dq' \rho_{\text{in}}(q, q') |q\rangle\langle q'|$$

as input is given by

$$\mathbb{P}_{\rho_{\text{in}}}(\beta) = \text{Tr}\left(M_\beta^\dagger M_\beta \rho_{\text{in}}\right) = \int_{\mathbb{R}} dq \rho_{\text{in}}(q, q) \exp\left(-|\alpha e^{i2\sqrt{\pi}q} - \beta|^2\right), \quad (5.15)$$

showing that β is concentrated around the rotated α . Figure 5.2 shows this probability $\mathbb{P}_{\text{vac}}(\beta)$, starting with $\bar{n} = |\alpha|^2 = 3$ and ρ_{in} the vacuum state. It also shows the Wigner function of the resulting state ρ_β for which $\mathbb{P}_{\text{vac}}(\beta)$ is maximal. Using the definition $\varphi \equiv \arg(\beta)$, an alternative way of writing M_β is

$$M_\beta = \frac{1}{\sqrt{\pi}} e^{-\frac{1}{2}(|\alpha|^2 + |\beta|^2)} \exp\left(\frac{K_{|\beta|}}{2} e^{i(2\sqrt{\pi}\hat{q} - \varphi)}\right), \quad (5.16)$$

defining the concentration parameter

$$K_{|\beta|} = 2|\alpha\beta|. \quad (5.17)$$

This leads to

$$M_\beta^\dagger M_\beta = \frac{1}{\pi} e^{-|\alpha|^2 - |\beta|^2} \exp(K_{|\beta|} \cos(2\sqrt{\pi}\hat{q} - \varphi)). \quad (5.18)$$

Because the measurement outcome is random, we are interested in the mean effective squeezing of the final state ρ_β , averaged over all possible outcomes β . This is hard to compute in the general case, although it can easily be evaluated numerically, see Fig. 5.7. The details of the numerical simulations and an error analysis are presented in Appendix A.1.3. Analytically, even for a vacuum state input, the computation of the mean effective squeezing $\langle \Delta_q \rangle = \int_{\mathbb{C}} d^2\beta \Delta_q(\rho_\beta)$ is non-trivial. For this reason, we consider the mean or average *sharpness* which equals $|\text{Tr}(S_q \rho_\beta)|$ averaged over different outcomes β , that is, we focus on estimating

$$\langle |\text{Tr}(S_q)| \rangle \equiv \int_{\mathbb{C}} d^2\beta \mathbb{P}(\beta) |\text{Tr}(S_q \rho_\beta)|. \quad (5.19)$$

It should be observed that $\int_{\mathbb{C}} d^2\beta |\text{Tr}(S_q \rho_\beta)| \neq \int_{\mathbb{C}} d^2\beta \text{Tr}(S_q \rho_\beta) = |\text{Tr}(S_q \rho_{\text{in}})|$ as $\text{Tr}(S_q \rho_\beta)$ is complex.

For the special case where the initial state is the vacuum state, it is possible to evaluate Eq. (5.19) explicitly. In this case, we have

$$\begin{aligned} \langle |\text{Tr}(S_q)| \rangle &\approx \int_{|\beta|_c}^{\infty} d|\beta| \frac{e^{-\pi}}{\pi \sqrt{2K_{|\beta|}\pi}} e^{-(|\alpha| - |\beta|)^2} \\ &\quad \times \int_{-\pi}^{\pi} d\varphi \left| \vartheta_3\left(i\pi - \frac{\varphi}{2}, e^{-\pi - 1/(2K_{|\beta|})}\right) \right|, \end{aligned} \quad (5.20)$$

see Section 5.7 for the derivation. Combining this result with the expression for Δ_q , we obtain the blue curve in Fig. 5.7.

5.5.2. MEASUREMENT SQUEEZING STRENGTH

If the initial state in the target oscillator is arbitrary, it is not possible to analytically evaluate the mean sharpness in Eq. (5.19). Moreover, we are interested in a quality measure of the measurement protocol which is *independent* of the initial state. To address this, we can use that the parameter $K_{|\beta|}$ has a very simple relation to the effective squeezing. If we assume an (unphysical) uniform distribution over q as initial state, then the final

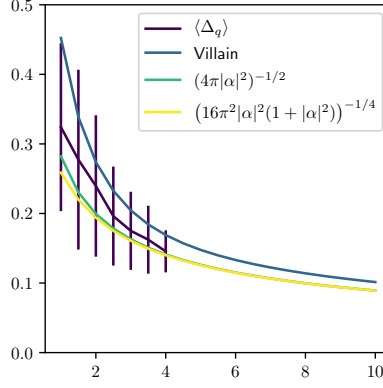


Figure 5.7: Purple: We numerically simulate the average amount of squeezing Δ_q (see Eqs. 5.1) obtained using a coherent state $|\alpha\rangle$ with $\bar{n} = |\alpha|^2$ photons to measure S_q on a vacuum input state. In more detail, we generate a β and ρ_β and calculate $\Delta_q(\rho_\beta)$, the error bars indicate the standard deviation over different measurement results β . Blue: Mean effective squeezing estimate according to Eq. (5.20), using the Villain approximation to evaluate the expectation value for the sharpness on a vacuum state. Green: A simple approximate expression for the mean effective squeezing is $\langle\Delta_q\rangle \approx 1/\sqrt{4\pi|\alpha|^2}$. Yellow: A lower bound on the green curve which replaces the average value $\langle|\beta|\rangle$ by $\sqrt{\langle|\beta|^2\rangle}$. Overall, the mean squeezing parameter goes down as $1/\sqrt{\bar{n}}$ where \bar{n} is the average number of photons in the ancilla state used to implement the modular q -measurement. Previously published in D. J. Weigand and B. M. Terhal, “Realizing modular quadrature measurements via a tunable photon-pressure coupling in circuit QED”, *Physical Review A* **101**, 053840 (2020), licensed under CC-BY 4.0 [21] © ⓘ.

state of the protocol will be of the form $|\psi_\beta\rangle \propto \int_{\mathbb{R}} dq M_\beta |q\rangle$. Using Eq. (5.18), we see that the outgoing wave function has probability distribution $\mathbb{P}(q) \propto M_\beta^\dagger M_\beta$, proportional to a von-Mises probability density $P_{VM}(x)$ with angle variable $x = 2\sqrt{\pi}q \bmod 2\pi$, mean φ and concentration $K_{|\beta|}$. The variance of the von-Mises distribution is approximately $1/K_{|\beta|}$ for large $K_{|\beta|}$. If we convert this to an effective squeezing in q , we therefore have $\Delta_q \approx \sqrt{1/(2\pi K_{|\beta|})}$.

Because the average concentration is given by $\langle K_{|\beta|} \rangle = 2\alpha \langle |\beta| \rangle$ due to Eq. (5.17), computing the expected value for $|\beta|$ gives a measure of how effectively squeezed the outgoing state will be. To estimate $\langle f(|\beta|) \rangle$ where $f(x)$ is some function, we note the following useful property which we prove as a lemma:

Lemma 5.5.1. *The input state in the target cavity ρ_{in} does not influence the expectation of any function $f(|\beta|)$ where β is the outcome of (heterodyne)-measuring in the ancilla mode in an overcomplete coherent basis.*

Proof. For a general input state ρ_{in} , we have:

$$\begin{aligned} \langle f(|\beta|) \rangle &= \int_{\mathbb{C}} d^2\beta \mathbb{P}_{\text{in}}(\beta) f(|\beta|) \\ &= \int_0^\infty d|\beta| |\beta| f(|\beta|) \int_{-\pi}^\pi d\varphi \mathbb{P}_{\rho_{\text{in}}}(|\beta| e^{i\varphi}) \\ &= \int_0^\infty d|\beta| |\beta| f(|\beta|) \int_{-\pi}^\pi d\varphi \text{Tr}(M_\beta^\dagger M_\beta \rho_{\text{in}}). \end{aligned}$$

We can use the Jacobi-Anger expansion

$$\begin{aligned}\exp(iz \cos(\theta)) &= \sum_{n \in \mathbb{Z}} i^n J_n(z) e^{in\theta} \\ &= J_0(z) + 2 \sum_{n=1}^{\infty} i^n J_n(z) \cos(n\theta),\end{aligned}$$

where $J_n(z)$ is the Bessel function of the first kind and using $J_{-n}(z) = (-1)^n J_n(z)$. The modified Bessel function of the first kind $I_n(z)$ is defined as $I_n(z) = i^{-n} J_n(iz)$ and it follows that $\exp(b \cos(x)) = \sum_{n \in \mathbb{Z}} I_n(b) \exp(inx)$ where $I_n(b)$ is the modified Bessel function of the first kind of order n . We can then use Eq. (5.18) to write

$$\begin{aligned}\int_{-\pi}^{\pi} d\varphi \operatorname{Tr}(M_{\beta}^{\dagger} M_{\beta} \rho_{\text{in}}) &= \frac{1}{\pi} e^{-|\alpha|^2 - |\beta|^2} \\ &\times \sum_{n \in \mathbb{Z}} \int dq \rho_{\text{in}}(q) I_n(K_{\beta}) e^{in2\sqrt{\pi}q} \int_{-\pi}^{\pi} d\varphi e^{-in\varphi}.\end{aligned}\quad (5.21)$$

The integral over φ leads to $n = 0$ being the only surviving term in $\sum_{n \in \mathbb{Z}}$, thus removing all dependence on ρ_{in} in the integral over q . Hence

$$\langle f(|\beta|) \rangle = 2e^{-|\alpha|^2} \int_0^{\infty} d|\beta| |\beta| f(|\beta|) e^{-|\beta|^2} I_0(K_{\beta}), \quad (5.22)$$

independent of ρ_{in} . □

Equation (5.22) allows us to get an expression for $\langle |\beta| \rangle$ as

$$\begin{aligned}\langle |\beta| \rangle &= 2e^{-|\alpha|^2} \int_0^{\infty} d|\beta| e^{-|\beta|^2} |\beta|^2 I_0(2\alpha|\beta|) \\ &= \frac{\sqrt{\pi}}{2} e^{-|\alpha|^2/2} \left[I_0\left(\frac{|\alpha|^2}{2}\right) + \alpha^2 I_0\left(\frac{|\alpha|^2}{2}\right) + \alpha^2 I_1\left(\frac{|\alpha|^2}{2}\right) \right],\end{aligned}\quad (5.23)$$

which for $\alpha \geq \sqrt{2}$ is virtually indistinguishable from $\langle |\beta| \rangle \approx \alpha$, as expected. Therefore, the expected effective squeezing can be approximated as $\langle \Delta_q \rangle \approx 1/\sqrt{4\pi|\alpha|^2}$ as plotted in Fig. 5.7. Fluctuations around this expected value are determined by

$$\begin{aligned}\langle |\beta|^2 \rangle &= 2e^{-|\alpha|^2} \int_0^{\infty} d|\beta| e^{-|\beta|^2} |\beta|^3 I_0(2\alpha|\beta|) \\ &= 1 + |\alpha|^2,\end{aligned}\quad (5.24)$$

so that $\operatorname{Var}(|\beta|) = \langle (|\beta| - \langle |\beta| \rangle)^2 \rangle \approx 1$. Since $\langle |\beta| \rangle \leq \sqrt{\langle |\beta|^2 \rangle}$, we can also use a squeezing lower bound which reads $\sqrt{1/(4\pi|\alpha|\sqrt{1+|\alpha|^2})}$ using that $\langle |\beta|^2 \rangle = 1 + |\alpha|^2$.

As expected, these statistics are identical to that of a direct overcomplete measurement in the coherent basis applied to a state $|\alpha\rangle$, i. e. without any coupling to a target oscillator. The only dependence on ρ_{in} is found in the phase φ . Figure 5.7 shows that these state-independent bounds are in good agreement with numerics as well as our analytical approximation when the input state is the vacuum state. In conclusion, the amplitude of the measurement result $|\beta|$ correlates with the accuracy of the measurement, the phase gets more precisely resolved the larger the measured coherent state is. Thus, the expectation value $\langle |\beta| \rangle$ gives an indirect, but easily accessible way to estimate the effective squeezing by the measurement.

5.6. HETERODYNE MEASUREMENT VIA RELEASE OF COHERENT OSCILLATOR STATE INTO A TRANSMISSION LINE

Here, we model the gradual release of the cavity state into a mobile wave packet traveling over a 1D transmission line or waveguide by an effective model. Our goal is to verify that the integration of a heterodyne measurement signal on small coherent states released *over time* can effectively give the same measurement operator as the direct heterodyne measurement of Section 5.5.1. This is not immediately obvious. Given a long enough measurement time t_{meas} , even if all photons in the oscillator are eventually measured to determine the angle, there are two combining features which could make such a measurement fundamentally more noisy than a direct heterodyne measurement and hence leading to less effective squeezing. Firstly, the instantaneous measurement is applied to a *small* coherent state, i. e. the one that arrives during a small interval in time, which has *large* angle uncertainty. Secondly, the overall output of the measurement is only a weighted *integration* of the heterodyne signal obtained from each small coherent state, i. e. we assume that we gain no knowledge of the individual trajectory of outcomes, but only integrate (using a filter) their values in time, see Eq. (5.25) below (although one could go beyond this and look at full trajectories, see [38, 39]). Note that in this effective model we do not include additional losses nor the amplification step in the measurement chain as we discuss their effect in Section 5.8.3. Naturally, due to the sequence of amplifiers and bringing the signal up to room temperature electronics, the actual states which are measured are not small coherent states, but classical voltage signals, but their quantum fluctuations are frozen in as classical noise.

In our analysis, we also do not include a spurious photon-pressure coupling (and hence a possible rotation) to the target oscillator during the release of the state in the ancilla oscillator. Naturally, if the oscillator state is further rotated while it is also being released, then this is likely to lead to additional noise in the measurement as the to-be-measured-phase is changing in each of the weak measurements in sequence.

Our model is that of a sequence of N beam splitter interactions with coupling strength $\sqrt{\delta t \times \kappa_{\text{open}}}$ between the ancilla oscillator and individual “measure” modes $j = 0, 1, \dots, J - 1$ which are each initialized in a vacuum state. For a non-tunable fixed set-up, the decay rate κ_{open} is determined by the capacitive coupling between ancilla oscillator and transmission line and enters a more complete Hamiltonian description of such an interaction, see e. g. Appendix A in [25]. When one uses a switch mechanism as in [36], one can use an effective decay rate $\kappa_{\text{open}} = 4\lambda^2/\kappa_{\text{out}}$ when $\lambda \ll \kappa_{\text{out}}$ where λ is the strength of the beam-splitter coupling to the lossy oscillator and κ_{out} is the decay rate of the lossy oscillator (set by its coupling strength to some transmission line, co-planar wave guide or co-axial cable hosting 1D continuous traveling modes).

The idea is that one has a beam-splitter interaction between oscillator mode and transmission line mode localized at a point in space: This interaction puts some of the coherent amplitude in this spatial mode which due to the transmission-line Hamiltonian propagates away at (speed of light) velocity v , returning the local spatial mode to the vacuum, see Appendix E, Section 2 pp. 73–77 in [40] for this perspective of the interaction of a (cavity) oscillator with the bath modes on the transmission line. Hence, the measure mode j will model the state that one can measure at time $t = j\delta t$ at a fixed spatial point

on the transmission line where the detector sits: A new measure mode is arriving at the detector after each time-step δt . We will take the continuum limit $\delta t \rightarrow 0$ and $J \rightarrow \infty$ in our expressions while keeping the total measurement time $t_{\text{meas}} = \delta t J$ finite. Note that we could include thermal noise in this model by having each measure mode initialized in a thermal state instead of a vacuum state. We will assume that each measure mode j undergoes a complete heterodyne measurement, providing an outcome β_j . In addition, we omit any time-dependence of the ancilla oscillator or the measure modes, i. e. our expressions assume that we work in a rotating frame at the ancilla oscillator frequency.

The outcome of the measurement is an estimate of the time-integrated (dimensionless) quadratures I_{out} and Q_{out} which we define as

$$\begin{aligned} I_{\text{out}} &= \sqrt{2\kappa_{\text{open}}} \int_0^{t_{\text{meas}}} dt f(t) \Re(\beta(t)), \\ Q_{\text{out}} &= \sqrt{2\kappa_{\text{open}}} \int_0^{t_{\text{meas}}} dt f(t) \Im(\beta(t)), \end{aligned} \quad (5.25)$$

where $f(t) = \exp(-\kappa_{\text{open}} t/2)$. For now, this choice of integration weight is arbitrary, we will show its justification in the following. The function $\beta(t)$ is the continuum limit of the outputs β_j detailed below. To make contact with the usual input-output formalism in which we have an outgoing field $\hat{b}_{\text{out}}(t) = \sqrt{\kappa_{\text{open}}} \hat{a}(t)$ for the cavity field \hat{a} [40] (represented here by the ancilla oscillator), we observe that the expected value $\langle I_{\text{out}} \rangle = \int_0^{t_{\text{meas}}} dt \langle \hat{q}_{\text{out}}(t) \rangle$ where $\hat{q}_{\text{out}}(t) = \frac{1}{\sqrt{2}}(\hat{b}_{\text{out}}(t) + \hat{b}_{\text{out}}^\dagger(t))$ (and similarly $\langle Q_{\text{out}} \rangle = \int_0^{t_{\text{meas}}} dt \langle \hat{p}_{\text{out}}(t) \rangle$). The superoperator represented by this measurement is thus given as

$$\mathcal{S}_{Q_{\text{out}}, I_{\text{out}}}(\rho_{\text{in}}) = \frac{\int_{Q_{\text{out}}, I_{\text{out}}} d\boldsymbol{\beta} M_{\boldsymbol{\beta}} \rho_{\text{in}} M_{\boldsymbol{\beta}}^\dagger}{\text{Tr} \left(\int_{Q_{\text{out}}, I_{\text{out}}} d\boldsymbol{\beta} M_{\boldsymbol{\beta}}^\dagger M_{\boldsymbol{\beta}} \rho_{\text{in}} \right)},$$

where a sequence of outcomes β_j , $j = 0, \dots, J-1$ is collectively denoted as a vector $\boldsymbol{\beta}$, and the integral goes over all $\boldsymbol{\beta}$ leading to integrated signal Q_{out} and I_{out} . Based on I_{out} and Q_{out} , the measurement estimates the eigenvalue $\exp(i\varphi)$ of S_q as $\varphi_{\text{out}} = \arctan(Q_{\text{out}}/I_{\text{out}})$. If we were to use a Q-switch and a lossy oscillator, the temporal profile of the outgoing field would not be the exponentially-decaying function $f(t)$ as the ancilla oscillator first has to build up some amplitude in the lossy oscillator before leaking out of it, and one could use such a compensated time-filter as in Eq. (S6) of [36].

Now let us consider the details of this measurement. Our expressions will depend on $\kappa_{\text{open}} t_{\text{meas}}$ which we assume to be large, capturing the fact that we measure until the coherent state has (almost) entirely leaked out of the ancilla oscillator. Each beam splitter interaction B applies a simple transformation on a coherent state $|\beta\rangle$ in the ancilla oscillator and a measure mode j :

$$\begin{aligned} B |\beta\rangle_A \otimes |0\rangle_j &= \left| \beta \cos(\sqrt{\kappa_{\text{open}} \delta t}) \right\rangle_A \left| \beta \sin(\sqrt{\kappa_{\text{open}} \delta t}) \right\rangle_j \\ &\approx \left| \beta \sqrt{1 - \kappa_{\text{open}} \delta t} \right\rangle_A \left| \beta \sqrt{\kappa_{\text{open}} \delta t} \right\rangle_j. \end{aligned}$$

Let us write down the heterodyne measurement operator $M_{\boldsymbol{\beta}}$ as a function of $\boldsymbol{\beta}$. Note that the state of the ancilla oscillator and the measure modes after J beam splitters

equals

$$B_{j-1} \dots B_2 B_0 |\alpha\rangle_A |0\rangle_{j-1} \dots |0\rangle_2 |0\rangle_0 = |\alpha(1 - \kappa_{\text{open}} \delta t)^{J/2}\rangle_A \prod_{j=0}^{J-1} |\alpha_j\rangle_j,$$

$$\alpha_j \equiv \alpha(\kappa_{\text{open}} \delta t)^{1/2} (1 - \kappa_{\text{open}} \delta t)^{j/2} \in \mathbb{R}.$$

As the measure modes $j = 0, \dots, J-1$ do not couple, the total measurement operator on the measure modes is simply a product over all modes. The measurement operator equals (using $\langle \beta | \alpha \rangle = \exp(-(|\alpha|^2 + |\beta|^2)/2) \exp(\beta^* \alpha)$):

$$\begin{aligned} M_{\beta} &= \frac{1}{\pi^{J/2}} \prod_{j=0}^{J-1} \langle \beta_j | \exp(i2\sqrt{\pi} \hat{q}) \alpha_j \rangle \\ &= \frac{1}{\pi^{J/2}} \exp\left(-\frac{1}{2} \sum_{j=0}^{J-1} (|\alpha_j|^2 + |\beta_j|^2)\right) \exp\left(\sum_{j=0}^{J-1} \alpha_j \beta_j^* \exp(i2\sqrt{\pi} \hat{q})\right) \\ &= \frac{1}{\pi^{J/2}} \exp\left(-\frac{1}{2} \sum_{j=0}^{J-1} (|\alpha_j|^2 + |\beta_j|^2)\right) \exp\left(\sum_{j=0}^{J-1} K_{|\beta_j|} \cos(2\sqrt{\pi} \hat{q} - \varphi_j)/2\right) \\ &\quad \times \exp\left(i \sum_{j=0}^{J-1} K_{|\beta_j|} \sin(2\sqrt{\pi} \hat{q} - \varphi_j)/2\right), \end{aligned} \quad (5.26)$$

using $K_{|\beta_j|} = 2\alpha_j |\beta_j|$. Not surprisingly, we see that the measurement operator has the same form as in Eq. (5.16). If we take the continuum limit, we note that the \hat{q} -dependent part in M_{β} does not explicitly depend on the measurement results β , but on a time-integrated average over the results as follows. We have

$$\begin{aligned} \sum_{j=0}^{J-1} \alpha_j \beta_j^* &= \sum_{j=0}^{J-1} \delta t \alpha \sqrt{\kappa_{\text{open}}} (1 - \kappa_{\text{open}} \delta t)^{j/2} \frac{\beta_j^*}{\sqrt{\delta t}} \\ &\rightarrow \int_0^{t_{\text{meas}}} dt \alpha(t) \beta^*(t), \end{aligned}$$

where we have defined $\beta(t) = \sqrt{\frac{\beta_j}{\delta t}}$ and $\alpha(t) = \alpha \sqrt{\kappa_{\text{open}}} e^{-\kappa_{\text{open}} t/2}$. Note that $\alpha(t)$ and $\beta(t)$ have dimension $t^{-1/2}$. Thus, the \hat{q} -dependent part of M_{β} is—in the continuum limit—proportional to

$$\exp\left(\int_0^{t_{\text{meas}}} dt \alpha(t) \beta^*(t) S_q\right) = e^{\frac{\alpha}{\sqrt{2}} (I_{\text{out}} - iQ_{\text{out}}) S_q}.$$

Since $\sum_j |\beta_j|^2 \rightarrow \int_0^{t_{\text{meas}}} dt |\beta(t)|^2$ and

$$\begin{aligned} \sum_j |\alpha_j|^2 &\rightarrow \kappa_{\text{open}} |\alpha|^2 \int_0^{t_{\text{meas}}} dt \exp(-\kappa_{\text{open}} t) \\ &= |\alpha|^2 (1 - \exp(-\kappa_{\text{open}} t_{\text{meas}})) \approx |\alpha|^2, \end{aligned}$$

the prefactor in M_{β} does depend on $\int_0^{t_{\text{meas}}} dt |\beta(t)|^2$, not only on Q_{out} and I_{out} . The conclusion is that by using an exponentially-decaying filter on the measured data as in

Eq. (5.25), one can ensure that a single measurement operator is applied on the input state given the measurement output $I_{\text{out}}, Q_{\text{out}}$ and this measurement operator does not depend on the specific temporal noisy sequence $\beta_0, \dots, \beta_{J-1}$. Hence, we expect that the effect of this integrated measurement in time does not lead to a more noisy outcome than one in which we record the entire sequence of values $\beta_0, \dots, \beta_{J-1}$.

We can make this explicit by estimating the effective squeezing as we have done in Section 5.5.1 for the direct measurement. We can find

$$M_{\beta}^{\dagger} M_{\beta} \propto \exp\left(\alpha \sqrt{2(Q_{\text{out}}^2 + I_{\text{out}}^2)} \cos(2\sqrt{\pi} \hat{q} - \varphi_{\text{out}})\right),$$

which defines an effective concentration $K_{\text{eff}} = \alpha \sqrt{2(Q_{\text{out}}^2 + I_{\text{out}}^2)}$. Hence, in analogy with the direct measurement where the effective squeezing is estimated by considering $\langle |\beta| \rangle$, here the goal is to estimate the expected value of K_{eff} . Translating back to the discrete representation, this requires estimating $\langle |\sum_j \alpha_j \beta_j^*| \rangle$. Instead of estimating this quantity directly, we evaluate $\sqrt{\langle |\sum_j \alpha_j \beta_j^*|^2 \rangle} \propto \sqrt{\langle Q_{\text{out}}^2 + I_{\text{out}}^2 \rangle}$ and obtain a lower bound on the effective squeezing in this manner.

Using the discrete sequence-of-measurements representation, it can be observed that the entire measurement is a simple product of individual measurements, each with outcome β_j , applied to a product state. Similar to the proof of Lemma 5.5.1, we first observe that

$$\begin{aligned} \left\langle \left| \sum_k \alpha_k \beta_k^* \right|^2 \right\rangle &= \int d\beta \mathbb{P}_{\text{in}}(\beta) \sum_{k,l} \alpha_k \alpha_l |\beta_k| |\beta_l| \exp(i(\varphi_k - \varphi_l)) \\ &= \sum_{k,l} \alpha_k \alpha_l \text{Tr} \prod_{j=0}^{J-1} \int d|\beta_j| |\beta_j| |\beta_k| |\beta_l| \int_{-\pi}^{\pi} d\varphi_j M_{\beta_j}^{\dagger} M_{\beta_j} \rho_{\text{in}} \exp(i(\varphi_k - \varphi_l)) \end{aligned}$$

with

$$\begin{aligned} M_{\beta_j}^{\dagger} M_{\beta_j} &= \frac{1}{\pi} e^{-|\alpha_j|^2 - |\beta_j|^2} \exp\left(K_{\beta_j} \cos(2\sqrt{\pi} \hat{q} - \varphi_j)\right) \\ &= \frac{1}{\pi} e^{-|\alpha_j|^2 - |\beta_j|^2} \sum_{n_j \in \mathbb{Z}} I_{n_j}(K_{\beta_j}) S_q^{n_j} \exp(-in_j \varphi_j). \end{aligned}$$

When $k = l$, we see that the integrals over φ_j lead to delta-functions at $n_j = 0$ and the dependence on ρ_{in} drops out as we can use $\text{Tr}(\rho_{\text{in}}) = 1$. For $k \neq l$, we project onto $n_l = -1$ and $n_k = +1$, picking up $I_{-1}(2\alpha_l |\beta_l|) S_q^{-1}$ and $I_1(2\alpha_k |\beta_k|) S_q$ factors. For $k \neq l$, we thus always apply a product $S_q S_q^{-1} = \mathbb{1}$ and again the dependence on ρ_{in} drops out. Using that $I_{-1}(x) = I_1(x)$, we get

$$\begin{aligned}
 \left\langle \left| \sum_k \alpha_k \beta_k^* \right|^2 \right\rangle &= 2^J \sum_{k=0}^{J-1} |\alpha_k|^2 \int_0^\infty d|\beta_k| |\beta_k|^3 e^{-|\alpha_k|^2 - |\beta_k|^2} I_0(2\alpha_k |\beta_k|) \\
 &\quad \times \prod_{j=0: j \neq k}^{J-1} \int_0^\infty d|\beta_j| |\beta_j| e^{-|\alpha_j|^2 - |\beta_j|^2} I_0(2\alpha_j |\beta_j|) \\
 &\quad + \sum_{k \neq l=0}^{J-1} \alpha_k \alpha_l \int_0^\infty d|\beta_k| |\beta_k|^2 e^{-|\alpha_k|^2 - |\beta_k|^2} I_1(2\alpha_k |\beta_k|) \\
 &\quad \times \int_0^\infty d|\beta_l| |\beta_l|^2 \exp(-\alpha_l^2 - |\beta_l|^2) I_1(2\alpha_l |\beta_l|) \\
 &\quad \times \prod_{j=0: j \neq k, j \neq l}^{J-1} \int_0^\infty d|\beta_j| |\beta_j| e^{-|\alpha_j|^2 - |\beta_j|^2} I_0(2\alpha_j |\beta_j|).
 \end{aligned}$$

The integrals can be simplified using $\int_0^\infty dx x \exp(-x^2 - y^2) I_0(2yx) = 1$, Eq. (5.24) and $2 \int_0^\infty dx x^2 \exp(-y^2 - x^2) I_1(2yx) = y$ to

$$\begin{aligned}
 \left\langle \left| \sum_k \alpha_k \beta_k^* \right|^2 \right\rangle &= \sum_k |\alpha_k|^2 (1 + |\alpha_k|^2) + \sum_{k \neq l} |\alpha_k|^2 |\alpha_l|^2 = \sum_k |\alpha_k|^2 + \left(\sum_k |\alpha_k|^2 \right)^2 \\
 &\rightarrow |\alpha|^2 (1 - e^{-\kappa_{\text{open}} t_{\text{meas}}}) (1 + |\alpha|^2 (1 - e^{-\kappa_{\text{open}} t_{\text{meas}}})) .
 \end{aligned}$$

Thus, when the measurement time is long enough so that the entire state has leaked out, $\kappa_{\text{open}} t_{\text{meas}} \gg 1$, we can upper bound the expected $K_{\text{eff}} \leq 2|\alpha|/\sqrt{1 + |\alpha|^2}$, resulting in a lower bound on Δ_q equal to $1/\sqrt{4\pi|\alpha|\sqrt{1 + |\alpha|^2}}$. For long enough t_{meas} , this is identical to our result for the direct measurement, which we have shown is closely related to the actual amount of squeezing in Fig. 5.7.

5.7. EFFECTIVE SQUEEZING WITH VACUUM INPUT STATE

In Section 5.5, we derived approximations for the effective squeezing after the measurement protocol because the average sharpness as in Eq. (5.19) is hard to evaluate.

Since S_q commutes with M_β we have

$$\langle |\text{Tr}(S_q)| \rangle = \int_{\mathbb{C}} d^2 \beta |\langle \text{vac} | S_q M_\beta^\dagger M_\beta | \text{vac} \rangle| \quad (5.27)$$

$$= \frac{1}{\pi \sqrt{\pi}} \int_{\mathbb{C}} d^2 \beta e^{-|\alpha|^2 - |\beta|^2} \left| \int_{\mathbb{R}} dq e^{-q^2 + i2\sqrt{\pi}q + K_{|\beta|} \cos(2\sqrt{\pi}q - \varphi)} \right|. \quad (5.28)$$

At $b \geq 2$, one can use the convenient Villain approximation [41]:

$$\exp(b \cos(x)) \approx \sum_{n \in \mathbb{Z}} \exp(b) \exp\left(-\frac{b}{2}(x - 2\pi n)^2\right).$$

For large $K_{|\beta|}$, the dominant contribution comes from small values of $|n|$: For $K_{|\beta|} \geq 2$, one can restrict the sum to $n = 0, \pm 1, \pm 2$ with $-\pi \leq \varphi \leq \pi$.

If we assume that the outcomes of β are concentrated around values where the Villain approximation holds (which is reasonable since we know that $\mathbb{P}(\beta)$ is concentrated around $|\beta| = \alpha$ from Eq. (5.15)), then one can apply this approximation and evaluate the resulting Gaussian integral to get

$$\begin{aligned} \langle |\text{Tr}(S_q)| \rangle &\approx \int_{|\beta|_c}^{\infty} d|\beta| \frac{e^{-\pi}}{\pi \sqrt{2K|\beta|}\pi} e^{-(|\alpha|-|\beta|)^2} \\ &\times \int_{-\pi}^{\pi} d\varphi \left| \vartheta_3 \left(i\pi - \frac{\varphi}{2}, e^{-\pi - 1/(2K|\beta|)} \right) \right|. \end{aligned} \quad (5.29)$$

Here, $\vartheta_3(z, q) = \sum_{n \in \mathbb{Z}} q^{n^2} e^{2inz}$ is the theta function and $|\beta|_c$ is a lower cut-off to allow for the Villain approximation. The lower cut-off $|\beta|_c$ is chosen such that firstly $\mathbb{P}(|\beta| < |\beta|_c) \ll 1$, and secondly $|\alpha\beta|_c \geq 1$ to allow for the Villain approximation with $K_{|\beta|} \geq 2$. We take $|\beta|_c = 1/|\alpha|$ so that for $\bar{n} \geq 5$ the probability for such $|\beta|_c$ is low (suppressed by $\exp(-(\sqrt{5} - 1/\sqrt{5})^2) \approx 0.04$). The function $\vartheta_3(z, q)$ is oscillatory with n , but contributions beyond $n = 0, \pm 1, \pm 2$ are negligible. Inserting the mean sharpness with its approximation in Eq. (5.29) in the expression for Δ_q , we obtain the purple curve in Fig. 5.7.

We can also consider the eigenvalue phase of S_q of the output state ρ_β , i.e.

$$\arg(\langle S_q \rangle) = \arg \left(\int_{\mathbb{R}} dq \rho_{\text{in}}(q, q) S_q e^{K_{|\beta|} \cos(2\sqrt{\pi}q - \varphi)} \right). \quad (5.30)$$

When $\rho_{\text{in}}(q, q)$ is a uniform distribution, i. e. there is no prior bias for \hat{q} (or S_q), the integral over q results in $\exp(i\varphi)$, confirming that the best choice for inferring the eigenvalue of S_q is indeed $\exp(i\varphi)$. If we have prior information on the input state to the measurement, e. g. it is the vacuum state, then one can use Eq. (5.30) as the outcome of the measurement.

As a sanity check we examine $\langle |\text{Tr}(S_p)| \rangle$ (or $\langle |\text{Tr}(X)| \rangle$) after the modular q -measurement. First of all, note that the expectation $\int_{\mathbb{C}} d^2\beta \text{Tr}(S_p \rho_\beta)$ is unchanged, since S_p commutes with the S_q -measurement, so $\int_{\mathbb{C}} d^2\beta \text{Tr}(S_p \rho_\beta) = \text{Tr}(S_p \rho_{\text{in}})$. Thus for the output state, the squeezing of S_p (or X) is unchanged as expected. In addition, if we consider the mean sharpness we can also see it is preserved when we start with the vacuum state:

$$\begin{aligned} \langle |\text{Tr}(S_p)| \rangle &= \int_{\mathbb{C}} d^2\beta |\langle \text{vac} | S_p M_\beta^\dagger M_\beta | \text{vac} \rangle| \\ &= \langle \text{vac} | S_p | \text{vac} \rangle = \exp(-\pi). \end{aligned}$$

Here, we used the fact that $\langle \psi | S_p M_\beta^\dagger M_\beta | \psi \rangle$ is nonnegative for any state $|\psi\rangle$ whose wave function is nonnegative in the q -basis, i. e. $\psi(q) \geq 0$, so we can omit the absolute value and use $\int_{\mathbb{C}} d^2\beta M_\beta^\dagger M_\beta = I$. One should observe that the preservation of the mean sharpness does not automatically follow from the commutation of S_p with M_β or M_β^\dagger .

5.8. NOISE AND IMPERFECTIONS

As compared to a perfect heterodyne measurement of the rotated coherent state in the ancilla oscillator, there will be several sources of loss and imperfections in the modular

quadrature measurement. In the sections below, we discuss the effect of photon loss on the ancilla and target oscillators as a change in the effective squeezing parameters. Importantly, photon loss on the ancilla oscillator during the photon-pressure coupling is an immediate cause for feedback dephasing errors, similar as when preparing a grid state via coupling to a transmon ancilla qubit [13]. Loss during read-out in the heterodyne measurement chain simply reduces the effective α that is used in the protocol, diminishing the strength of the measurement.

After the discussions on photon loss, we investigate the leading nonlinear term acting on the target oscillator in Section 5.8.5. As the nonlinear term only acts during the interaction of the target and ancilla oscillators, it acts as an additional unitary operation. We discuss and numerically simulate its effect as a change of the effective squeezing parameters.

Finally, we investigate the effect of flux noise during the interaction, as the coupling Hamiltonian between the target and ancilla oscillators depends on an external flux. A small, quasi-static flux offset has the effect that the measured quadrature is slightly rotated, i.e. a flux offset ϵ means that the photon-pressure Hamiltonian is changed to $\tilde{H}_{\text{pp}} \sim \hat{a}^\dagger \hat{a} (\cos(\epsilon) \hat{q} \pm i \sin(\epsilon) \hat{p})$. We will see that the parametric drive already provides a first order correction to this type of noise because the sign in the modified Hamiltonian \tilde{H}_{pp} changes with frequency ω_T , which is large compared to $1/t_{\text{coupl}}$.

5.8.1. PHOTON LOSS IN ANCILLA OSCILLATOR DURING PHOTON-PRESSURE INTERACTION

Imagine that prior to the heterodyne measurement to measure S_q , but during the action of the photon-pressure coupling U_{pp} , photon loss occurs from the ancilla resonator at rate κ_c . This error will feedback to the target oscillator as a dephasing error in the $|q\rangle$ basis and such a dephasing error will affect Δ_p . In addition, photon loss affects the quality of the S_q measurement itself by effectively reducing the amplitude of the coherent state which is used in the measurement.

We assume that we are in the targeted regime, in which there is at most a single photon loss error in a time t_{coupl} , or $\kappa_c t_{\text{coupl}} |\alpha|^2 \ll 1$. Let $\gamma = \kappa_c t_{\text{coupl}}$. The no-photon loss operator $E_0 = \mathbb{1} - \gamma \hat{n}/2 \approx \exp(-\gamma \hat{n}/2)$ commutes with the evolution of H_{pp} , but the single-photon loss operator $E_1 = \sqrt{\gamma} \hat{a}$ does not. Hence, the state of ancilla and target oscillator at time t is

$$\begin{aligned} \rho(t) &= e^{-\gamma \hat{n}/2 - i2\sqrt{\pi} \hat{q} \hat{n}} \rho_{\text{in}} \otimes |\alpha\rangle\langle\alpha| e^{-\gamma \hat{n}/2 + i2\sqrt{\pi} \hat{q} \hat{n}} \\ &\quad + \kappa_c \int_0^{t_{\text{coupl}}} dt A(t) \rho_{\text{in}} \otimes |\alpha\rangle\langle\alpha| A^\dagger(t), \\ A(t) &= e^{-i(2\sqrt{\pi} - t\sqrt{2}g) \hat{q} \hat{n}} a e^{-it\sqrt{2}g \hat{q} \hat{n}}. \end{aligned} \quad (5.31)$$

When we apply the heterodyne measurement to the ancilla oscillator and obtain outcome β , we thus transform ρ_{in} as

$$\begin{aligned} \rho_{\text{in}} \rightarrow \rho_\beta &= (1 - \alpha^2 \gamma) M_\beta(\alpha e^{-\gamma}) \rho_{\text{in}} M_\beta^\dagger(\alpha e^{-\gamma}) \\ &\quad + \frac{\alpha^2 \gamma}{t_{\text{coupl}}} M_\beta(\alpha) \left[\int_0^{t_{\text{coupl}}} dt e^{-i\sqrt{2}g \hat{q} t} \rho_{\text{in}} e^{i\sqrt{2}g \hat{q} t} \right] M_\beta^\dagger(\alpha). \end{aligned}$$

The last term can be viewed as applying, with probability $\sim \alpha^2\gamma$, a mixture of shift errors with an average shift of strength $\sqrt{2}gt_{\text{coupl}}/2 = \sqrt{\pi}$. This dephasing feedback error tends to localize the q -quadrature, hence affecting the extent to which the state can be an eigenstate of S_p or X . The average feedback shift error upon photon loss is a logical shift Z , immediately leading to the loss of the logical information.

To gain a better intuition, we explicitly look at the effect of photon loss in the initialization measurement when $\rho_{\text{in}} = |\text{vac}\rangle\langle\text{vac}|$. Since the expression for $\text{Tr}(S_q\rho_\beta)$ for any input state ρ_{in} only involves diagonal terms $|q\rangle\langle q|$, the dephasing in the q -basis due to photon loss has no effect. This means that we can view such loss as occurring after the interaction, simply leading to $|\alpha\rangle \rightarrow |\alpha \exp(-\gamma/2)\rangle$. This loss affects the measurement quality in the same way as any readout loss, see Section 5.8.3.

We can consider the effect of the feedback error on the effective squeezing in \hat{p} , Δ_p as follows. After the S_q measurement with outcome β we consider the expected eigenvalue sharpness of S_p (or, similarly X). Ideally, it will stay unchanged. For this, we need to evaluate:

$$\int_{\mathbb{C}} d^2\beta |\text{Tr}(S_p\rho_\beta)| = \int_{\mathbb{C}} d^2\beta \left| (1 - \alpha^2\gamma) \text{Tr} \left(S_p M_\beta^\dagger (\alpha e^{-\gamma}) M_\beta (\alpha e^{-\gamma}) \rho_{\text{in}} \right) + \alpha^2\gamma \text{Tr} \left(\left[\frac{1}{t_{\text{coupl}}} \int dt e^{i\sqrt{2}g\hat{q}t} S_p e^{-i\sqrt{2}g\hat{q}t} \right] M_\beta^\dagger (\alpha) M_\beta (\alpha) \rho_{\text{in}} \right) \right|. \quad (5.32)$$

The commutation relation

$$\exp(iu\hat{q}) \exp(-i2\sqrt{\pi}\hat{p}) = \exp(-i2\sqrt{\pi}\hat{p}) \exp(iu\hat{q}) \exp(i2\sqrt{\pi}u)$$

can be used to do the averaging integral over t which leads to the contribution from the single-photon loss term to be zero. This essentially means that upon the loss of an actual photon the eigenvalue of S_p is fully randomized. The expected value for X , i. e. $\int_{\mathbb{C}} d^2\beta |X\rho_\beta|$ suffers similarly, i. e. upon the actual loss of a photon the eigenvalue of X gets fully randomized. The randomization leads to

$$\begin{aligned} \int_{\mathbb{C}} d^2\beta |\text{Tr}(S_p\rho_\beta)| &= (1 - \alpha^2\gamma) \int_{\mathbb{C}} d^2\beta \left| \text{Tr} \left(S_p M_\beta^\dagger (\alpha e^{-\gamma}) M_\beta (\alpha e^{-\gamma}) \rho_{\text{in}} \right) \right| \\ &= (1 - \alpha^2\gamma) |\text{Tr}(S_p\rho_{\text{in}})|, \end{aligned}$$

where the last equality follows immediately when the wave function of ρ_{in} is real in the q -basis (for example the vacuum state). One can also observe that $\int_{\mathbb{C}} d^2\beta S_p\rho_\beta = (1 - \alpha^2\gamma) |\text{Tr}(S_p\rho_{\text{in}})|$, since S_p no longer commutes with the S_q measurement due to the photon loss.

Using Eqs. 5.1 and approximating the logarithm for the case where the effective squeezing of the initial state is $\Delta_p < 1$, we can show that the feedback error due to photon loss will reduce the effective squeezing to $\tilde{\Delta}_p \approx \sqrt{\frac{\alpha^2\gamma}{\pi} + \Delta_p^2} > \Delta_p$.

5.8.2. COMPARISON WITH SEQUENTIAL-QUBIT PHASE ESTIMATION MEASUREMENT AND PHOTON LOSS ON TARGET OSCILLATOR

Previous work has analyzed how to measure the eigenvalue of S_q (or S_p) via coupling the target oscillator with a sequence of qubits, using a qubit-controlled displacement

interaction, followed by qubit measurement. In this scheme, each qubit measurement (via a read-out oscillator) provides at most 1 bit of information. For this sequential qubit read-out, one can use a tunable longitudinal interaction between transmon qubit and storage cavity of the form $\sqrt{2}g\frac{L-Z}{2}\hat{q}$. This form of the coupling implies that the interaction time t_{coupl} is the same value as in the photon-pressure protocol with a large coherent state. If the ancilla oscillator is harmonic, one can use the vacuum state $|0\rangle$ and Fock state $|1\rangle$ as the two qubit states. Hence, the longitudinal interaction is merely the photon-pressure coupling applied to these Fock states. However, the input state of this sequential scheme and the subsequent measurement of the qubits cannot be directly mapped onto the photon-pressure scheme using a coherent state.

To compare the sequential qubit scheme with the proposed modular quadrature measurement, we have to separately discuss the two dominant sources of error, photon loss on the ancilla oscillator and photon loss on the target oscillator. With respect to photon loss on the ancilla oscillator: An important possible advantage of the photon-pressure scheme proposed is that a single oscillator-measurement is used instead of a sequence of qubit measurements, making it possible that the photon-pressure scheme is much faster. This would lead to lower photon loss error rate on the target oscillator (as it is waiting while the ancillary system is being measured). To compare times, in [36] the release and measurement take time $O(1)\mu\text{s}$ while in the same set-up the high-fidelity single transmon qubit measurement took a similar amount of time. If we use a coherent state with $\bar{n} = 3$, Fig. 5.7 shows that one can obtain $\Delta_q \approx 0.18$ assuming no losses. Data from [16] show that one needs at least $M = 12$ rounds to get to $\Delta_q = 0.2$. Also, in [5] a grid state was stabilized after about 20 rounds of qubit measurements of duration 600 ns (including losses) to $\sigma = 0.16$ which corresponds to $\Delta = 0.22$ here.

With respect to photon loss on the ancilla qubit or oscillator, one can make the following observations. First, note that in the sequential execution of a protocol using ancilla qubits, arguments can be made that the squeezing parameter Δ_q will decrease as $1/\sqrt{M}$ where M is the number of rounds in phase estimation protocol [13, 16]. Then, similar as in the photon-pressure protocol, there is a probability $\gamma = \kappa_c t_{\text{coupl}}$ for amplitude damping (i. e. photon loss) and hence a feedback error which fully randomizes the eigenvalue of S_p or X for each qubit measurement. Hence, after M such rounds, the probability for a Z error scales as $\sim \gamma M \sim \gamma/\Delta^2$. In our proposed strong measurement scheme, the error probability is $\gamma\bar{n} \sim \gamma/\Delta^2$, showing that both schemes effectively have the *same* tradeoff. It is thus a matter for what \bar{n} one has $\kappa_c t_{\text{coupl}}\bar{n} \ll 1$ which determines whether a strong measurement with $\bar{n} > 1$ is more effective.

In this context, it should also be noted that it is not the aim for a GKP state preparation protocol to necessarily prepare the highest possible Δ . Photon loss on the target oscillator during the protocol and during measurement of the ancillary system will lead to drift and diffusion of the coordinates of the Wigner function $W(q, p)$: a GKP state with smaller Δ has more photons, incurring a larger error probability due to photon loss. Based on the interplay between these two mechanisms, Appendix S4.1 in [5] suggests that $\sigma = \frac{1}{2}\sqrt{\frac{\kappa_c T}{2}}$, with T the total duration of the S_p and S_q measurement protocol, is a target value for squeezing (in our convention corresponding to $\Delta = \frac{1}{2}\sqrt{\kappa_c T}$). A shorter cycle time T can thus allow for a smaller Δ , leading to a GKP qubit with a lower logical error rate.

We can compare our scheme with the proposed fault-tolerant syndrome detector of a GKP qubit in [18]. In that paper, it is proposed that a Kerr-cat qubit with $|0\rangle \approx |\alpha\rangle$ and $|1\rangle \approx |-\alpha\rangle$, is used for sequentially extracting bits of phase information of S_q instead of a transmon ancilla qubit as in [5]. The advantage of using a Kerr-cat qubit is that unlike the transmon qubit or the scheme proposed here, there is little feedback error since the X -error rate on the Kerr-cat qubit is purposefully low, with photon loss leading only to Z -errors which do not feed back. Note also that in [18] the required coupling between the Kerr-cat qubit and the target (GKP) oscillator is not directly a photon-pressure coupling but a tunable beam splitter interaction $\sim \hat{a}^\dagger \hat{b} + \hat{a} \hat{b}^\dagger$.

5.8.3. READOUT LOSS

After the interaction of the target and the ancilla oscillator — during the release and heterodyne measurement of the state of the ancilla oscillator — one expects losses, and possibly thermalization, due to coupling to extraneous modes in the co-planar or coaxial waveguide, circulators or the amplifier, affecting the total coherent amplitude of the ancilla oscillator state to be read out. Since these losses result from various (partially unknown) sources, a common approach to model them is as a process mapping the coherent amplitude α onto $\alpha_{\text{eff}} < \alpha$, i. e. $U_{\text{loss}} |\alpha\rangle_A |0\rangle_{\text{env}} \rightarrow |\cos(\theta)\alpha\rangle_A |\sin(\theta)\alpha\rangle_{\text{env}}$ with $\cos^2(\theta)\alpha^2 = \alpha_{\text{eff}}^2$ where $|\gamma\rangle_{\text{env}}$ is some environment mode. We thus assume that these losses do not further influence the phase of the state $|\alpha\rangle$. The cumulative effect of losses is not expected to be small, for example in [36] $\eta_{\text{eff}} = (\alpha_{\text{eff}}/\alpha)^2 \approx 0.43$. It should be noted that it is crucial that a near quantum limited amplifier is used, the readout efficiency with transistor based amplifiers is much lower. We also note that photon loss and thermal noise are used as interchangeable effective models in the literature: The amplifier design used in [36] for example was previously characterized by a noise temperature T_N about 125 mK [42]. The following analysis is based on a model of photon loss during readout, however a model of two mode squeezing with an idler in a thermal state (see for example [43]) is analogous and gives the same results.

The effect of these losses is that some of the information about S_q ends up in the environment and is not observed, leading to noise. We can simply modify the analysis in Section 5.5.1 by inserting U_{loss} after U_{PP} of Eq. (5.3) and prior to the heterodyne measurement action with outcome β , tracing over the environment mode. We get

$$\begin{aligned} \rho_{\text{in}} \rightarrow \rho_\beta &= \frac{1}{\pi} \iint_{\mathbb{R}^2} dq dq' \left\langle \alpha S_{q'} \sqrt{1 - \eta_{\text{eff}}} | \alpha S_q \sqrt{1 - \eta_{\text{eff}}} \right\rangle \\ &\times \langle \beta | \alpha_{\text{eff}} S_q \rangle \langle \alpha_{\text{eff}} S_{q'} | \beta \rangle \langle q | \rho_{\text{in}} | q' \rangle | q \rangle \langle q' |, \end{aligned} \quad (5.33)$$

where S_q and $S_{q'}$ are understood to be phases not operators. Let us again analyze the two possible effects of loss. First, for the diagonal elements of ρ_{in} in the $|q\rangle$ -basis, the effect of the measurement is to apply the measurement operator $M_\beta(\alpha_{\text{eff}})$. Since the expected value for Δ_q only depends on the diagonal elements $\langle q | \rho_{\text{in}} | q \rangle$, this results in a higher expected value for Δ_q simply due to $\alpha \rightarrow \alpha_{\text{eff}}$: It is as if one executes the S_q -measurement with a smaller coherent state with amplitude α_{eff} . Secondly, is there additional dephasing effect in the q -basis? Note that the measurement with subsequent loss in the ancilla oscillator still commutes with the operator X or S_p , similar as the ideal measurement that we examined previously. This directly means that $|\text{Tr}(S_p \int_{\mathbb{C}} d^2\beta \rho_\beta)| =$

$|\text{Tr}(S_p \rho_{\text{in}})|$ and the same for X , i. e. the average state has the same sharpness. We can also examine the sharpness averaged over different outcomes, that is, $\int_{\mathbb{C}} d^2\beta |\text{Tr}(X \rho_\beta)|$. Using that $\langle q|X|q'\rangle = \langle q|q' + \sqrt{\pi}\rangle = \delta(q - q' - \sqrt{\pi})$ and that S_q is $\sqrt{\pi}$ periodic (corresponding to the commutation of S_q with X and S_p) we can write

$$\begin{aligned} \int_{\mathbb{C}} d^2\beta |\text{Tr}(X \rho_\beta)| &= \\ &= \int_{\mathbb{C}} d^2\beta \left| \int_{\mathbb{R}} dq |\langle \beta | \alpha_{\text{eff}} S_q \rangle|^2 \langle q | \rho_{\text{in}} | q - \sqrt{\pi} \rangle \right| \\ &= \int_{\mathbb{C}} d^2\beta \int_{\mathbb{R}} dq |\langle \beta | \alpha_{\text{eff}} S_q \rangle|^2 \langle q | \rho_{\text{in}} | q - \sqrt{\pi} \rangle \\ &= \text{Tr}(X \rho_{\text{in}}), \end{aligned}$$

whenever $\langle q | \rho_{\text{in}} | q - \sqrt{\pi} \rangle \geq 0$. Similarly, when $\langle q | \rho_{\text{in}} | q - 2\sqrt{\pi} \rangle \geq 0$, the mean sharpness $\int_{\mathbb{C}} d^2\beta |\text{Tr}(S_p \rho_\beta)| = \text{Tr}(S_p \rho_{\text{in}})$, is also unchanged by the S_q -measurement. These conditions are clearly fulfilled for the vacuum state.

The upshot of these considerations is that noise further down in the measurement chain only changes the effective strength of the coherent state that is used: If the measurement efficiency is such that $\eta_{\text{eff}} = 50\%$ and we use $\bar{n} = 4$, we will effectively get the squeezing as if $\bar{n} = 2$, but there is no other extra noise or feedback error affecting the quality of the squeezing with respect to S_p and S_q .

5.8.4. EXPANSION OF THE CIRCUIT HAMILTONIAN

In the circuit analysis in Section 5.3.3, we expand the potential part of the circuit Hamiltonian Eq. (5.6) around the approximate minimum $\hat{x}_A = \hat{x}_T = 0$ of the potential term. In this section, we discuss this approximation in more detail as this point is not exactly the minimum of the potential.

Although the minimum of Eq. (5.6) is not soluble analytically, we can find an upper bound on the errors made. We do this by investigating the maximal possible shift in the position of the minimum as a function of $x_{\text{ext}}(t)$. First, we expand the potential exactly using the addition formula of the cosine:

$$E_J \cos(\hat{x}_T - \hat{x}_A - x_{\text{ext}}(t)) = E_J \sin(x_{\text{ext}}(t)) \sin(\hat{x}_T - \hat{x}_A) - E_J \cos(x_{\text{ext}}(t)) \cos(\hat{x}_T - \hat{x}_A).$$

Because $E_J < E_{L_T}, E_{L_A}$, we can see that the potential always has a unique minimum, and because the cosine is an even function, the location of that minimum only depends on the sine part of the equation. Therefore, the maximal shift of the position of the minimum away from $\hat{x}_T = \hat{x}_A = 0$ occurs at $x_{\text{ext}}(t) = \pm\pi/2$. That is, we can upper bound the error made by expanding the potential around $\hat{x}_A = \hat{x}_T = 0$ by investigating the case where $x_{\text{ext}}(t) = \pm\pi/2$.

If we set $x_{\text{ext}} = \pi/2$ and expand the potential to first order around $\hat{x}_A = \hat{x}_T = 0$, we have:

$$\begin{aligned} U(\hat{x}_A, \hat{x}_T) &\approx \frac{E_{L_A} \hat{x}_A^2}{2} + \frac{E_{L_T} \hat{x}_T^2}{2} + E_J (\hat{x}_T - \hat{x}_A) \\ &= \frac{E_{L_A}}{2} \left(\hat{x}_A - \frac{E_J}{E_{L_A}} \right)^2 + \frac{E_{L_T}}{2} \left(\hat{x}_T + \frac{E_J}{E_{L_T}} \right)^2 - \frac{E_J^2}{2E_{L_T}} - \frac{E_J^2}{2E_{L_A}}. \end{aligned} \quad (5.34)$$

Thus, for $x_{\text{ext}}(t) = \pm\pi/2$, the minimum of the potential term Eq. (5.6) is located around $\hat{x}_T = \mp \frac{E_J}{E_{L_T}}$ and $\hat{x}_T = \pm \frac{E_J}{E_{L_T}}$. By defining $\hat{x}'_T = \hat{x}_T \pm \frac{E_J}{E_{L_T}}$, $\hat{x}'_A = \hat{x}_A \pm \frac{E_J}{E_{L_T}}$, we can absorb this correction into the external flux drive $x_{\text{ext}}(t)$:

$$U(\hat{x}'_A, \hat{x}'_T, x_{\text{ext}}(t) = \pm\pi/2) = \frac{E_{L_A} \mathbf{x}'_A{}^2}{2} + \frac{E_{L_T} \mathbf{x}'_T{}^2}{2} - E_J \cos\left(\hat{x}'_T - \hat{x}'_A \pm 2\frac{E_J}{E_{L_T}} \mp \pi/2\right),$$

where the minimum of the potential is now to first order given by $\hat{x}'_A = \hat{x}'_T = 0$. Because the sine is monotone between 0 and $\pi/2$, we know that the location of the true minimum of the potential is also monotone between $0 < x_{\text{ext}}(t) < \pi/2$. From the structure of Eq. (5.34), we can also see that the shift of the minimum for \hat{x}_T is also always opposite to that of \hat{x}_A and that the sign of this minimum changes for $-\pi/2 < x_{\text{ext}}(t) < 0$:

$$U(\hat{x}'_A, \hat{x}'_T) = \frac{E_{L_A} \mathbf{x}'_A{}^2}{2} + \frac{E_{L_T} \mathbf{x}'_T{}^2}{2} - E_J \cos(\hat{x}'_T - \hat{x}'_A + 2\epsilon + x_{\text{ext}}(t)),$$

where $|\epsilon| \lesssim \frac{E_J}{E_{L_T}}$ is the true location of the minimum of $U(\hat{x}'_A, \hat{x}'_T)$ and the sign of ϵ depends on the sign of $\sin(x_{\text{ext}}(t))$. The expansion around $\hat{x}_A = \hat{x}_T = 0$ made in Section 5.3.3 is therefore similar to the effect of oscillating flux noise. Furthermore, just like for flux noise, there is an echo effect reducing any contributions from this offset because the offset changes sign with frequency $\sim \omega_T$.

In summary, the problem that arises is that the external drive changes the potential for both variables, which follow the change of minimum, with some delay. Due to this delay, the instantaneous potential is not quite what we expect, but the error is small, as it scales as $E_J/E_L \ll 1$. Note that this effect is deterministic, so it could be counteracted by a change in the external drive.

5.8.5. THIRD-ORDER NONLINEARITY

In this section, we examine what happens when we include a leading-order correction in the Hamiltonian obtained from the circuit analysis from Section 5.3.3 and Section 5.3.3. The most important term neglected in the circuit analysis is the term

$$\xi_T^3 \left(\hat{b}^\dagger e^{i\omega_T t} + \hat{b} e^{-i\omega_T t} \right)^3,$$

as this term is partially made resonant by the drive $x_{\text{ext}}(t)$. We will see that it is crucial that any device fulfills $\xi_T^2/\xi_A^2 \ll 1$ (which can be approximated as $E_{C_T} E_{L_A} \ll E_{C_A} E_{L_T}$) because this ratio sets the strength of the unwanted unitary operation due to the leading-order correction compared to the desired unitary evolution U_{PP} . We start with the original Hamiltonian in the rotating frame, see Eq. (5.9), but also keep the terms in the $\sin()$ part $\propto \xi_T^3$:

$$\begin{aligned} \tilde{H}_{on} &\approx \frac{E_J}{2} \left[-\xi_T \xi_A^2 \hat{a}^\dagger \hat{a} (\hat{b}^\dagger + \hat{b}) + \frac{\xi_T^3}{6} \left((\hat{b}^\dagger + \hat{b})^3 - (\hat{b}^\dagger)^3 - \hat{b}^3 \right) \right] \\ &= \frac{E_J}{\sqrt{2}} \left[-\xi_T \xi_A^2 \hat{a}^\dagger \hat{a} \hat{q} + \frac{\xi_T^3}{6\sqrt{2}} \left(2\sqrt{2} \hat{q}^3 - (\hat{b}^\dagger)^3 - \hat{b}^3 \right) \right]. \end{aligned}$$

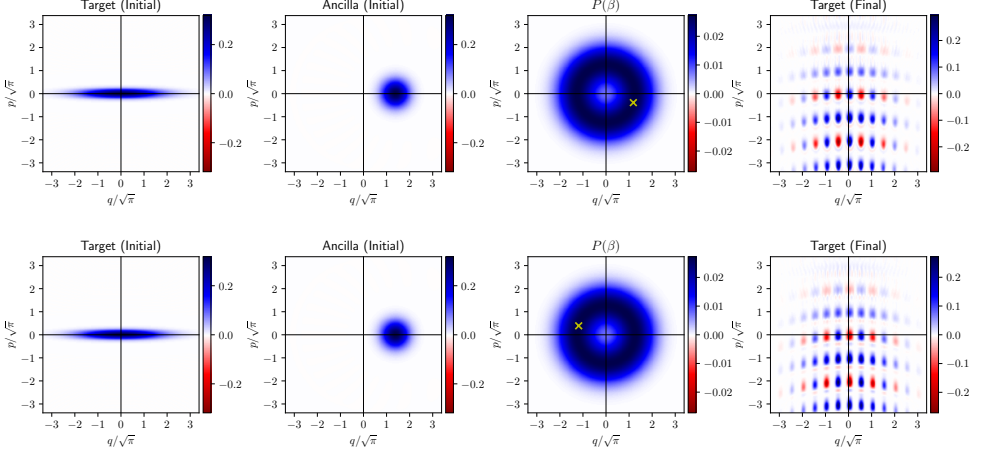


Figure 5.8: Wigner functions and probability distribution $\mathbb{P}(\beta)$ over measurement results using the heterodyne measurement of the ancilla oscillator, including the leading nonlinear term. The initial states are a squeezed vacuum state with $\Delta_q = 3$ and $\Delta_p = 1/3$ in the target oscillator and the coherent state $|\alpha = \sqrt{3}\rangle$ in the ancilla oscillator. The measurement result is the one with the maximum likelihood with respect to $\mathbb{P}(\beta)$. The strength of the third order term is set to $\frac{\xi_T^2}{\xi_A^2} = 10^{-3}$, compare Table 5.1. Top: Original third-order nonlinearity according to Eq. (5.35). The effective squeezing of the final state is $\Delta_p = 0.42, \Delta_q = 0.2$. Bottom: Third-order nonlinearity with a modified drive, see Eq. (5.37). The effective squeezing of the final state is $\Delta_p = 0.41, \Delta_q = 0.18$, demonstrating that Δ_q is unchanged compared to the ideal measurement in Fig. 5.2. Previously published in D. J. Weigand and B. M. Terhal, “Realizing modular quadrature measurements via a tunable photon-pressure coupling in circuit QED”, *Physical Review A* **101**, 053840 (2020), licensed under CC-BY 4.0 [21] © ⓘ.

This Hamiltonian acts for a fixed time $t_{\text{coupl}} = \frac{2\sqrt{2}\pi}{E_J \xi_T \xi_A^2}$. If we also drop the unconditional displacement, the target and ancilla oscillators will be coupled by the modified unitary operator

$$\tilde{U}_{\text{PP}} = \exp \left(i2\sqrt{\pi} \hat{a}^\dagger \hat{a} \hat{q} + i \frac{\sqrt{\pi}}{3\sqrt{2}} \frac{\xi_T^2}{\xi_A^2} \left(2\sqrt{2} \hat{q}^3 - \hat{b}^3 - (\hat{b}^\dagger)^3 \right) \right). \quad (5.35)$$

For $\epsilon = \frac{\sqrt{\pi} \xi_T^2}{3 \xi_A^2 \sqrt{2}} \ll 1$, we can rewrite and approximate this unitary as

$$\begin{aligned} \tilde{U}_{\text{PP}} &\approx U_{\text{PP}} \exp(i2\sqrt{2}\epsilon \hat{q}^3) \exp \left(-i\epsilon \left(\hat{b}^3 + (\hat{b}^\dagger)^3 \right) \right) \exp \left(\sqrt{\pi}\epsilon \hat{a}^\dagger \hat{a} \left[\hat{q}, \left(\hat{b}^3 + (\hat{b}^\dagger)^3 \right) \right] \right) \\ &= U_{\text{PP}} \exp(i2\sqrt{2}\epsilon \hat{q}^3) \exp \left(-i\epsilon \left(\hat{b}^3 + (\hat{b}^\dagger)^3 \right) \right) \exp \left(\frac{3\sqrt{\pi}\epsilon}{\sqrt{2}} \hat{a}^\dagger \hat{a} \left((\hat{b}^\dagger)^2 - \hat{b}^2 \right) \right), \end{aligned} \quad (5.36)$$

where we have neglected the commutators $\propto \epsilon^2$ and used that $[\hat{q}, \hat{b}^3 + (\hat{b}^\dagger)^3] = \frac{3}{\sqrt{2}}((\hat{b}^\dagger)^2 - \hat{b}^2)$. We observe two effects:

First, the incorrect unitary induces a systematic (third-order) error of strength $\sim \epsilon$ on the target oscillator, independent of the ancilla oscillator, hence not affecting the outcome of the S_q measurement itself. This systematic error does however cause a deformation of the Wigner function of a GKP code state. Namely: If one applies to an approximate GKP state a unitary of the form $\exp(i\delta q^3)$ with some parameter δ , it will not change

its squeezing Δ_q , but it does lead to enhanced Δ_p . Also, if we apply a unitary of the form $V = \exp(i\delta(\hat{b}^3 + (\hat{b}^\dagger)^3))$ to a GKP state, it negatively affects the squeezing Δ_q as V does not commute with S_q . Both effects are more pronounced the more photons the GKP state has.

Secondly, we observe that Eq. (5.36) contains an additional coupling of the form $\exp(\delta\hat{a}^\dagger\hat{a}((\hat{b}^\dagger)^2 - \hat{b}^2))$ between target and ancilla oscillator⁴. We can see this as squeezing induced by the ancilla oscillator on the target oscillator which gets stronger the more photons the ancilla oscillator contains. Alternatively, the heterodyne measurement statistics will be slightly altered by the presence of this additional term.

This photon-number dependent squeezing limits the number of photons that can be used in the ancilla oscillator. To alleviate this issue and ensure that the effective squeezing Δ_q is unchanged, one could apply a modified, two-tone drive such that $\sin(x_{\text{ext}}(t)) \approx \cos(3\omega_T) + \cos(\omega_T)$, which has the effect of making \hat{b}^3 and $(\hat{b}^\dagger)^3$ terms resonant again. With the modified drive, the unitary time evolution only depends on q :

$$\tilde{U}_{\text{pp}}^{\text{corr}} = \exp\left(i2\sqrt{\pi}\hat{a}^\dagger\hat{a}\hat{q} + i2\sqrt{2}\epsilon\hat{q}^3\right) = U_{\text{pp}}e^{i2\sqrt{2}\epsilon\hat{q}^3}. \quad (5.37)$$

This corrected unitary transformation will then not affect the measurement statistics of S_q as the additional term commutes with \hat{q} . The effective squeezing Δ_q of the measured state will be unchanged as compared to using U_{pp} . The effective squeezing Δ_p is still affected by the $\exp(i\delta\hat{q}^3)$ deformation. The deformation can be seen as a displacement that has a quadratic dependence on the \hat{q} quadrature, leading to a “parabola” of displacements acting on the final state of the target oscillator, see Fig. 5.8.

The upshot is that with additional drive engineering one can mitigate the effect of the third-order non-linearity. The numerics in Fig. 5.8 show that for sufficiently small corrections the effect on the squeezing parameters is moderate.

5.8.6. FLUX NOISE

Because an external flux drive is used to enable the coupling, the setup will be susceptible to flux noise. (Quasi)-static flux noise acts as a constant offset on the drive in Eq. (5.13). Thus, with a constant flux offset ϵ , i. e. $\tilde{x}_{\text{ext}}(t) = x_{\text{ext},\pm}(t) + \epsilon$ with $x_{\text{ext},\pm}(t)$ chosen as in Eq. (5.13) and maximal coupling strength ($\delta = 1$), the interaction Hamiltonian (in the rotating frame) is given by

$$\begin{aligned} \tilde{H}_{\text{RWA}} &\approx E_J \cos(\epsilon \pm (-1)^k \omega_T) \left(\xi_T \left(1 - \frac{\xi_A^2}{2} \right) (\hat{b}^\dagger e^{i\omega_T t} + b e^{-i\omega_T t}) \right. \\ &\quad \left. - \xi_T \xi_A^2 \hat{a}^\dagger \hat{a} (\hat{b}^\dagger e^{i\omega_T t} + b e^{-i\omega_T t}) \right) \\ &= \frac{E_J}{2} \left(\xi_T \left(1 - \frac{\xi_A^2}{\sqrt{2}} \right) (\hat{q} \cos(\epsilon) \mp (-1)^k \hat{p} \sin(\epsilon)) - \xi_T \xi_A^2 \hat{a}^\dagger \hat{a} (\hat{q} \cos(\epsilon) \mp (-1)^k \hat{p} \sin(\epsilon)) \right), \end{aligned}$$

⁴If we had kept the unconditional displacement interaction in Eq. (5.12), we would also get some ancilla oscillator independent squeezing.

where the sign \pm depends on the chosen drive and $k = \lfloor \frac{\omega_T t}{2\pi} \rfloor$ indicates the number of periods $\omega_T/(2\pi)$ that has passed by the time $0 < t < t_{\text{coupl}}$. This Hamiltonian is still of the photon-pressure type, but it no longer couples the \hat{q} quadrature to the number of photons in the ancilla oscillator, but a slightly rotated quadrature. However, we can also see that this rotation is time-dependent due to its dependence on k and changes direction with frequency ω_T . This means that the drive defined in Eq. (5.13) already provides some protection against such static flux noise. In the case where a drive with reduced amplitude $\delta < 1$ (see Section 5.4.1) is used, the situation is more complicated. We discuss flux noise for $\delta < 1$ in Section 5.8.7.

Another effect of flux noise is the following. The resonance frequency of both oscillators also depends on the external flux drive $x_{\text{ext}}(t)$, see Section 5.3.3 and Table 5.1. In the presence of static flux noise, it means that the rotating frame will be slightly out of sync with respect to the true resonance frequency of the oscillators, leading to inaccuracy in the phase of the oscillator state. Typically, flux noise is small compared to Φ_0 (which is the amplitude of the flux drive $x_{\text{ext}}(t)$), suggesting that the difference between the expected and true resonance frequencies can be neglected.

5

5.8.7. FLUX NOISE WITH REDUCED DRIVE AMPLITUDE

We have discussed flux noise for the case with maximal coupling strength ($\delta = 1$) in Section 5.8.6. Following the discussion there, we now discuss flux noise in the case where the drive strength is reduced ($\delta < 1$). In this case, the prefactor in the coupling Hamiltonian is given by

$$\begin{aligned} \sin(x_{\text{ext},\pm}(t) + \epsilon) &= (1 - \delta + \delta \cos(\omega_T t)) \cos(\epsilon) \\ &\quad \pm (-1)^{\lfloor \frac{\omega_T t}{2\pi} \rfloor} \sqrt{1 - (1 - \delta + \delta \cos(\omega_T t))^2} \sin(\epsilon). \end{aligned} \quad (5.38)$$

Again, there is some built-in correction for the additional phase, the term $\propto \sin(\epsilon)$ will approximately cancel over multiple periods (recall that the ideal drive is with zero flux off-set $\epsilon = 0$). However, there is an additional effect that the amplitude of the drive also changes over time, and the change of amplitude is on resonance with the change of the phase, i. e. the rotation of the measured quadrature no longer completely cancels. In order to alleviate this issue, one could use a similar strategy as the CZ gate used for transmon qubits [44], using the fact that the equation $\sin(x_{\text{ext},\pm}(t)) = 1 - \delta + \delta \cos(\omega_T t)$ has two alternating solutions, $x_{\text{ext},+}$ and $x_{\text{ext},-}$ see Eq. (5.13). Because the undesired term due to flux noise for the two drives always has opposite sign, see Eq. (5.38), it is possible to restore the echo effect by alternating between the two drives. Although this transition is not smooth (see Fig. 5.5), it is continuous for all choices of δ . Furthermore, the quick roll off with high harmonics is preserved, the most complex drive that could be obtained with the strategy is a triangle wave at frequency ω_T , see Fig. 5.5.

5.9. DISCUSSION

In this chapter, we have proposed to use a simple coherent state ancilla to get more than 1 bit of information about the eigenvalue of a unitary displacement operator, effectively realizing a modular quadrature measurement. These measurements can be used to prepare or read out a GKP code state. We have presented and analyzed an electric circuit

which generates a strong photon-pressure coupling needed to imprint the eigenvalue information onto the coherent state of the ancilla oscillator. As we have seen a large coherent amplitude α makes for a higher-precision stabilizer measurement, but in the presence of photon loss or unwanted nonlinearities, α should be chosen moderately. Our results and numerics show that circuit parameters can be chosen which demonstrate good performance at $|\alpha|^2 \approx 3$.

It should be noted that the circuit presented in Section 5.3.3 is not the only way to implement a sufficiently strong photon-pressure coupling to be able to use the GKP stabilizer measurements presented here. In fact, *any* experimental setup that is sufficiently far in the single photon regime can be employed to this end, however the circuit we analyze is particularly well suited for the task. One major advantage is that we only require a single Josephson junction in the loop: This eliminates the experimentally challenging requirement of symmetric junctions found in more traditional circuit designs.

Although the protocol is susceptible to photon loss in the ancilla oscillator, we still expect an advantage compared to schemes using a transmon qubit as ancilla because the loss rate of the ancilla oscillator compared to the interaction time is much more favorable than the amplitude damping rate of a transmon qubit over multiple measurement rounds, while the error mechanism of the two approaches is comparable. Furthermore, concatenation with an error correcting code in the ancilla oscillator is straight forward: If a rotationally symmetric code [45] is used as initial state of the ancilla oscillator, it will be possible to correct photon loss without increasing the number of photons in the oscillator or reducing the effective squeezing.

As with most implementations of the GKP code, single qubit Pauli and Hadamard gates can easily be done by a displacement acting on the target oscillator or a change of rotating frame, respectively [9]. The photon-pressure coupling Hamiltonian is very versatile, with a simple modification of the flux drive, it can also be used to enable a beam-splitter between the target and ancilla oscillators [29–31]. If the circuit is extended such that an ancilla oscillator is shared by two target oscillators, such a beam splitter could for example be used to swap encoded states. Similar to swapping to distant qubits via an ancilla qubit, such a scheme would require a sequence of three beam splitting operations: First between target mode one and ancilla mode, then between ancilla mode and target mode two, and finally between the ancilla mode and the first target mode. With other configurations of the drive, it is possible to enable either a bosonic CNOT gate, or a two-mode squeezing between the target and ancilla oscillators. The latter operation is of special interest because it enables to use the GKP-two-mode-squeezing encoding [46]. In this encoding, an arbitrary state in the ancilla oscillator can be protected against Gaussian noise in *both* quadratures, using a GKP state in the target oscillator as a resource.

ACKNOWLEDGEMENTS

Our work was supported by ERC grant EQEC No. 682726 and a QuantERA grant for the QCDA consortium. We thank Alexandre Blais, Daniel Bothner, Alessandro Ciani, Jonathan Conrad, Ines Corveira Rodrigues, David DiVincenzo and Wolfgang Pfaff for feedback and discussions.

REFERENCES

- [1] D. J. Weigand and B. M. Terhal, “Realizing modular quadrature measurements via a tunable photon-pressure coupling in circuit QED”, [Physical Review A](#) **101**, 053840 (2020).
- [2] N. Ofek, A. Petrenko, R. Heeres, P. Reinhold, Z. Leghtas, B. Vlastakis, Y. Liu, L. Frunzio, S. M. Girvin, L. Jiang, M. Mirrahimi, M. H. Devoret, and R. J. Schoelkopf, “Extending the lifetime of a quantum bit with error correction in superconducting circuits”, [Nature](#) **536**, 441 (2016).
- [3] L. Hu, Y. Ma, W. Cai, X. Mu, Y. Xu, W. Wang, Y. Wu, H. Wang, Y. P. Song, C. -L. Zou, S. M. Girvin, L.-M. Duan, and L. Sun, “Quantum error correction and universal gate set operation on a binomial Bosonic logical qubit”, [Nature Physics](#) **15**, 503 (2019).
- [4] C. Flühmann, T. L. Nguyen, M. Marinelli, V. Negnevitsky, K. Mehta, and J. P. Home, “Encoding a qubit in a trapped-ion mechanical oscillator”, [Nature](#) **566**, 513 (2019).
- [5] P. Campagne-Ibarcq, A. Eickbusch, S. Touzard, E. Zalys-Geller, N. E. Frattini, V. V. Sivak, P. Reinhold, S. Puri, S. Shankar, R. J. Schoelkopf, L. Frunzio, M. Mirrahimi, and M. H. Devoret, “Quantum error correction of a qubit encoded in grid states of an oscillator”, [Nature](#) **584**, 368 (2020).
- [6] A. Grimm, N. E. Frattini, S. Puri, S. O. Mundhada, S. Touzard, M. Mirrahimi, S. M. Girvin, S. Shankar, and M. H. Devoret, “Stabilization and operation of a kerr-cat qubit”, [Nature](#) **584**, 205 (2020).
- [7] B. M. Terhal, J. Conrad, and C. Vuillot, “Towards scalable bosonic quantum error correction”, [Quantum Science and Technology](#) **5**, 043001 (2020).
- [8] Z. Leghtas, G. Kirchmair, B. Vlastakis, R. J. Schoelkopf, M. H. Devoret, and M. Mirrahimi, “Hardware-efficient autonomous quantum memory protection”, [Physical Review Letters](#) **111**, 120501 (2013).
- [9] D. Gottesman, A. Kitaev, and J. Preskill, “Encoding a qubit in an oscillator”, [Physical Review A](#) **64**, 012310 (2001).
- [10] V. V. Albert, K. Noh, K. Duivenvoorden, D. J. Young, R. T. Brierley, P. Reinhold, C. Vuillot, L. Li, C. Shen, S. M. Girvin, B. M. Terhal, and L. Jiang, “Performance and structure of single-mode Bosonic codes”, [Physical Review A](#) **97**, 032346 (2018).
- [11] K. Noh, V. V. Albert, and L. Jiang, “Quantum capacity bounds of Gaussian thermal loss channels and achievable rates with Gottesman-Kitaev-Preskill codes”, [IEEE Transactions on Information Theory](#) **65**, 2563 (2019).
- [12] S. Glancy and E. Knill, “Error analysis for encoding a qubit in an oscillator”, [Physical Review A](#) **73**, 012325 (2006).
- [13] B. M. Terhal and D. J. Weigand, “Encoding a qubit into a cavity mode in circuit QED using phase estimation”, [Physical Review A](#) **93**, 012315 (2016).
- [14] Y. Shi, C. Chamberland, and A. W. Cross, “Fault-tolerant preparation of approximate GKP states”, [New Journal of Physics](#) **21**, 093007 (2019).

- [15] C. Flühmann, V. Negnevitsky, M. Marinelli, and J. P. Home, “Sequential modular position and momentum measurements of a trapped ion mechanical oscillator”, *Physical Review X* **8**, 021001 (2018).
- [16] K. Duivenvoorden, B. M. Terhal, and D. J. Weigand, “Single-mode displacement sensor”, *Physical Review A* **95**, 012305 (2017).
- [17] B.-G. Englert, K. L. Lee, A. Mann, and M. Revzen, “Periodic and discrete Zak bases”, *Journal of Physics A* **39**, 1669 (2006).
- [18] S. Puri, A. Grimm, P. Campagne-Ibarcq, A. Eickbusch, K. Noh, G. Roberts, L. Jiang, M. Mirrahimi, M. H. Devoret, and S. M. Girvin, “Stabilized cat in a driven nonlinear cavity: a fault-tolerant error syndrome detector”, *Physical Review X* **9**, 041009 (2019).
- [19] S. Haroche and J.-M. Raimond, *Exploring the quantum: atoms, cavities, and photons* (Oxford University Press, USA, Oxford, 2006).
- [20] S. R. Jammalamadaka and A. Sengupta, *Topics in circular statistics* (World Scientific, 2001).
- [21] *Creative Commons Attribution-ShareAlike 3.0 Unported License*, Creative Commons Corporation, <https://creativecommons.org/licenses/by-sa/3.0/>.
- [22] C. Eichler, D. Bozyigit, and A. Wallraff, “Characterizing quantum microwave radiation and its entanglement with superconducting qubits using linear detectors”, *Physical Review A* **86**, 032106 (2012).
- [23] A. Blais, R.-S. Huang, A. Wallraff, S. M. Girvin, and R. J. Schoelkopf, “Cavity quantum electrodynamics for superconducting electrical circuits: an architecture for quantum computation”, *Physical Review A* **69**, 062320 (2004).
- [24] H. Wiseman and G. Milburn, *Quantum measurement and control* (Cambridge University Press, Cambridge, 2010).
- [25] S. Barzanjeh, D. P. DiVincenzo, and B. M. Terhal, “Dispersive qubit measurement by interferometry with parametric amplifiers”, *Physical Review B* **90**, 134515 (2014).
- [26] S. Touzard, A. Kou, N. E. Frattini, V. V. Sivak, S. Puri, A. Grimm, L. Frunzio, S. Shankar, and M. H. Devoret, “Gated conditional displacement readout of superconducting qubits”, *Physical Review Letters* **122**, 080502 (2019).
- [27] J. Ikonen, J. Goetz, J. Ilves, A. Keränen, A. M. Gunyho, M. Partanen, K. Y. Tan, D. Hazra, L. Grönberg, V. Vesterinen, S. Simbierowicz, J. Hassel, and M. Möttönen, “Qubit measurement by multichannel driving”, *Physical Review Letters* **122**, 080503 (2019).
- [28] N. Didier, J. Bourassa, and A. Blais, “Fast quantum nondemolition readout by parametric modulation of longitudinal qubit-oscillator interaction”, *Physical Review Letters* **115**, 203601 (2015).
- [29] M. Aspelmeyer, T. J. Kippenberg, and F. Marquardt, “Cavity optomechanics”, *Reviews of Modern Physics* **86**, 1391 (2014).

- [30] C. Eichler and J. R. Petta, “Realizing a circuit analog of an optomechanical system with longitudinally coupled superconducting resonators”, *Physical Review Letters* **120**, 227702 (2017).
- [31] J. R. Johansson, G. Johansson, and F. Nori, “Optomechanical-like coupling between superconducting resonators”, *Physical Review A* **90**, 053833 (2014).
- [32] D. Bothner, I. C. Rodrigues, and G. A. Steele, “Photon-pressure strong coupling between two superconducting circuits”, *Nature Physics*, <https://doi.org/10.1038/s41567-020-0987-5> (2020).
- [33] A. Vrajitoarea, Z. Huang, P. Groszkowski, J. Koch, and A. A. Houck, “Quantum control of an oscillator using a stimulated Josephson nonlinearity”, *Nature Physics* **16**, 211 (2019).
- [34] Y. Yin, Y. Chen, D. Sank, P. J. J. O’Malley, T. C. White, R. Barends, J. Kelly, E. Lucero, M. Mariantoni, A. Megrant, C. Neill, A. Vainsencher, J. Wenner, A. N. Korotkov, A. N. Cleland, and J. M. Martinis, “Catch and release of microwave photon states”, *Physical Review Letters* **110**, 107001 (2013).
- [35] M. Pierre, I.-M. Svensson, S. Raman Sathyamoorthy, G. Johansson, and P. Delsing, “Storage and on-demand release of microwaves using superconducting resonators with tunable coupling”, *Applied Physics Letters* **104**, 232604 (2014).
- [36] W. Pfaff, C. J. Axline, L. D. Burkhardt, U. Vool, P. Reinhold, L. Frunzio, L. Jiang, M. H. Devoret, and R. J. Schoelkopf, “Controlled release of multiphoton quantum states from a microwave cavity memory”, *Nature Physics* **13**, 882 (2016).
- [37] E. Flurin, N. Roch, J. D. Pillet, F. Mallet, and B. Huard, “Superconducting quantum node for entanglement and storage of microwave radiation”, *Physical Review Letters* **114**, 090503 (2015).
- [38] M. Hatridge, S. Shankar, M. Mirrahimi, F. Schackert, K. Geerlings, T. Brecht, K. M. Sliwa, B. Abdo, L. Frunzio, S. M. Girvin, R. J. Schoelkopf, and M. H. Devoret, “Quantum back-action of an individual variable-strength measurement”, *Science* **339**, 178 (2013).
- [39] Z. K. Mineev, S. O. Mundhada, S. Shankar, P. Reinhold, R. Gutiérrez-Jáuregui, R. J. Schoelkopf, M. Mirrahimi, H. J. Carmichael, and M. H. Devoret, “To catch and reverse a quantum jump mid-flight”, *Nature* **570**, 200 (2019).
- [40] A. A. Clerk, M. H. Devoret, S. M. Girvin, F. Marquardt, and R. J. Schoelkopf, “Introduction to quantum noise, measurement, and amplification”, *Reviews of Modern Physics* **82**, 1155 (2010).
- [41] W. Janke and H. Kleinert, “How good is the Villain approximation?”, *Nuclear Physics B* **270**, 135 (1986).
- [42] N. Bergeal, F. Schackert, M. Metcalfe, R. Vijay, V. E. Manucharyan, L. Frunzio, D. E. Prober, R. J. Schoelkopf, S. M. Girvin, and M. H. Devoret, “Phase-preserving amplification near the quantum limit with a Josephson ring modulator”, *Nature* **465**, 64 (2010).
- [43] C. M. Caves, “Quantum limits on noise in linear amplifiers”, *Physical Review D* **26**, 1817 (1982).

- [44] M. A. Rol, F. Battistel, F. K. Malinowski, C. C. Bultink, B. M. Tarasinski, R. Vollmer, N. Haider, N. Muthusubramanian, A. Bruno, B. M. Terhal, and L. DiCarlo, “Fast, high-fidelity conditional-phase gate exploiting leakage interference in weakly anharmonic superconducting qubits”, [Physical Review Letters](#) **123**, 120502 (2019).
- [45] A. L. Grimsmo, J. Combes, and B. Q. Baragiola, “Quantum computing with rotation-symmetric Bosonic codes”, [Physical Review X](#) **10**, 011058 (2020).
- [46] K. Noh, S. M. Girvin, and L. Jiang, “Encoding an oscillator into many oscillators”, [Physical Review Letters](#) **125**, 080503 (2020).

6

CONCLUSION AND OUTLOOK

6.1. CONCLUSION

ENCODING a qubit in an oscillator has proven to be a promising approach for long-living qubit designs. In particular, the code developed by Gottesman, Kitaev, and Preskill (GKP code) is very robust against photon loss, has a relatively simple gate set, and also enables multiple applications beyond quantum computing. However, efficiently encoding a qubit in this code is a major challenge. In this thesis, various schemes have been developed to address this issue. The following paragraphs highlight the most important aspects of this thesis:

- In Chapter 2, we introduced some of the background for working with the GKP code. As we have seen, there are multiple different representations, which are all suited for different purposes. The representation as a wave function is useful to get some intuition about code states and their behavior, but is typically difficult to work with. The shifted code states introduced by Glancy and Knill are a handy tool to analyze error correction and similar operations that transform the code state. The Fock basis representation, although not well suited, remains important because most numerical simulations are written for this basis.

We also discussed how a GKP code state, obtained e. g. from an experiment or simulations, can be analyzed. We introduced the effective squeezing parameters and discussed how they can be obtained analytically from a wave function, but also directly from experimental data or numerics. The effective squeezing parameters make the assumption that the underlying approximate code states are Gaussian, but this is typically a good approximation. The big advantage is that the effective squeezing parameters are comparatively easy to estimate. In fact, both experimental implementations of the GKP code used the average expectation value of the Pauli operators as quality measure, which is an approximation of the sharpness, and therefore closely related to the effective squeezing parameters [1, 2].

- In Chapter 3, we introduced the class of phase estimation algorithms, and how it can be used to encode a GKP code state. We also discussed how a controlled displacement, the central part of any phase estimation scheme, can be implemented in various physical settings.

The chapter concludes with a numerical simulation of an encoding protocol using phase estimation. Although the protocol used in the numerical simulations is now outdated, the main results are still valid: The encoding procedure is quite robust against readout errors of the ancilla qubit, but a nonlinearity of the oscillator of more than a few kHz would almost immediately destroy the encoded qubit. In the recent experiment, the nonlinearity was only 1 Hz — a value that was completely unreasonable in 2016 [2]. Although the simulations show that the impact of amplitude damping is not significant on average, a sudden bit flip of the qubit during a vulnerable time would immediately decohere an encoded qubit. A clever trick to mitigate this issue has been published by Rosenblum *et al.* [3]: By using the transmon as a three level system $|0\rangle, |1\rangle, |2\rangle$, and ensuring that qubit-oscillator coupling is of the form $\hat{a}^\dagger \hat{a}(|1\rangle\langle 1| + |2\rangle\langle 2|)$, they can mitigate the backaction of amplitude damping. This error mitigation technique would also be beneficial for en-

coding the GKP code. Alternatively, employing a simple bit-flip code would also be beneficial. In fact, even “simple” error detection would be sufficient to eliminate propagation of errors from the ancilla qubit to the oscillator, provided that the time of an amplitude damping event can be determined with good accuracy.

- Due to its robustness against photon loss, the GKP code is very promising for the optical regime, because error correction of a flying mode is often simply not practical. In Chapter 4, we focus on a breeding protocol originally devised to generate GKP states in the optical regime. The original protocol was developed by Vasconcelos *et al.* [4], however, it relied on post-selection. By mapping the protocol to phase estimation, we could show that almost any result of the protocol yields a good GKP state, and showed how the necessary corrections can be computed.

We also could show analytically that the protocol converges. Although the calculations are quite tedious, a nice technique developed to this end was to derive a class of states that is closed under the protocol, that is, the functional form of the code states does not change, only the parameters.

A major challenge when using feedback to encode a GKP state is that the feedback has to be computed and applied before the stored state decoheres [2]. This issue is exacerbated in the optical regime, where the single-photon life time is often lower than in the microwave regime. Still, the scheme presented in this thesis has the advantage that post-processing is only needed at the end of the encoding procedure, without need to sync different modes during encoding.

- In Chapter 5, we focused on the question how to implement a single-shot eigenvalue measurement of a displacement. The motivation behind such a single-shot measurement is that, so far, mostly phase estimation schemes, i. e. a series of weak measurements, has been used. These measurements typically take a considerable time, and the hope is to speed this process up.

To achieve a single shot measurement, we followed the proposal by Gottesman *et al.* to implement a Hamiltonian of the form $\hat{q}\hat{a}^\dagger\hat{a}$ between two oscillators. Such an interaction is nontrivial, and requires both a purpose-designed circuit and a parametric drive.

A nice feature of the circuit we propose is that it features only a *single* Josephson junction and uses a small inductance to close the loop, so that it is still flux-tunable. Although of little consequence for the circuit analysis, this virtually eliminates a source of noise present in many experiments: No two Josephson junctions are exactly equal, but a fully flux-tunable design usually requires a pair of equal junctions.

Perhaps surprisingly, the overarching theme of this thesis are applications of the phase estimation algorithm and variants thereof. Using phase estimation to encode a GKP qubit is probably not the optimal choice — the measurements take a long time, feedback is difficult to calculate in real time during an experiment, and the photon number of the encoded state grows in an uncontrollable manner. However, mapping a procedure to phase estimation is the key to understand what happens, and to see how one might improve upon it:

For the breeding protocol discussed in Chapter 4, the connection is obvious because a mapping of the protocol to phase estimation is literally the approach taken there. We can also see the protocol developed by Campagne-Ibarcq *et al.* [2] as a variant of the maximal information gain strategy (see Section 3.1.4). In their paper, the authors use a feedback that centers the state again in phase space, using a fixed feedback strength. If the state is centered in phase space before the measurement, then the probability to obtain either 0 or 1 as a measurement will be equal. If the state is again centered after the measurement, the probabilities for the next measurement will be equal, too. Thus, their feedback strategy is equivalent to the maximal information gain strategy in the steady state of the protocol. Finally, we can also understand the optomechanical interaction from Chapter 5 as a phase estimation variant. If we use the Holstein-Primakoff transformation, we can map both the ancilla oscillator and the optomechanical coupling to an interaction between many qubits and the target oscillator. Then, we can see that the measurement protocol with an optomechanical coupling is equivalent to phase estimation by repetition with multiple ancilla qubits. For the detailed derivation, see Appendix A.2.

6.2. OUTLOOK

OVER the last years, there have been significant advances for qubits encoded in bosonic modes, and in particular for the GKP code. Maybe most significant for the scope of this thesis were the two experiments demonstrating this code [1, 2]. However, there is still much to be done before the GKP code can be used in a scalable fashion with a large number of encoded qubits.

- Building upon the analytical results in Chapter 4, one might ask whether the asymptotic behavior of other encoding protocols can be proven in a similar way. An interesting candidate for such an analysis is the simplified phase estimation scheme by Campagne-Ibarcq *et al.* [2]. One point the authors raised is that it seems necessary to include an artificial “dissipation” channel, which ensures that the number of photons of the GKP state converges to some constant. Although photon loss would also ensure that the photon number converges eventually, with current single photon life times this would only happen if the encoded state has hundreds of photons. Because the logical error rate increases again for large photon numbers, this necessitates another mechanism to keep photon numbers low. They do this by interleaving measurements of the stabilizers S_p, S_q with measurements of small displacements $D(\epsilon), D(i\epsilon)$. However, the drawback is that the number of measurements needs to be doubled to generate this dissipative process. An approach to solve this issue would be to change the stabilizer measurements. If one were to measure the eigenvalues of $D(\sqrt{2\pi} \pm i\epsilon), D(i\sqrt{2\pi} \pm \epsilon)$ in an alternating manner, one might be able to have a converging photon number, and still obtain some stabilizer information with every measurement. Although this protocol remains to be demonstrated analytically, preliminary numerical simulations show promising results.
- To be able to use the breeding protocol, a reliable source of squeezed Schrödinger cat states is required as input. However, generating these states still remains a ma-

jor challenge. In a recent experiment, Eaton *et al.* made some progress towards that goal, by putting a coherent state and a single photon state into a beam splitter, followed by number-resolving detection [5]. An interesting avenue of future research is the question whether photon catalysis protocols such as the one by Eaton *et al.* can be made more efficient to encode a GKP code state, in a similar way as the breeding protocol.

- Numerical simulations of GKP qubits are memory intensive, because the state is usually represented in the Fock basis. As the GKP code is a stabilizer code, one open question is if the Gottesman-Knill theorem can be applied to simulate noise. The generating function of a GKP code is much more efficient than representing the state explicitly in the Fock basis. Although some noise types (e.g. dephasing) are clearly not efficiently tractable as a transformation of the stabilizers, it remains to be seen whether, e.g., photon loss could be simulated in such a way.

Another approach would be to leverage techniques from computational chemistry. As the von Neumann lattice technique is used to simulate large Hilbert spaces of many interacting harmonic oscillators, efficient programs have been developed for this type of state. The GKP code is defined by the same displacements as the von Neumann lattice, and has therefore an efficient representation in such a lattice, meaning that any advances made by the computational chemistry community should be easily transferable.

- Finally, the one-shot stabilizer measurements developed in Chapter 5 are interesting to either store GKP code states or be used as a source of encoded ancilla qubits. In the chapter, we briefly discussed how a CNOT gate could work, but a scalable architecture still needs to be developed. In particular, the question how multiple storage modes can be coupled is still open.

REFERENCES

- [1] C. Flühmann, T. L. Nguyen, M. Marinelli, V. Negnevitsky, K. Mehta, and J. P. Home, “Encoding a qubit in a trapped-ion mechanical oscillator”, *Nature* **566**, 513 (2019).
- [2] P. Campagne-Ibarcq, A. Eickbusch, S. Touzard, E. Zalys-Geller, N. E. Frattini, V. V. Sivak, P. Reinhold, S. Puri, S. Shankar, R. J. Schoelkopf, L. Frunzio, M. Mirrahimi, and M. H. Devoret, “Quantum error correction of a qubit encoded in grid states of an oscillator”, *Nature* **584**, 368 (2020).
- [3] S. Rosenblum, P. Reinhold, M. Mirrahimi, L. Jiang, L. Frunzio, and R. J. Schoelkopf, “Fault-tolerant detection of a quantum error”, *Science* **361**, 266 (2018).
- [4] H. M. Vasconcelos, L. Sanz, and S. Glancy, “All-optical generation of states for “Encoding a qubit in an oscillator””, *Optics Letters* **35**, 3261 (2010).
- [5] M. Eaton, R. Nehra, and O. Pfister, “Non-Gaussian and Gottesman-Kitaev-Preskill state preparation by photon catalysis”, *New Journal of Physics* **21**, 113034 (2019).

A

APPENDIX

Appendix [A.1.1](#) has been published with minor differences in K. Duivenvoorden, B. M. Terhal, and D. J. Weigand, “Single-mode displacement sensor”, [Physical Review A **95**, 012305 \(2017\)](#). Appendix [A.1.3](#) has been published with minor differences in D. J. Weigand and B. M. Terhal, “Realizing modular quadrature measurements via a tunable photon-pressure coupling in circuit QED”, [Physical Review A **101**, 053840 \(2020\)](#)

A.1. DETAILS OF NUMERICAL SIMULATIONS

A.1.1. STABILIZER MEASUREMENTS USING PHASE ESTIMATION

In this section, we discuss some details of the numerical simulations used in Section 3.3. The code is built upon the numerical simulations used in earlier work [3], with significant changes to enable the simulation of noise. The full code is available under <https://gitlab.com/djweigand/qubit-oscillator>.

The simulations are performed in the photon number basis, using a Hilbert space of finite size N . All operators acting on the system are obtained from truncated creation and annihilation operators. Thus, the simulation is only accurate if the support of a state outside of the finite Hilbert space is small. As the simulation of non-stochastic errors is fairly efficient, we can choose $N = 400$ for $M = 12$ rounds. In case of stochastic errors acting over a finite time (e. g. photon loss), the accuracy of the simulation is also limited by the employed differential equation solver. As the precision is mostly independent of the size of the Hilbert space, the cumulative impact grows with its size. A suitable compromise between errors from the cutoff and errors from the ODE Solver is a Hilbert space with $N = 100$ photons, allowing for $M = 8$ rounds. While the computational cost for stochastic errors scales much less favorable than in the other cases, this would only be an issue for $N > 100$.

A.1.2. SIMULATION OF BREEDING

In this section, we discuss the numerical simulations used in Chapter 4. The source code is available under <https://gitlab.com/djweigand/cat-breeding>. Two separate approaches were used for the full simulation of the protocol using Schrödinger cat states and for initial von Mises distributed states.

SCHRÖDINGER CAT STATES

For the numerical simulation of breeding using squeezed Schrödinger cat states as input, the states are stored and manipulated in the \hat{q} quadrature basis. The beam splitters are implemented using the action of a beam splitter in phase space, see Eqs. 4.4. When storing a wave function in discrete coordinates, an operation like $\hat{q}_1 \rightarrow (\hat{q}_1 - \hat{q}_2)/\sqrt{2}$ changes the number of points. To keep the memory requirements constant, the wave function was therefore interpolated to the original coordinates using a cubic spline (see the function `scipy.interpolate.UnivariateSpline` in the SciPy package [4]). The wave functions are stored using $(2^{12} + 1)$ points, so interpolation should not add significant errors. In order to switch between the measurement and standard bases, a fast Fourier transform is used.

VON MISES DISTRIBUTED STATES

The simulation of von Mises distributed states is based on the analytical result for the output of a breeding round, see Eqs. (4.25) and (4.26). Because the main part of this simulation is based on analytical results, numerical errors from the simulation itself are mostly negligible.

We simulate a protocol using $M = 6$ rounds of breeding, where the initial state is chosen such that the effective squeezing is $\Delta_q = 0.2$. Because the result of all $(2^{M+1} - 1)$ homodyne measurements within one run of the protocol is continuous, it is infeasible

to use a brute-force approach where all possible measurement outcomes are simulated. For this reason, we repeat the procedure 1000 times for each $M = 1 \dots 6$, obtaining a single final state per run.

The implementation has the same structure as Fig. 4.4, see the code below. In order to improve performance, the states are not stored explicitly. Because the post measurement state only depends on the parameters κ_1, κ_2 and the rescaled measurement result x (see Eq. (4.25)), it is sufficient to store only the parameters κ of the von Mises distribution. The simulation works as follows:

1. (l. 11) Initialize 2^M identical states of the form Eq. (4.20), with $\lim_{\Delta} \rightarrow 0$.
2. (l. 15) repeat the following for rounds $k = 0, \dots, (M - 1)$:
 - (a) (l. 17) Assign the 2^{M-k} states pair-wise as input for the 2^{M-k-1} beam splitters.
 - (b) (l. 24) For each pair, compute the probability $\mathbb{P}(x)$ to measure the rescaled result x according to Eq. (4.26).
 - (c) (l. 26) For each pair, randomly choose the rescaled measurement result according to $\mathbb{P}(x)$.
 - (d) (l. 30) Given the measurement results, compute κ for all 2^{M-k-1} output states according to Eq. (4.25).
3. (l. 33) For the single remaining state, compute the effective squeezing parameter according to Eq. (2.23).
4. (l. 34) Return the effective squeezing parameter.

```

0 def mises_breed(k_init:float, M:int)->float, float:
1     """
2     Breed 2**M von Mises distributed states with parameter k_init for M rounds
3
4     Arguments:
5         k_init {float} -- initial kappa
6         M {int} -- number of rounds
7
8     Returns:
9         delta {float}, weight {float} -- effective squeezing, probability to obtain
10        the simulated results
11    """
12    k = np.array([k_init] * 2**M)
13    w = np.array([1] * 2**M)
14
15    # Do breeding for M rounds
16    for _ in range(M):
17        # Assign the states pair-wise to the beam splitters
18        k = k.reshape(2, -1)
19        w = w.reshape(2, -1)
20        w = np.product(w, axis=0)
21        w = w / np.sum(w)    # Using in-place division causes TypeError
22
23        x = []
24        # For each beam splitter, do a breeding measurement

```

```

24     for i, line in enumerate(_prob_p(*k)):
25         line /= np.sum(line)
26         idx = np.random.choice(IDX, p=line)
27         x.append(PHASE_COS[idx])
28         w[i] *= line[idx]
29     x = np.asarray(x)
30     k = np.sqrt(k[0]**2 + k[1]**2 + 2 * k[0] * k[1] * p)
31     assert len(k) == 1          # At the end of the protocol, one state is left
32     weight = w[-1]
33     delta = mises_std(k[-1])    # Calculate the effective squeezing, given kappa
34     return delta, weight

```

A.1.3. SIMULATIONS OF MODULAR QUADRATURE MEASUREMENTS

In this section, we discuss details of the numerical simulations used in Chapter 5. The full code is available under <https://gitlab.com/djweigand/photonpressure>.

The numerical simulations were implemented using the Qutip Python package [5]. In the numerics, we apply a counter-displacement drive $Z^{-\bar{n}}$, where \bar{n} is the mean photon number of the initial state of the ancilla oscillator, in order to minimize the photon number of the state in the target oscillator. The Hamiltonian for the interaction between target and oscillator in the ideal case is then

$$H_{\text{num}} := \frac{g|\alpha|^2}{2}(\hat{b}^\dagger + \hat{b}) - g\hat{a}^\dagger \hat{a}(\hat{b}^\dagger + \hat{b}),$$

where $|\alpha|^2$ is the number of photons in the initial state of the ancilla oscillator and the Hamiltonian is turned on for time $t_{\text{coupl}} = \sqrt{2\pi}/g$, see the end of Section 5.3.3.

All simulations model a direct, perfect heterodyne measurement by projecting the ancilla oscillator onto a coherent state. The measurement result is chosen by computing the Husimi-Q function, and drawing 200 randomly chosen samples (unless mentioned otherwise) with the Husimi-Q function as probability distribution. Because this model of measurement is very strong, the photon numbers of the post measurement state may be very large, with some events exceeding 100 photons, see Fig. A.1 on the left. Note that for GKP states, the distribution of the photon number is very wide, with the standard deviation equal to the expected photon number. Therefore, the Hilbert spaces of the target and ancilla oscillators were approximated using 500 and 20 Fock states, respectively.

To estimate the accuracy of the simulations, we use that the effective squeezing Δ_p of the vacuum state should stay constant in the case of a noiseless protocol. The results are shown in Fig. A.1 on the right. As shown there, errors are negligible up to an initial ancilla state with $\bar{n} = 3.5$ photons, and the relative error for $\bar{n} = 4$ photons is still below 1% in most cases. For these reasons, and because the effective squeezing achieved with $|\alpha = 2\rangle$ as initial ancilla state is already very strong, we restrict the simulations to $\bar{n} = 1, \dots, 4$.

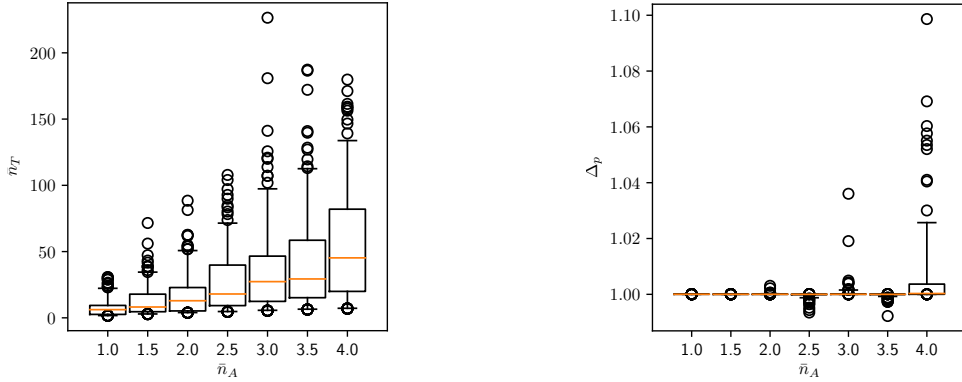


Figure A.1: Box and whisker plot of the expected number of photons (left) and the effective squeezing Δ_p (right) of the final state after a measurement of S_q . The target oscillator starts in the vacuum state, and the ancilla oscillator with the coherent state $|\alpha = \sqrt{\bar{n}}\rangle$ (compare Fig. 5.7). For every α , a total of 200 samples was simulated. The orange line indicates the median, the box indicates the 25 and 75 percentiles, the whiskers the 5 and 95 percentiles, events above or below these thresholds are shown individually. For some events, the final state of the target oscillator has a mean photon number exceeding 100, therefore a large Hilbert space is required to faithfully represent those states. From analytical considerations, we know that $\Delta_p = 1$ should be constant, independent of the measurement results. As can be seen, errors are negligible up to $\bar{n} = 3.5$, for $\bar{n} = 4$, the relative error for most events is still below 1%. Previously published in D. J. Weigand and B. M. Terhal, “Realizing modular quadrature measurements via a tunable photon-pressure coupling in circuit QED”, *Physical Review A* **101**, 053840 (2020), licensed under CC-BY 4.0 [6] © ⓘ.

A.2. RELATING A PHOTON-PRESSURE COUPLING TO PHASE ESTIMATION

The photon pressure coupling in Chapter 5 can also be interpreted as a variant of phase estimation. To this end, we will first rewrite the initial coherent state $|\alpha\rangle$ of the ancilla oscillator as a state in a system with sufficiently large spin using the Holstein-Primakoff transformation. Afterwards, we replace the single large spin by a collection of small spins (qubits) to obtain a spin coherent state, and see what the action of the photon-pressure coupling on such a state is.

A.2.1. INITIAL STATE

In the harmonic oscillator, a coherent state $|\alpha\rangle$ can be written as a displacement $D(\alpha)$ acting on the vacuum state:

$$|\alpha\rangle = D(\alpha)|\text{vac}\rangle = \exp(\alpha\hat{a}^\dagger - \alpha^*\hat{a})|\text{vac}\rangle.$$

For the Holstein-Primakoff transformation, we identify the spin ladder operators with those of the harmonic oscillator [7]:

$$S_+ \equiv \sqrt{2S}\sqrt{1 - \frac{\hat{a}^\dagger\hat{a}}{2S}}\hat{a} \approx \sqrt{2S}\hat{a}, \quad S_- \equiv \sqrt{2S}\hat{a}^\dagger\sqrt{1 - \frac{\hat{a}^\dagger\hat{a}}{2S}} \approx \sqrt{2S}\hat{a}^\dagger, \quad S_z \equiv S - \hat{a}^\dagger\hat{a}, \quad (\text{A.1})$$

where the approximation is $\hat{a}^\dagger\hat{a} \ll S$ and S is the total spin. From the map between S_z and the photon number operator $\hat{a}^\dagger\hat{a}$, we can see that the “vacuum state” in the spin

is defined as the eigenstate $S_z |\text{vac}_s\rangle = S |\text{vac}_s\rangle$, where the subscript s indicates that the state is defined on a spin. In Chapter 5, we argued that α can be assumed to be real without loss of generality. For real α , we can define

$$|\alpha_s\rangle = D(\alpha_s) |\text{vac}_s\rangle = \exp\left(\frac{\alpha}{\sqrt{2S}}(S_- - S_+)\right) |\text{vac}_s\rangle = \exp\left(-\frac{i\alpha}{\sqrt{2S}}2S_y\right) |\text{vac}_s\rangle.$$

In the second step, we identify the state large spin S with a product state of $M = 2S$ qubits. We have¹

$$S_x \equiv \sum_{j=0}^{M-1} \sigma_{x,j}, \quad S_y \equiv \sum_{j=0}^{M-1} -\sigma_{y,j}, \quad S_z \equiv \sum_{j=0}^{M-1} \sigma_{z,j}, \quad |\text{vac}_s\rangle \equiv \prod_{j=0}^{2S-1} |0\rangle_j,$$

where j labels qubits $0, \dots, M$. The coherent state $|\alpha_s\rangle$ given by

$$\begin{aligned} |\alpha_s\rangle &= \prod_{j=0}^{M-1} \exp\left(\frac{i\alpha}{\sqrt{M}}2\sigma_{y,j}\right) |0\rangle_j = \prod_{j=0}^{M-1} \left(\cos\left(\frac{\alpha}{\sqrt{M}}\right) \mathbb{1} + i \sin\left(\frac{\alpha}{\sqrt{M}}\right) Y\right) |0\rangle_j \\ &= \prod_{j=0}^{M-1} \left(\cos\left(\frac{\alpha}{\sqrt{M}}\right) |0\rangle_j + \sin\left(\frac{\alpha}{\sqrt{M}}\right) |1\rangle_j\right) \\ &= \sum_{k=0}^M \binom{M}{k}^{1/2} \cos\left(\frac{\alpha}{\sqrt{M}}\right)^{M-k} \sin\left(\frac{\alpha}{\sqrt{M}}\right)^k |D_k^M\rangle, \end{aligned} \quad (\text{A.2})$$

where

$$|D_k^M\rangle = \binom{M}{k}^{-1/2} \sum_{\substack{\mathbf{k} \in \{0,1\}^M \\ w(\mathbf{k})=k}} |\mathbf{k}\rangle$$

is a Dicke state, i.e. a symmetric superposition over all M qubit states with Hamming weight k . If we compute the “photon number” distribution $\mathbb{P}(k)$ for $|\alpha_s\rangle$, we obtain a binomial distribution. We can also see that the distribution converges to the Poissonian distribution expected for a coherent state in the harmonic oscillator if we take the limit of a large number of qubits $M \rightarrow \infty$:

$$\lim_{M \rightarrow \infty} \mathbb{P}(k) = \lim_{M \rightarrow \infty} \binom{M}{k} \left(1 - \sin\left(\frac{\alpha}{\sqrt{M}}\right)^2\right)^{M-k} \left(\sin\left(\frac{\alpha}{\sqrt{M}}\right)^2\right)^k = e^{-|\alpha|^2} \frac{|\alpha|^2}{k!}.$$

A.2.2. PHOTON-PRESSURE HAMILTONIAN

Using Eq. (A.1), we can also rewrite the photon pressure interaction as a Hamiltonian acting on many qubits:

$$H_{\text{PP}} = \sqrt{2}g \hat{a}^\dagger \hat{a} \hat{q}_T \longrightarrow \sqrt{2}g \left(S - \sum_{j=0}^{M-1} \sigma_{z,j}\right) \hat{q}_T = \sum_{j=0}^{M-1} \left(\sqrt{2}g \left(\frac{1}{2} - \sigma_{z,j}\right) \hat{q}_T\right).$$

¹Note the change of sign for σ_y . This is because $|0\rangle$ is a high-energy state in a spin, but a low energy state in the qubit.

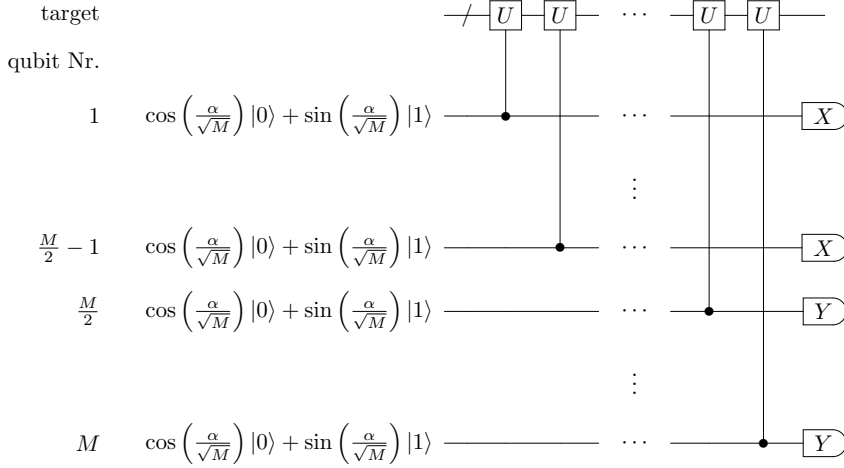


Figure A.2: Equivalent circuit to a photon number controlled displacement, using $M = 2n$, $n \in \mathbb{N}$ ancilla qubits. The target system is some harmonic oscillator (symbolized by the slash). The equivalence to the scheme from Chapter 5 (see Fig. 5.1) is exact for $M \rightarrow \infty$. In the limit, the initial state of the ancilla qubits behaves like a coherent state. Measuring half of the ancilla qubits in the Pauli X basis and the other half in the Pauli Y basis is equivalent to a heterodyne measurement.

We can see that this is the same conditional displacement coupling each qubit to the oscillator. If we turn this Hamiltonian on for time $t_{\text{coupl}} = \sqrt{2\pi}/g$, the time evolution operator is given by (compare Eq. (5.3))

$$U_{\text{PP},s} = \prod_{j=0}^{M-1} \exp\left(i2\sqrt{\pi}\hat{q}\left(\frac{1}{2} - \sigma_{z,j}\right)\right).$$

Applying this time evolution to the initial state from Eq. (A.2), the pre-measurement state is thus

$$U_{\text{PP},s}|\alpha_s\rangle = \prod_{j=0}^{M-1} \left(\cos\left(\frac{\alpha}{\sqrt{M}}\right)|0\rangle_j + \exp(i2\sqrt{\pi}\hat{q})\sin\left(\frac{\alpha}{\sqrt{M}}\right)|1\rangle_j \right). \quad (\text{A.3})$$

A.2.3. HETERODYNE MEASUREMENT

Using the mapping from Eq. (A.1) a third time, we can identify the \hat{q} quadrature of the oscillator with the operator S_x for the qubits and the \hat{p} quadrature with the operator S_y . The heterodyne measurement in the optical setting is implemented by sending the coherent state through a beam splitter, and then measuring one arm in the \hat{q} basis and the other arm in the \hat{p} basis.

In the qubit setting, every qubit will be in the same state after the coupling, see Eq. (A.3). We can therefore easily emulate the beam splitter by simply assigning half of the qubits to group A , and the other half to a second group B . As expected from a beam splitter where one of the input ports is in the vacuum state, the average Hamming weight (i. e. the average “photon number”) of each group is half the average Hamming

weight of all qubits. Following the mapping of the quadratures, the heterodyne measurement is then a joint measurement of the total spin operator $S_{x,A}(S_{y,B})$ for group A (B). As $S_x \equiv \sum_{j=0}^{M-1} \sigma_{x,j}$ and $S_y \equiv \sum_{j=0}^{M-1} -\sigma_{y,j}$, this means simply that we measure each qubit of group A (B) individually in the Pauli X (Y) basis, respectively. The measurement result for the operator $S_{x,A}(S_{y,B})$ is then simply the Hamming weight of the measurement record for group A (B).

Before the measurement, all qubits are in the same state. Therefore, all permutations of a particular measurement result are equivalent, and any linear combination of equivalent measurement results has the same back action on the target oscillator. This implies that the back action on the target oscillator is the same whether the qubits are measured simultaneously or sequentially, as long as the eigenvalue of the total spin operator $S_x(S_y)$ is the same. With the same reasoning, we can see that the probability to obtain a result for the eigenvalue of $S_x(S_y)$ is also the same whether we measure sequentially or simultaneously.

To make the correspondence to non-adaptive phase estimation more clear, consider the evolution of a single qubit belonging to group A , e.g. qubit 1 in Fig. A.2. The pre-measurement state is

$$HU_{PP,s}|\alpha_s\rangle_1 = \left[\frac{1}{\sqrt{2}} \left(\cos\left(\frac{\alpha}{\sqrt{M}}\right) + e^{i2\sqrt{\pi}\hat{q}} \sin\left(\frac{\alpha}{\sqrt{M}}\right) \right) |+\rangle_1 + \frac{1}{\sqrt{2}} \left(\cos\left(\frac{\alpha}{\sqrt{M}}\right) - e^{i2\sqrt{\pi}\hat{q}} \sin\left(\frac{\alpha}{\sqrt{M}}\right) \right) |-\rangle_1 \right],$$

where H is the Hadamard gate and $|\alpha_s\rangle_1$ indicates the term involving qubit 1 within the larger product state $|\alpha_s\rangle$. This state has the same form as the pre-measurement state for non-adaptive phase estimation and measurement in the Pauli X basis, see Section 3.1.2. It is straightforward to see the pre-measurement state of group B has the same form as the pre-measurement state of non-adaptive phase estimation and measurement in the Pauli Y basis. Assuming that the target oscillator is in a position eigenstate $|q\rangle$ with eigenvalue q , the probabilities to obtain result 0 for the X and Y measurements of group A and B are given by

$$\begin{aligned} \mathbb{P}_X = \mathbb{P}(0|A) &= \frac{1}{2} + \cos\left(\frac{\alpha}{\sqrt{M}}\right) \sin\left(\frac{\alpha}{\sqrt{M}}\right) \cos(2\sqrt{\pi}q) \\ \mathbb{P}_Y = \mathbb{P}(0|B) &= \frac{1}{2} + \cos\left(\frac{\alpha}{\sqrt{M}}\right) \sin\left(\frac{\alpha}{\sqrt{M}}\right) \sin(2\sqrt{\pi}q) \end{aligned}$$

The eigenvalue q can now be obtained as a function of \mathbb{P}_X and \mathbb{P}_Y :

$$2\sqrt{\pi}q = \arg\left(\frac{\mathbb{P}_X + i\mathbb{P}_Y - \frac{1+i}{2}}{\cos\left(\frac{\alpha}{\sqrt{M}}\right) \sin\left(\frac{\alpha}{\sqrt{M}}\right)} \right). \quad (\text{A.4})$$

Note that this is a similar form as the interpretation of measurement results in non-adaptive phase estimation, compare Eq. (3.2).

Thus, approximating the ancilla oscillator and the optomechanical coupling with many ancilla qubits gives a variation of non-adaptive phase estimation (see Section 3.1.2),

in a limit where each individual measurement is made weaker, but the number of measurements is increased accordingly. In fact, if we choose $\alpha = \frac{\pi\sqrt{M}}{4}$, Eqs. (3.2) and (A.4) are identical and we recover non-adaptive phase estimation with M qubits exactly (Although the approximation in Eq. (A.1) is not valid for such large α).

REFERENCES

- [1] K. Duivenvoorden, B. M. Terhal, and D. J. Weigand, “Single-mode displacement sensor”, *Physical Review A* **95**, 012305 (2017).
- [2] D. J. Weigand and B. M. Terhal, “Realizing modular quadrature measurements via a tunable photon-pressure coupling in circuit QED”, *Physical Review A* **101**, 053840 (2020).
- [3] B. M. Terhal and D. J. Weigand, “Encoding a qubit into a cavity mode in circuit QED using phase estimation”, *Physical Review A* **93**, 012315 (2016).
- [4] P. Virtanen, R. Gommers, T. E. Oliphant, M. Haberland, T. Reddy, D. Cournapeau, E. Burovski, P. Peterson, W. Weckesser, J. Bright, S. J. van der Walt, M. Brett, J. Wilson, K. J. Millman, N. Mayorov, A. R. J. Nelson, E. Jones, R. Kern, E. Larson, C. J. Carey, Í. Polat, Y. Feng, E. W. Moore, J. VanderPlas, D. Laxalde, J. Perktold, R. Cimrman, I. Henriksen, E. A. Quintero, C. R. Harris, A. M. Archibald, A. H. Ribeiro, F. Pedregosa, and P. van Mulbregt, “SciPy 1.0: fundamental algorithms for scientific computing in Python”, *Nature Methods* **17**, 261 (2020).
- [5] J. Johansson, P. Nation, and F. Nori, “QuTiP 2: a Python framework for the dynamics of open quantum systems”, *Computer Physics Communications* **184**, 1234 (2013).
- [6] *Creative Commons Attribution-ShareAlike 3.0 Unported License*, Creative Commons Corporation, <https://creativecommons.org/licenses/by-sa/3.0/>.
- [7] T. Holstein and H. Primakoff, “Field dependence of the intrinsic domain magnetization of a ferromagnet”, *Physical Review* **58**, 1098 (1940).

CURRICULUM VITÆ

Daniel Jonathan WEIGAND

25-05-1990 Born in Neustadt an der Weinstraße, Germany.

EDUCATION

2000–2008	High School Leibniz Gymnasium, Neustadt an der Weinstraße, Germany
2008–2009	Civil Service Qualification as Advanced Emergency Medical Technician (Rettungssanitäter)
2009–2013	Bachelor in Physics RWTH Aachen University, Germany
2013–2015	Master in Physics RWTH Aachen University, Germany
2015–2017	PhD in Physics RWTH Aachen University, Germany
2017–2020	Delft University of Technology, Netherlands <i>Thesis:</i> Encoding a Qubit into an Oscillator with Near-Term Experimental Devices <i>Promotor:</i> Prof. dr. B. M. Terhal

LIST OF PUBLICATIONS

5. **D. J. Weigand**, B. M. Terhal *Realizing modular quadrature measurements via a tunable photon-pressure coupling in circuit-QED*, [Physical Review A **101**, 053840 \(2020\)](#).
4. **D. J. Weigand**, B. M. Terhal, *Generating grid states from Schrödinger-cat states without post-selection*, [Physical Review A **97**, 022341 \(2018\)](#).
3. M. Menzel, J. Reckfort, **D. J. Weigand**, H. Köse, K. Amunts, and M. Axer, *Diattenuation of brain tissue and its impact on 3D polarized light imaging*, [Biomedical Optics express **8**, 3163-3197 \(2017\)](#).
2. K. Duivenvoorden, B. M. Terhal, and **D. J. Weigand**, *Single-mode displacement sensor*, [Physical Review A **95**, 012305 \(2017\)](#).
1. B. M. Terhal and **D. J. Weigand**, *Encoding a qubit into a cavity mode in circuit QED using phase estimation*, [Physical Review A **93**, 012315 \(2016\)](#).